

Assessment of Structural Loads in Wind Farms under Consideration of Wake Redirection Control

A thesis accepted by the Faculty of Aerospace Engineering and Geodesy of the
University of Stuttgart in partial fulfilment of the requirements for the degree of
Doctor of Engineering Sciences (Dr.-Ing.)

by

Matthias Kretschmer

born in Esslingen am Neckar, Germany

Main referee: Prof. Dr. Po Wen Cheng
Co-referee: Prof. Dr. Dominic von Terzi

Date of defense: 17.02.2023

Institute of Aircraft Design
University of Stuttgart
2024

Acknowledgements

At the end of this journey, I would like to take a step back and express my deepest gratitude to a few people. First, I would like to thank Po Wen Cheng for your encouragement, freedom and advice. Thank you to Dominic von Terzi for providing the second opinion and especially for the detailed feedback and suggestions.

I would like to thank my colleagues at the SWE for their support in all matters and for providing such a pleasant atmosphere. My sincerest gratitude goes to Matthias and Friedemann for kickstarting me in wind energy research as well as Birger, Umut, Kolja, Stefan, Ines, Maayen, Florian, Martin, Oliver, Alex, Ricardo, Holger, Tim, Sarah, Steffen, Frank, Fiona, Vasilis, Viola and all other colleagues. Further, I would like to thank all my students, in particular Nico, Julian, Omar, Frederik, German, Domenico, Philipp, Carsten, Felix. A special thanks goes to the people at NREL Jason, Kelsey, Emmanuel, Scott, Fabian, Jeremy, Liz, Caitlyn, Hannah with whom I had the pleasure of collaborating and sharing some enjoyable skiing trips. I want to extend my appreciation to the members of the RAVE consortium, who work diligently to provide the measurement data from the alpha ventus wind farm.

I thank my family, Mama and Papa for always having my back. And finally, to the most important person in my life, Lena. Thank you for always being there, for your patience, encouragement and unlimited support. You and our wonderful children, Frida and Jakob, remind me of the really important things in life.

Contents

Abbreviations	ix
List of Symbols	xi
Abstract	xiii
Kurzfassung	xv
1 Introduction	1
1.1 Motivation	1
1.2 Research objectives	2
1.3 Related Work	2
1.4 Outline	4
2 Background	5
2.1 Atmospheric boundary layer	5
2.1.1 Turbulence	6
2.1.2 Atmospheric stability	8
2.1.3 Vertical wind speed profile	10
2.2 Fatigue loading of wind turbines	12
2.2.1 Fatigue load representation and calculation	13
2.2.2 Long-term fatigue evaluation	14
2.3 Wake effects	15
2.3.1 Velocity deficit	16
2.3.2 Wake meandering	18
2.3.3 Effects of yawed operation	18
2.4 Wind farm control	20
2.4.1 Axial induction control	20
2.4.2 Wake redirection control	21
3 Simulation modelling	23
3.1 Atmospheric boundary layer modelling	23
3.1.1 Mann uniform shear turbulence model	23
3.1.2 Large eddy simulations	27
3.2 Wind farm flow modelling	27
3.2.1 Steady-state low-fidelity flow simulation	29

3.2.2	Coupled large eddy simulations	31
3.3	Aeroelastic wind farm simulation	32
3.3.1	FAST.Farm implementation	32
3.3.2	Aeroelastic simulation of a single wind turbine	33
3.3.3	Wake dynamics: Implementation of the dynamic wake meandering model	34
3.3.4	Wake-added turbulence model	38
3.3.5	Spatial and temporal discretisation	40
4	Simulation model calibration and validation	43
4.1	Calibration of wake-added turbulence model	43
4.1.1	Reference simulations: PALM-LES	44
4.1.2	Wake-added turbulence model parametrisation	46
4.1.3	Wake-added turbulence model discretisation	52
4.2	Aeroelastic turbine model validation for free-stream conditions	57
4.2.1	Alpha ventus measurement data base	57
4.2.2	Load case definition and simulation setup	59
4.2.3	Transfer of environmental conditions to simulations	61
4.2.4	Validation results	62
4.3	Aeroelastic turbine model validation for single wake situations	65
4.3.1	Load case definition and simulation setup	67
4.3.2	Validation results	67
4.3.3	Discussion	76
4.3.4	Conclusions	77
4.4	Low-fidelity model calibration for wind farm optimisation	78
4.4.1	Load case definition and simulation setup	78
4.4.2	Optimisation of FLORIS model parameters	81
5	Structural loads under consideration of wake redirection control	85
5.1	Wind turbine model and sensor specification	85
5.2	Definition of environmental conditions	86
5.2.1	Synthetic short-term atmospheric conditions	87
5.2.2	Measured short-term atmospheric conditions	87
5.2.3	Measured long-term atmospheric conditions	88
5.3	Structural loads of a free-stream turbine during yawed operation	88
5.3.1	Load case definition and simulation setup	89
5.3.2	Structural load distributions at component level	90
5.3.3	Long-term evaluation	92
5.3.4	Conclusions	95
5.4	Single wake characteristics	95
5.4.1	Load case definition and simulation setup	96
5.4.2	Wake meandering characteristics	96
5.4.3	Wake profiles	97
5.4.4	Conclusions	103
5.5	Structural loads of a waked turbine during yawed operation	105
5.5.1	Load case definition and simulation setup	105
5.5.2	Structural load distributions at component level	106
5.5.3	Conclusions	110

6	Optimisation of wind farm operation	113
6.1	Load case definition	113
6.2	Optimisation of yaw angles	114
6.2.1	Surrogate model for the structural loads	114
6.2.2	Cost functions for different objectives	116
6.3	Assessment of wind farm operation strategies	118
6.3.1	Long-term evaluation	118
6.3.2	Detailed evaluation of specific operational points	122
6.4	Conclusions	130
7	Conclusions	131
7.1	Summary and main conclusions	131
7.1.1	Calibration and validation of the aeroelastic simulation model	132
7.1.2	Structural loads under consideration of wake redirection control	133
7.1.3	Optimisation of wind farm operation	135
7.2	Outlook	135
A	Appendix	137
A.1	Additional results from the wake-added turbulence calibration	138
A.2	Additional results from the OpenFAST validation	146
A.3	Additional results from the FLORIS calibration	147
A.4	Additional load distributions of a free stream turbine in yawed operation	149
A.4.1	Short-term evaluation	149
A.4.2	Long-term evaluation	164
A.5	Additional load distributions of a waked turbine in yawed operation	167
A.6	Additional results from the optimisation of operation strategies	182
A.7	Manual of the wake-added turbulence feature in FAST.Farm	187
A.7.1	Background	187
A.7.2	Implementation	187
A.7.3	Setup	189
	Bibliography	191
	Curriculum Vitae	205

Abbreviations

1P	One-per-Revolution
3P	Three-per-Revolution
ABL	Atmospheric Boundary Layer
ACD	Actuator Disc
ACL	Actuator Line
AEP	Annual Energy Production
AS	Atmospheric Stability
AWAE	Ambient Wind and Array Effects
BEM	Blade Element Momentum
CFD	Computational Fluid Dynamics
DEL	Damage Equivalent Load
DLC	Design Load Case
DLL	Dynamic Link Library
DoE	Design of Experiments
DoF	Degree of Freedom
DWM	Dynamic Wake Meandering
ew	edgewise
fa	fore-aft
FAST	Fatigue, Aerodynamics, Structures, and Turbulence
FFoR	Fixed Frame of Reference
FFT	Fast Fourier Transform
FLORIS	FLOw Redirection and Induction in Steady State
fw	flapwise
IEC	International Electrotechnical Commission
IFB	Institut für Flugzeugbau (Institute of Aircraft Design)
IPC	Individual Pitch Control
JONSWAP	Joint North Sea Wave Observation Project
LCoE	Levelised Cost of Energy
LES	Large Eddy Simulation
LIDAR	Light Detection and Ranging
LSS	Low-Speed Shaft
MABL	Marine Atmospheric Boundary Layer
MBS	Multibody Simulation
MFoR	Meandering Frame of Reference

NREL	National Renewable Energy Laboratory
PALM	Parallelised Large-Eddy Simulation Model
PDF	Probability Density Function
PSD	Power Spectral Density
RANS	Reynolds-Averaged Navier-Stokes
RAVE	Research at alpha ventus
SC	Super Controller
SCADA	Supervisory Control and Data Acquisition
SLSQP	Sequential Least Squares Programming
ss	side-side
SWE	Stuttgart Wind Energy
TKE	Turbulent Kinetic Energy
TSO	Transmission Grid Operator
WD	Wake Dynamics

List of Symbols

Greek letters

α_k	Kolmogorov's spectral constant
α_{shear}	Wind shear exponent of exponential power law approximation
δ	Lateral wake deflection from rotor-centre (m)
ϵ	Rate of viscous dissipation of specific turbulent energy ($\text{m}^2 \text{s}^{-3}$)
Γ	Anisotropy parameter of Mann's spectral tensor
κ	Von Kármán constant, Poisson constant
Λ	Integral length scale (m)
ν_T	Eddy viscosity ($\text{m}^2 \text{s}^{-1}$)
φ	Wind direction ($^\circ$)
ϕ	Angular coordinate (rad)
σ	Standard deviation
θ_m	Yaw misalignment angle ($^\circ$)
θ_w	Wake skew angle ($^\circ$)
Θ	Potential temperature (K)
Θ_v	Virtual potential temperature (K)
ζ	Dimensionless stability parameter

Roman letters

a	Axial induction factor
c_T	Thrust coefficient
C	Weibull scale parameter (m s^{-1})
D_W	Wake deficit diameter (m)
ΔS	Load range from rainflow counting
D	Rotor diameter (m); damage
f_c	Cut-off frequency (s^{-1})
f	Frequency (s^{-1})
g	Gravitational constant (m s^{-2})
i	Running variable
j	Running variable
k	Wavenumber (m^{-1})
k_{m1}	Calibration factor of the wake-added turbulence model in FAST.Farm
k_{m2}	Calibration factor of the wake-added turbulence model in FAST.Farm
k_{mt}	Calibration factor of the wake-added turbulence model in FAST.Farm
k	Weibull shape parameter

L	Length scale (m)
L_*	Obukhov length (m)
L_M	Length scale of Mann's spectral tensor (m)
m	Exponent for the calculation of equivalent load cycles
N	Reference number of load cycles
p	Pressure (Pa)
\mathbf{r}	Spatial separation vector (m)
\tilde{r}	Radial coordinate normalised by rotor radius
R	Rotor radius (m)
r	Radial coordinate (m); distance between points (m); mixing ratio of water vapor
r_L	Mixing ratio of liquid water in the air
t	Time (s)
T	Time range (s); Temperature (K)
TI_{WAT}	Turbulence intensity from wake-added turbulence
TI	Turbulence intensity
$TI_{amb,Rotor}$	Spatial turbulence intensity around the rotor
u	Longitudinal wind speed (m s^{-1})
\bar{u}	Mean wind speed (m s^{-1})
u'	Turbulent fluctuation component of the longitudinal velocity (m s^{-1})
v'	Turbulent fluctuation component of the lateral velocity (m s^{-1})
w'	Turbulent fluctuation component of the vertical velocity (m s^{-1})
u_*	Friction velocity (m s^{-1})
u_{def}	Velocity deficit
u_∞	Freestream wind speed (m s^{-1})
v	Lateral wind speed (m s^{-1})
\mathbf{v}	Velocity vector (m s^{-1})
$V_{DiskAvg}$	Rotor disk-averaged ambient wind speed normal to the disk (m s^{-1})
V_r	Radial velocity (m s^{-1})
V_x	Axial velocity (m s^{-1})
w	Vertical wind speed (m s^{-1}); weighting factor
$\overline{w'T'}$	Kinematic virtual heat flux (m K s^{-1})
\mathbf{x}	Position vector (m)
x	Longitudinal coordinate (m); longitudinal displacement (m)
y	Lateral coordinate (m); lateral displacement (m)
z_0	Roughness length (m)
z	Vertical coordinate (m); vertical displacement (m)

Abstract

Wind farm control enables the operation of wind farms in a collective optimum that considers all turbines instead of operating the individual wind turbines in their local optima. A collective optimum of a wind farm is dependent on the objective, which can be, for instance, increasing the energy yield, reducing the structural loading of the wind turbines or providing ancillary services to the electricity grid. The development of new wind farm control techniques requires knowledge in various disciplines that include wind turbine engineering (control design and implementation, structural and aerodynamic design, load assessment and validation), multidisciplinary optimisation, wind resource modelling and atmospheric boundary layer modelling connected with the modelling of wakes.

This thesis covers many of the aforementioned disciplines in order to investigate the wake redirection control concept as one option for wind farm control in detail. Wake redirection control is based on the concept of deflecting the wake behind a wind turbine through yaw-misaligned operation. The aim is to mitigate the wake effects on the downstream turbine by redirecting the wake. Hence, the downstream turbine can generate, for instance, more power than, ideally, compensates or exceeds the power losses at the upstream turbine caused by yaw-misalignment in below-rated conditions.

For the numerical assessment, the aeroelastic simulation tool FAST.Farm is utilised. An adequate setup of the tool is developed to allow the investigation of various realistic operating conditions including different atmospheric stabilities. In addition, FAST.Farm is improved by implementing a model to include the wake-added small-scale turbulence. FAST.Farm is then calibrated against high-fidelity large eddy simulations and validated by using measurement data from the alpha ventus wind farm. Overall, good agreement between simulations and measurements is achieved for the structural loads in terms of statistical results and frequency response at the tower-base and blade-root. The inclusion of wake-added turbulence is crucial to avoid underestimation of the turbulence in the wake and consequently the loads. This is especially relevant in stable atmospheric conditions, where the ambient turbulence intensity is low and the meandering of the wake is weak. Without wake-added turbulence, the Damage Equivalent Loads (DELs) of the bending moment in the fore-aft direction are underestimated

by up to 87% in full-wake conditions compared to the measurement data; the error reduces to 2% when the wake-added turbulence module is activated in the simulations.

An extensive investigation of the wake redirection control concept and its consequences on the structural loads is performed in a simulation study with the validated tool FAST.Farm. For a turbine in free-stream conditions, the fatigue loads at different turbine components are analysed, with changing atmospheric conditions and yaw misalignment angles. The largest effects of yaw misalignment on the load variations are found for stable atmospheric conditions with strong vertical wind shear and low turbulence intensity. In contrast, the influence of yaw misalignment on the fatigue loads becomes less important in unstable atmospheric stability with low vertical wind shear and high turbulence intensity. The investigation is extended for a turbine that is subjected to waked inflow conditions. Especially in partial wake situations, where the wake-centre lays between $\pm 0.75 D$ (turbine diameter) measured from the rotor-centre of the waked turbine, the load distributions differ significantly from free-stream conditions. A directional dependency of the loads is found with respect to the lateral wake offset: The loads tend to be higher for negative lateral wake offsets compared to the loads from the same positive lateral wake offsets, because of higher load amplitudes over one rotor revolution.

The gained knowledge is finally applied in the derivation of optimal operation strategies by using the wake redirection control approach for exemplary wind farm configurations and changing environmental conditions. An optimisation is performed using different objective functions including maximising the energy yield and reducing the structural loads at the wind turbines. The resulting optimal operation strategies are assessed by using aeroelastic simulations in FAST.Farm. The long-term evaluation suggests that the Annual Energy Production (AEP) of the considered turbine array setups can be increased compared to the baseline scenario without wind farm control, when the main objective is set to power maximisation while the fatigue loads at the turbines are not or equally weighted. Consequently, the strategies that focus on minimising the fatigue loads result into less AEP compared to the baseline strategy. The consideration of fatigue loads in the optimisation of operation strategies is realised with an efficient surrogate model. With this approach, strategies are derived that are able to reduce the fatigue loads at specific components significantly.

Kurzfassung

Im Gegensatz zur getrennten Betrachtung der einzelnen Windenergieanlagen (WEA) im Windpark ermöglicht die Windparkregelung den Betrieb von Windparks in einem übergeordneten Optimalzustand, der alle WEA berücksichtigt. Dieser hängt von der gewünschten Zielvorgabe ab, die z.B. eine Erhöhung der Leistungsproduktion, eine Reduktion der Strukturlasten oder das Bereitstellen von Hilfsdienstleistungen für das elektrische Netz sein kann. Die Entwicklung von neuen Algorithmen zur Windparkregelung erfordert Kenntnisse in verschiedenen Bereichen, zu denen die Technik der WEA (Entwurf und Implementierung der Regelung, Entwurf der Struktur, Lastannahmen und deren Validierung), die Modellierung der Windressource sowie der atmosphärischen Grenzschicht in Verbindung mit Nachlaufeffekten gehören.

In dieser Arbeit werden einige der genannten Bereiche abgedeckt, um das Windparkregelungskonzept der Nachlaufablenkung detailliert zu untersuchen. Bei der Nachlaufablenkung wird der Nachlauf einer WEA durch gezielte Schräganströmung des Rotors abgelenkt, um Nachlaufeffekte auf eine stromabwärts stehende Anlage zu reduzieren. Dadurch kann die stromabwärts stehende WEA beispielsweise eine höhere Leistung erzeugen, welche idealerweise die Verluste an der stromaufwärts stehenden Anlage, welche durch die Schräganströmung entstehen, kompensiert oder übersteigt.

Für die numerische Beurteilung wird das aeroelastische Simulationsprogramm FAST.Farm eingesetzt. Für FAST.Farm werden geeignete Einstellungen erarbeitet, um unterschiedliche Betriebsbedingungen einschließlich verschiedener atmosphärischer Stabilitätsbedingungen realistisch abzubilden. Darüber hinaus wird zur Verbesserung von FAST.Farm ein Modell zur Berechnung der Effekte resultierend aus der nachlaufinduzierten kleinskaligen Turbulenz implementiert. Die empirischen Parameter in FAST.Farm werden mittels hochaufgelöster Large-Eddy Simulationen kalibriert. FAST.Farm wird mit Hilfe von Messdaten aus dem Windpark alpha ventus validiert. In der Auswertung der statistischen Strukturlastdaten sowie der Frequenzantwort der Struktur wird eine gute Übereinstimmung zwischen den Simulationen und Messdaten im Bereich des Turmfußes und der Blattwurzel festgestellt. Die Einbeziehung der nachlaufinduzierten Turbulenz ist dabei wichtig für die Berechnung der erhöhten Turbulenz im Nachlauf und somit auch für die Strukturlasten der WEA im Nachlauf. Dies ist besonders

relevant in stabilen atmosphärischen Bedingungen, in welchen die Umgebungsturbulenz niedrig ist und das Mäandrieren des Nachlaufs nur schwach ausgeprägt ist. Ohne nachlaufinduzierte Turbulenz werden die schadensequivalenten Lasten des Turmfußbiegemoments im Vergleich zu den Messdaten um bis zu 87% unterschätzt; der Fehler reduziert sich auf 2% bei aktivierter nachlaufinduzierter Turbulenz.

Mit dem validierten Simulationsprogramm FAST.Farm wird eine umfangreiche Simulationsstudie durchgeführt, um die Auswirkungen des Regelungskonzepts der Nachlaufablenkung auf die Strukturlasten zu untersuchen. Zunächst werden die Ermüdungslasten an verschiedenen Komponenten einer WEA in freier Anströmung unter Berücksichtigung variierender Anströmbedingungen und Winkel der Schräganströmung (Gierversatz) analysiert. Die größten Belastungsschwankungen resultierend aus der Schräganströmung treten in stabilen atmosphärischen Bedingungen mit starker vertikaler Windscherung und niedriger Turbulenzintensität auf. Im Gegensatz dazu ist der Einfluss der Schräganströmung auf die Ermüdungslasten in instabilen atmosphärischen Bedingungen mit geringer Windscherung und hoher Turbulenzintensität weniger stark ausgeprägt. Im weiteren Verlauf wird die Untersuchung ausgedehnt für eine WEA, die im Nachlauf steht. Die Lastverteilungen bezüglich unterschiedlicher Gierversatzwinkel weichen dabei deutlich von den Lastverteilungen in freier Anströmung ab. Dies ist insbesondere der Fall in Nachlaufsituationen, in denen der Rotor partiell abgeschattet wird und das Nachlaufzentrum sich zwischen $\pm 0.75 D$ (Rotordurchmesser) gemessen vom Rotorzentrum befindet. Zudem wird eine Richtungsabhängigkeit der Lasten in Bezug auf den seitlichen Nachlaufversatz festgestellt: Die Lasten sind tendenziell höher für negative seitliche Nachlaufversätze im Vergleich zu den Lasten aus denselben positiven seitlichen Nachlaufversätzen, weil die Lastamplituden über eine Rotorumdrehung höher sind.

Die gewonnenen Erkenntnisse werden schließlich bei der Ableitung optimaler Betriebsstrategien unter Nutzung der Nachlaufablenkung für beispielhafte Windparkkonfigurationen und wechselnde Umweltbedingungen angewendet. Es wird eine Optimierung mit verschiedenen Zielfunktionen durchgeführt, wie z.B. die Maximierung des Energieertrags oder die Reduzierung der strukturellen Belastung der WEA. Die daraus resultierenden optimalen Betriebsstrategien werden mit Hilfe von aeroelastischen Simulationen in FAST.Farm beurteilt. Die Auswertung der langfristigen Auswirkungen ergibt, dass der Energieertrag der betrachteten Turbinenanordnungen im Vergleich zum Basisszenario ohne Windparkregelung erhöht werden kann, wenn die Zielfunktion die Maximierung des Energieertrags enthält; die Ermüdungslasten werden dabei entweder nicht berücksichtigt oder nur gleich gewichtet. Folglich senken die Strategien, die sich auf die Minimierung der Ermüdungslasten konzentrieren, den Energieertrag im Vergleich zum Basisszenario. Die Berücksichtigung der Ermüdungslasten bei der Optimierung der Betriebsstrategien über ein effizientes Ersatzmodell wird dabei erfolgreich demonstriert. Mit diesem Ansatz werden Strategien abgeleitet, mit denen die Ermüdungsbelastungen an bestimmten Komponenten signifikant reduziert werden können.

1

Introduction

1.1 Motivation

Wind energy is one of the key technologies to transform the energy system from fossil energy sources to renewable energy sources. In the European Union, a significant share of the electricity generation with wind energy is planned to be achieved by the deployment of offshore wind farms; the current goal is set to an installed capacity of 60 GW in 2030 [1] (compared to 12 GW in 2021). One example of offshore wind farms already in operation is the German Bight, where ≈ 1300 installed wind turbines with a capacity of ≈ 7 GW in total have been in operation at the end of 2020 [2]. This comes along with a dense spacing of the turbines, which has the advantage of sharing the infrastructure (e.g. grid connection, operation and maintenance). However, the associated wake losses are larger compared to a sparser spacing of the turbines.

The optimisation of the operation of wind farms aims to reduce the Levelised Cost of Energy (LCoE) given the boundaries of a fixed turbine layout. Different objectives can be formulated and include, for instance, the maximisation of power, a life time management that considers the structural loading of all wind turbines and a better integration into the electricity grid. In order to achieve these objectives, an integrated wind farm control strategy is necessary, which optimises the operation of all wind turbines in a wind farm collectively rather than finding local optima for each turbine individually. The research on wind farm control strategies connected with system integration into the future electricity grid is part of the “Grand challenges in the science of wind energy” formulated in [3].

The development of wind farm control techniques requires knowledge in various disciplines that include [4]: wind turbine engineering (control design and implementation, structural de-

sign, load assessment and validation), wind resource modelling, atmospheric boundary layer modelling connected with the modelling of wakes. For the acceptance and so-called bankability (which is the willingness of established financial institutions to finance a project at a reasonable interest rate [4]), a substantial factor is the demonstration of the capability to simulate the implementation and impact of wind farm control on the energy and loading of the turbines with robust modelling techniques. A deeper understanding of the structural loads occurring in conjunction with wind farm control is also identified as a major research gap in [5] and the main motivation of this thesis.

1.2 Research objectives

The work performed within this thesis contributes to the research area of wind farm control. In particular, the wake redirection control strategy is assessed with respect to the associated structural loads using an integrated, aeroelastic simulation environment. Therefore, the following objectives are defined:

- Validating the aeroelastic simulation environment in terms of the prediction of power and structural loads in wake conditions against measurement data from operating turbines.
- Increasing the accuracy of the load calculations of waked turbines by the implementation of a module to model the wake-added small-scale turbulence and verification against high-fidelity simulations.
- Analysing the effects from yawed operation on the structural loads of free-stream and waked turbines under consideration of different environmental conditions.
- Developing and evaluating optimised wind farm operation strategies with the goals of power maximisation as well as fatigue load management.

1.3 Related Work

The numerical simulation of wind farm effects has greatly advanced in the past years. Wind farm simulations are primarily considered to be a problem of fluid mechanics, because of the interactions of the wind turbines with the Atmospheric Boundary Layer (ABL). The involvement of a wide range of turbulent scales (small scales, in the order of millimetres, around the blades to large scales, in the order of kilometres, for the entire wind farm) makes it a complex problem that should be tackled with models of different fidelity [6]. High fidelity models are applied to gain deeper understanding in the flow physics [7, 8] and the turbine's response [9], but they are only applicable to a few selected situations due to their high computational costs. In contrast, low fidelity models require significantly lower computational resources, have a lower accuracy

and are typically used only for steady-state calculations in many cases (e.g. AEP calculations) [10]. A trade-off between accuracy and computational costs is the aim for the development of midfidelity models. Here, the Dynamic Wake Meandering (DWM) model presented first in [11] is a prominent representative, which has been gradually improved by different groups [12, 13, 14] in the past years and is also accepted by the IEC 61400-1 standard [15]. It enables the aeroelastic simulation of wind farms within a reasonable time-frame and is the basis for the newly developed simulation software FAST.Farm [12] used in this thesis.

In the past, the optimisation of the operation of wind farms was predominantly motivated by the maximisation of the total power output. Different approaches were investigated, under which the wake redirection control strategy was identified as most promising [16]. Therefore, this strategy received most attention by the research community. Significant contributions are made in [17] by developing yaw-based optimisation strategies as well as control-oriented low-fidelity flow models. Wake steering is further improved by using of high-fidelity simulations [18], wind tunnel experiments [19] and field test campaigns [20]. The potential benefits of the application of Light Detection and Ranging (LIDAR) devices for tracking the wake position are explored in [21]. In recent years, the objectives of structural load mitigation and electricity grid integration [22] gained more popularity and dedicated wind farm control strategies were designed [23].

In the state of the art in the design of new wind farm control strategies, the structural loading of the turbines is typically either neglected [24] or it is considered in a simplified way. In the latter case, the structural loads are usually determined using a database which is created beforehand based on the results of aeroelastic single turbine simulations for a variety of environmental conditions [25, 26]; the loads are then interpolated with respect to a calculated wind farm state that is derived by the use of a control-oriented low-fidelity flow model. The numerical test of the developed control strategies is performed with high-fidelity simulations for a few load cases in some studies [18]. However, the detailed numerical testing is often omitted because of the high computational costs. In more recent studies, the testing of the new control concepts is performed with midfidelity models, which enable the analysis of the turbine's aeroelastic response for many load cases [27, 28]. This is especially considered to be crucial for the future certification of new wind farm control strategies [22].

1.4 Outline

After the introduction (Chapter 1), this thesis continues with the description of the necessary theoretical background information in Chapter 2. It includes explanations related to the ABL, in which wind turbines and farms are operated. Furthermore, the load mechanisms leading to fatigue on wind turbines are discussed and the interactions between the wind turbines and the ABL flow as well as the concepts to control the flow are explained. In Chapter 3, the methods are introduced which are applied to simulate the mutual effects between the ABL and the wind turbines including their structural loading.

In Chapter 4, the aeroelastic simulation environment used in this thesis is calibrated and validated using high-fidelity simulations as well as measurement data; in particular, newly added functionalities to the simulation tool are addressed. Furthermore, the simulation tool is calibrated to be suitable for the application in the optimisation of wind farm operation strategies considered. Chapter 5 is dedicated to the investigation of the effects connected with wake-redirecting control. The associated wake characteristics are examined and the structural loads of a wind turbine subjected to yawed operation in free-stream and waked conditions are assessed.

The knowledge and results from the previous chapters are eventually applied in the optimisation of wind farm operation strategies in Chapter 6. The wake-redirecting control concept is employed to optimise the wind farm operation according to different objectives that include the maximisation of the wind farm power output as well as the reduction of the fatigue loads. The results from the optimisation are evaluated in terms of short-term and long-term effects by the usage of aeroelastic simulations.

A summary of the thesis is given in Chapter 7; the main conclusions are drawn and an outlook for further research is provided.

2

Background

The theory and concepts applied in this thesis are introduced and related literature reviewed. In Section 2.1, the structure and characteristics of the ABL are presented in order to provide information on the regime, in which wind turbines are operated. In Section 2.2, the load mechanisms leading to fatigue on wind turbines are defined and the methods for the calculation of fatigue loads are explained. The influence of the wind turbines on the ABL flow is the topic of Section 2.3, where the wake effects caused by normal operation and yawed operation are discussed. An introduction to different wind farm control approaches is given in Section 2.4 and their potential is reviewed.

2.1 Atmospheric boundary layer

The ABL defines the lower part of the troposphere that is affected by the earth's surface [29]. In the ABL, the wind speed is decreased compared to the geostrophic wind leading to a vertical wind profile. The height of the ABL varies from 0.1 to 3 km and is dependent on atmospheric conditions, which include thermal stratification as well as low/high pressure conditions [29, 30, 31]. Shear stresses, created by wind shear and thermal conditions, induce turbulence in the ABL.

In an idealised way, the structure of the ABL layer can be divided into three layers in the vertical direction [32]. The lowest layer is laminar and its vertical dimension is a few millimeters; for wind energy applications this layer is not relevant. On top of the laminar layer is the surface layer (also called Prandtl layer) which covers 10 % of the ABL on average [31]. It is often described as the constant flux layer because all vertical energy and momentum fluxes

vary by less than 10 % of their magnitude [29, 31]. Compared to the other layers, the strongest vertical wind speed gradients occur in the surface layer, reaching approximately 70-80 % of the geostrophic wind at its top [33]. The mixed layer (also called Ekman layer) takes the largest portion of the ABL with approximately 90 %. Turbulent fluxes decrease with increasing height and shear stresses tend to be zero at the top of the mixed layer [33]. The Coriolis force induces a variation of the wind direction with height.

In contrast to flow over a land surface, the atmospheric boundary layer over sea surface (Marine Atmospheric Boundary Layer (MABL)) shows little variations over a diurnal cycle. Due to the large heat capacity of water, energy from the sun is absorbed to a high extent without increasing the temperature of the sea surface much [29]. The MABL has a distinct seasonal cycle.

2.1.1 Turbulence

Turbulence in fluid flows describes the chaotic and random behaviour of a flow that is superposed over the mean flow [34]. Turbulent flow is unsteady, three-dimensional and rotational. In contrast to laminar flow, momentum exchange perpendicular to the mean flow direction occurs. These characteristics make turbulent flow a multi-scale problem, which is illustrated by the energy spectrum in Figure 2.1. It shows the kinetic energy distribution over the wavenumber k ; the wavenumber describes the oscillations per length unit L and is defined as

$$k = \frac{2\pi}{L}. \quad (2.1)$$

The region of small wavenumbers (the so-called integral range), equivalent to large length scales, contains the bulk of the turbulent energy and is where energy production takes place. In ABL flows, turbulent energy is produced by wind shear and buoyancy forces. The maximum of the spectrum indicates the typical size of turbulent eddies; the integral length-scale Λ can be approximated by $k \sim 1/\Lambda$ [30]. Towards higher wave numbers, the energy cascade follows. In the so-called inertial subrange, energy is neither produced nor dissipated, but larger eddies are decomposed to smaller eddies. The energy distribution should be proportional to $E(k) \sim k^{-5/3}$ [30] for isotropic decaying turbulence. Eventually, in the dissipation range the kinetic energy of the smallest eddies is dissipated into heat. Under the assumption of Taylor's frozen turbulence, wavenumber and frequency are directly proportional.

For the mathematical description of a turbulent flow quantity, the Reynolds decomposition is commonly used. For example, the wind speed u can be split into its mean wind speed component \bar{u} and its turbulent fluctuation component u' :

$$u = \bar{u} + u' \quad (2.2)$$

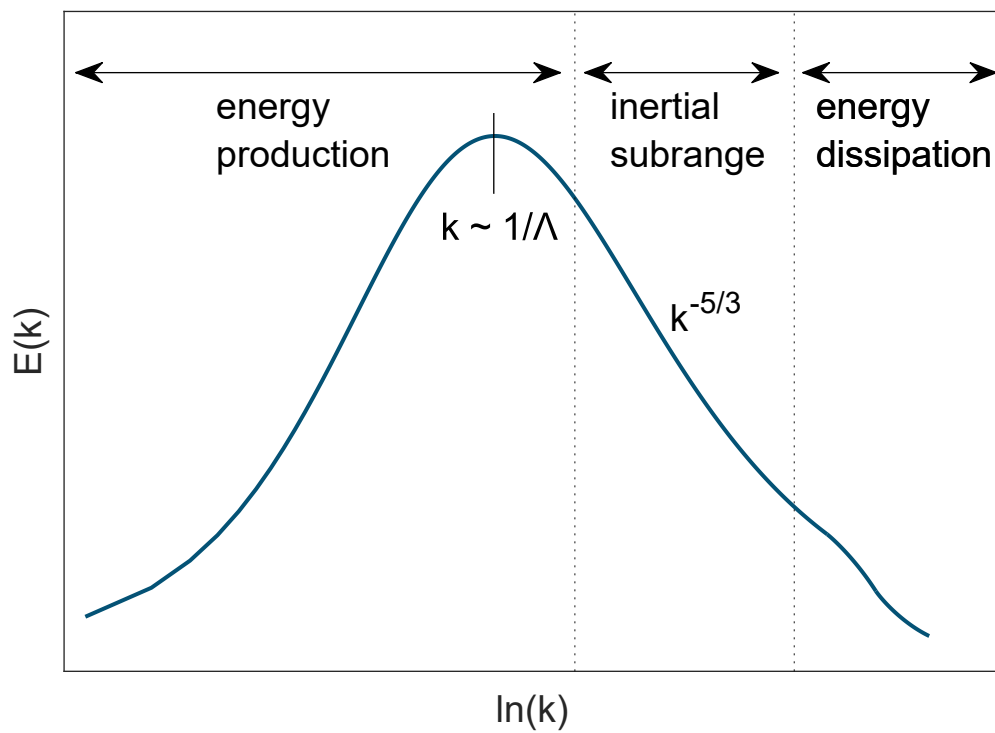


Figure 2.1: Schematic illustration of an energy spectrum of a turbulent flow in the ABL. Adapted from [30].

The mean value of the turbulent fluctuation component over a time T equals zero:

$$\bar{u}' \equiv \lim_{T \rightarrow \infty} \frac{1}{T} \int_0^T u' dt = 0 \quad (2.3)$$

A common measure in wind energy for the statistical description of turbulence is the Turbulence Intensity (TI) defined as the standard deviation of the wind speed σ_u divided by the mean wind speed \bar{u} :

$$TI = \frac{\sigma_u}{\bar{u}}. \quad (2.4)$$

2.1.2 Atmospheric stability

The ABL can be in different states that are dependent on the thermal stratification. In general, three basic types are distinguished [32]. An unstable ABL appears when cool air flows over warm surfaces. This leads to an upward directed heat flux and air rises due to buoyancy forces. In higher layers, pressure is reduced leading to an expansion of the risen air with combined adiabatic cooling. If no thermal equilibrium with the surrounding air is achieved, the air will keep rising. In a stable ABL, warm air flows over cool surfaces. A downward directed heat flux is observed and vertical movement by air is damped. Compared to unstable ABL, the vertical dimension of the ABL and vertical momentum exchange are less. The neutral ABL is characterised by a thermal equilibrium of risen air particles with the surrounding air due to adiabatic cooling.

In order to classify the state of the atmosphere a commonly used parameter in micro meteorology is the Obukhov length L_* [31]. It relates contributions from shear and buoyancy generated turbulence to the turbulent kinetic energy in the surface layer by defining:

$$L_* = - \frac{u_*^3}{\kappa \frac{g}{\Theta_v} \overline{w'T'}}. \quad (2.5)$$

where κ is the von Kármán constant and the friction velocity u_* represents the contribution from shear generated turbulence (see Equation 2.12). The buoyancy production term $\overline{w'T'}g/\Theta_v$ is formed by the gravitational acceleration constant g , the kinematic virtual heat flux of the surface layer $\overline{w'T'}$ and a reference virtual potential temperature Θ_v :

$$\Theta_v = \Theta(1 + 0.61r - r_L). \quad (2.6)$$

In Equation 2.6, r is the mixing ratio of water vapor and r_L is the mixing ratio of liquid water

Table 2.1: General classification of atmospheric stability

Atmospheric stability	kinematic virtual heat flux	L_*	ζ
Unstable	$\overline{w'T'} > 0$	< 0	< 0
Neutral	$\overline{w'T'} = 0$	∞	0
Stable	$\overline{w'T'} < 0$	> 0	> 0

Table 2.2: Specific classification of atmospheric stability in this thesis adopted from [35]

Atmospheric stability class	L_* interval [m]
Very unstable	$-100 \leq L_* \leq -50$
Unstable	$-200 \leq L_* \leq -100$
Near unstable	$-500 \leq L_* \leq -200$
Neutral	$ L_* \geq 500$
Near stable	$200 \leq L_* \leq 500$
Stable	$50 \leq L_* \leq 200$
Very stable	$10 \leq L_* \leq 50$

in the air; Θ is the actual potential temperature that is calculated by:

$$\Theta = T(p_0/p)^\kappa, \quad (2.7)$$

with the temperature T , the pressure p , the standard pressure p_0 and the Poisson constant κ .

L_* defined in Equation 2.5 can be interpreted as a characteristic height for thermal stratification where the production of turbulent energy from shear equals the production of turbulent energy from thermal processes [33]. When L_* is related to the height over the ground z , the dimensionless stability parameter ζ can be formed:

$$\zeta = \frac{z}{L_*}. \quad (2.8)$$

The direction of the kinematic virtual heat flux determines the sign of L_* and the state of the ABL correspondingly (see Table 2.1). By defining appropriate intervals for the Obukhov length L_* different states of the ABL can be classified. In this thesis, the classification from [35] is adopted and shown in Table 2.2. In particular, the three atmospheric stability class definitions of unstable, neutral and stable from Table 2.2 are used for most of the presented analyses to limit complexity.

Besides the Obukhov length, atmospheric stability can be determined by using the Richardson

number [31]. There exist different definitions of the Richardson number, from which the bulk Richardson number is used in this thesis. It relates the vertical potential temperature gradient $\Delta\Theta$ to the wind speed gradient Δu by defining:

$$Ri_B = -\frac{g}{\Theta_0} \frac{\Delta\Theta\Delta z}{(\Delta u)^2}, \quad (2.9)$$

where Θ_0 is the potential temperature at sea surface and Δz is the height between the temperature measurements. Over the ocean, the bulk Richardson number can be used to derive ζ with the empirical relationship provided by [36]:

$$\zeta = \begin{cases} \frac{10 Ri_B}{(1-5 Ri_B)}, & \zeta > 0 \\ 10 Ri_B, & \zeta \leq 0. \end{cases} \quad (2.10)$$

Atmospheric stability is correlated with wind speed and the vertical wind profile [32]. Unstable conditions occur often at lower wind speeds and induce a more uniform vertical wind profile because of strong turbulent mixing. Stable conditions happen more frequently at higher wind speeds and come along with a highly sheared wind profile. At very high wind speeds, neutral conditions are observed mostly because shear generated turbulence dominates over buoyancy generated turbulence.

2.1.3 Vertical wind speed profile

Atmospheric boundary layer flows develop a vertical wind shear profile due to the surface friction implying zero wind speed at the surface. The shape of the profile depends on the mechanical surface characteristics such as the shape and roughness. In addition, thermodynamic properties of the surface (e.g. heat emissivity, heat capacity, albedo) have an influence on the energy and momentum exchange between the surface and the atmosphere [32]. Together with the thermal stratification of the ABL, they all determine the shape of the vertical wind shear profile.

For the description of the vertical wind shear profile, the logarithmic law and power law are the most commonly used approaches in wind energy. They are strictly valid in the surface layer only [32], where the strongest wind gradients occur. The logarithmic wind profile for a neutral ABL can be derived from physical considerations based on Prandtl's mixing length hypothesis [32]. Its mathematical description is given in Equation 2.11:

$$u(z) = \frac{u_*}{\kappa} \ln \frac{z}{z_0}, \quad (2.11)$$

where the van Kármán constant is defined as $\kappa = 0.4$ and z_0 is the roughness length that is dependent on the surface. The friction velocity u_* is a measure of the vertical momentum exchange and can be simplified to Equation 2.12 when the main wind direction is the same as

the longitudinal wind speed component u :

$$u_*^2 = -\overline{u'w'}, \quad (2.12)$$

where u' and w' are the turbulent fluctuations of the longitudinal and vertical wind speed component.

For non-neutral atmospheric conditions, a stability dependent correction function Ψ can be introduced that is added to Equation 2.11 as follows:

$$u(z) = \frac{u_*}{\kappa} \ln \frac{z}{z_0} + \Psi(\zeta). \quad (2.13)$$

Ψ is dependent on the stability parameter ζ (Equation 2.8). Different formulations of Ψ exist in the literature from which the following is chosen as explained in [37] and [38]:

$$\Psi = \begin{cases} -a\zeta, & \text{when stable} \\ 2 \ln \frac{1+\chi}{2} + \ln \frac{1+\chi^2}{2} - 2 \arctan \chi + \frac{\pi}{2}, & \text{when unstable,} \end{cases} \quad (2.14)$$

where $a = 5$ and $\chi = (1 - b\zeta)^{1/4}$ with $b = 15$.

Exemplarily, vertical wind shear profiles for different atmospheric stabilities and roughness lengths are shown in Figure 2.2. An increase of roughness length causes stronger wind shear because of higher surface friction. This implies additionally a higher friction velocity u_* leading to the same reference wind speed at the reference height z_{ref} , thus the vertical momentum exchange is higher. The changes of the wind speed profile in non-neutral conditions compared to neutral conditions become visible: The thermal stratification in unstable conditions amplifies the vertical momentum exchange, which reflects in less vertical wind shear and a higher friction velocity for the same surface roughness. In contrast, stable atmospheric conditions damp the vertical momentum exchange; this is reflected in a lower friction velocity and leads to stronger vertical wind shear.

The logarithmic wind profile can be approximated with the empirical power law, which can be written as:

$$u(z) = u_{ref} \left(\frac{z}{z_{ref}} \right)^{\alpha_{shear}}, \quad (2.15)$$

where the reference wind speed u_{ref} at the reference height z_{ref} and the exponent α_{shear} are used to define the vertical wind speed profile. The quality of its approximation of the logarithmic profile is discussed in more detail in [32]; it shows that the power law provides good approximations of the wind speed profile in the surface layer for very smooth terrain (e.g. offshore). Therefore, it is applied for the description of the vertical wind speed profile in this thesis.

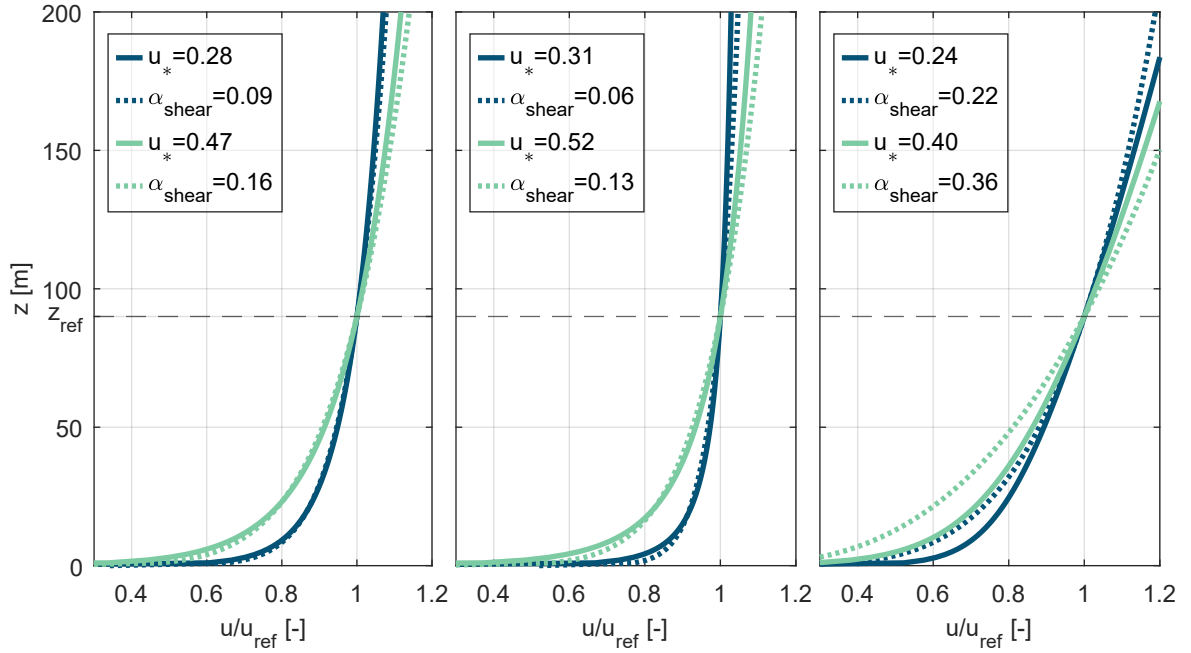


Figure 2.2: Vertical wind shear profiles normalised by the reference wind speed $u_{ref} = 8 \text{ m s}^{-1}$ at $z_{ref} = 90 \text{ m}$. Left panel: neutral Atmospheric Stability (AS); middle panel: unstable AS; right panel: stable AS. Colour code: blue: $z_0 = 0.001 \text{ m}$; green: $z_0 = 0.1 \text{ m}$. Solid lines represent the logarithmic law, dashed lines are derived from the power law.

2.2 Fatigue loading of wind turbines

Fatigue plays a major role in the design and operation of wind turbines. The design lifetime of wind turbines is usually between 20-30 years; a continuous operation leads to approximately 10^8 - 10^9 rotor revolutions per lifetime [39]. Different load effects can be distinguished that lead to fatigue of wind turbine components [40]:

- **Periodic loads:** The regular recurrence or variation of excitation forces due to the rotation of blades leads to periodic loads. The blades are subject to gravitational loads that induce a cyclic loading mainly in the edgewise direction. Imbalances in the rotor, e.g. due to different blade masses or blade pitch offsets, cause additional periodic loads in the support structure. Further periodic aerodynamic excitation comes from tower blockage effects as well as external inflow conditions such as wind shear and yawed inflow.
- **Random loads:** The turbulence in the incoming wind is the dominating source for random loads. The turbulent structures vary strongly and are, for instance, dependent on atmospheric stability and surface/terrain conditions. Another source of random loads are stochastic waves which mainly affect the support structure and tower of offshore wind turbines.

- Transient loads: Characterised by temporarily limited extension are transient events. These events are triggered for example by start-up and shut-down events as well as sudden wind direction or wind speed changes (wind gusts); in many cases high peak loads occur during transient events.

In this thesis, transient loads are out of scope; only periodic and random loads are taken into account because the considered wind farm control strategies are applied in normal operating conditions. Furthermore, fatigue loading is examined from a system perspective. This means that the term loading is referred to internal forces and moments acting on the turbine's structure. More detailed considerations of fatigue loading such as stress concentration, crack propagation or fracture mechanics are not covered. In the following, the calculation of fatigue loads performed throughout this thesis and corresponding fatigue life evaluation is discussed.

2.2.1 Fatigue load representation and calculation

Fatigue loads can be represented with different level of detail: A complete fatigue load information of a component is stored in the load time history. However, the processing of large time series is time consuming and time histories are not directly comparable, thus fatigue load information is often condensed associated with a loss of information. Load cycles are obtained from the full load time series by using cycle counting algorithms; widely used rainflow-counting algorithms determine the number of load cycles with different load amplitudes. In this work, the algorithm from [41] is used. By assuming linear damage accumulation, the total damage of a component can be estimated by the combination of all partial damages or, alternatively, a damage equivalent load can be calculated for easy comparison of load histories.

Linear damage accumulation

A widely used approach in fatigue damage calculation, e.g. [42], is the assumption of linear damage accumulation often referred as Miner's rule [39]. It states that the total damage D can be calculated by linearly adding the damage caused by the load cycles n_i of a specific amplitude specified by index i :

$$D = \sum_{i=1} \frac{n_i}{N_{crit,i}}. \quad (2.16)$$

The critical load cycle count $N_{crit,i}$ is obtained from the material's S/N-curve and gives the maximum allowed cycles for a specific stress range before failure. A failure of the structure occurs when $D \geq 1$.

Damage equivalent load

The idea of the damage equivalent load is motivated by the shape of a S/N-curve that is a straight line with the slope $1/m$ when plotted on a double logarithmic scale; the constant m is material specific. The equivalent load range $S_{eq,Nref,m}$ with the reference load cycle count N_{ref} causes, in theory, the same damage as the damage induced by the load history with a combination of different stress ranges and cycles:

$$\Delta S_{eq,Nref,m} = \sqrt[m]{\frac{\Delta S^m N}{N_{ref}}} \quad (2.17)$$

Using the linear damage accumulation law, a damage equivalent load range with the reference cycle number N_{ref} can be obtained by combining different load ranges ΔS_i with corresponding N_i load cycles from a load distribution:

$$\Delta S_{eq,Nref,m} = \sqrt[m]{\frac{\sum_{i=1}^n \Delta S_i^m N_i}{N_{ref}}} \quad (2.18)$$

This damage equivalent load range is often referred to as Damage Equivalent Load (DEL) and reduces a complicated load distribution into a single value. Compared to a full load time series or load spectrum, DEL is certainly a simplification. However, it is very useful when comparing different load cycle distributions. Hereby, the exponent m plays an important role because it weights the individual load ranges exponentially. By varying m , an interpretation of the contribution of individual load cycle ranges is possible. DELs calculated with large exponents are sensitive to a very few large load cycles. On the contrary, DELs derived with small exponents are mainly influenced by a large number of small load amplitudes.

In this thesis, the short-term DEL $\Delta S_{eq,Nref,m}$ is computed as 1-Hz DEL, which is equivalent to $N_{ref} = 600$ load cycles for a 10-min time series. Hereby, the indication of the index N_{ref} is omitted.

2.2.2 Long-term fatigue evaluation

A wind turbine experiences a large variety of operational conditions in its lifetime. The typical fatigue life prediction of a wind turbine component can be summarised by the following steps [39]:

1. A short-term load distribution is derived by calculating the elastic response of the wind turbine for a specific environmental condition (e.g. wind speed, wind turbulence).
2. The contribution of the short-term load distributions is added up according to the long-term site-specific conditions and weighted with the probability of occurrence of those

specified conditions.

3. Additional load contributions from transient events (e.g. start-up shut-down) are added to the fatigue life.
4. Partial safety factors from certification guidelines are applied.
5. An appropriate damage model for the considered component is chosen and the fatigue lifetime is calculated.

In this work, a complete fatigue life assessment for specific components is not performed, thus only steps one and two are of relevance. For the calculation of a long-term DEL, the short-term DELs derived for specific environmental conditions are weighted with their probability of occurrence w_i . The long-term DEL is determined as:

$$\Delta S_{eq,m,long} = \sqrt[m]{\sum_{i=1}^n w_i \Delta S_{eq,Nref,m,i}^m}, \quad (2.19)$$

where the short-term DELs are derived with the same reference cycle number and exponent.

2.3 Wake effects

A wind turbine extracts kinetic energy from ABL flows and converts it to electrical energy. The flow region behind the turbine, that is affected by it, is commonly referred to as wake. The main wake effects, due to the interaction of the turbine with the wind, are a decreased flow velocity (wake deficit) and an increased TI compared to the incoming wind. The increased turbulence in the wake includes a often called “apparent turbulence” [43], which originates from the meandering of the wake leading to wind speed fluctuations at a fixed spatial position (see also Figure 2.3). In addition, a wake-added turbulence, which is of rather small scale nature, contributes to the total turbulence in the wake of a turbine. Besides the introduced wake effects, the effects of a yawed turbine operation on the wake are discussed in more detail in the following.

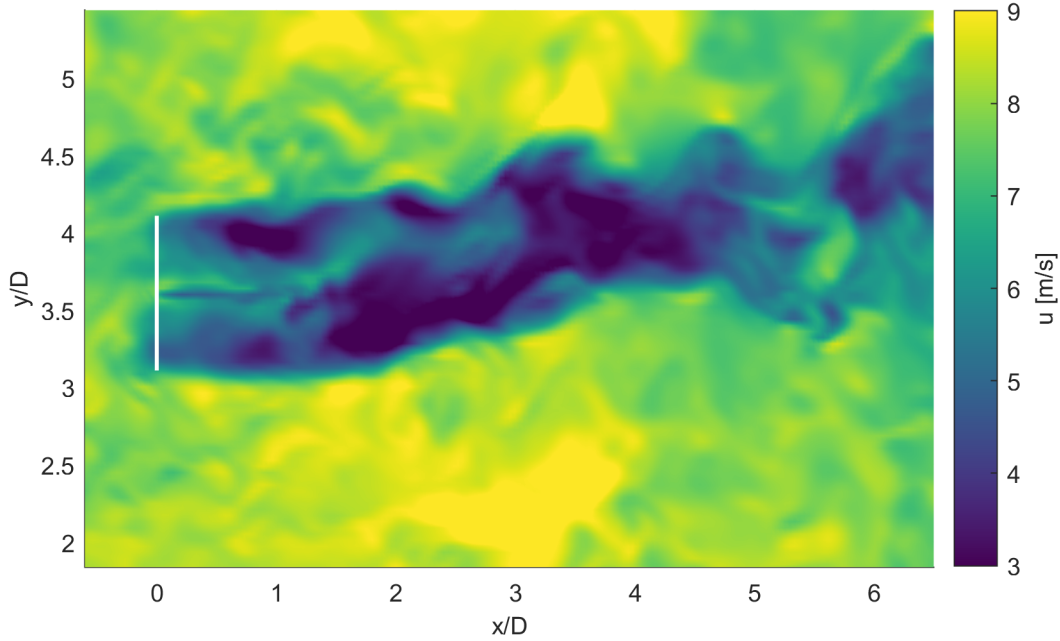


Figure 2.3: Instantaneous flow field of the longitudinal wind speed component u in a horizontal plane at hub height from a large eddy simulation. The wake of a single wind turbine is visualised including the wake meandering. The turbine rotor location is indicated by the white line.

2.3.1 Velocity deficit

The wake region is characterised by a decreased flow velocity compared to free-stream conditions due to the extraction of kinetic energy by the wind turbine rotor. The so-called wake shear layer develops at the boundary of the wake flow and the undisturbed surrounding air; turbulent mixing is enhanced and momentum from the undisturbed flow is transferred into the wake region leading to the recovery of the velocity deficit.

The downstream evolution of the wake can be separated into different regions that are associated with the velocity deficit [45] (see Figure 2.4). The near-wake region starts directly behind the rotor and extends to approximately 1-2 rotor diameters (D) downstream. Following one-dimensional stream-tube theory [46], the static pressure, increased before passing the rotor, drops behind the rotor and recovers to the ambient pressure; a commonly used definition marks the point of full pressure recovery as the end of the near-wake region [45]. In addition, the velocity decreases further until the full deficit is formed at the point of complete pressure recovery and the wake expands correspondingly due to mass conservation. The tip and root vortices typically break down within the first 2 D [47]; in low turbulent atmospheric conditions, they can exist longer downstream [47, 48].

In the intermediate (transition) wake region, the wake shear layer expands and reaches the wake centre axis after 2-5 D . Turbulent mixing transfers momentum from the surrounding flow into the wake leading to the recovery of the velocity deficit. The maximum TI is observed

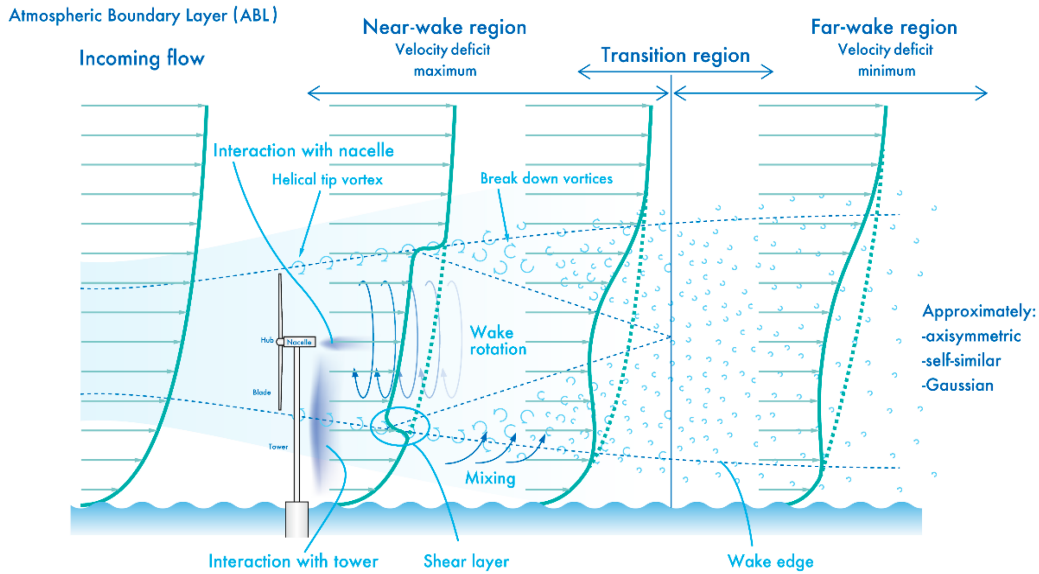


Figure 2.4: Illustration of the different wake regions and their characteristics. Taken from [44] in accordance with the Creative Commons Attribution 4.0 License without alterations.

between 2-6D depending on atmospheric conditions [49]. At the point of maximum TI , the turbulence in the wake is considered to be in quasi-equilibrium with the mean flow [50].

The velocity deficit and turbulence profile in the far-wake region have a nearly Gaussian-shape caused by turbulent mixing. The properties of the far-wake are mainly functions of the rotor radius, rotor thrust, wind speed and ambient TI . Other turbine properties such as the blade profile, hub and nacelle geometry as well as the tower have no significant effect on the far-wake.

The recovery rate of the velocity deficit depends on the magnitude of the momentum entrainment from the surrounding flow into the wake zone, thus it is largely dependent on the turbulence characteristics in the atmospheric flow. The turbulence characteristics are different for changing atmospheric stability. In particular, the momentum fluxes in the vertical direction (expressed with $\overline{u'w'}$) and in the lateral direction (expressed with $\overline{u'v'}$) are relevant to the momentum entrainment [51]. Higher momentum fluxes imply higher momentum exchange in the corresponding direction which eventually leads to a faster wake recovery. Typically, the momentum fluxes in unstable atmospheric conditions are higher compared to neutral AS; they are the lowest in stable conditions due to the negative surface buoyancy fluxes, which damp the turbulence [51].

2.3.2 Wake meandering

The wake profile is not fixed at a centred position downstream but oscillates randomly in the horizontal and vertical directions. A widely accepted explanation is given by [11] postulating that the velocity deficit follows the turbulent eddies of the ambient flow that are larger than two rotor diameter. In full-scale experiments, the phenomenon of wake meandering was identified by utilising a LIDAR device; it was measured and correlated with the incoming large scale turbulence in [52] and [53]. In wind tunnel experiments [54], wake meandering was only observed when turbulent eddies with dimensions of much larger than a rotor diameter exist in the incoming flow confirming the aforementioned postulation by [11].

The magnitude of wake meandering is dependent on atmospheric conditions. In experimental work by [54], it was found that increasing ambient TI leads to larger amplitudes of the wake meandering. This was confirmed by numerical analyses in [49]. In addition, both investigations show that the horizontal wake meandering is larger than the vertical meandering which is attributed to the larger turbulent kinetic energy in the lateral direction. They also report in agreement with [55], that the amplitude of the wake meandering becomes larger with increasing downstream distances.

Besides the TI , the turbulent energy distribution over length scales in the flow (see Figure 2.1) is equally important for the wake meandering. The large turbulent eddies ($>2D$) influence the wake meandering, while small eddies affect the velocity deficit evolution through turbulent diffusion. The turbulent length scale correlates with the atmospheric stability; in an unstable ABL, turbulent structures with large length scales are present, whereas in stable conditions the length scales are typically smaller (see Table 3.1 for an example of length scales in flat and homogeneous terrain). The influence of atmospheric stability on the wake meandering was studied in [56] using numerical simulations by explicitly keeping the TI constant. They observed a much stronger wake meandering during unstable atmospheric conditions compared to stable conditions emphasising the importance of including atmospheric stability as a parameter in wind farm analyses.

2.3.3 Effects of yawed operation

The operation of a wind turbine under yawed conditions (i.e. the rotor is not aligned with the incoming wind direction) has not only implications on the turbine itself but also on the downstream wake. The mean centre position of the wake that originates from a yawed turbine is deflected compared to the wake of an aligned turbine. This is illustrated in Figure 2.5, where the wake is deflected in the negative direction caused by a positive (anti-clockwise) yaw-misalignment angle θ_m . In addition, the shape of the velocity deficit in the far-wake differs from a Gaussian-shape, especially in the vertical direction.

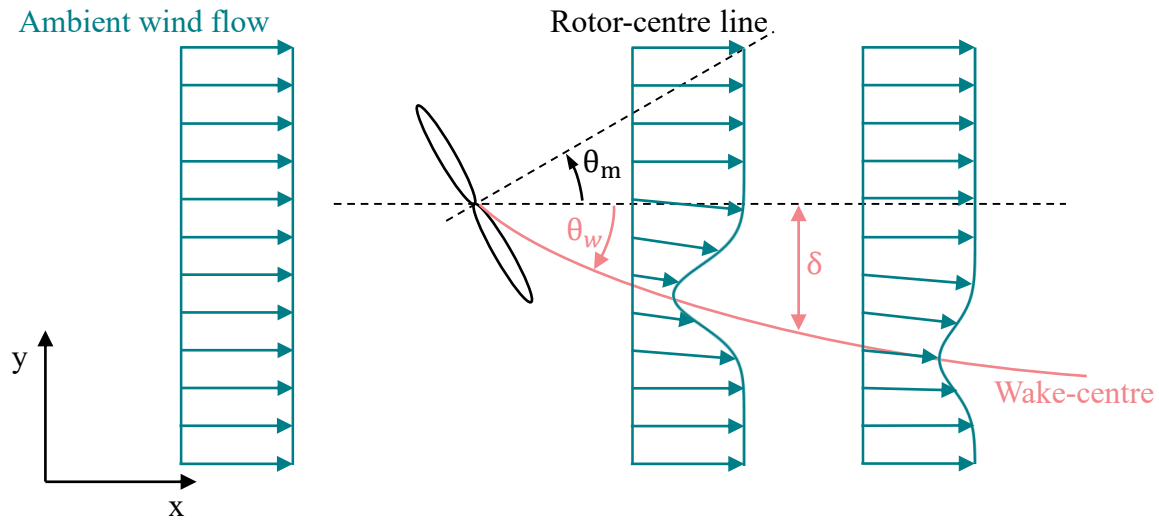


Figure 2.5: Illustration of wake deflection caused by yawed operation. The turbine rotates anti-clockwise with the positive yaw-misalignment angle θ_m . The wake-centre is deflected by the distance $\delta(x)$ and the skew angle $\theta_w(x)$.

Motivated by new wind farm control methods (see Section 2.4.2), research on the far-wake originating from a yawed turbine has gained more attraction recently. By utilising high-fidelity numerical simulations as well as wind tunnel and full-scale experiments, the following dependencies of the wake centre deflection were found in various studies:

- Turbine’s yaw angle: The wake centre deflection increases with higher yaw-misalignment angles as shown in the numerical study by [57] and in the full-scale experiment by [58].
- Yaw direction: The yaw direction has an influence on the magnitude of wake centre deflection which is connected with the wake rotation caused by the rotation of the rotor as seen in [57] and explained in [59]: Assuming the same yaw angle in the positive and negative direction, the wake centre is deflected more for positive yaw angles compared to negative yaw angles (assuming clockwise rotation of the rotor).
- Turbine’s thrust coefficient: Increasing the rotor thrust leads to increased wake centre deflections as reported by [60].
- Downstream distance: In numerical investigations [57] and fullscale tests [61], it is observed that larger wake deflection occurs at farther downstream distances.
- Ambient TI : With low incoming TI the wake deflection effect is found to be stronger as shown in [59].
- Atmospheric stability: In stable atmospheric conditions, larger wake deflection is observed compared to neutral and unstable conditions [62, 63].

For larger yaw-misalignments ($> 20^\circ$), the shape of the velocity deficit in the far-wake cannot be considered Gaussian anymore, but it looks more like a kidney due to the presence of a counter-rotating vortex pair [64]. This is observed in Large Eddy Simulation (LES) by [65] [66] and confirmed in wind tunnel experiments by [59].

2.4 Wind farm control

The basic concept of wind farm control is to operate individual wind turbines inside a wind farm in a coordinated way in order to achieve predefined objectives. This is motivated by the wake effects and by the desire to reduce their impact. In general, there are two methods of wind farm control, the axial induction control (see Section 2.4.1) and the wake redirection control (see Section 2.4.2). The application of wind farm control can reduce the LCoE; to be more precise, the objectives of wind farm control can be split into three categories:

- Power maximisation: The first goal is power maximisation as it is directly connected with higher revenue.
- Load reduction/balancing: Wake effects impose higher structural fatigue on downstream turbines. Wind farm control can reduce the impact of the wakes and to balance structural load distributions between the individual wind turbines inside a wind farm evenly.
- Provision of grid services: Wind farms are connected to the electrical grid. With wind farm control, the wind farm can provide services for stabilising the grid.

2.4.1 Axial induction control

Static axial induction control aims to mitigate wake effects on downstream turbines by reducing the thrust and thus, decreasing the aerodynamic efficiency of the upstream turbine compared to normal operation. The tip-speed ratio of the upstream turbine is altered by changing the generator torque and/or pitching the blades [67]. In the past, literature reported very limited potential of the method in increasing a wind farm's total power output; power gains of a few percent or even power loss were observed in high fidelity simulations [68], wind tunnel experiments [69] and fullscale experiments [70]. In more recent work [71, 72], dynamic axial induction control was explored as a variant of Individual Pitch Control (IPC) by introducing modulated cyclic pitching of the blades leading to faster recovery of the wake deficit. First investigations show better results in maximising the total power output of a wind farm albeit coming at the cost of increased fatigue.

Axial induction control offers higher potential for structural load alleviation within a wind farm [73]. It can be applied to balance the fatigue consumption of the individual turbines inside

a wind farm [26]. This is often combined with active power control where, for instance, a given power output of the wind farm is prescribed by the Transmission Grid Operator (TSO) [23].

2.4.2 Wake redirection control

Wake redirection control intends to reduce wake effects on the downstream turbines by redirecting the wake. Different approaches can be utilised to introduce a deflection of the wake centre position:

- Yaw-based redirection control exploits the wake characteristics that evolve during yawed operation of a wind turbine (see Section 2.3.3). Hereby, the turbine's yaw motor is used as an actuator to intentionally misalign the rotor with respect to the incoming wind, thus redirecting the wake centre position downstream [60].
- The rotor plane can be tilted to deflect the wake centre position up- or downwards [74]. The concept is based on the same principles as yaw-based wake redirection control, but would require a redesign of current state-of-the-art wind turbines.
- IPC can be modified in order to induce a moment on the wake flow causing a redirection of the wake centre [57]. An evaluation of the concept in [57] revealed limited potential of this method when purely applied for wake redirection. However, in combination with the control concept of modulated cyclic pitching of the blades mentioned in Section 2.4.1 wake redirection can be triggered as a secondary effect that can potentially make the former strategy even more effective.

The most common approach is the yaw-based wake redirection control, hence it is applied in this thesis and discussed in more detail in the following. It is mainly used to maximise the wind farm's total power output [75]. In high fidelity simulations, power gains of up to 15 % could be achieved for a three turbine setup in certain conditions compared to a non-controlled scenario [18]. This is in line with the results from wind tunnel experiments [76]. In recent field test campaigns, varying results for power maximisation were obtained. For example in [77], in certain conditions, an increase in power of up to 15 % for a three turbine setup and up to 35 % for a two turbine setup were achieved. However, in other scenarios no improvement or even power loss was observed. This was also seen in other fullscale studies, e.g. [78, 79, 80], demonstrating a large uncertainty range in the current implementations.

In previous studies, structural load reduction/balancing was rarely a primary objective for yaw-based wake redirection control, e.g. [81, 82], but it was investigated in conjunction with power maximisation or active power control as secondary objective. In general, the space of optimal yaw-angle configurations in a wind farm for power maximisation is reduced, when structural loads are taken into account [83]. It is possible to maximise the collective power

output while reducing the loading due to partial wake overlap [84]. However, possible fatigue load reductions are also dependent on the component and on the implemented cost function, when both power and loads are optimised [85].

Yaw-based wake redirection control has inherently slow actuation times, thus it is only applicable for the provision of certain grid services. It can be applied to provide tertiary control reserves, which for instance require a complete activation within 15 minutes in Germany. First simulation results indicate a general functionality of the concept but also show large uncertainties that must be further analysed [27].

Overall, taking the findings from Section 2.3.3 into account, the wake redirection control strategy for wind farms is most effective for the maximisation of the wind farm's power output under the following circumstances: An increase of the overall power production is only possible in below-rated wind conditions, which corresponds to high thrust conditions. Additionally, the power maximisation at the downstream turbines is potentially higher when the turbines are located slightly misaligned to each other. Furthermore, the strategy is more effective in conditions of low ambient turbulence and for positive yaw-misalignment angles due to the effects from wake rotation.

3

Simulation modelling

The modelling approaches are introduced and described. In Section 3.1, the methods for simulating flows in the ABL including turbulence are explained. The modelling of the interaction effects between the ABL and the wind turbine aerodynamics is explained in Section 3.2. The description of the applied aeroelastic wind farm simulation approach is in Section 3.3; in this Section, the modelling approach applied in this thesis is presented.

3.1 Atmospheric boundary layer modelling

For the aeroelastic simulation of wind farms, an adequate representation of the ABL and its flow structures is required as input. The aim is to reproduce important characteristics of the ABL such as the stability, turbulence distribution and wind profile. In this thesis, the modelling of ABL flows is performed with a spectral tensor method and LES; they are explained in the following sections.

3.1.1 Mann uniform shear turbulence model

The Mann spectral model [86] is one of the recommended models by the IEC 61400-1 Ed. 4 standard [15] to reproduce the turbulence in the ABL. It is a semi-empirical model that is strictly valid for homogeneous turbulence in the neutral atmospheric surface layer.

In general, for a homogeneous turbulent velocity field, the correlation of two points in space

is only a function of the separation vector \mathbf{r} ; the covariance tensor R_{ij} can be defined as [87]:

$$R_{ij}(\mathbf{r}) = \langle u'_i(\mathbf{x}) u'_j(\mathbf{x} + \mathbf{r}) \rangle, \quad (3.1)$$

where the indices $\{i,j\}=1,2,3$ denote the velocity components and $\langle \cdot \rangle$ takes the ensemble average. The covariance tensor for the single point ($\mathbf{r} = 0$) statistics is:

$$R_{ij}(\mathbf{r} = 0) = \begin{bmatrix} \langle u'u' \rangle & \langle u'v' \rangle & \langle u'w' \rangle \\ \langle v'u' \rangle & \langle v'v' \rangle & \langle v'w' \rangle \\ \langle w'u' \rangle & \langle w'v' \rangle & \langle w'w' \rangle \end{bmatrix} = \begin{bmatrix} \sigma_u^2 & \sigma_{uv} & \sigma_{uw} \\ \sigma_{vu} & \sigma_v^2 & \sigma_{vw} \\ \sigma_{wu} & \sigma_{wv} & \sigma_w^2 \end{bmatrix}, \quad (3.2)$$

where the matrix elements represent the variances and covariances of the three-dimensional velocity field.

The Fourier transform of the covariance tensor R_{ij} defines the spectral velocity tensor and can be written as:

$$\Phi_{ij}(\mathbf{k}) = \frac{1}{(2\pi)^3} \iiint_{-\infty}^{+\infty} R_{ij}(\mathbf{r}) \exp(-i\mathbf{k} \cdot \mathbf{r}) d\mathbf{r}, \quad (3.3)$$

with the wave number $\mathbf{k} = (k_1, k_2, k_3)$. The spectral velocity tensor contains information about the second order statistics of the three velocity components. The Mann model derives the spectral velocity tensor by using the isotropic von Kármán turbulent energy spectrum (Equation 3.4) as initial condition. It depends on the Kolmogorov spectral constant α_k , the rate of viscous dissipation of specific turbulent energy ϵ and a length scale L .

$$E(k) = \alpha_k \epsilon^{\frac{2}{3}} L^{\frac{5}{3}} \frac{(Lk)^4}{(1 + (Lk)^2)^{\frac{17}{6}}} \quad (3.4)$$

The initially isotropic spectral tensor is then transformed to an anisotropic spectral tensor using rapid distortion theory and uniform velocity shear. In combination with the assumption on the turbulent eddy's life-time, the anisotropic spectral velocity tensor reaches a stationary state. The complete derivation of the spectral velocity tensor and the full set of equations are presented in [86].

In total, three parameters are needed to determine the spectral velocity tensor with Mann's approach:

- $\alpha \epsilon^{2/3}$: The product of Kolmogorov's constant α_k and the dissipation rate ϵ raised to the power of two-thirds.
- L_M : A length scale that defines the size of the most energy-containing turbulent eddies.
- Γ : The non-dimensional anisotropy parameter Γ is related to the eddy lifetime and is

used to describe the degree of anisotropy of the turbulence. When $\Gamma = 0$, turbulence is isotropic.

With Mann's spectral velocity tensor, the coherence of a turbulent wind field is described in three dimensions. In order to compare the model with measurements that are usually carried out at one point, the cross-spectra χ_{ij} between two points in a y-z plane separated by a distance dy and dz can be derived. Hereby, the spectral tensor is numerically integrated over the wave numbers in the directions k_2 and k_3 :

$$\chi_{ij}(k_1, dy, dz) = \iint_{-\infty}^{+\infty} \Phi_{ij}(\mathbf{k}, \alpha_k \epsilon^{2/3}, L_M, \Gamma) \exp(ik_2 dy + ik_3 dz) dk_2 dk_3. \quad (3.5)$$

By setting the distance to zero ($dy=0, dz=0$) the one-point spectra $F_i(k_1) = \chi_{ij}(k_1, 0, 0)$ can be calculated.

The spectral velocity tensor in combination with the discrete Fourier series can be applied to generate a turbulent wind field; the process is explained in detail in [88]. It is numerically implemented in the turbulence generator [89] which is used in this thesis to generate three-dimensional turbulent wind fields.

Model parametrisation

In this thesis, three-dimensional wind fields are generated with the Mann model. The model parameters L_M and Γ change with the atmospheric stability. They are based on the results from [35], where the Mann model is fitted to measurements from a met mast; it is shown, that the Mann model predicts well the measured spectra from different atmospheric stabilities with an appropriate parameter selection, although the model is derived for neutral conditions.

The values of the parameters L_M and Γ are summarised in Table 3.1. For the wind field generation, the parameter $\alpha \epsilon^{2/3}$ is modified according to the target TI , thus it depends on the wind speed as well as L_M and Γ . The parameters are taken at the height $z = 90$ m that equals approximately the hub height position of the turbines used in this thesis. The resulting one-point spectra are shown in Figure 3.1. Hereby, the values for $\alpha \epsilon^{2/3}$ are chosen to match the variance of the longitudinal wind component u for each AS: $\sigma_{u,unstable}^2 = \sigma_{u,neutral}^2 = \sigma_{u,stable}^2$. It can be seen that an increased length scale L_M results in a shift of the spectra towards lower wave numbers. Additionally, increasing the anisotropy parameter Γ leads to lower variances in the lateral σ_v^2 and vertical σ_w^2 wind component, hence lower turbulent kinetic energy.

Table 3.1: Values of the Mann model parameters used within this thesis

	Atmospheric stability	Length scale L_M [m]	Anisotropy parameter Γ [-]
IEC 61400-1 Ed.4	-	33.6 (for heights ≥ 60 m)	3.9
Høvsøre parameter set at $z = 90$ m from Figure 4 in [35]	unstable	69.2	2.09
	neutral	33.1	2.57
	stable	11.6	2.79

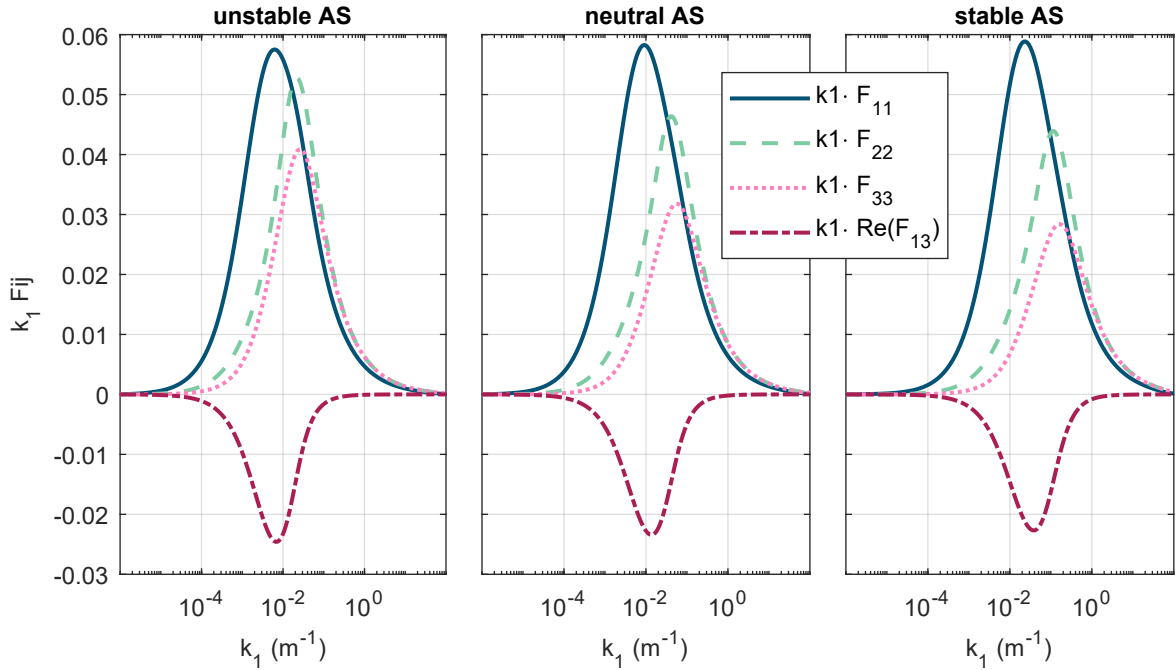


Figure 3.1: One-point spectra F_{ij} for different atmospheric stabilities (AS) calculated with the parameters given in Table 3.1. The parameter $\alpha\epsilon^{2/3}$ is chosen to match the variance of the longitudinal wind component u for all AS: $\sigma_{u,unstable}^2 = \sigma_{u,neutral}^2 = \sigma_{u,stable}^2$.

3.1.2 Large eddy simulations

Large eddy simulations (LES) solve the Navier-Stokes equations in order to simulate turbulent flows. Hereby, the turbulent energy spectrum (see also Figure 2.1) is split in a way that only the large turbulent eddies in a flow are resolved directly, whereas eddies that are smaller than a defined cut-off wave number are modelled with a subgrid-scale model [34]. LES are computationally expensive and require typically high-performance clusters. In this thesis, results from LES performed with the open-source code Parallelised Large-Eddy Simulation Model (PALM) are used as reference for model calibration purposes.

The PALM code solves the non-hydrostatic, filtered, and incompressible Boussinesq approximation of the Navier-Stokes equations by using central differences on a structured grid. It is particularly suited for the simulation of atmospheric and oceanic flows. More information can be found in [90].

3.2 Wind farm flow modelling

Inside a wind farm, the wakes from individual wind turbines interact with the ABL flow which leads to new inflow conditions at downstream located turbines. With the modelling of wind farm effects, it is aimed to understand the physics and to predict the response of individual wind turbines as well as the wind farm as a whole to various environmental conditions and corresponding states. The gained knowledge is applied for the optimisation of turbine design, micro siting and farm operation, thus the uncertainties and the associated technical and economic risks are reduced.

The modelling of wind farm flows is complex because of the wide range of turbulent scales that influence the flow dynamics. Therefore, different model complexities are developed: High-fidelity models resolve the underlying physics accurately but require high computational resources. Models of lower fidelity introduce simplifications to the underlying physics and/or reduce the temporal and spatial resolution. A comprehensive review on wind farm flow modelling is given in [64]. In the following, a brief overview of different model fidelities is provided and the classification of the models used in this thesis is performed; they are then explained in the subsequent sections in more detail.

- High fidelity models: They solve the governing Navier-Stokes equations typically with a LES approach (see also Section 3.1.2) or by a hybrid simulation combining LES with the Reynolds-Averaged Navier-Stokes (RANS) method [91]. They resolve the physics of the large turbulent structures directly and are capable of simulating ABL flows with different thermal stratification.

There are different methods for the representation of the rotor. The most detailed approach is to model the blade's geometry directly as solid boundaries in the CFD domain.

This requires very fine meshes and normally hybrid LES-RANS or unsteady RANS approaches are applied, where the turbulence in the blade's boundary layer is modelled. The main purpose is to understand the flow physics around the rotor, in the near-wake and how the far-wake is affected by the near-wake flow. Investigations using a fully resolved rotor are typically performed for single turbine cases [92, 93] or small wind farm configurations [91].

The Actuator Line (ACL) method replaces the physical representation of the blades by body forces that capture the influence of the blades on the flow. They are calculated by using tabulated blade profile data and the local inflow conditions. Compared to the fully resolved rotor, computational resources are significantly reduced because the blade's boundary layer is not resolved. Nevertheless, the flow physics in the wake are captured accurately [94], which makes it a reasonable simplification to investigate the wake physics. Examples of analyses of the wake physics are performed for single wind turbines [51, 95] and multiple turbines [96, 97].

The Actuator Disc (ACD) concept is a simplification of the ACL method and introduces an azimuthal averaging of the body forces. This enables a coarser time step, thus a speed-up in simulation time. The calculation of the body forces with the ACD can be, on the one hand, based on tabulated blade profile data. On the other hand, the calculation can be based on the integral thrust force of the rotor, which requires only the turbine's c_T -curve. The flow behind an ACD does not include all the details in the near-wake (e.g. vortex structure) but this is acceptable for the far-wake. Thus, it is typically applied in simulations of large wind turbine clusters [98, 99, 100, 101] or even to study intra-farm effects [102].

- Medium fidelity models: Three different models are classified as medium fidelity models which are physics based but also introduce simplifications to flow features to reduce computational times. For example, models based on the RANS-equations are steady-state and calculate a time averaged solution of the wind farm flow. This implies challenges to the turbulence modelling which can be performed in different levels of detail. Examples of RANS-simulations are provided in [103] and [104].

Another type of medium fidelity models is the free vortex wake model which is based on potential-flow theory [105]. It is capable of simulating the rotor induction and near-wake aerodynamics including the vortex structures but lacks accuracy in the far-wake due to the assumption of inviscid flow.

The third type is the DWM model, which is mainly used in this thesis and explained in detail in Section 3.3.3. It introduces a split in the turbulent scales and treats small-scale turbulence based on a reduced form of the Navier-Stokes equations and large-scale turbulence based on the passive tracer analogy suggested by [11]. It requires the use

of three-dimensional turbulent wind fields and calculates the wind farm response in the time domain. This makes it an ideal model for aeroelastic wind farm calculations while keeping the computational time in the order of minutes (for 5-10 turbines on a normal desktop computer).

- Low fidelity models: They are typically based on some form of reduced order physics to achieve fast computational run times in the order of (milli-)seconds (for large wind turbine clusters on a normal desktop computer). They calculate typically a two-dimensional steady state solution of the flow field and involve empirical calibration constants that need to be changed for different operational conditions. Examples are the Jensen wake model [106] and the Gaussian wake model [107]. The latter is applied in this thesis and discussed in Section 3.2.1. An example of a dynamic reduced-order model is given in [108].

3.2.1 Steady-state low-fidelity flow simulation

A low-fidelity wind farm flow simulation model is usually required in the context of wind farm design or optimisation of operational strategies to simulate many parameter variations. In this thesis, the FLOW Redirection and Induction in Steady State (FLORIS) wind plant optimisation tool [109] in the version 2.4.0 developed by the National Renewable Energy Laboratory (NREL) is used. It includes a variety of models to calculate the velocity deficit behind a wind turbine as well as the wake-centre deflection caused by yaw-misaligned operation.

In this thesis, the Gaussian velocity deficit and wake-centre deflection model is used. Its full description is given in [110]. The model is based on the research in [107, 51, 111, 59], but it includes secondary effects from wake steering. Secondary steering means the deflection of the wake of a downstream, aligned turbine caused by the counter-rotating vortices developed behind an upstream turbine under yawed operation. The model is derived for the far-wake region and uses calibrated boundary conditions from the near-wake region. According to [59], it should be applied for yaw-misalignment angles that are smaller than $|\theta_m| < 30^\circ$. The authors in [59] reason this limitation with the usage of the Gaussian distribution for the velocity profile that is not valid for high yaw angles due to the kidney shape of the velocity profile in the z-direction (see Section 2.3.3).

The Gaussian velocity deficit and wake-centre deflection models are introduced in the following. Several calibration parameters are used within these models; their tuning is performed in Section 4.4.

Gaussian velocity deficit model

The velocity deficit $u_{def}(x, y, z) = u(x, y, z)/u_\infty$ in the far wake region behind a wind turbine is approximated with a Gaussian function,

$$u(x, y, z)/u_\infty = 1 - C \exp \frac{(y - \delta)^2}{2\sigma_y^2} \exp \frac{-(z - z_h)^2}{2\sigma_z^2}, \quad (3.6)$$

with the velocity deficit at the wake center C :

$$C = 1 - \sqrt{1 - \frac{(\sigma_{y0}\sigma_{z0})c_T}{\sigma_y\sigma_z}}. \quad (3.7)$$

Here, δ is the lateral wake deflection from the rotor centre, z_h is the hub height of the turbine, c_T is the turbine's thrust coefficient, σ_y and σ_z define the wake width in the y - and z -directions respectively. The subscript "0" attributes the initial values at the start of the far-wake; for the calculation of these values which depend on the ambient TI and c_T , the reader is referred to [59]. The Cartesian coordinate system (x, y, z) has its origin in the rotor centre of the wake-emitting turbine.

The wake width in the y - and z -direction (σ_y and σ_z) becomes wider with increasing downstream distance due to the turbulent mixing with the free-stream flow. It is calculated by using the equations

$$\frac{\sigma_y}{D} = k_y \frac{x - x_0}{D} + \frac{\sigma_{y0}}{D}, \quad (3.8)$$

$$\frac{\sigma_z}{D} = k_z \frac{x - x_0}{D} + \frac{\sigma_{z0}}{D}, \quad (3.9)$$

where D is the rotor diameter and k_y and k_z are parameters that define the expansion rate of the wake. In the current implementation of FLORIS, k_y equals k_z leading to the same expansion rate in the lateral and vertical directions:

$$k_y = k_z = k_a TI + k_b, \quad (3.10)$$

where k_a and k_b are calibration constants.

The calculation of the resulting wind speed profile from multiple wakes is based on the sum of squares method presented in [112].

Gaussian wake-centre deflection model

The lateral position of the wake centre δ with respect to the rotor centre behind a turbine operating with a yaw-misalignment can be calculated with the equation derived in [59]:

$$\delta = \delta_0 + \frac{\theta_m E_0}{5.2} \sqrt{\frac{\sigma_{y0}\sigma_{z0}}{k_y k_z c_T}} \ln \left[\frac{(1.6 + \sqrt{c_T}) \left(1.6 \sqrt{\frac{\sigma_y \sigma_z}{\sigma_{y0} \sigma_{z0}}} - \sqrt{c_T} \right)}{(1.6 - \sqrt{c_T}) \left(1.6 \sqrt{\frac{\sigma_y \sigma_z}{\sigma_{y0} \sigma_{z0}}} + \sqrt{c_T} \right)} \right], \quad (3.11)$$

where θ_m is the turbine's yaw-misalignment angle (see Figure 2.5) and $E_0 = C_0^2 - 3e^{1/12}C_0 + 3e^{1/3}$ with C_0 indicating the initial far-wake velocity deficit at the wake centre.

The initial wake-centre deflection at the start of the far-wake δ_0 that is developed in the near-wake is calculated with

$$\delta_0 = x_0 \tan \theta_{w,rotor}, \quad (3.12)$$

where x_0 is the length of the near-wake and $\theta_{w,rotor}$ is the initial wake deflection angle at the rotor due to yaw-misalignment, which is approximated by

$$\theta_{w,rotor} \approx \frac{0.3 \theta_m}{\cos \theta_m} \left(1 - \sqrt{1 - c_T \cos \theta_m} \right). \quad (3.13)$$

3.2.2 Coupled large eddy simulations

The PALM code (see Section 3.1.2) is capable of performing wind farm simulations by including the wind turbines with actuator discs or actuator lines. The aerodynamic forces exerted by the wind turbines are applied as momentum sources in the discretised Navier-Stokes equations by projecting them onto the underlying grid.

The results from the PALM simulations used in this thesis are based on an actuator sector model that is coupled to the aeroelastic simulation code Fatigue, Aerodynamics, Structures, and Turbulence (FAST) (see Section 3.3.2). At the turbine's location, the flow field velocities are transferred from PALM to FAST which calculates the resulting blade forces. The aerodynamic forces are then distributed on the actuator disc in PALM, which is divided into radial and azimuthal segments to consider spatial variations. The azimuthal segmentation of the rotor allows the use of different time steps depending on the azimuthal span of the segments, thus it increases the simulation efficiency compared to a rotor representation by actuator lines. A more detailed description of the coupling method is given in [113].

The simulations results are produced with PALM in the revision 3401 and FAST in the version FASTv8. The aerodynamic force calculation in FAST is conducted with the module Aerodyn in the version 14.

3.3 Aeroelastic wind farm simulation

For the full numerical assessment of wind turbines located in wind farms, an aeroelastic simulation model is required that accounts for wake interaction effects on turbine performance and structural loading. In this thesis, aeroelastic wind farm simulations are performed with the multiphysics tool FAST.Farm developed by NREL. FAST.Farm adds functionalities for the calculation of wake effects to the existing simulation tool OpenFAST, which solves the aero-hydro-servo-elasto dynamics of individual turbines. An overview of FAST.Farm as well as explanations of important features and model extensions are presented in the following sections. A comprehensive description of FAST.Farm can be found in [12] and in the user's guide and theory manual [114].

3.3.1 FAST.Farm implementation

The general structure of FAST.Farm is modular and the different calculation steps of a wind farm simulation are performed in dedicated submodules. A governing driver code interconnects the submodules, enables information exchange between the submodules and drives the time-domain solution forward. In particular, the following submodules exist:

- OpenFAST: Each turbine inside a FAST.Farm simulation is modelled with OpenFAST. It solves the aero-hydro-servo-elastic dynamics for an individual turbine and is explained in more detail in Section 3.3.2.
- Wake Dynamics (WD): For each rotor, the WD module calculates the wake effects including wake advection, deflection and meandering. The implementation is based on the DWM model and is described in Section 3.3.3.
- Ambient Wind and Array Effects (AWAE): This module processes ambient wind and wake interactions across the wind farm domain. It includes a wake-merging submodel, which identifies zones of wake overlap and calculates the resulting wake deficit of multiple wakes. Wind fields can be used from a synthetic turbulence generator (e.g. TurbSim or the Mann model) or from a high-fidelity LES.
- Super Controller (SC): The SC module allows the connection to an external controller library that calculates wind farm wide setpoints for the individual turbines. The module enables the communication of such a wind farm controller with each turbine in OpenFAST.

All presented results within this thesis were produced with the governing version 2.4.0 of the OpenFAST framework. The specific version of FAST.Farm, which includes the implementation of a wake-added turbulence model (see Section 3.3.4), is made available under [115].

3.3.2 Aeroelastic simulation of a single wind turbine

The dynamic response of a wind turbine can be calculated by means of a coupled Multibody Simulation (MBS) model. The MBS methodology is applied in the simulation software OpenFAST [116], which is used for the load calculations of single wind turbines in this thesis as well as for the load calculations of individual turbines inside a FAST.Farm simulation.

Multibody simulation

In general, a MBS is used to calculate the kinematics and dynamics of multiple bodies that experience large displacements with respect to each other. The bodies can be rigid or flexible and are connected with joints. External forces can be applied on the MBS model to represent excitation from, for instance, aerodynamic forces.

In this work, the blades and the tower are modelled as flexible bodies. The flexibility is described using a linear modal representation. The structural properties are specified by stiffness and mass distributions along the span of the members. In addition, for each flexible mode, mode shape functions are defined as polynomials, which are generated beforehand by a finite-element code. The flexibility of the blades is defined with two flapwise and one edgewise bending-mode as Degrees of Freedom (DoFs). For the tower, two bending-modes are used each in the fore-aft and side-side directions.

In OpenFAST, external forces from aerodynamics, hydrodynamics and controller dynamics are computed in dedicated submodels and applied to the equations of motion.

Rotor aerodynamics

Rotor aerodynamics are modelled using the Blade Element Momentum (BEM) theory, which is commonly accepted as state-of-the-art. It calculates on the one hand the local forces at the blade elements distributed over the radius based on the local inflow conditions and airfoil characteristics (e.g. lift- and drag-polars). On the other hand, the induced velocities at the rotor are derived by using an one-dimensional stream tube, satisfying momentum conservation. The relation of the local blade forces and the global momentum conservation is solved iteratively until an equilibrium is reached. The BEM is implemented in the Aerodyn v15 code that is a submodule of OpenFAST.

For the aerodynamic calculation of wind turbine rotors, several correction models are usually applied to overcome the limitations that are present in the original BEM theory. For example, they include the correction for root and tip loss effects, the inclusion of wake dynamics and the correction for the turbulent wake state. For wake redirection control, the correction models for yawed inflow and dynamic stall are considered as especially relevant. They are discussed here in more detail:

- **Yawed inflow:** In yawed operation, the wake behind the rotor cannot be assumed to be axisymmetric (see Section 2.3.3), thus the induction distribution over the rotor is inhomogeneous. In this case, pure BEM theory is not valid and a correction model becomes necessary to calculate the induction distribution over the rotor. It should capture decrease of the induced velocity towards the leading edge of the inclined rotor and the increase towards the trailing edge of the rotor.

For the aerodynamic calculation in this work, the correction model for yawed inflow is based on Glauert, which states

$$a_{yaw} = a \left(1 + K(\chi) \frac{r}{R} \sin(\psi) \right), \quad (3.14)$$

where a_{yaw} is the corrected local induction factor, a is the induction from axisymmetric momentum balancing, K is a model dependent empirical factor that is normally dependent on the wake-skew angle χ and ψ is the azimuthal rotor position.

The complete model is described in [117] and defines the factor $K(\chi)$ based on the Pitt and Peters model. In addition, it takes into account the effects on both axial and tangential induction.

- **Dynamic stall:** The non-axisymmetric induction distribution over the rotor during yawed operation leads to cyclic variations of the local blade-airfoil aerodynamics (similar behaviour is observed from wind shear and rotor tilt). The changing local inflow angle can lead to a separation of the vortices that causes a hysteresis of the lift coefficient and is referred to as dynamic stall.

In order to account for the dynamic stall effect, the Beddoes-Leishman model is used with extensions from [118] and [119]. The details of the model are quite complicated, hence the reader is referred to [120] who describe the model and its implementation in the Aerodyn v15 code.

3.3.3 Wake dynamics: Implementation of the dynamic wake meandering model

The calculation of wake aerodynamics in FAST.Farm is based on the DWM model, which was originally introduced in [11]. It essentially splits the turbulent scales present in ABL flows into two parts: large turbulent eddies (greater than two rotor diameters) affect the wake meandering (see Section 2.3.2) and small turbulent eddies (less than two rotor diameters) have an influence on the wake deficit evolution. The core parts of the original DWM model include the calculation of the wake deficit, the wake meandering and the wake-added turbulence. In FAST.Farm, additional models were developed to consider the wake deflection due to yawed operation and to correct the wake-deficit calculation in the near-wake. The aforementioned models are described in the following. The wake-added turbulence model is implemented into

FAST.Farm within this work and is explained in Section 3.3.4.

The DWM model is a semi-empirical model which is based on physics but also includes simplifications of the governing equations that require the use of calibration parameters. The calibration of the parameters used in FAST.Farm is performed against LES and is explained in more detail in [121] as well as in [114]. The calibrated default values are not changed in this thesis unless explicitly specified.

Wake meandering

The DWM model treats the wake meandering (see also Section 2.3.2) in a way that the wake acts as a passive tracer following the large turbulent structures in the ABL flow. In order to model wake meandering, axial, transversal and vertical wake transport velocities are derived. These velocities essentially define the movement of the wake planes in the Fixed Frame of Reference (FFoR) and depend on the local flow features that are varying with changing downstream distances. In FAST.Farm, they are achieved by calculating the weighted spatial average of the wind velocity within the circle having the diameter of $C_{Meander} D_W$ around the wake centre on a wake plane; D_W is the wake diameter and $C_{Meander}$ is a calibration constant which is set to 2 in the original definition of the DWM model [11] following from the characteristic dimension for wake meandering. The wake transport velocity vector is:

$$\mathbf{v}_{plane} = \frac{\sum_{n=1}^N w_n \mathbf{v}_{wind,n}}{\sum_{n=1}^N w_n}, \quad (3.15)$$

where \mathbf{v}_{plane} is the vector giving the wake transport velocities for a wake plane; N is the total number of considered points within the circle; \mathbf{v}_{wind} is the vector defining the wind speed components at point n . Different implementations for the spatial weighting factor w_n are available in FAST.Farm, $w_n = 1$ provides a simple spatial average.

Wake deficit

The calculation of the wake deficit is conducted in the Meandering Frame of Reference (MFoR) which follows the movements triggered by the wake meandering. It is based on the thin shear-layer approximation of the RANS equations under quasi-steady-state conditions. Cylindrical coordinates are used for the mathematical description. An eddy-viscosity formulation is applied for the turbulence closure [122]. The thin shear-layer approximation is derived by assuming that the velocity gradients are much bigger in the radial direction than in the axial direction. In addition, for a thin-shear layer, the pressure can be approximated by its value at the edges of the shear layer, thus it can be discarded from the equations. With these simplifications, the

analytical expression for the conservation of momentum is:

$$V_x \frac{\delta V_x}{\delta x} + V_r \frac{\delta V_x}{\delta r} = \frac{1}{r} \frac{\delta}{\delta r} \left(r \nu_T \frac{\delta V_x}{\delta r} \right), \quad (3.16)$$

while the expression for the conservation of mass becomes:

$$\frac{\delta V_x}{\delta x} + \frac{1}{r} \frac{\delta}{\delta r} (r V_r) = 0. \quad (3.17)$$

The axial and radial velocities are V_x and V_r , respectively; ν_T is the eddy viscosity. All variables are dependent on the axial and radial coordinates x and r .

The eddy viscosity is an important parameter because it controls the recovery rate of the velocity deficit. The complete calculation of the eddy viscosity in FAST.Farm is explained in [114]. However, the variable $TI_{amb,Rotor}$ used in the calculation of the eddy viscosity is mentioned here as it is further discussed in Section 5.4.3. The variable $TI_{amb,Rotor}$ calculates the ambient turbulence intensity around the rotor at each time-step serving as an input to the eddy viscosity function. It is defined by the following equation:

$$TI_{amb,Rotor} = \frac{\sqrt{\frac{1}{3N} \sum_{n=1}^N \left\| \mathbf{v}_{wind,n} - \left\{ \frac{1}{N} \sum_{n=1}^N \mathbf{v}_{wind,n} \right\} \right\|_2^2}}{\left\| \left\{ \frac{1}{N} \sum_{n=1}^N \mathbf{v}_{wind,n} \right\} \right\|_2}, \quad (3.18)$$

where \mathbf{v}_{wind} is the vector defining the wind speed components at point n . The point counter n considers all points N within a circle having the diameter of $C_{Meander} D_W$ around the rotor centre on the rotor plane; D_W is the wake diameter and $C_{Meander}$ is a calibration constant which is calibrated to 1.9 in [121]. The two-norm of a vector \mathbf{v} is denoted by $\|\mathbf{v}\|_2$. The bracketed term in Equation 3.18 is the spatial average for all wind components inside the aforementioned circle. The definition of the $TI_{amb,Rotor}$ can be physically interpreted as the spatial turbulence intensity that is varying for each cross plane passing the rotor. The $TI_{amb,Rotor}$ takes effects from atmospheric shear, veer and other ambient wind characteristics inherently into account and consequently affects the magnitude of the eddy viscosity and in turn the wake deficit evolution. Hence, higher values of the $TI_{amb,Rotor}$ lead to an increased eddy viscosity which is followed by a faster velocity deficit recovery.

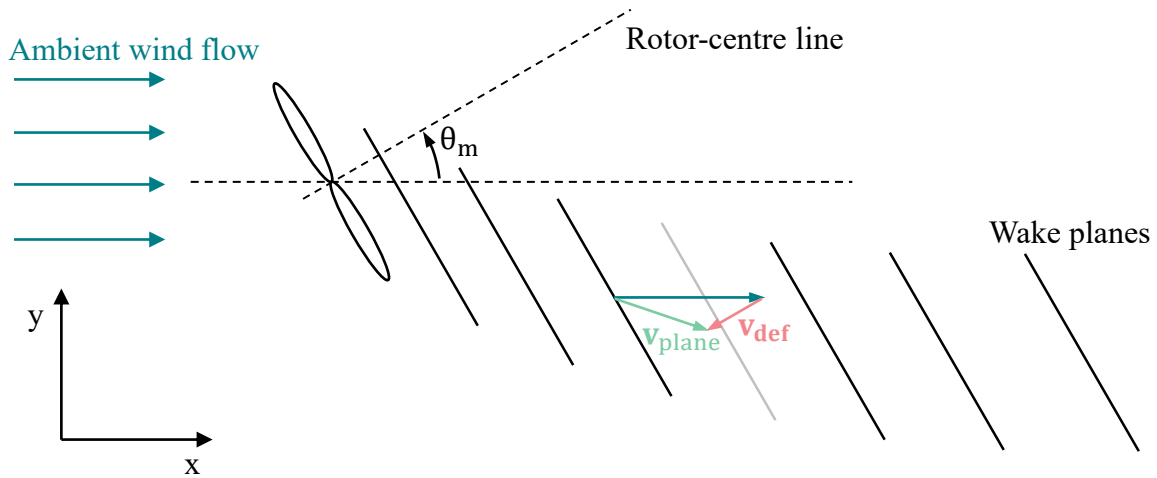


Figure 3.2: Simplified illustration of the calculation of the wake centre deflection in FAST.Farm. θ_m is the yaw-misalignment angle, \mathbf{v}_{def} is the velocity deficit vector and \mathbf{v}_{plane} is the resulting plane velocity vector.

Wake deflection

The passive tracer solution for the lateral and vertical wake meandering from the DWM model is extended in FAST.Farm to take the effects from yawed operation on the wake centre position into account (see also Section 2.3.3). This is mainly achieved by orientating the wake planes with the rotor-centre line instead of the main wind direction. Consequently, the wake deficit normal to the disc \mathbf{v}_{def} introduces a velocity component which is not parallel to the main wind direction (see Figure 3.2). The resulting velocity of the wake planes \mathbf{v}_{plane} lead to a horizontal and vertical deflection of the wake centre that is dependent on the rotor orientation and velocity deficit magnitude.

In addition, a correction function for the lateral wake centre deflection is used, which corrects the results from the velocity-based calculation of the wake centre deflection. It is a linear function (with slope and offset dependent on the yaw-misalignment angle) and involves empirical constants which can be calibrated to known solutions from, for instance, higher-fidelity models or measurements.

Near-wake correction

The near-wake correction model of FAST.Farm calculates the axial and radial velocity deficit profiles which are used as boundary condition for the computation of the wake deficit evolution. It considers the wake expansion in the pressure-gradient zone and the corresponding decreasing velocity up to the point of complete pressure recovery (see also Section 2.3.1).

The model differentiates between low thrust ($c_T < \frac{24}{25}$) and high thrust conditions ($1.1 < c_T \leq 2$). In low thrust conditions, momentum theory is valid and is applied to derive the radial distribution of the axial induction factor a in dependency on the radial thrust coefficient $c_T(r)$ as follows:

$$a(r) = \frac{1}{2} \left(1 - \sqrt{1 - c_T(r)} \right). \quad (3.19)$$

At high thrust conditions, the initial velocity deficit of the wake is derived based on a Gaussian fit to the results from LES simulations which is explained in [123]. A linear blending function is used for the region where the accuracy of both low- and high-thrust models starts to decrease, i.e. $\frac{24}{25} < c_T \leq 1.1$).

3.3.4 Wake-added turbulence model

In addition to the modelling of wake deficit and wake meandering (see Section 3.3.3), the DWM model described by [43] contains modelling of wake-added turbulence. During the research leading to this thesis, a wake-added turbulence model was implemented in FAST.Farm, which is described in [124] serving as basis for this section.

The term wake-added turbulence describes the generation of turbulence behind a wind turbine rotor due to shear forces in the wake, as well as the breakdown of mainly the tip and root vortices. The contribution of wake-added turbulence to the total turbulence level inside a turbine's wake is higher for low ambient turbulence conditions [125]. Therefore, the inclusion of wake-added turbulence is especially important for offshore conditions where ambient turbulence levels are often low (i.e. less than 10 %). This is also evaluated in more detail by comparing simulations results with measurement data in Section 4.3.2.

The herein presented implementation of wake-added turbulence in FAST.Farm follows mainly the approach by [43] and [125], which is included in the IEC 61400-1 standard [15]. In addition to the ambient turbulence domain, it uses a new wake-added turbulence domain defined in the meandering frame of reference. This domain is generated with Mann's spectral turbulence model [86], defining turbulence as homogeneous and isotropic with a length scale that is equal to the rotor diameter. The domain should have a fine spatial discretisation to resolve the smaller turbulent scales of the wake-added turbulence. A discretisation study is conducted in Section 4.1.3.

The wake-added turbulence velocity components are scaled with the factor k_{mt} defined by

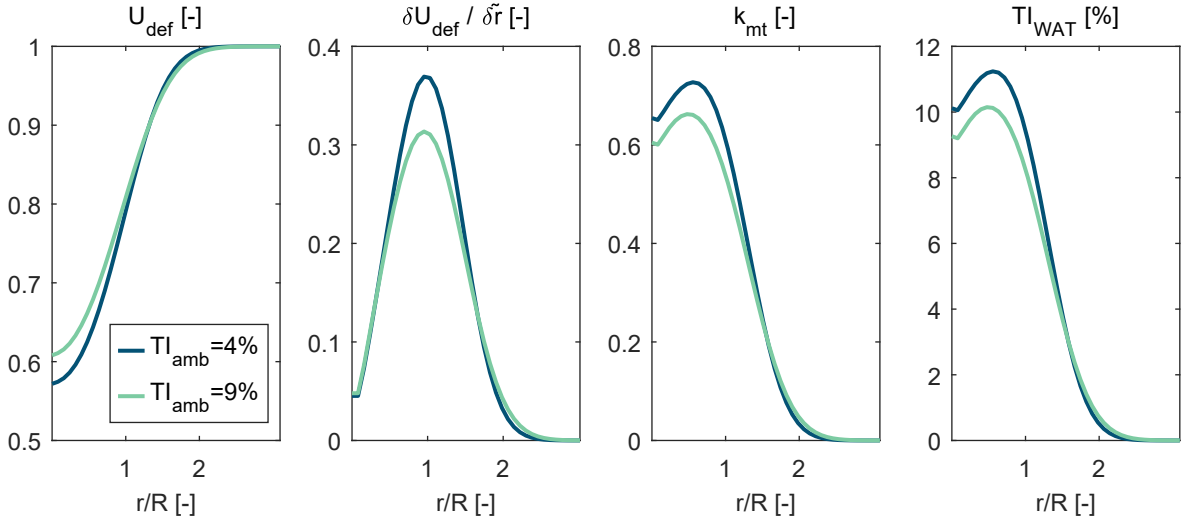


Figure 3.3: Exemplary results from the calculation of wake-added turbulence from left to right: velocity deficit distribution, radial gradient of the velocity deficit, scaling factor k_{mt} , resulting distribution of the turbulence intensity from the wake-added turbulence TI_{WAT} . Calculations are made for two ambient turbulence levels at 6D behind the rotor. Simulations are performed with FAST.Farm in neutral atmospheric conditions with a mean wind speed of 6.5 m s^{-1} at hub height.

Equation 3.20. It consists of two terms, which are influenced by: 1) the quasi-steady wake deficit $u_{def}(x, \tilde{r}) = u(x, \tilde{r})/V_{DiskAvg}$, expressed with the wake velocity $u(x, \tilde{r})$ that is normalised by the rotor disk-averaged ambient wind speed normal to the disk $V_{DiskAvg}$, and 2) the radial wake deficit gradient. The contributions of those terms are controlled with the empirical coefficients k_{m1} and k_{m2} . The factor k_{mt} is dependent on the axial distance to the rotor x and the radial location \tilde{r} normalised by the rotor radius.

$$k_{mt}(x, \tilde{r}) = k_{m1} \left| 1 - \frac{u(x, \tilde{r})}{V_{DiskAvg}} \right| + \frac{k_{m2}}{V_{DiskAvg}} \left| \frac{\delta u(x, \tilde{r})}{\delta \tilde{r}} \right| \quad (3.20)$$

Exemplary distributions of the TI from the wake-added turbulence TI_{WAT} and the corresponding velocity deficit profiles are displayed in Fig. 3.3. The empirical constants involved in Equation 3.20 were re-calibrated to $k_{m1} = 1.48$ and $k_{m2} = 1.01$ by using results from high-fidelity LES outlined in Section 4.1. These calibrated values differ slightly from the values obtained by the first calibration of the wake-added turbulence model in FAST.Farm in [124]. This first calibration is based on the measurement data from the alpha ventus wind farm (see Section 4.2.1), leading to the constants $k_{m1} = 1.44$ and $k_{m2} = 0.84$. The recommended values by the IEC 61400-1 standard are $k_{m1} = 0.6$ and $k_{m2} = 0.35$. The reason for the discrepancy between the IEC values and the re-calibrated values is not clear. However, the resulting turbulence levels from the wake-added turbulence model seen in Fig. 3.3 are similar to turbulence values found in the literature, e.g. from [56] and [125].

The implementation of wake-added turbulence in the FAST.Farm code consists of three major

additions:

1. A new instance of the FAST.Farm module InflowWind is initialised for the wake-added turbulence domain; it is reused for each turbine in the simulation domain to ensure computational efficiency. The turbulent wind box that is created beforehand with the DTU Mann turbulence generator [89] is loaded into this instance of InflowWind. In the course of a FAST.Farm simulation, the wake-added turbulence wind field is propagated with the ambient wind speed at hub height. The use of a Mann turbulence field is mainly motivated by practical reasons with regard to the implementation in InflowWind; when using a Mann turbulence field, a reference wind speed can be directly defined inside InflowWind, which is eventually used to propagate the wake-added turbulence box downstream.
2. The scaling factor k_{mt} is calculated in the meandering frame of reference inside the WD module of FAST.Farm. The calculation is based on the quasi-steady velocity deficit and its radial gradient, that are already available inside the WD module.
3. In the module AWAE of FAST.Farm, the velocities of the wake-added turbulence field are interpolated based on their spatial location and scaled with the spatially interpolated value of the factor k_{mt} . The resulting velocities are added to the ambient wind vector via vector addition in the low- and high-resolution domains of FAST.Farm and transformed from the meandering frame of reference to the fixed frame of reference.

3.3.5 Spatial and temporal discretisation

Simulations with FAST.Farm require adequate temporal and spatial discretisation in order to solve the discretised equations numerically. In particular, a simulation in FAST.Farm contains different domains which are explained in the following. Their discretisation used in this thesis is explained; it is guided by the recommendations given in [126].

- Low-resolution domain: This domain covers the entire wind turbine array and is used to propagate the wakes downstream including the wake meandering. The relevant phenomena (large-scale turbulence, wake-meandering) can be resolved with a relatively coarse discretisation because of the large temporal and spatial scales involved. For the simulations in this thesis, a time step of $dt_{low} = 2 \text{ s}$ and a spatial step size of $ds_{low} = 12 \text{ m}$ are set unless specified differently. The total size of the domain depends on the wind farm configuration. However, in all simulations, additional space in the horizontal direction ($\approx 2 D$) and vertical direction ($\approx 1.2 D$) is reserved at the boundaries of the domain to allow horizontal and vertical wake meandering.

- High-resolution domain: A high-resolution domain contains each individual turbine within the considered wind farm. A fine discretisation is required to resolve the rotor aerodynamics sufficiently. Therefore, the time step is set to $dt_{high} = 0.2 \text{ s}$ and the spatial step size is $ds_{high} = 4.5 \text{ m}$ which is approximately the maximum chord length of the blades from the turbines used within this thesis.
- Wake deficit domain: The wake deficit is computed on an axisymmetric finite-difference grid in FAST.Farm. The radial direction is discretised with a step size of $dr_{WD} = 5 \text{ m}$ being approximately the maximum chord length of the blades from the turbines used within this thesis. The wake deficit is propagated downstream with wake planes that are shed from the turbine at each time step of the low-resolution domain. Their propagation speed is dependent on the ambient wind speed and the wake deficit itself. In this thesis, the velocity deficits are modelled up to a downstream distance of $10 D$ where it is assumed that the wake deficit is nearly recovered. Consequently, the total number of wake planes is set per simulation correspondingly in order to ensure the predefined simulated length of the velocity deficit.
- Wake-added turbulence domain: The modelling of wake-added turbulence is implemented in FAST.Farm by using a turbulence box generated with Mann's method (see Sections 3.1.1, 3.3.4). The temporal and spatial discretisation is the same as for the high-resolution domain, i.e. $ds_{WAT} = 4.5 \text{ m}$ and $dt_{WAT} = 0.2 \text{ s}$. The wake-added turbulence domain covers approximately the dimensions of the wake deficit in the lateral and vertical directions, thus the length of the domain edges is $\approx 2.5 D$. The derivation of the values is explained in detail in Section 4.1.3.

All parameters of the discretisation used in this thesis are summarised in Table 3.2. As discussed in [126], the values are chosen to keep discretisation errors below 2 %.

Table 3.2: Temporal and spatial discretisation values used in the FAST.Farm simulations

Description	Parameter	Value
Spatial increment of low-resolution domain	ds_{low}	12.0 m
Time step of low-resolution domain	dt_{low}	2.0 s
Spatial increment of high-resolution domain	ds_{high}	4.5 m
Time step of high-resolution domain	dt_{high}	0.2 s
Spatial increment of wake-added turbulence domain	ds_{WAT}	4.5 m
Time step of wake-added turbulence domain	dt_{WAT}	0.2 s
Radial increment of wake deficit domain	dr_{WD}	5.0 m

4

Simulation model calibration and validation

The simulation tool FAST.Farm used in this thesis is calibrated and validated in this Chapter. In particular, the new wake-added turbulence module developed within this work is calibrated and validated against high-fidelity LESs in Section 4.1. Subsequently, FAST.Farm is validated in terms of the calculation of the aeroelastic turbine response in free-stream (Section 4.2) and single wake (Section 4.3) conditions against measurement data from the alpha ventus wind farm. Here, the validation of the wake-added turbulence model against measurement data is performed as well. In Section 4.4, the low-fidelity wind farm flow simulation tool FLORIS is calibrated with respect to FAST.Farm simulations. FLORIS is then used for the optimisation of wind farm control strategies.

4.1 Calibration of wake-added turbulence model

The wake-added turbulence model was implemented in FAST.Farm in the course of this work (see Section 3.3.4). Its current implementation includes two empirical parameters (k_{m1} , k_{m2}) that must be calibrated. Therefore, results from LES are processed and compared to results from FAST.Farm that is run with wind fields generated by LES. The calibration of the two factors is then performed by using an optimisation, where the difference of turbulence profiles in the wake between LES and FAST.Farm is minimised. A final discretisation study is conducted in order to derive recommendations on minimal grid requirements for the wake-added turbulence model.

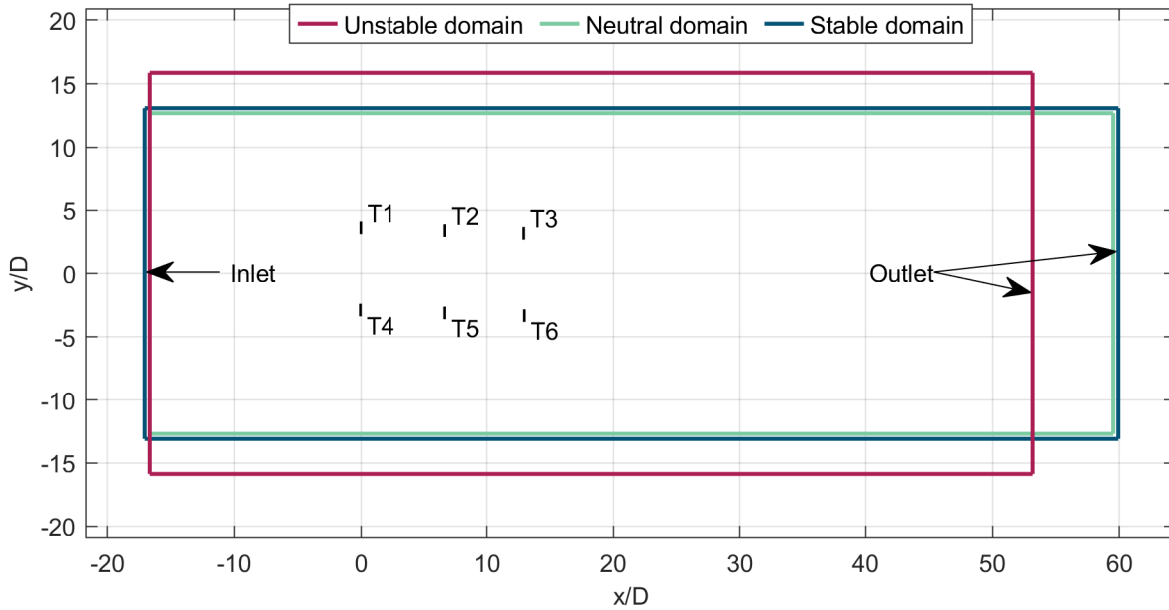


Figure 4.1: Visualisation of the domain sizes used in the reference PALM-LES. The x - and y -coordinates are normalised by the rotor diameter D . The turbines are indicated by the black lines T1-T6.

4.1.1 Reference simulations: PALM-LES

Results from LES are used as reference for the calibration. They were prepared with the PALM code (see Section 3.2.2) by colleagues from the University of Oldenburg in the course of the OWP Control project [127]. Due to the high computational costs of LES, three cases in total are considered representing unstable, neutral and stable atmospheric conditions. In the following, the simulation setup of the LES is explained and the resulting wind field characteristics are discussed.

Simulation setup

In all cases, an ABL flow is initialised in advance by using precursor simulations with cyclic boundary conditions. After reaching an equilibrium, the results from the precursor simulations are applied as boundary conditions in the main simulations. On the one hand, these are performed without any wind turbines in order to serve as wind fields in FAST.Farm. On the other hand, wind turbines are included as actuator discs to acquire the reference results. The wind turbines are NREL 5MW machines with slight modifications presented in [128]; their hub height is at 92 m.

The simulation domain was originally created for a six-turbine scenario as shown in Figure 4.1. The domain size is the same for the neutral and stable case but it is slightly different for the

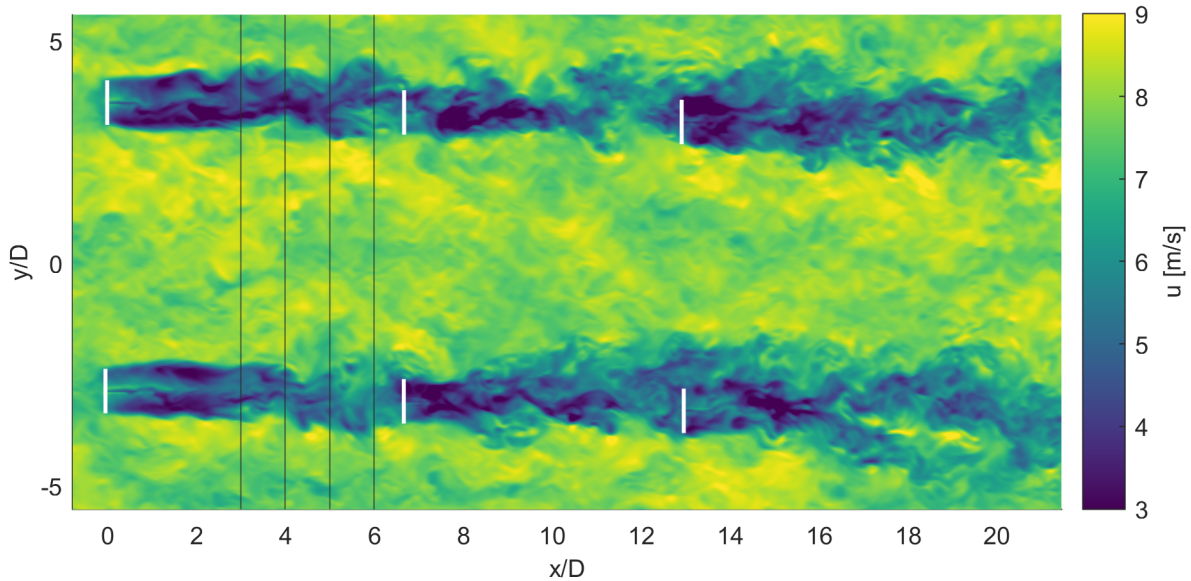


Figure 4.2: Flow field of the wind speed component u at the horizontal plane at hub height. Instantaneous snapshot captured from the neutral ABL case at the simulation time of $t = 2000$ s. The white lines indicate the turbine rotor locations, the black lines at x -positions 3-6 D indicate the locations of the wake profile analyses in Section 4.1.2.

unstable case. At the inlet, the pre-generated turbulence data is used as boundary condition. At the lateral boundaries, cyclic boundary conditions are used. A radiation boundary condition ensures undisturbed outflow at the outlet. At the bottom, a kinematic heat flux is set for the stable ($-0.001 \text{ K m s}^{-1}$) and unstable (0.02 K m s^{-1}) cases. For more information on the simulation domain setup and the boundary conditions, the reader is referred to [90] and [127].

In the present application, only the wakes of the first two free-stream turbines are analysed because of the problems with the waked turbines that operate near the cut-in wind speed and show unstable behaviour originating from the controller. An instantaneous snapshot of the flow field with wind turbines at hub height is shown in Figure 4.2.

The simulations are initialised with appropriate initial conditions to achieve the desired ABL states. In all cases, the desired wind speed at hub height is 8 m/s , where the turbines operate in below rated conditions with high thrust coefficients (free-stream turbine: $c_T \approx 0.82$). A total simulation length of 3960 s is obtained. The parameters for the initialisation of the LES are explained in more detail in [127].

Table 4.1: Statistical parameters of the LES for the time period between 200-3800 s. Δz_{Rotor} refers to the vertical span of the rotor ranging from $z = 29$ m to $z = 155$ m.

Atmospheric stability	\bar{u} at hub height [m s ⁻¹]	TI at hub height [%]	Fitted α_{shear} over Δz_{Rotor} [-]	Veer $\Delta\varphi/\Delta z_{Rotor}$ [° m ⁻¹]	L_* [m]
unstable	8.1	5.9	0.03	0.0002	-65
neutral	7.9	4.5	0.08	0.02	1000000
stable	7.8	2.7	0.09	0.04	492

Wind field characteristics

The mean wind speed, mean wind direction and turbulence profiles for the three ABL scenarios are shown in Figure 4.3. In all cases, the desired mean wind speed of 8 m s^{-1} is nearly achieved (see Table 4.1 for exact values). The mean wind speed profiles show stronger vertical shear for stable and neutral conditions, whereas unstable conditions exhibit a nearly uniform profile due to strong turbulent mixing. In the simulation with stable conditions, the upper limit of the ABL is visible at around 230 m (compare Figure 4.3 (a)). Turbulence is the lowest in stable atmospheric conditions and the highest in unstable conditions. In all cases, the TI and Turbulent Kinetic Energy (TKE) are gradually decreasing over height except near the ground, where the grid resolution is not high enough to resolve the turbulence adequately. The wind direction variation with height (veer) has a larger gradient in stable AS compared to neutral, and especially unstable conditions, in which wind veer is negligible.

Further characteristic parameters of the LES are summarised in Table 4.1. The Obukhov length equals -65 m for unstable conditions indicating a strongly unstable ABL; in stable conditions, the Obukhov length is 492 m which characterises a weakly stable ABL.

4.1.2 Wake-added turbulence model parametrisation

Simulations in FAST.Farm were performed using the LES wind fields that were generated by PALM and presented in the previous section. In a first step, the wake-added turbulence model is deactivated and the predicted wake centre positions compared between FAST.Farm and PALM.

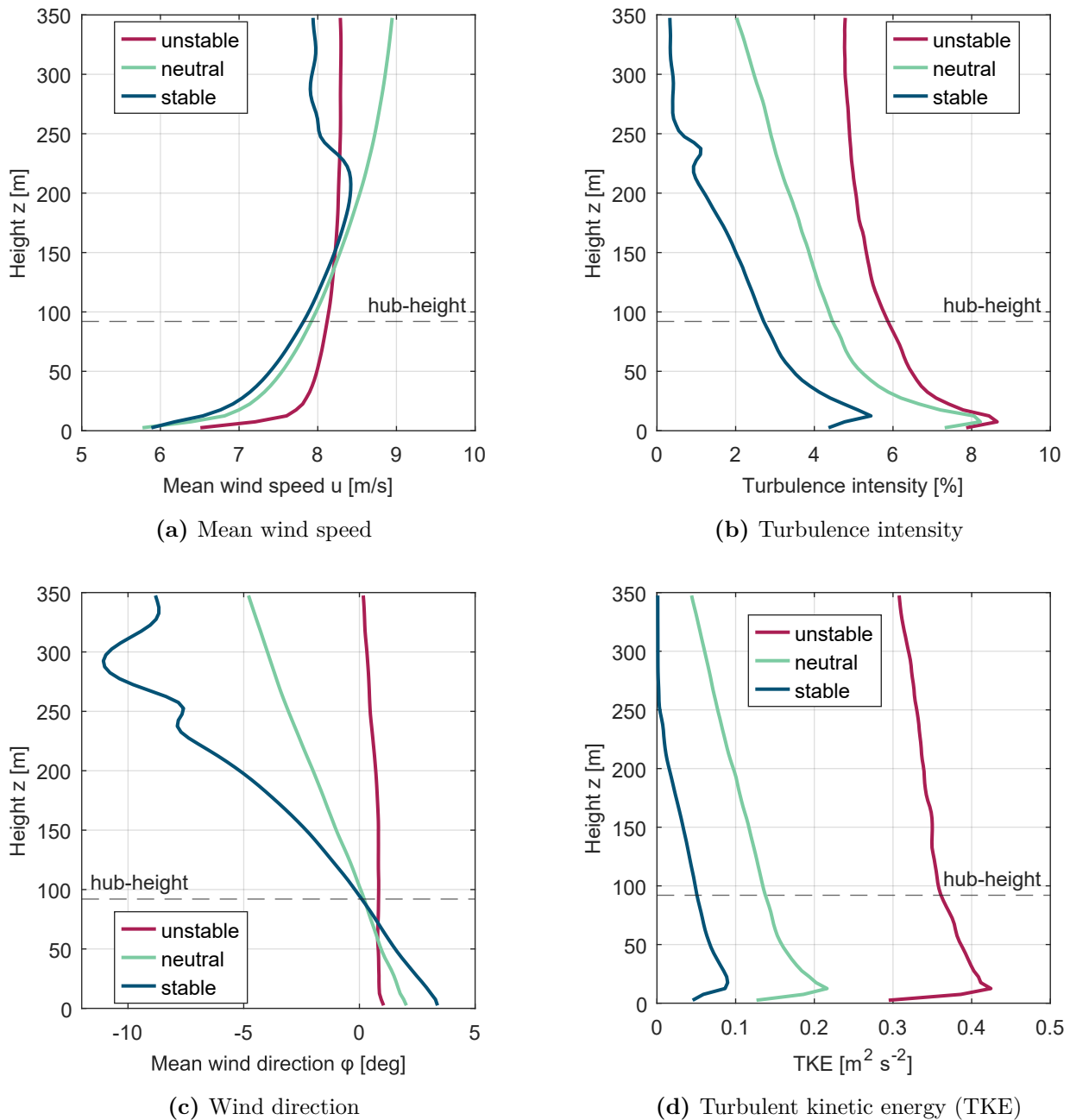


Figure 4.3: Vertical profiles of the LES representing free-stream conditions captured at the x-location of the upper free-stream turbine. Statistics are calculated for the time period between 200-3800 s and are averaged over the y-direction.

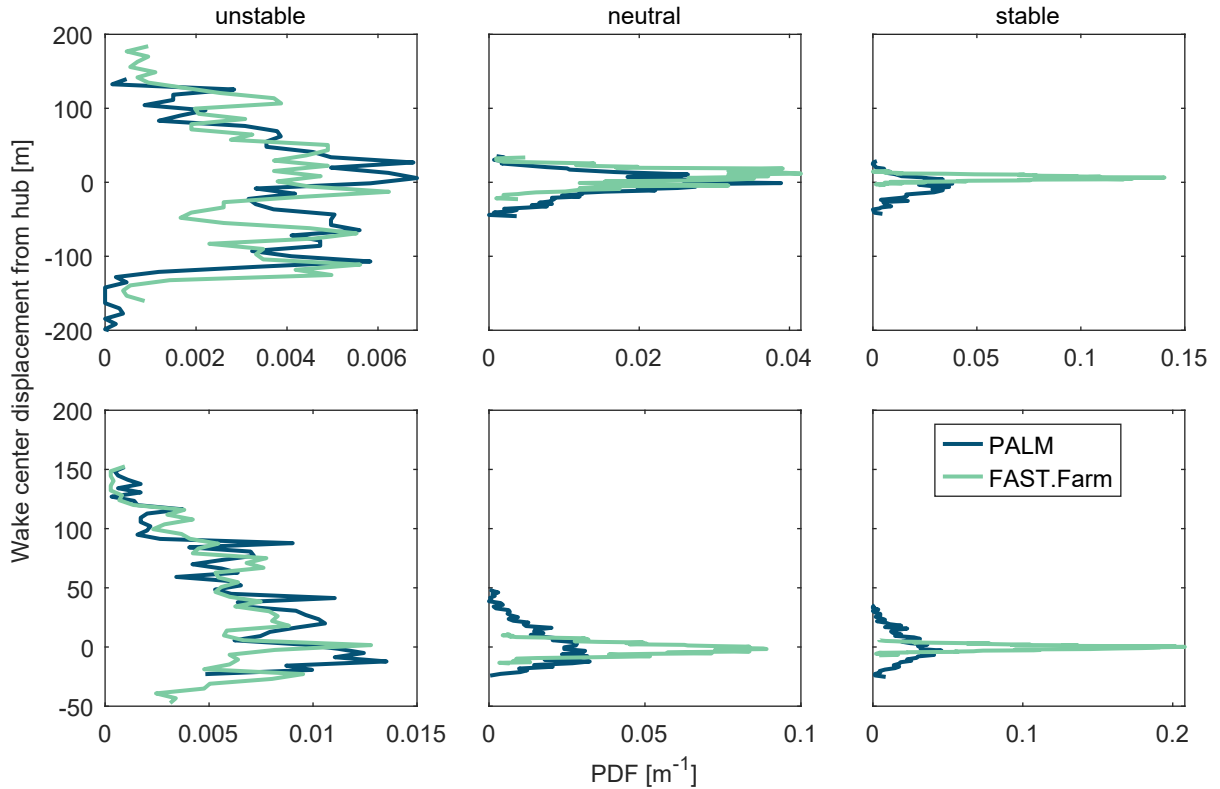


Figure 4.4: Histograms of wake centre displacement expressed as probability density function (PDF) relative to the hub of the upper free-stream turbine in the lateral (upper row) and vertical (lower row) directions at a downstream distance of $6D$.

Comparison of wake centre positions

Wake meandering leads to displacements of the wake centre and is dependent on the large-scale turbulent structures in the wind field. The predictions of the wake-centre positions by FAST.Farm and PALM are displayed in Figure 4.4 for the three ABL situations. The wake centre position in PALM is estimated by calculating the available power in the wind which is minimal at the wake locations [63]. Largest displacements in both horizontal (up to $\approx 1.5D$) and vertical (up to $\approx 1.2D$) direction are observed in unstable conditions. In contrast, wake displacements are much less in neutral and stable conditions.

The FAST.Farm predictions are mostly in good agreement with the LES results. Trends in the different stability scenarios are captured well. For the stable case, an underestimation of the wake meandering is found for FAST.Farm compared to PALM. This deviation is acceptable because the wake meandering is generally low in these conditions and the wake centre estimation technique for the LES has some uncertainties on its own (see [63]).

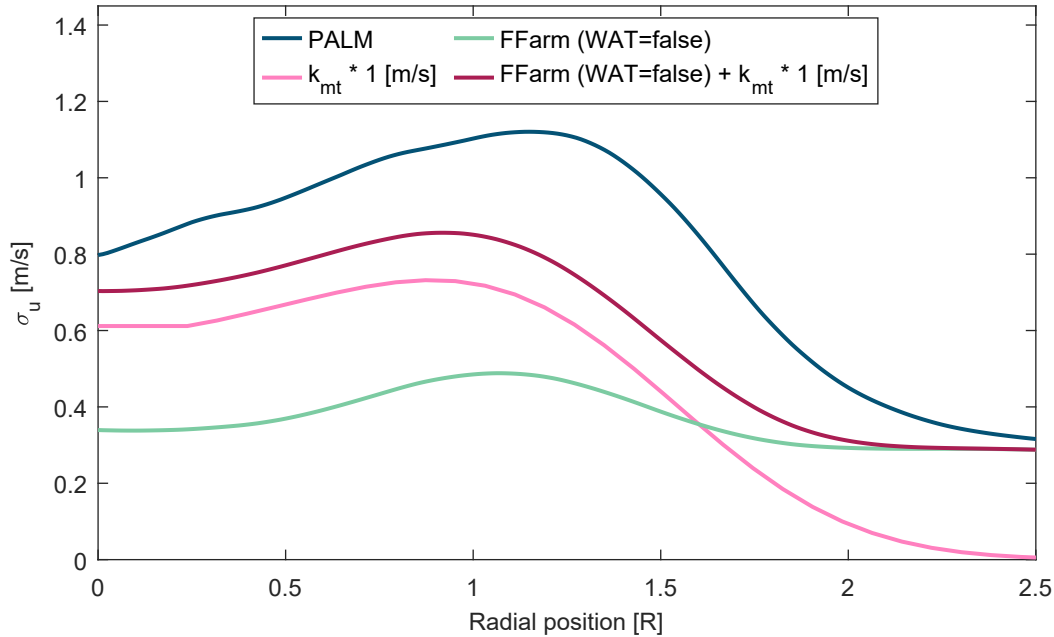


Figure 4.5: Exemplary distribution of turbulence expressed as the standard deviation σ_u over the rotor radius. FAST.Farm (FFarm) results are shown without wake-added turbulence (WAT=false) and with added k_{mt} distribution. The values are averaged over the azimuth for the upper half of the rotor.

Derivation of wake-added turbulence calibration

In the previous section, it is concluded that FAST.Farm calculates the wake meandering with reasonable accuracy. Consequently, discrepancies in the turbulence profiles in the wake between FAST.Farm and PALM can be attributed to the wake-added turbulence. This assumption is utilised for the calibration of the wake-added turbulence model in FAST.Farm.

The distribution and composition of turbulence over the radius in the wake is illustrated exemplarily in Figure 4.5 with respect to the fixed frame of reference. The reference results from PALM include the wake-added turbulence plus the apparent turbulence originating from the wake meandering. The results from FAST.Farm are shown without the wake-added turbulence model, hence they include only contributions from the wake meandering. By including the wake-added turbulence in FAST.Farm with an adequate calibration, it is possible to close the modelling gap to the PALM reference turbulence profile; therefore, the following procedure is applied:

1. Turbulence profiles in the wake from a FAST.Farm simulation without wake-added turbulence serve as the baseline and include the turbulence contribution from wake meandering.
2. Based on the velocity profiles of the wake deficit from the FAST.Farm baseline simulation, the amplification factor k_{mt} is calculated with the Equation 3.20 and new values for the

calibration factors k_{m1} and k_{m2} . The distribution of k_{mt} is calculated for each time step and is corrected with the position of the wake centre that is displaced by the wake meandering.

3. The distribution of k_{mt} over the radius is multiplied with the standard deviation of $\sigma = 1 \text{ m s}^{-1}$ (see Section 3.3.4) and added to the baseline turbulence profile.
4. The final turbulence profiles are then compared to the reference PALM results. An optimisation problem is formulated that minimises the error of the turbulence profiles $\sigma_{u,v,w}(x, y, z)$ at various downstream locations (3 D, 4 D, 5 D, 6 D; see Figure 4.2) between FAST.Farm and PALM by varying the calibration constants k_{m1} and k_{m2} :

$$\min (\sigma_{u,v,w,Palm}(x, y, z) - \sigma_{u,v,w,FFarm}(x, y, z, k_{m1}, k_{m2})) \quad (4.1)$$

The optimisation is solved with the `fminsearch` function from Matlab.

The calibration of the wake-added turbulence model parameters k_{m1} and k_{m2} is performed for each ABL case. The rather long PALM simulations are split into segments of 600s in order to increase the amount of events. The results of the calibration are presented in Figure 4.6. The calibrated values of the two parameters change with the atmospheric stability. For unstable conditions, the scatter for both parameters is large, whereas only small variations are found for neutral and stable conditions. The total turbulence level in the wake for unstable conditions is dominated by the contribution from the wake meandering; consequently, a reliable calibration of the wake-added turbulence parameters is challenging and it is decided to exclude these conditions from the final value selection.

The values given by the IEC 61400-1 Ed.4 standard [15] for the two parameters are lower compared to the calibrated values. A clear explanation has not been found; a slightly different implementation of the wake-added turbulence model presented in [125], on which the IEC values are based, may be a possible cause. However, the mean value of the ratio $k_{m2}/k_{m1} \approx 0.65$ for the calibrated values in neutral and stable conditions is close to the value of 0.58 given by the IEC guideline. Recent work on the calibration of the two parameters suggests a dependency on the ambient TI [129]. This dependency cannot be confirmed by the current data set.

Finally, the selected values for the two constants are $k_{m1} = 1.48$ and $k_{m2} = 1.01$. They represent the mean values gathered only from the stable ABL simulations. This choice is motivated by the fact that the wake-added turbulence model is most relevant in stable conditions and the results are little affected by wake meandering.

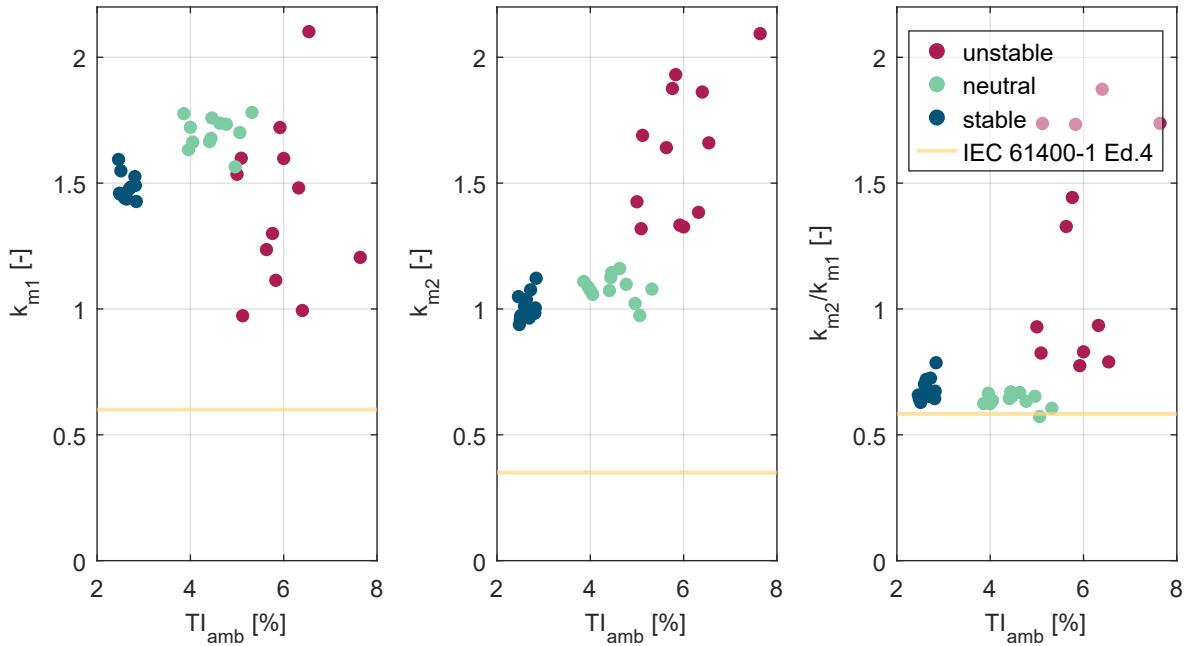


Figure 4.6: Calibrated wake-added turbulence parameters k_{m1} and k_{m2} plus their relation for the different atmospheric stabilities and time segments. The ambient TI_{amb} is averaged over the rotor disc at the turbine’s location.

Check of model parametrisation

The chosen parametrisation of the wake-added turbulence model in FAST.Farm is checked by performing simulations with the calibrated values $k_{m1} = 1.48$ and $k_{m2} = 1.01$. The resulting turbulence profiles are compared for the three velocity components u, v, w and at different downstream distances in the horizontal direction (Figure 4.7) as well as the vertical direction (Figure 4.8) for the stable ABL. The results for unstable and neutral conditions are provided in the Appendix A.1.

It is shown that the turbulence profiles predicted by FAST.Farm are in much better agreement with the PALM-LES when the wake-added turbulence model is active. Especially in stable conditions, the inclusion of wake-added turbulence is considered to be crucial. In the u -component of the horizontal turbulence profiles (Figure 4.7), very little contribution from the wake meandering to the turbulence level is observed by looking at the FAST.Farm simulation without wake-added turbulence; in the v - and w -component, the turbulence level shows no difference compared to the free-stream conditions.

The turbulence predictions in the wake by FAST.Farm with activated wake-added turbulence model show good agreement with the PALM-LES especially for the downstream distances from 3-5 D. For example, the mean error across the rotor-disc from the prediction of the standard deviation between FAST.Farm without wake-added turbulence and PALM-LES is $\approx 75\%$ for all

velocity components at the downstream distance of 5 D. With activated wake-added turbulence, the error is reduced significantly to $\approx 15\%$ for all velocity components. At the distance of 6 D, FAST.Farm underestimates the turbulence level compared to the LES by approximately 35% on average. A conclusive explanation for this behaviour has not been found, since the velocity deficit is predicted with reasonable accuracy by FAST.Farm (see Figures A.2-A.7); an influencing factor in the PALM-LES is the presence of another wind turbine at a distance of 6.7 D which could lead to the deviations. It is observed that the horizontal and vertical extension of the wake-induced turbulence increase from FAST.Farm is smaller compared to the results from the PALM-LES. This is a result of the slight underestimation of the wake-meandering by FAST.Farm in stable conditions (see Figure 4.4).

The turbulence profiles from the PALM-LES support the isotropic definition of the wake-added turbulence model because the standard deviations from the three velocity components have similar levels. The effect of the wake-meandering on the turbulence level is mostly seen in the u-component and is best visible for unstable AS (see also A.9). It is concluded that the wake-added turbulence model is especially important in stable atmospheric conditions. In neutral and unstable conditions, the wake-added turbulence increases the accuracy in the prediction of the turbulence mainly in the lateral and vertical wind velocity components. The calibration of the wake-added turbulence model in FAST.Farm gives reasonable results with respect to the reference results from the PALM-LES.

4.1.3 Wake-added turbulence model discretisation

A discretisation study for the wake-added turbulence model is conducted to analyse the dependence of the simulation results on the spatial and temporal discretisation of the wake-added turbulence domain. Simulations are performed in FAST.Farm with two aligned NREL 5 MW turbines (see Section 5.1 for more information). Ambient turbulence is generated with Mann's method applying the parameters for a stable ABL (see Table 3.1). The ambient TI is set to 6% and the vertical wind shear is modelled according to the power law with an exponent of $\alpha_{shear} = 0.14$. Three wind speeds are considered representing below-rated (8 m s^{-1}), near-rated (12 m s^{-1}) and above-rated (18 m s^{-1}) conditions. The results are evaluated by comparing the structural loads at different locations of the waked wind turbine. A more detailed explanation of the analysed sensors is given in Section 5.1.

For the spatial discretisation study, the step size ds_{WAT} is varied from 3 m to 18 m. The time step is kept constant at a low value of $dt_{WAT} = 0.1 \text{ s}$. The results are assessed by computing the percent error with regard to the finest spatial discretisation and are displayed in Figure 4.9. Overall, the results converge to the lowest considered spatial step size with decreasing increments. Highest discretisation errors (up to 6% for the fore-aft bending moment at the tower-top) are observed for the wind speed of 8 m s^{-1} . The aim is to keep the discretisation

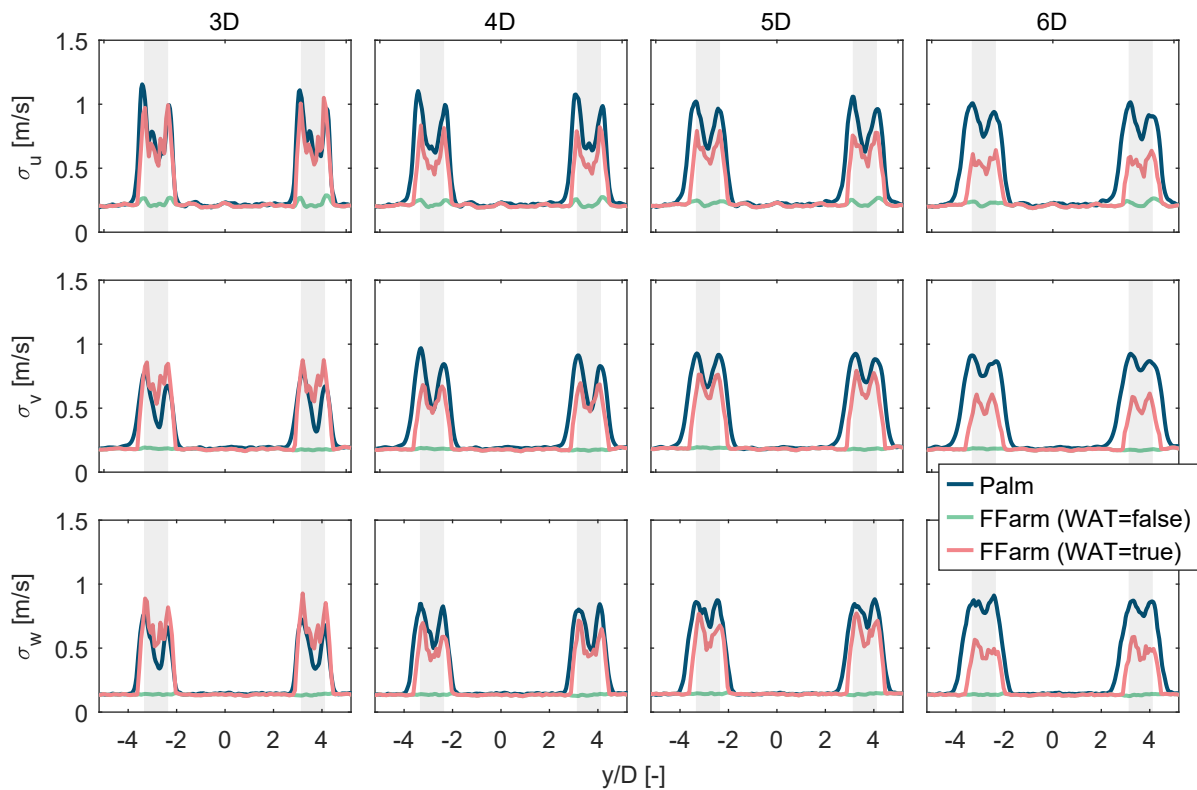


Figure 4.7: Turbulence profiles (expressed as standard deviation of the three velocity components $\sigma_{u,v,w}$) in the horizontal direction at various downstream distances (3-6 D) at hub height ($z=92$ m) for stable atmospheric conditions. FAST.Farm (FFarm) results are plotted with activated (WAT=true) and deactivated (WAT=false) wake-added turbulence model. The rotor position of the turbines T1 and T4 is indicated by the grey patches.

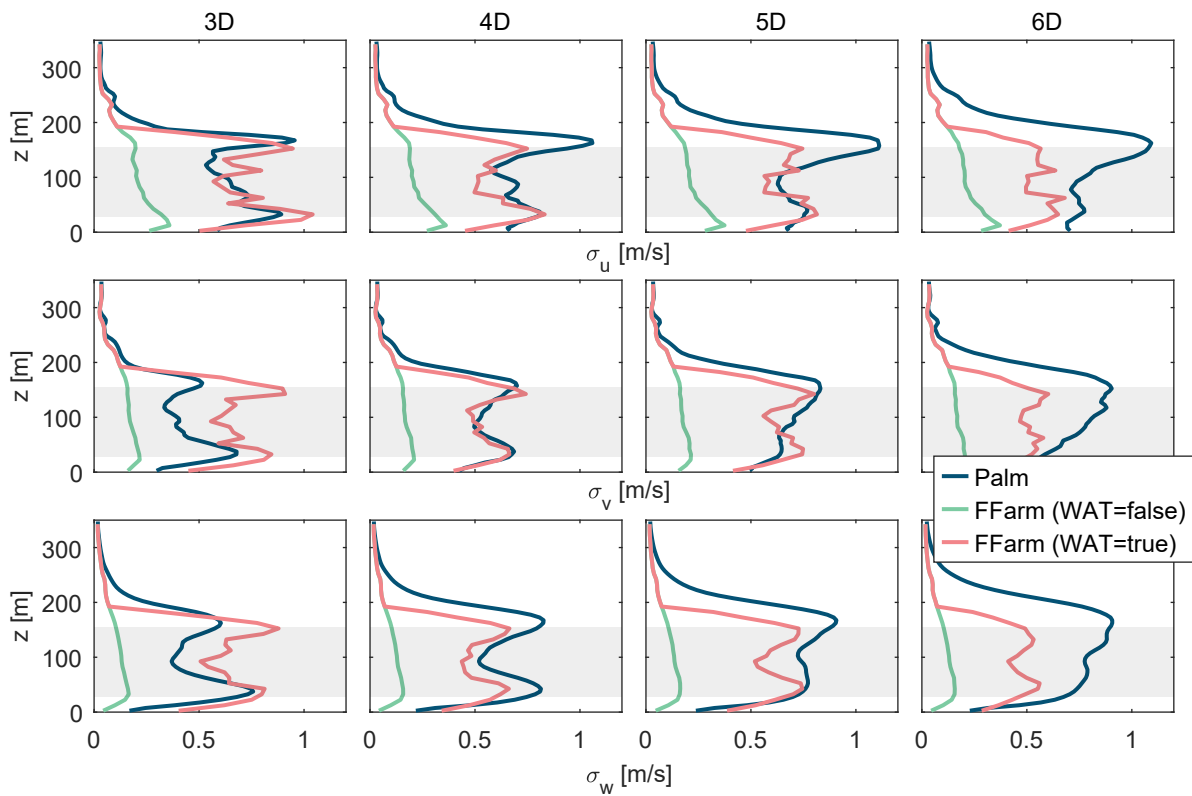


Figure 4.8: Turbulence profiles (expressed as standard deviation of the three velocity components $\sigma_{u,v,w}$) in the vertical direction at various downstream distances (3-6 D) behind the upper free-stream turbine for stable atmospheric conditions. FAST.Farm (FFarm) results are plotted with activated (WAT=true) and deactivated (WAT=false) wake-added turbulence model. The rotor position of the turbines T1 and T4 is indicated by the grey patches.

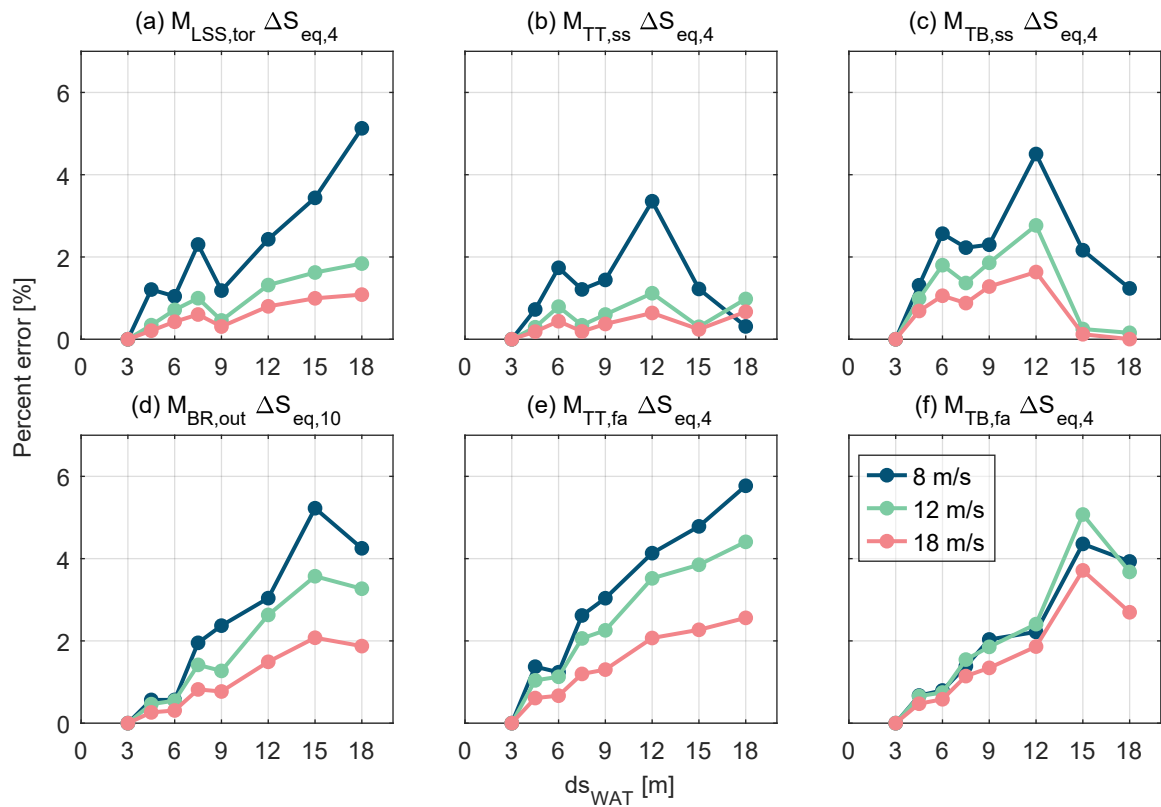


Figure 4.9: Percent error of the damage equivalent loads at different locations (torsional moment at the low-speed shaft (a), side-side bending moment at the tower-top (b) and at the tower-base (c), out-of-plane bending moment at the blade-root (d), fore-aft bending moment at the tower-top (e) and at the tower-base (f)) with respect to the finest increment (3 m) of the spatial discretisation.

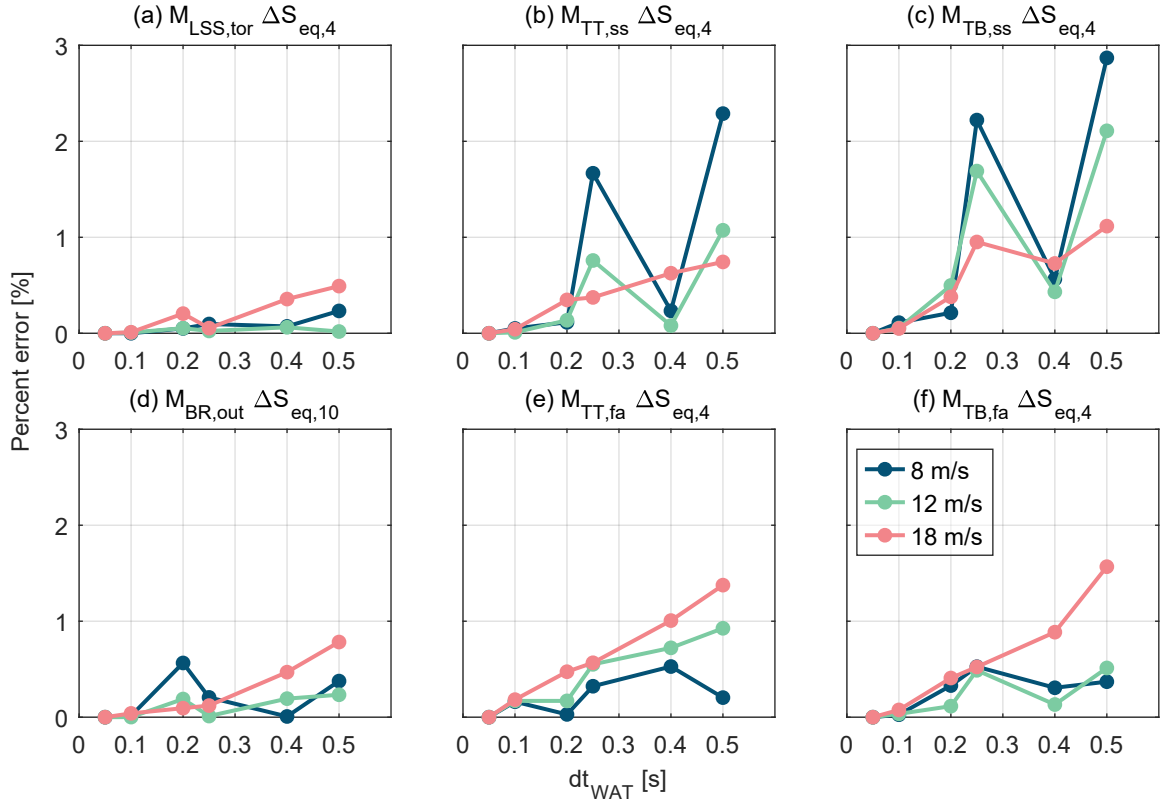


Figure 4.10: Percent error of the damage equivalent loads at different locations (torsional moment at the low-speed shaft (a), side-side bending moment at the tower-top (b) and at the tower-base (c), out-of-plane bending moment at the blade-root (d), fore-aft bending moment at the tower-top (e) and at the tower-base (f)) with respect to the finest increment (0.05 s) of the temporal discretisation.

errors below 2%. Hence, a recommended spatial increment of $ds_{WAT} = 4.5$ m is derived which is applied on all simulations in this thesis.

The results from the temporal discretisation study are plotted in Figure 4.10, while the spatial resolution is fixed to $ds_{WAT} = 3$ m. It is observed that the discretisation errors are below 3% for all considered load sensors. The sensitivity regarding the time step is highest for the bending moments in the side-side direction at the tower-base and tower-top. In contrast, the DEL of the torsional moment at the Low-Speed Shaft (LSS) is found to be insensitive to the time step. Based on these results, a time step of $dt_{WAT} = 0.2$ s is recommended to limit the discretisation errors below 2%.

Table 4.2: Publicly available key parameters of the Senvion 5M turbine model [133].

Parameter	Value
Hub height	≈ 92 m
Rotor diameter D	126 m
Rated power	5 MW
Rated rotor speed	12.1 rpm
Rated wind speed	13.0 m/s

4.2 Aeroelastic turbine model validation for free-stream conditions

Before validating the simulation model for wake conditions (see Section 4.3), one needs to verify if the model can accurately predict the turbine's response in free-stream conditions. The results in terms of the turbine's performance and the structural loads are presented in Section 4.2.4. The description of the measurement data from the alpha ventus wind farm is given in Section 4.2.1; the setup of the simulations is explained in Section 4.2.2; in Section 4.2.3, the environmental conditions and their implementation in the simulations are presented. Note that parts of this section are already published in [124].

4.2.1 Alpha ventus measurement data base

The wind farm alpha ventus is located 45 km north of the German island Borkum in the North Sea. It consists of twelve turbines with a rated power of 5 MW, which is shown in Fig. 4.11. The model validation for free-stream and wake conditions focuses on the turbines AV4 and AV5, which are Senvion 5M turbines and their key parameters are given in Table 4.2. They are mounted on a jacket substructure and are located approximately $6.7D$ apart. Within the initiative Research at alpha ventus [130], measurement data from both turbines have been acquired since 2011. These data are used in load validation studies for free-stream conditions by [131] and [132]. The measurement data used in the Sections 4.2 and 4.3 was acquired in the period from 01/2016-07/2018; this data is chosen because of good availability and initial quality. In front of turbine AV4, the FINO1 met mast is located at a distance of approximately $3.2D$ providing the environmental data.

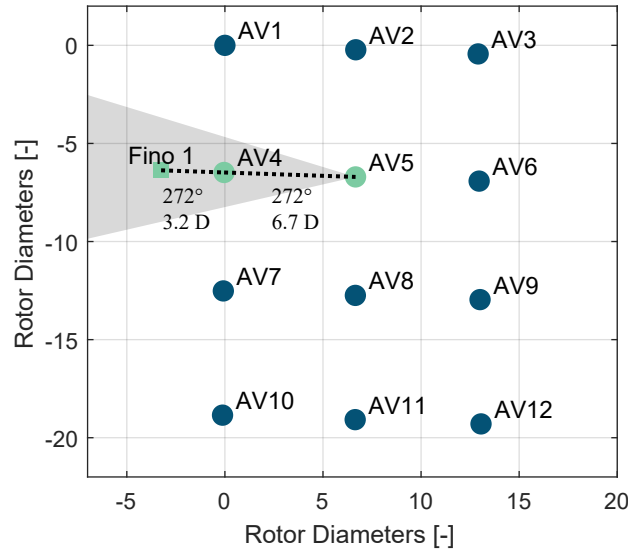


Figure 4.11: Wind farm layout of alpha ventus including FINO1 met mast. AV1-6: Type Senvion 5M. AV7-12: Type Adwen AD 5-116. North is pointing upward. Shaded triangle indicates the wind direction sector 257° - 287° seen from AV5.

Turbine measurements

The turbines are equipped with load sensors at various locations. Additionally, data from the turbine's Supervisory Control and Data Acquisition (SCADA) system are available. The time resolution of all sensors is 50 Hz. The following list explains the sensors used in this study and their calibration:

- SCADA: Generator power, generator speed and blade-pitch angle measurements are directly taken from the SCADA system.
- Nacelle yaw position: These data are also available through the SCADA system. Over longer time periods, a drift is observed in the data. This is corrected by using nacelle rotation events and correlating the known tower-base strain gauge positions with the nacelle-yaw signal. In this way, sensor offset values are derived to make the data consistent over time.
- Tower-base bending moments are calculated from strain gauges located above the transition piece. The strain gauges are placed at four locations separated by 90° around the tower cylinder. By combining the strain gauge measurements with the nacelle's yaw position, fore-aft (fa) and side-side (ss) bending moments are derived. Nacelle rotation events during turbine shutdown and calm wind conditions are used to determine calibration factors in terms of slope and offset.

- Blade-root bending moments in edgewise (ew) and flapwise (fw) direction are measured using four strain gauges placed near the blade root. They are calibrated with rotor idling events during calm winds as well as 10-min mean operational data. The measurements are made consistent over time by adjusting slope and offset. Strain gauge signals are combined to reduce cross-talk effects.

Environmental data

Meteorological and sea conditions are measured at the FINO1 met mast and are available as 10-min statistics. Wind speed is measured with cup anemometers at 7 locations starting at 41.5 m height above sea level (a.s.l.) and increasing in approx. 10-m increments to 100 m height a.s.l. Wind speed data are corrected for met mast shadow effects as explained by [134].

Wind direction is taken from the wind vane located at 91.5 m height, with the correction given by [135]. An additional offset of 3° is applied on wind direction, which is derived by correlating the wake deficit of turbine AV4 with the measured wind direction at FINO1.

Sea state is measured in terms of significant wave height and peak wave period with a directional waverider buoy (DWR-MkIII by Datawell).

Around alpha ventus, new wind farms have been commissioned over the years. This changes inflow conditions at alpha ventus compared to situations where no other wind farms were in close vicinity, as shown by [136]. In this work, these effects are partly taken into account because measured environmental conditions are directly transferred to simulations on a 10-min event basis rather than relying on long-term statistics.

4.2.2 Load case definition and simulation setup

The simulations are performed with the aeroelastic turbine simulation software OpenFAST that is introduced in Section 3.3.2. One-to-one simulations are conducted, where the measured environmental conditions of 10-min events are directly used as simulation inputs. Here, six random and uncorrelated turbulence realisations of the wind field are created. The turbulent wind fields are generated with Mann's model (see Section 3.1.1) which is further discussed in Section 4.2.3; this is in contrast to the results presented in [124], where the tool TurbSim (based on the Veer's method) is used for the wind field creation. The sea state is modelled with six random realisations of the Joint North Sea Wave Observation Project (JONSWAP) spectrum using the measured significant wave height and peak wave period.

The spatial resolution of the wind fields in the lateral and vertical directions is $dy = dz = 6$ m; the time step is $dt = 0.05$ s which equals to 20 Hz. At the beginning of each simulation, a transient period of 200 s is removed to not include initial oscillations caused by initial conditions which are not in equilibrium. The turbulent wind fields are 600 s long and set to be periodic

in order to achieve a total simulation length of 800 s.

Data filtering approach

The measurement data are clustered in 10-min events for which the statistics are calculated to allow appropriate filtering. In particular, the following filter criteria were applied:

- Only events are considered which have a data availability of more than 99 %.
- Wind direction is constrained from 240° to 252° . In this sector, both turbines AV4 and AV5 have nearly free-stream inflow conditions, thus their data can directly be compared. This is detected by correlating the measured loads of turbine AV5 with the wind direction. Effects from wind farm blockage are ignored.
- Both turbines are operated under normal conditions. For example, down-regulation, startup, or shutdown events are excluded.
- No yaw-action takes place during an event.

Calibration of aeroelastic turbine model

The aeroelastic simulation model is generated with structural and aerodynamic information provided by the manufacturer. Simulations are performed with the original turbine controller. In addition, a thorough calibration of the simulation model of both turbines AV4 and AV5 is performed to match the turbines measured load characteristics in the field as closely as possible. This involves the determination of structural damping of the first tower eigenmodes in the fa and ss direction by analysing turbine shutdown events.

Furthermore, imbalances in the rotating system are identified by looking at the frequency response during free-stream events with low TI conditions. The imbalances are introduced for each blade i as variation in blade mass $B_{M,i}$, variation in blade fw $B_{FK,i}$ and ew $B_{EK,i}$ stiffness, and blade-pitch offset $B_{PO,i}$. A summary of the introduced imbalances in the simulation model is listed in Table 4.3. Using these values, the turbines' frequency response from the field is reproduced at the desired sensor locations (tower-base, blade-root) with satisfactory accuracy. It is noted that these imbalances do not necessarily reflect the real existing imbalances; however, this is a practical approach to address the missing blade calibration measurements such as static blade deflection tests.

Table 4.3: Identified simulation model imbalances of the turbines AV4 and AV5 from alpha ventus. Values without units are factors that are multiplied with the given parameter.

	$B_{M,1}$	$B_{M,2}$	$B_{M,3}$	$B_{FK,1}$	$B_{FK,2}$	$B_{FK,3}$	$B_{EK,1}$	$B_{EK,2}$	$B_{EK,3}$	$B_{PO,1}$	$B_{PO,2}$	$B_{PO,3}$
AV4	1	0.996	1	1	1	0.95	1	1	0.95	0°	-0.5°	+0.5°
AV5	1	1	1	0.95	1	1	0.95	1	1	-0.5°	+0.5°	+0.5°

4.2.3 Transfer of environmental conditions to simulations

An important goal of a validation procedure is to obtain high quality simulation inputs which can represent the actual atmospheric conditions adequately. Here, the meteorological conditions measured at FINO1 are used to generate turbulent wind fields with Mann's method. Subsequently, the three independent parameters of the model are chosen according to the following relations:

- Γ : The value of the anisotropy parameter Γ is dependent on the AS and is set based on Table 3.1.
- L_M : The turbulence length scale is specified for each event individually using the approximation derived in [137]:

$$L_M \approx z \frac{TI}{\alpha_{shear}} \quad (4.2)$$

In this study, the TI measurement at $z = 91.5$ m height and the fitted power law shear coefficient α_{shear} from FINO1 are used as inputs.

- $\alpha\epsilon^{2/3}$: This parameter is defined for each event specifically to match the standard deviation of a 10-min time series of the wind speed at $z = 91.5$ m (\approx hub height) measured at FINO1. The data from the cup anemometer is used, assuming that the cup anemometer only measures turbulent fluctuations of the wind speed component u .

Vertical wind shear is described in terms of by the power law. The exponent α_{shear} is derived by fitting the power law on the wind speed measurements from all available heights of the FINO1 meteorological mast.

For this validation study, atmospheric stability is estimated by using the power law shear exponent α_{shear} and applying the limits given in Table 4.4. This simplified approach is motivated by [138] as the α_{shear} can be easily estimated from measurements. It is considered to be sufficient for this study because it can be used to differentiate the environmental conditions as accurate estimates of atmospheric stability are difficult. The limits for the three stability classes are set according to the derived values from [138].

Table 4.4: Classification of atmospheric stability with power law exponent α_{shear} for the model validation study. The values are derived in [138].

Atmospheric stability	Power law exponent α_{shear}
unstable	$\alpha_{shear} \leq 0.07$
neutral	$0.07 < \alpha_{shear} < 0.15$
stable	$0.15 \leq \alpha_{shear}$

4.2.4 Validation results

The results are presented in terms of statistics of measured quantities, which are plotted against the wind speed and wind direction. The data are clustered in wind speed bins of the size 0.5 m s^{-1} . For each bin, the mean value plus 15th-85th percentile range is shown. In total, 2980 simulations are conducted. Although an individual calibration of both turbines AV4 and AV5 is derived, the differences between the turbines are negligible; hence, only the results of the AV4 calibration is shown.

All results are normalised with reasonable user defined values due to data confidentiality. Measurements are labelled with "AV4" and "AV5", whereas simulations are named "OpenFAST".

Measured meteorological conditions

The meteorological conditions for the validation of the OpenFAST simulations are presented in terms of the TI and power law shear exponent α_{shear} in Figure 4.12. The mean value of the TI for all events is $\approx 6.5\%$ and the standard deviation is $\approx 1.6\%$; these values are nearly constant for all considered wind speeds. Few events (less than 7%) have a $TI > 9\%$. The mean value of the α_{shear} distribution is ≈ 0.087 . With increasing wind speed, the mean value α_{shear} increases. High values of α_{shear} (> 0.15) occur in less than 6% of the cases. Note that only the values from the events filtered for the load validation are plotted in Figure 4.12. Statistically converged results in terms of the meteorological conditions are shown in Figure 5.1.

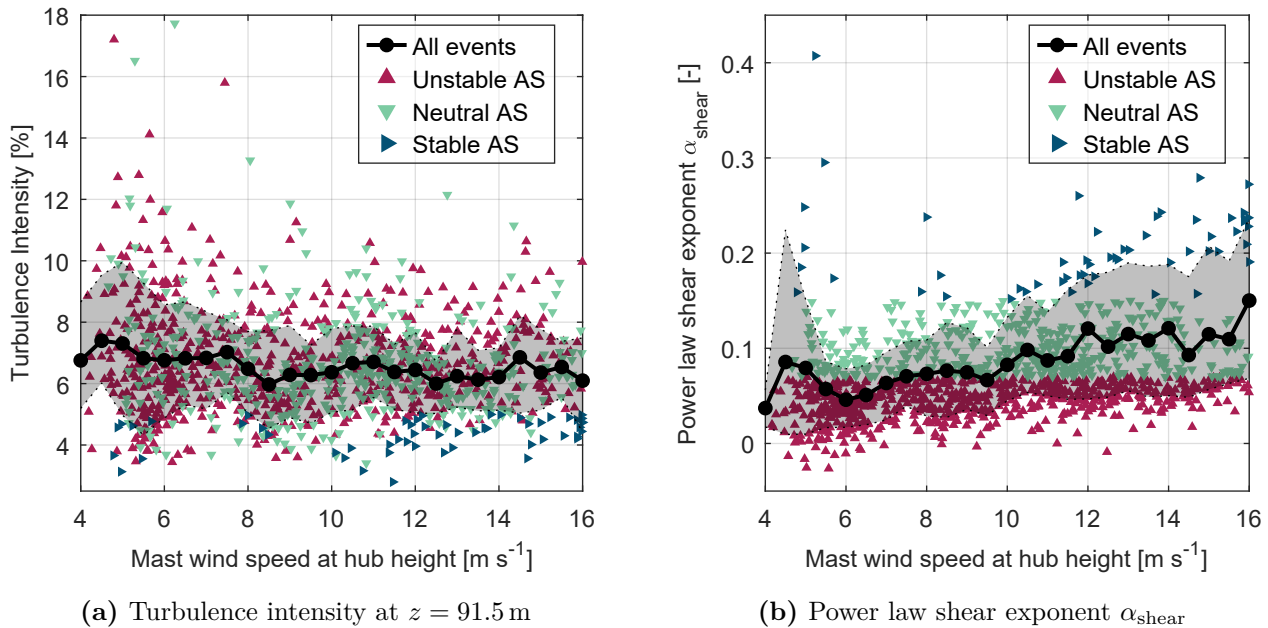


Figure 4.12: Measured meteorological conditions at FINO1 for the OpenFAST validation. Statistics are shown as mean values per wind bin. Shaded area indicates 15th and 85th percentiles. Scatter shows value for single 10-min events. Wind direction: 240°-252°; Measurement period: 01/2016-07/2018).

Turbine performance

The comparison of the mean values of the performance data (generator power, blade pitch angle, generator speed) is shown in Figure 4.13 (complementary plots are provided in the Appendix A.2). Good agreement with discrepancies of less than 5% between simulations and measurements is found for all shown sensors. Hence, it is demonstrated that the simulation model setup is appropriate and can reproduce the performance characteristics of the Senvion turbines at alpha ventus. In particular, the controller used in the simulations performs very similarly to the controller implemented in the turbines at alpha ventus. Slight discrepancies are observed which is likely caused by small adjustments of the controller; these are not reflected in the simulations due to the closed source code.

Structural loads

In Figure 4.14, the structural loads in terms of the mean value and the DEL are shown at the tower-base in the fa direction and at the blade-root in the fw direction. It can be seen that the mean values (Figures 4.14 (a),(b)) from the simulations are in good agreement (errors of less than 5%) with the measurements. The DEL computed for the fa bending moment at the tower-base (Figure 4.14 (c)) shows a close match with a difference of less than 5% for most of the wind speeds in below-rated conditions (6-11 m s⁻¹). At low wind speeds (4-6 m s⁻¹) and above-rated wind speeds, larger discrepancies (10-30%) are observed between the simulations

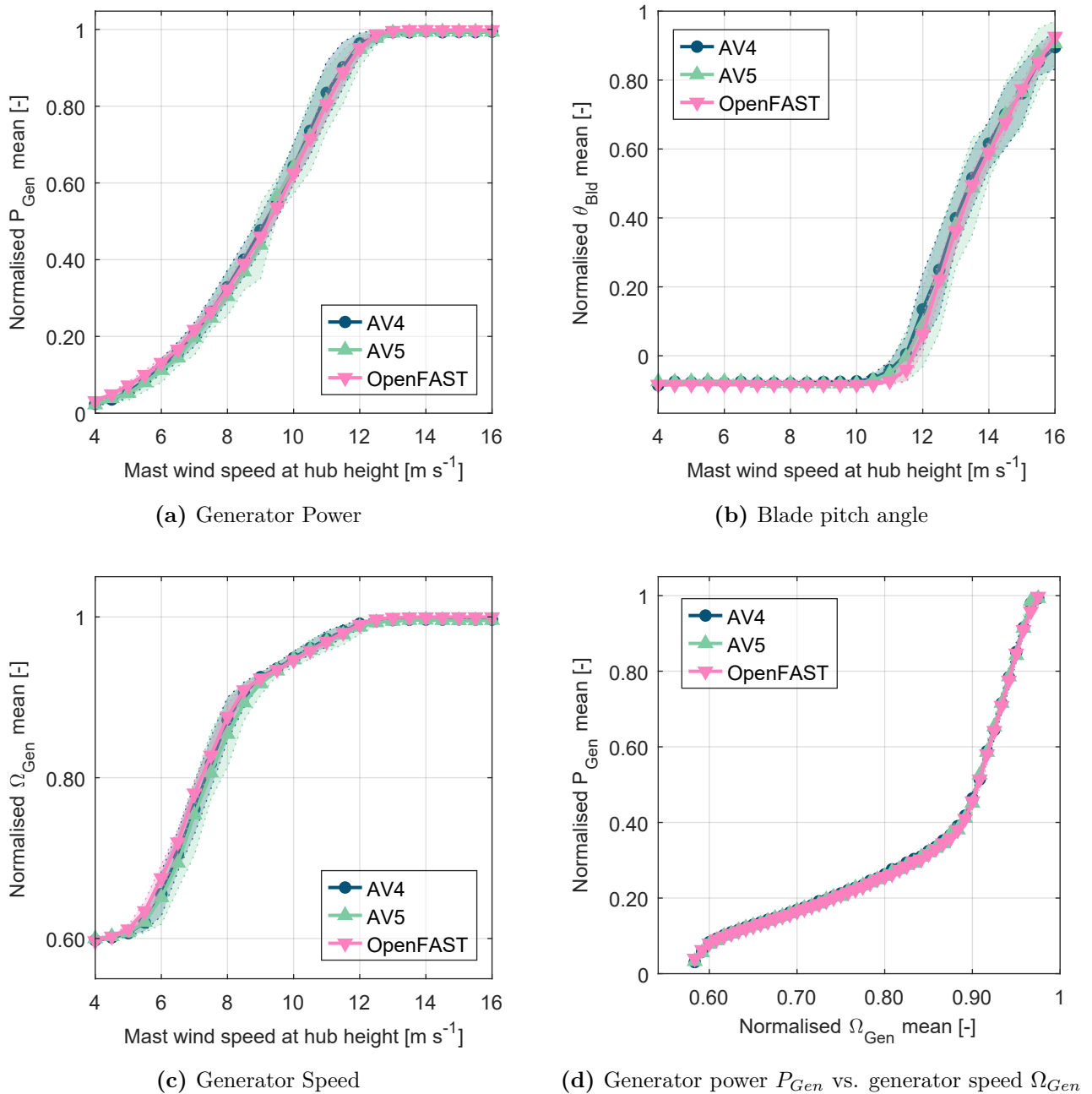


Figure 4.13: Comparison of free-stream (wind direction 240°-252°) turbine performance characteristics between measurements (AV4, AV5) and simulations (OpenFAST: results are shown with calibration based on AV4). Statistics are shown as mean values per wind bin. Shaded area indicates 15th and 85th percentiles.

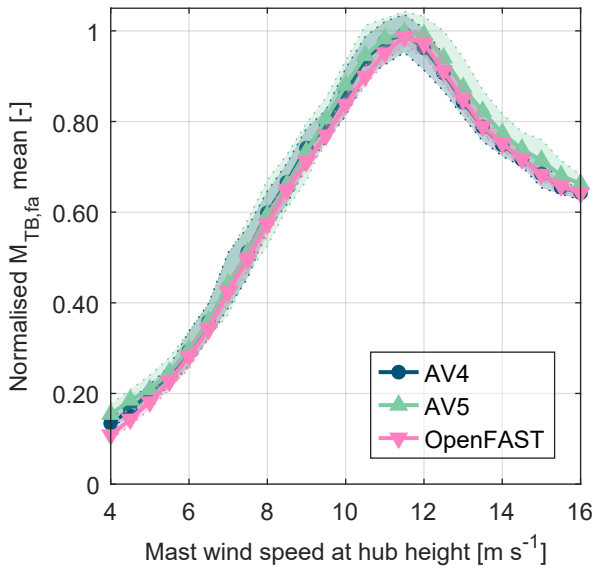
and the measurements. In addition, at above-rated wind speeds, the loads of turbine AV5 are up to $\approx 20\%$ higher compared to turbine AV4. This difference could be caused by an imbalance in the rotor system during blade-pitch actuation but could not be confirmed. The comparison of the DELs at the blade-root (Figure 4.14 (d)) reveals that the measurements of both turbines as well as the simulations match each other well with differences of less than 10%. The range indicated by the 15th and 85th percentiles agrees also well between simulations and measurements.

Overall, the simulations can predict the measured DELs in free-stream conditions with high accuracy. This indicates that the aeroelastic simulation model is set up properly and that the meteorological conditions are well represented by the wind fields. The exact representation of hydrodynamic excitation in terms of wave loads is considered of less importance because the substructure can be considered as hydrodynamically transparent and only sensors above the sea water level are taken into account in this study.

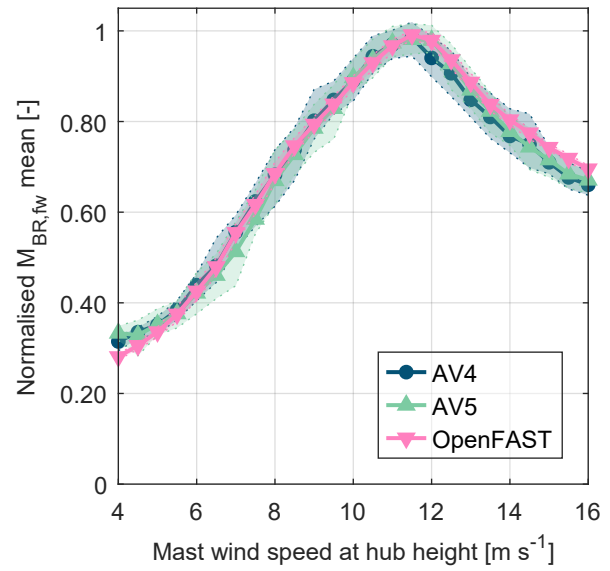
4.3 Aeroelastic turbine model validation for single wake situations

FAST.Farm is validated with LESs in the prediction of wake characteristics, turbine power and structural loads for a three turbine case in [139]. They show that FAST.Farm results are in good agreement with the reference LESs for most analysed quantities. However, in low ambient turbulence conditions, larger differences are observed which can be attributed to a missing wake-added turbulence feature in FAST.Farm in that study. [140] perform a validation of FAST.Farm against full-scale data of the turbine's SCADA system (generator power, rotor speed, blade pitch) of a five turbine configuration. Despite the problems with the used generic controller, FAST.Farm captures the trends of the measurements accurately. In the Scaled Wind Farm Technology (SWiFT) benchmark study by [6], FAST.Farm calculates the flow characteristics of a single wake in good agreement with the other considered simulation tools. Underperformance in capturing the wakes compared to the flow measurements are predominantly caused by inaccurate inflow modelling.

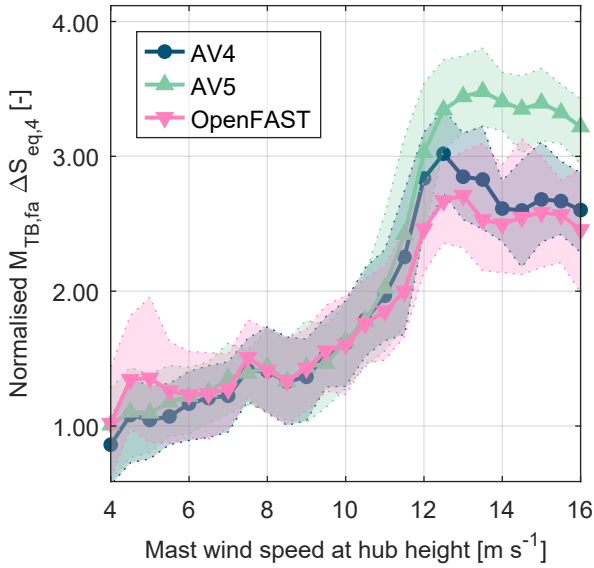
The validation of FAST.Farm with respect to the performance and structural loads of a turbine subjected to single wake conditions is presented in this Section. The measurement data from alpha ventus are used as reference; the database is described in Section 4.2.1. The approach of generating turbulent wind fields is explained in 4.2.3. Note that parts of this section are already published in [124].



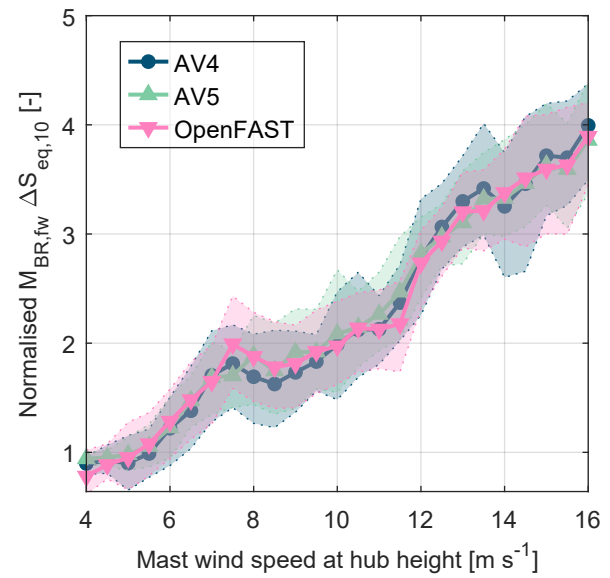
(a) Tower-base fore-aft bending moment



(b) Blade-root flapwise bending moment



(c) Tower-base fore-aft bending moment



(d) Blade-root flapwise bending moment

Figure 4.14: Comparison of free-stream (wind direction 240° - 252°) turbine load characteristics between measurements (AV4, AV5) and simulations (OpenFAST: results are shown with calibration based on AV4). Statistics are shown as mean values per wind bin. Shaded area indicates 15th and 85th percentiles.

4.3.1 Load case definition and simulation setup

The simulations are set up in the tool FAST.Farm. One-to-one simulations are performed, where the measured environmental conditions of 10-min events are directly used as simulation inputs. Six random and uncorrelated turbulence realisations of the wind field are created. The turbulent wind fields are generated with Mann's model (see Section 3.1.1). Similarly, the sea state is modelled with six random realisations of the JONSWAP spectrum using the measured significant wave height and peak wave period. The wake analysis focuses on two wind speed bins in below rated conditions: 1) wind speed $6.5\text{-}7.5\text{ m s}^{-1}$ in the following with "I", 2) wind speed $9.0\text{-}10.0\text{ m s}^{-1}$ labelled with "II". These bins are chosen because they imply high rotor thrust values and hence strong wake effects.

The numerical setup of FAST.Farm follows the definitions given in Section 3.3.5 which involve the spatial and temporal discretisation of the domains in FAST.Farm. At the beginning of each simulation, a transient period of 400 s is removed to allow the wakes to develop and to damp initial oscillations. The Mann wind fields for the ambient turbulence have a length of 600 s and are set to be periodic in order to achieve a total simulation time of 1000 s. The Mann wind fields for the wake-added turbulence cover 3 D in the longitudinal direction. The turbulence box is periodic, thus the wake-added turbulence domain can be extended to more than 3 D.

The filtering of the measurement data follows the definitions provided in 4.2.2. However, the following modifications are included:

- Wind direction is constrained from 257° to 287° to ensure that only wake effects of turbine AV4 affect AV5. At the boundaries of this wind direction sector, nearly free-stream conditions exist for both turbines; effects from wind farm blockage are ignored.
- No yaw-action takes place during an event. Additionally, both turbines operate at similar yaw angles, allowing only events where the difference in the mean yaw position is less than 6° .

The aeroelastic turbine model calibration of both turbines is described in Section 4.2.2.

4.3.2 Validation results

The results are presented in terms of statistics of measured quantities, which are plotted against the wind direction. The data are clustered in wind direction bins of the size 2.5° . For each bin, the mean value plus 15th-85th percentile range is shown. In total, 1014 FAST.Farm simulations are run for wind speed bin I and 1072 for wind speed bin II.

To protect proprietary data of the manufacturer, all results are normalised by either user defined values or by values of the free-stream turbine, which is indicated in the figure legend.

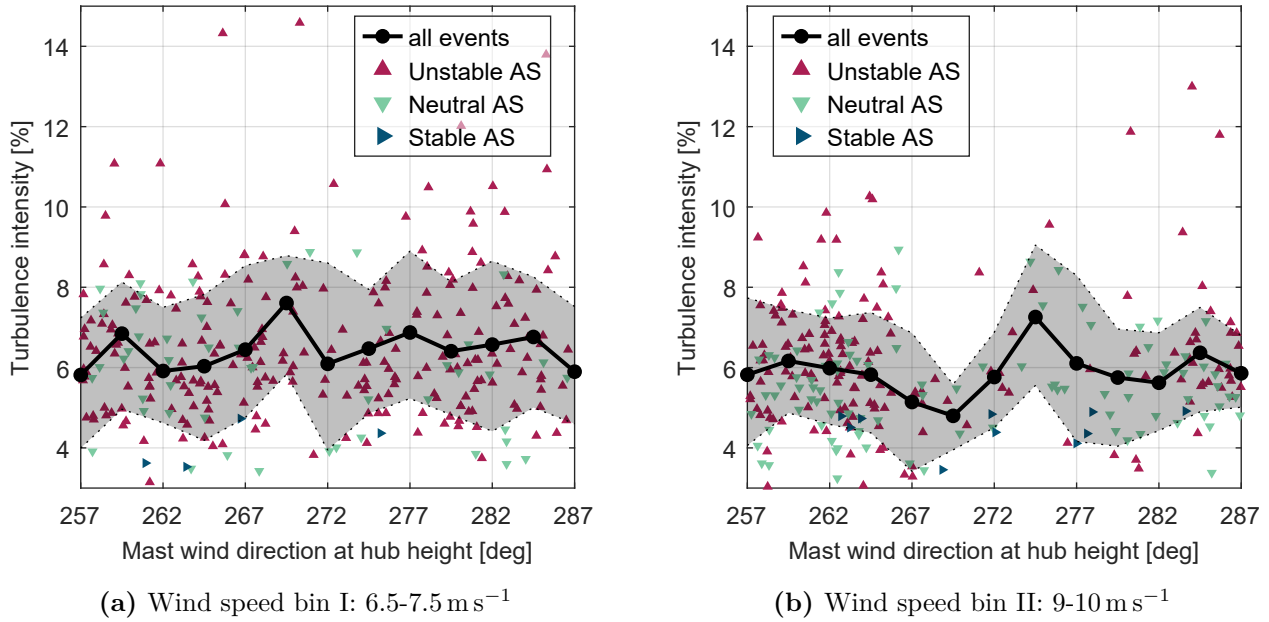


Figure 4.15: Turbulence intensity measured at 91.5 m height at FINO1. Statistics are shown as mean values per wind bin. Shaded area indicates 15th and 85th percentiles. Scatter shows TI of single 10-min events. AS = atmospheric stability.

Measurements are labelled with "AV4" and "AV5", whereas simulations are named "FFarm4" and "FFarm5" making reference to the turbine numbers 4 and 5.

Measured meteorological conditions

For the analysed wind speed bins, the TI distribution over wind direction is shown in Figure 4.15. The mean TI for wind speed bin I is $\approx 6.4\%$ and $\approx 5.9\%$ for wind speed bin II. Highest TI values are found in unstable atmospheric conditions whereas lowest TI values occur in stable conditions. Especially in wind speed bin II, more events are found from wind directions from the southwest, which is the predominant wind direction. A more uniform distribution of the wind direction is found for wind speed bin I. Figure 4.16 shows the distribution of the power law shear exponent α_{shear} over wind direction. It can be seen that wind speed bin II contains higher α_{shear} values on average compared to wind speed bin I.

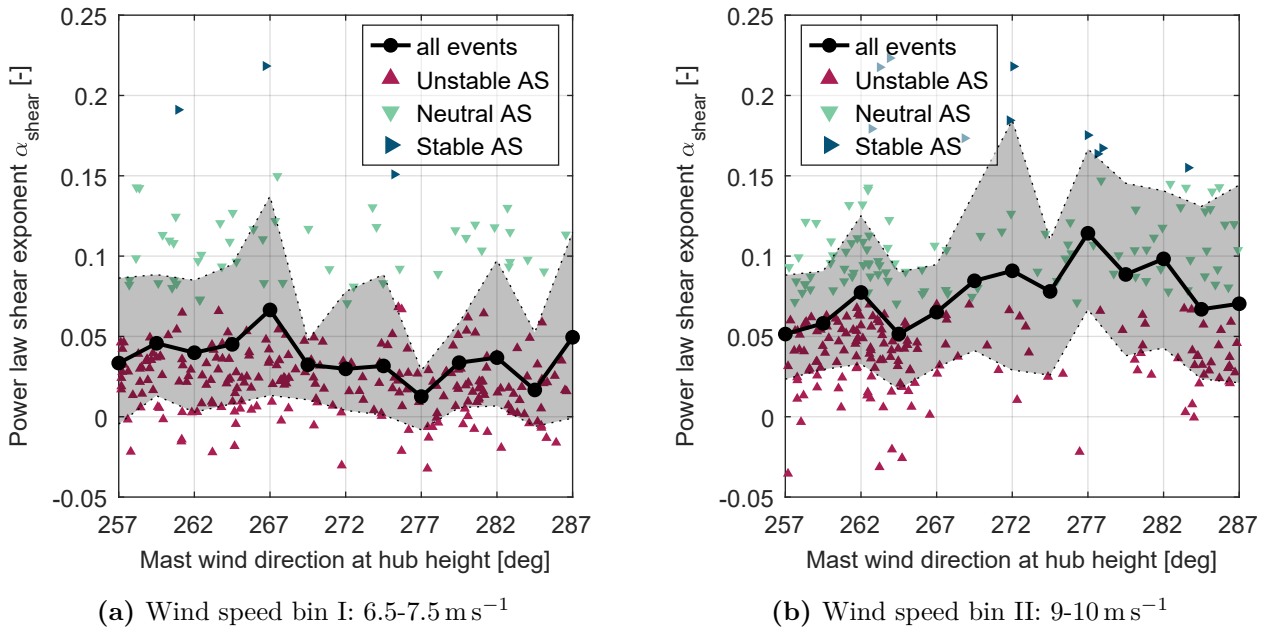


Figure 4.16: Power law shear exponent α_{shear} derived from FINO1 measurements. Statistics are shown as mean values per wind bin. Shaded area indicates 15th and 85th percentiles. Scatter shows α_{shear} of single 10-min events. AS = atmospheric stability.

Turbine performance: statistics

Results of the mean generator power prediction are presented in Figure 4.17. They show a maximum power loss of 48% in full wake conditions for wind speed bin I. At nearly 43%, power loss is slightly less for wind speed bin II due to a decreased rotor thrust coefficient compared to wind speed bin I. Wake effects are visible as power decrease over a wind direction sector of 25°. FAST.Farm is able to predict the width and depth of the power deficit accurately compared to the measurements for wind speed bin I (Figures 4.17 (a) and (b)). For wind speed bin II, deviations of 5-10% are observed in Fig. 4.17 (c). Relative comparisons are shown in Figures 4.17 (b) and (d), where results of the waked turbine are divided by the free-stream results of the simulations and measurements respectively. It can be seen that relative plotting produces a better match of the FAST.Farm results with the measurements. Similar levels in the scatter of events indicated by the error range are found for simulations and measurements.

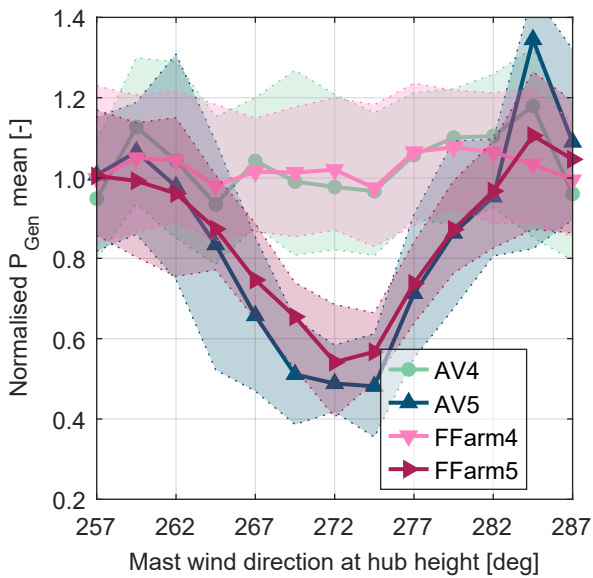
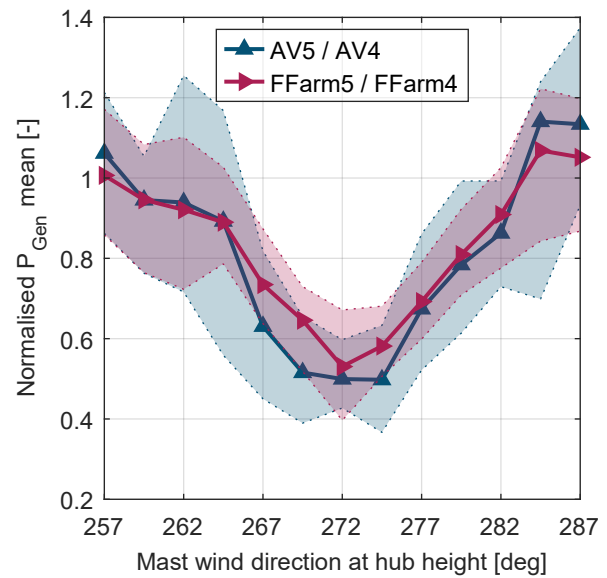
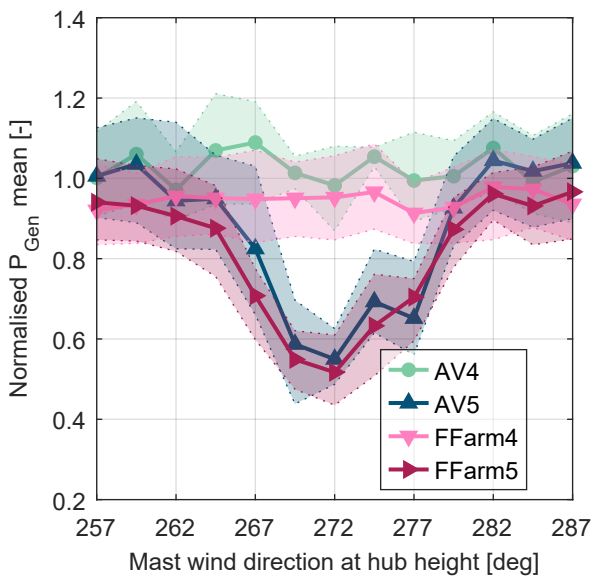
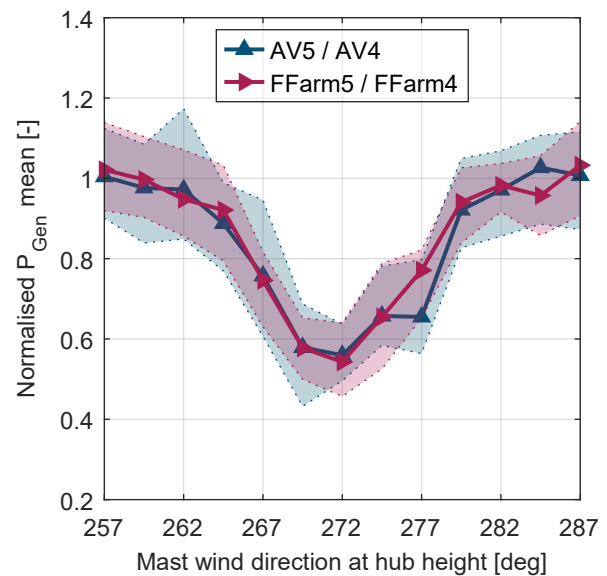
(a) Wind speed bin I ($6.5\text{-}7.5\text{ m s}^{-1}$)(b) Wind speed bin I ($6.5\text{-}7.5\text{ m s}^{-1}$) normalised by free-stream values(c) Wind speed bin II ($9\text{-}10\text{ m s}^{-1}$)(d) Wind speed bin II ($9\text{-}10\text{ m s}^{-1}$) normalised by free-stream values

Figure 4.17: Comparison of generator power in wake conditions between measurements (AV4, AV5) and simulations (FFarm4, FFarm5). Statistics are shown as mean values per wind direction bin. Shaded area indicates 15th and 85th percentiles.

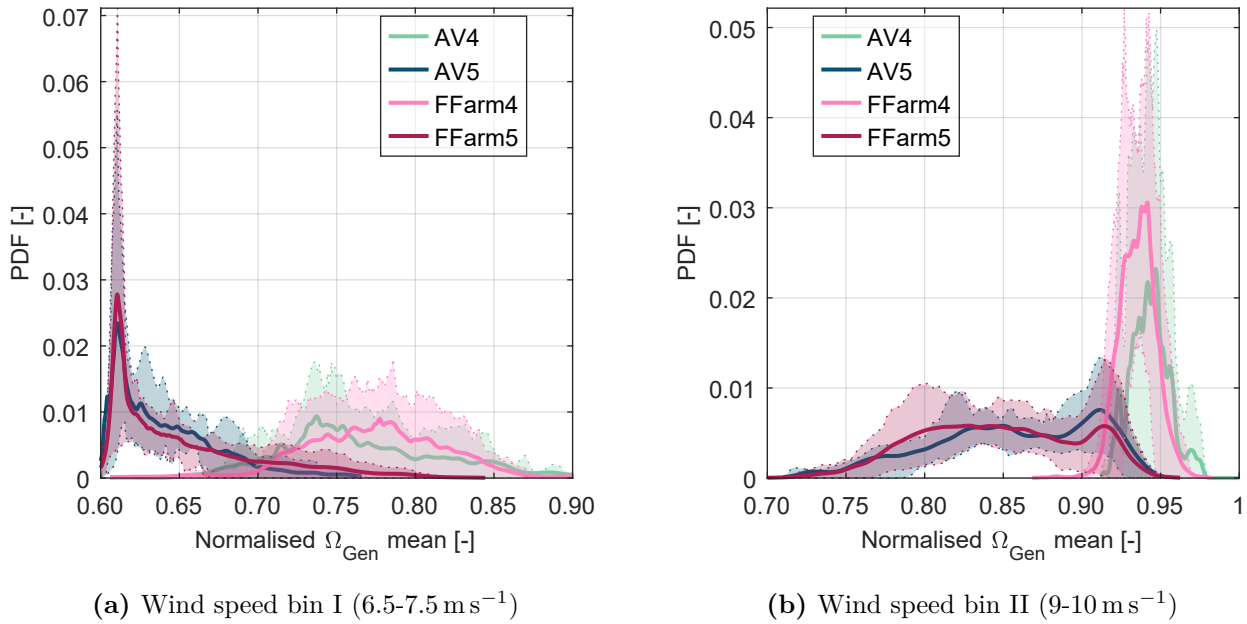


Figure 4.18: Probability density function (PDF) of generator speed for measurements (AV4, AV5) and simulations (FFarm4, FFarm5) in the wind direction sector 270.75°-273.25°. Thick lines show the mean of the PDFs of all considered events. Shaded area indicates 15th and 85th percentiles.

Turbine performance: detailed results

A more detailed analysis of the turbine performance is shown in Figure 4.18 by plotting the Probability Density Function (PDF) of the generator speed. The PDF is calculated for each 10-min event in the wind direction sector corresponding to full-wake conditions. Afterwards, mean values with error range expressed as 15th and 85th percentiles across the PDFs of all events are derived. In both wind speed bins, a reduction of generator speed is found for the waked turbine, caused by the wind speed deficit from the upstream turbine. In wind speed bin I, the downstream turbine operates near the cut-in wind speed, which is indicated by the peak around the normalised generator speed of 0.6 in Figure 4.18 (a). From Fig. 4.18 (b), it can be seen that the waked turbine covers a wider range of generator speeds compared to the free-stream turbine. This can be related to a varied operational point due to the velocity deficit. Additionally, it can be partly attributed to the increased turbulence in the wake originating from wake-added turbulence as well as wake meandering. In both wind speed bins, FAST.Farm predicts the distributions from the measurements with high accuracy.

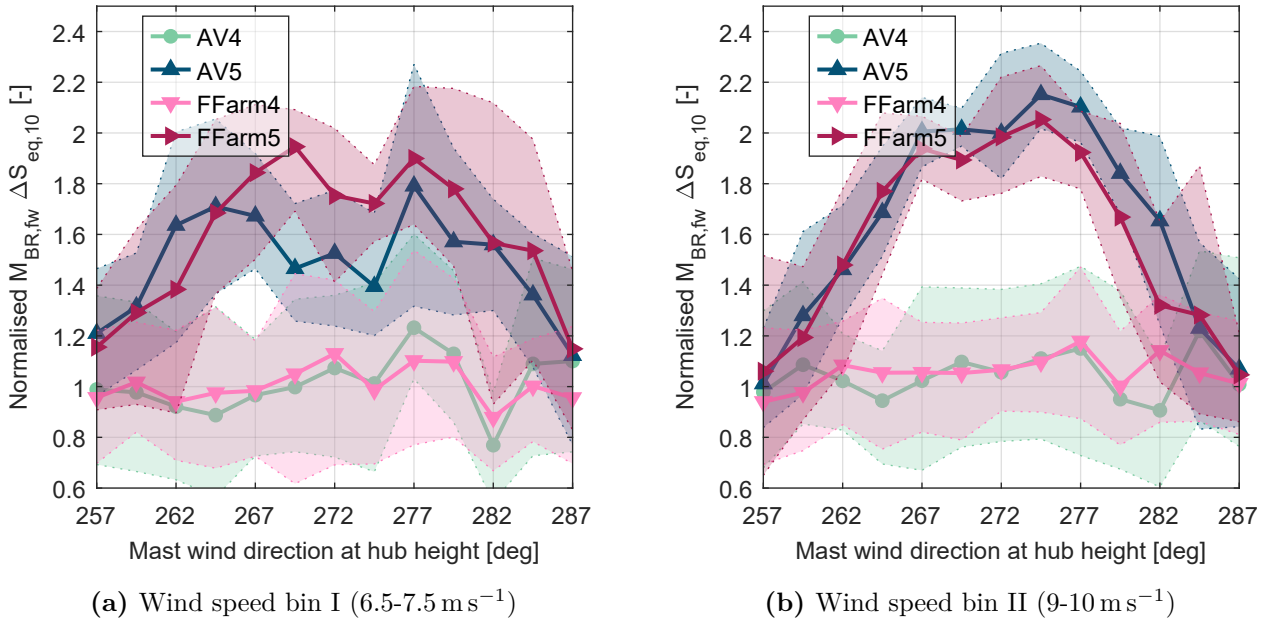


Figure 4.19: Comparison of the blade-root bending moment in the flapwise direction in waked conditions between measurements (AV4, AV5) and simulations (FFarm4, FFarm5). Statistics are shown as mean values per wind direction bin. Shaded area indicates 15th and 85th percentiles.

Structural loads: statistics

Figure 4.19 shows results of the fatigue loads expressed as DEL of the blade-root bending moment in the fw direction. By comparing the two wind speed bins, different load distributions over wind direction for the waked turbine are observed. For wind speed bin I (Figure 4.19 (a)), a dip in the DEL for the downstream turbine occurs around full wake conditions at 272°; this is not visible for wind speed bin II (Figure 4.19 (b)). Influencing factors on the load distribution for the waked turbine are the wind direction and connected mean wake position, magnitude of wake meandering, ambient wind conditions, and operational point of the turbine. Varying combinations of these effects lead to different load distributions. With the chosen one-to-one simulation approach, the aim is to reduce the uncertainty arising from the different combinations. Hence, it is seen for both wind speed bins that FAST.Farm agrees well with the measurements and predicts the increase in loads and trends over wind direction with good accuracy. Overall, a load increase of approximately factor 1.8 (wind speed bin I) and factor 2.0 (wind speed bin II) are identified for the waked turbine.

Figure 4.20 displays the DELs of the tower-base bending moment in the fa direction. In contrary to the fatigue loads at the blade-root, a higher increase in loads for the waked turbine is observed for wind speed bin I compared to wind speed bin II. In particular, DELs are increased by factor 2.4 (wind speed bin I) and factor 2.0 (wind speed bin II) for the waked turbine compared to the DELs of the free-stream turbine. FAST.Farm produces results in

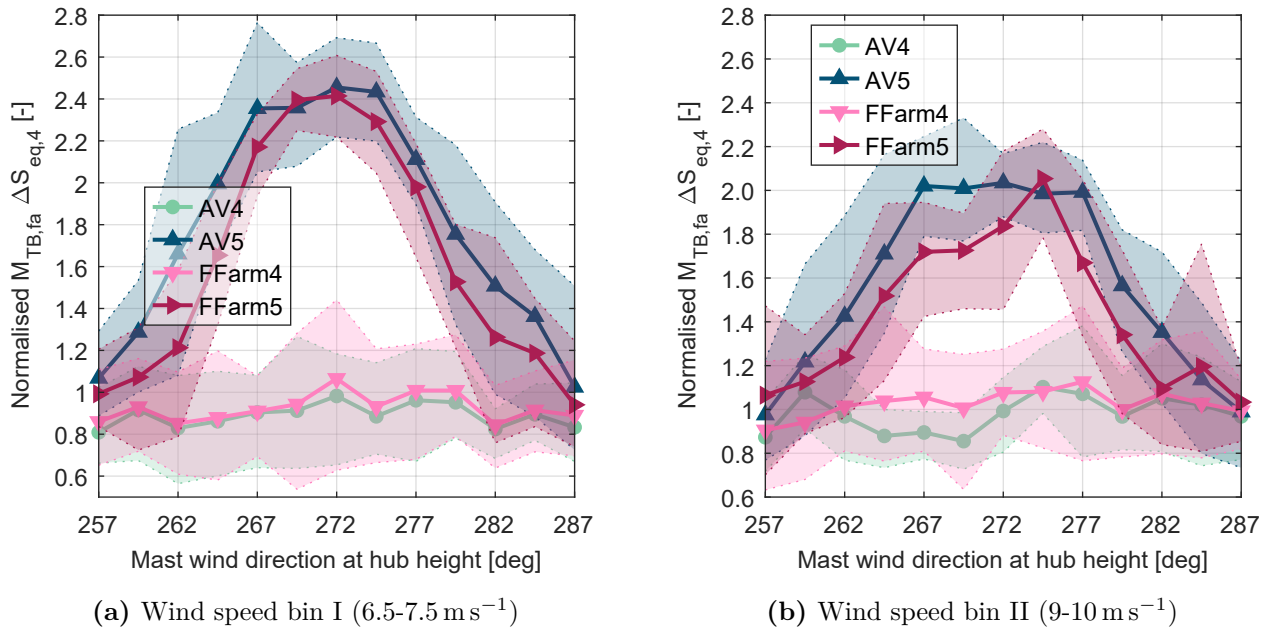


Figure 4.20: Comparison of the tower-base bending moment in the fore-aft direction in waked conditions between measurements (AV4, AV5) and simulations (FFarm4, FFarm5). Statistics are shown as mean values per wind direction bin. Shaded area indicates 15th and 85th percentiles.

good agreement with the measurements in terms of magnitude and wind direction dependency. For most of the considered wind directions, the discrepancy in the mean value per bin between FAST.Farm and the measurements is less than 10%; in some wind directions, the difference is increased to 25%. The uncertainty range per bin indicated by the percentile range is predicted by FAST.Farm with good agreement to the measurements.

Structural loads: frequency response

Figure 4.21 depicts the power spectrum of the response of the structure at the tower base and blade root. Only events during nearly full wake conditions (wind direction 270.75°-273.25°) in wind speed bin I are considered. For each 10-min event, the Power Spectral Density (PSD) is calculated. Then mean values for each frequency with corresponding uncertainty range expressed as 15th and 85th percentiles are determined. They are shown for the blade-root bending moment in the fw direction (Figure 4.21 (a)) and the tower-base bending moment in the fa direction (Figure 4.21 (b)).

In case of the blade (Fig. 4.21 (a)), an increase of energy at the blade passing frequency 1P in the rotating frame is observed for the waked turbine compared to the free-stream turbine. It comes along with a reduction of the blade passing frequency (free-stream: 1P \approx 0.15 Hz, wake: 1P \approx 0.13 Hz) due to the reduced wind speed inside the wake and consequently a reduction of rotor speed. The magnitude of the first blade passing frequency of turbine AV5 is predicted by

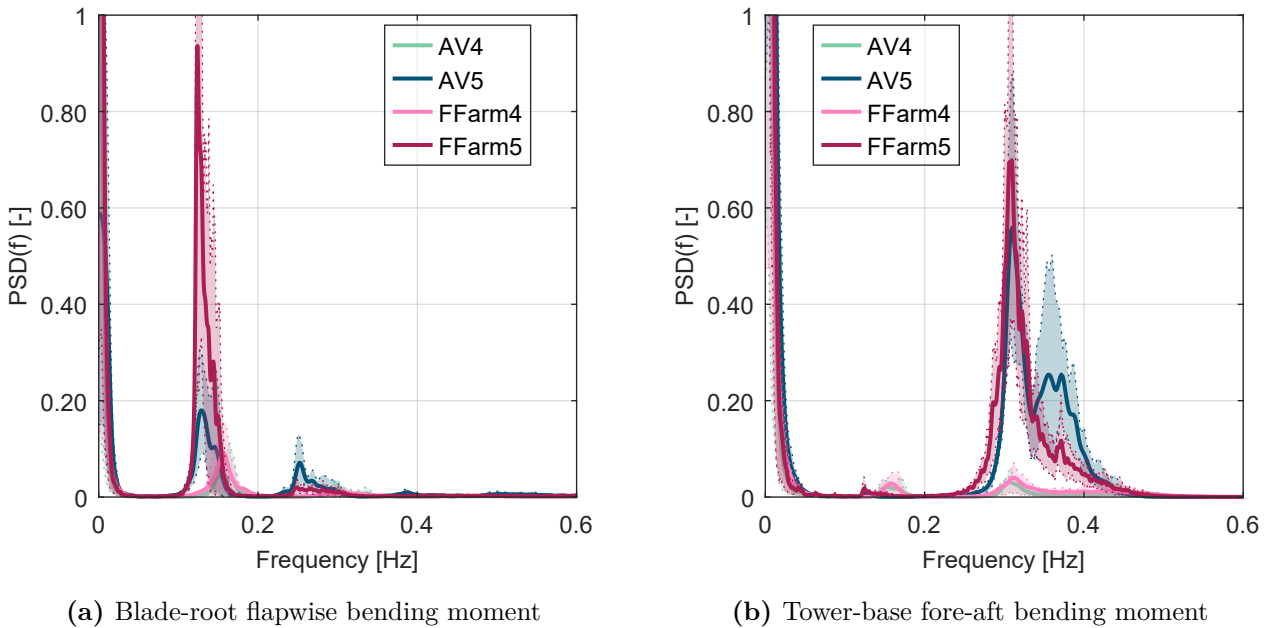


Figure 4.21: Comparison of power spectral densities (PSD) between measurements (AV4, AV5) and simulations (FFarm4, FFarm5) for wind speed bin I (wind direction 270.75° - 273.25°). Thick lines show the mean of the PSDs for all considered events. Shaded area indicates 15th and 85th percentiles.

FAST.Farm to be a factor of 4 higher compared to the measurements. In contrast, the excitation frequency $2P$ indicated by the peaks between 0.2-0.3 Hz is higher in the measurements. A possible explanation is the modelling of the wake, which has a Gaussian shape in FAST.Farm. In reality, the wake is more likely to be distorted, leading to smoother transitions to undisturbed winds. Similar observations are made by [139], who compare FAST.Farm with LES. However, more detailed analyses are required, e.g. using LES, to derive a conclusive explanation for the observed characteristics in the frequency response.

The signal at the tower base (Figure 4.21 (b)) reveals a strong excitation of the first global mode at around 0.3 Hz for the waked turbine. This is observed in both the measurements and FAST.Farm, whose prediction of the peak is 20 % higher compared to the measurements. Higher energy content is also seen in the frequency range 0.35-0.4 Hz for the waked turbine compared to the free-stream turbine. Although FAST.Farm captures an increase in the energy content compared to the free-stream turbine, it underestimates the energy level detected in the measurements by 50 % in this frequency range.

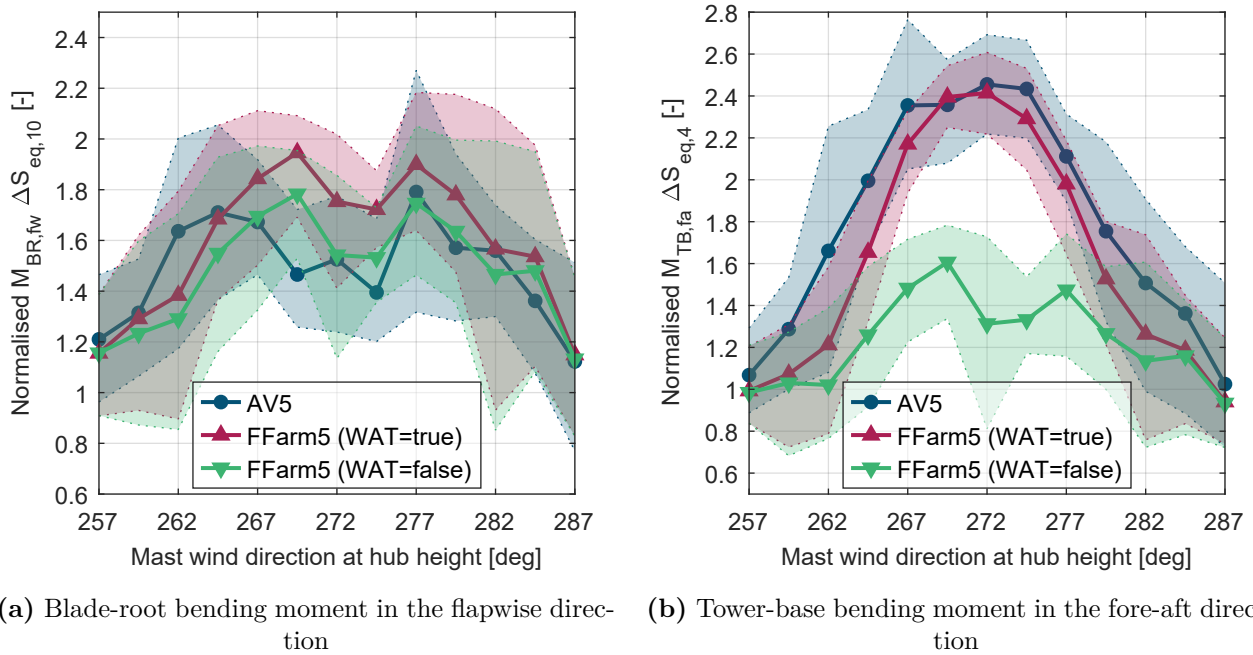


Figure 4.22: Comparison of FAST.Farm simulations with activated (WAT=true) and deactivated (WAT=false) wake-added turbulence with respect to the measurements (AV5) for wind speeds $6.5\text{--}7.5\text{ m s}^{-1}$. Statistics are shown as mean values per wind direction bin. Shaded area indicates 15th and 85th percentiles.

Wake-added turbulence model

The functionality of the wake-added turbulence model in FAST.Farm introduced in Section 3.3.4 and calibrated plus validated against LESs in Section 4.1 is investigated by using the measurement data. The results in terms of load statistics from the simulations with activated and deactivated wake-added turbulence model are compared against the measurement data in Figure 4.22. It is found that the effects of the wake-added turbulence model are small (up to 13% difference between activated and deactivated wake-added turbulence model) for the fatigue loads at the blade-root (Figure 4.22 (a)). Hence, the increase of the loads for the waked turbine can be mostly attributed to the effects from wake meandering. In contrast, a significant influence of the wake-added turbulence on the loads at the tower-base is observed (Figure 4.22 (b)). Without the inclusion of wake-added turbulence in the FAST.Farm simulations, the DELs of the bending moment in the fore-aft direction are underestimated by up to 87% in full-wake conditions compared to the measurement data. With the activated wake-added turbulence module in FAST.Farm, the difference to the measurements reduces to 2% in full-wake conditions, thus the agreement with the measurement data is significantly improved.

The effects of including the wake-added turbulence in the FAST.Farm simulations are analysed in more detail by plotting the frequency response of the structure at the blade-root and at the tower-base for full-wake conditions (Figure 4.23). Similarly to the statistical results, it

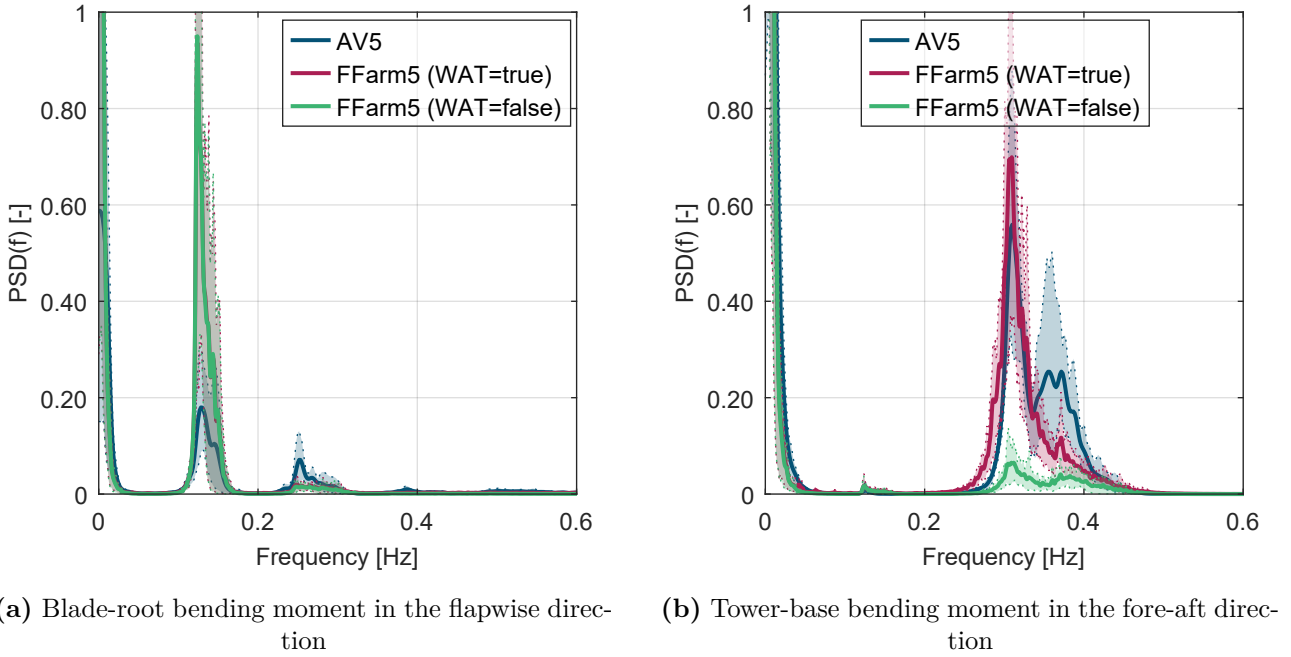


Figure 4.23: Comparison of power spectral densities (PSD) between measurements (AV5) and FAST.Farm simulations with activated (WAT=true) and deactivated (WAT=false) wake-added turbulence for wind speeds $6.5\text{--}7.5\text{ m s}^{-1}$ (wind direction $270.75^\circ\text{--}273.25^\circ$). Thick lines show the mean of the PSDs for all considered events. Shaded area indicates 15th and 85th percentiles.

is seen that the frequency response at the blade-root is changed little when the wake-added turbulence module is activated. On the contrary, the frequency response at the tower-base in terms of the bending moment in the fore-aft direction shows a considerable excitation of the first global mode around 0.3 Hz when the wake-added turbulence model is active, which is also seen in the measurements. Without the implementation of the wake-added turbulence module, this excitation cannot be reproduced.

4.3.3 Discussion

The present investigation concentrates on two wind speed bins in below rated conditions. This choice is motivated by the high rotor thrust conditions and hence strong wake effects. Another reason is that the behaviour of both turbines AV4 and AV5 is comparable in the measurements, whereas in above rated conditions, differences occur even under free-stream inflow for both turbines (see Figure 4.14 (c)). For the analysis of structural loads, it is focused on sensors and directions that are mainly affected by the change of the turbulence characteristics in the wake, i.e. tower-base fore-aft (fa) bending moment and blade-root flapwise (fw) bending moment.

A crucial part of this load validation is the generation of adequate wind fields representing the environmental conditions at alpha ventus. Especially, coherence and turbulence scales have an influence on wake meandering magnitude, which in turn affects the loads of the downstream

turbine (see also [126] and [141]). Unstable and neutral atmospheric conditions imply larger turbulent length scales and larger coherent turbulent structures than stable conditions. This leads to higher wake meandering magnitudes and higher loads for the downstream turbine. For the loads at the blade-root, adequate capturing of wake meandering is most important, whereas for the loads at the tower-base, both wake meandering and wake-added turbulence must be modelled. It is observed that in the simulations, a direct relationship between ambient TI conditions and wake loads exists. Consequently, higher ambient TI values lead to higher loads at the downstream turbine. In the measurements, this relationship holds true but it is also found that low ambient TI conditions can lead to high wake loads. This shows that there is some uncertainty in modelling the environmental conditions and wake features that should be investigated in future.

In offshore full-scale load validation, there are many potential sources of uncertainty. Starting with the modelling of environmental conditions, it is aimed to minimise those uncertainties by making use of findings from previous research, which is available for the site. However, there are limits in the methods used. In the considered period of measurements and wind direction sector, alpha ventus operates in the wake of the wind farm "Trianel Borkum I", which is located ≈ 6.5 km east. The flow structures evolving from this farm-wake are likely to be different from ideal free-stream conditions, for which the wind field generation method is originally derived. Overall, to reduce the input uncertainties, a one-to-one simulation approach is followed where the measured environmental conditions are utilised directly as simulation inputs.

4.3.4 Conclusions

The simulation tool FAST.Farm is validated for the prediction of power output and structural loads in single wake conditions with respect to measurement data from the offshore wind farm alpha ventus. In addition, the wake-added turbulence model implemented in FAST.Farm within this work (see Section 3.3.4) is validated. It is essential to calculate the small-scale turbulence in the wake; this is considered of importance especially for low ambient turbulence intensity conditions and for tower-base loading. The results show that FAST.Farm predicts the mean power deficit with sufficient accuracy compared to the measurements. Additionally, the PDF of the simulated generator speed agrees well with the measurements for the free-stream and downstream turbine. Fatigue loads are analysed in terms of DELs of the bending moments at the blade root in the fw direction and at the tower base in the fa direction. Distributions over wind direction show a good match between simulations and measurements with deviations of less than 10% for most of the investigated wind directions.

More detailed insights in the aforementioned structural loads are made visible by the power spectra. They show that FAST.Farm predicts trends in the structural response with good agreement to the measurements in the frequency domain. In particular, excitation at the tower

base of the waked turbine is reproduced well with FAST.Farm, which can be attributed to the wake-added turbulence feature in FAST.Farm. However, by looking at the PSD at the blade-root, one can see that not all phenomena are captured sufficiently by FAST.Farm, leaving room for further improvements such as the modelling of the wake-shape.

It has been demonstrated that the proposed one-to-one simulation approach works well for the validation in offshore single wake conditions. It is concluded that calibration of the aeroelastic model with respect to imbalances as well as proper transfer of environmental conditions to the simulations is important. Here, a differentiation of atmospheric stability is beneficial to refine simulation inputs for the wind field generation. However, stable atmospheric conditions remain challenging to model to obtain the correct loads of a waked turbine.

4.4 Low-fidelity model calibration for wind farm optimisation

The low-fidelity wind farm flow calculation tool FLORIS (see Section 3.2.1) is prepared in order to be used for the development of optimal wind farm operation strategies in Chapter 6. The parameters of the applied Gaussian velocity deficit and wake deflection models depend on the environmental conditions and farm configuration and must be calibrated accordingly as demonstrated in [142]. In the context of this thesis, the parameters of FLORIS are calibrated with respect to the reference simulations from FAST.Farm.

4.4.1 Load case definition and simulation setup

The velocity deficit model and wake deflection model are calibrated independently with slightly differing setups. The wind farm setup for the calibration of the velocity deficit model is composed of three turbines (see Figure 4.24) whose lateral and longitudinal distances are varied according to Table 4.5. The calibration of the wake deflection model is based on one turbine that operates under different yaw misalignment angles. The turbine model is the NREL 5 MW machine that is described in Section 5.1.

The environmental conditions are the same for the calibration of both velocity deficit and wake deflection model calibration. The wind speed and AS are defined according to Table 4.5; the TI and vertical wind shear depend on the AS and follow the measured conditions from FINO1 which are provided in Section 5.2.2.

The reference FAST.Farm simulations are set up with the default parameters and discretisation settings given in Section 3.3.5. The parameters of the FLORIS model to be calibrated are presented for the velocity deficit and wake deflection model separately in the following section.

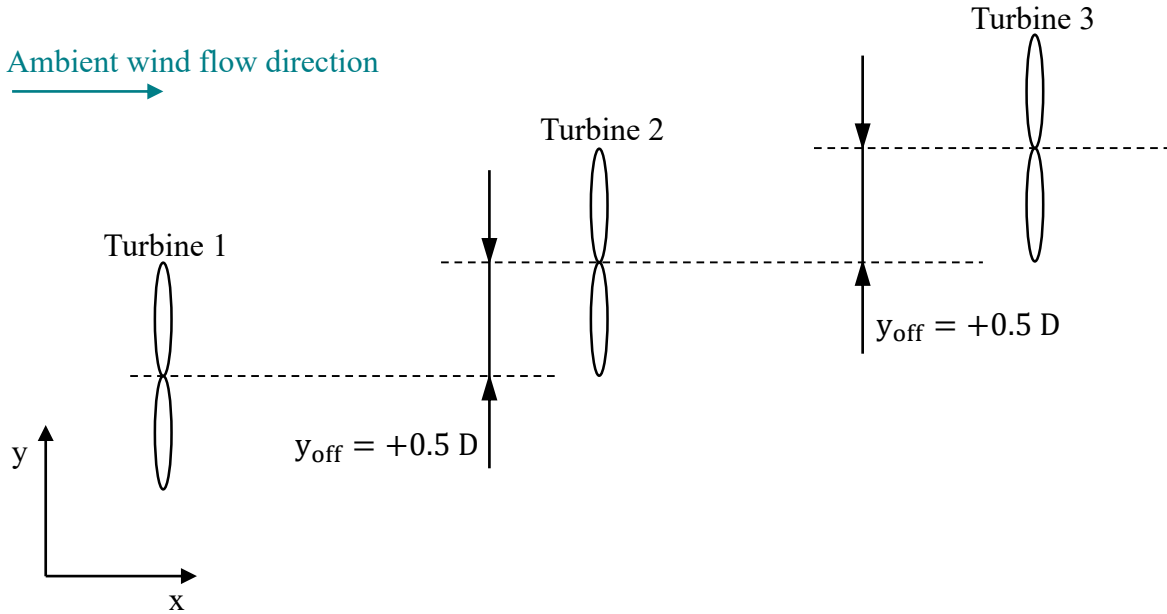


Figure 4.24: Turbine positioning for the calibration of the FLORIS parameters. The offset in the lateral direction of the waked turbine with respect to the closest upstream turbine is set as y_{off} in turbine diameters D .

Table 4.5: Operating conditions for the calibration of the FLORIS parameters. The notation $[a : q : b]$ is used, hence a parameter is varied within the bounds a and b with steps of q .

	Velocity deficit	Wake deflection
Wind speed [m s^{-1}]	[5 : 1 : 16]	[5 : 1 : 11]
Atmospheric stability	[unstable, neutral, stable]	
Turbine spacing [D]	[5, 7, 9]	-
Lateral offset y_{off} [D]	[-1.5 : 0.5 : 1.5]	-
Yaw misalignment θ_m [$^\circ$]	-	[-30 : 5 : 30]

Table 4.6: Calibration parameters of the velocity deficit model in FLORIS and their boundaries for the optimisation.

Parameter	Lower bound	Upper bound
k_a	0.05	1.5
k_b	0.0	0.02
α	0.125	2.5
β	0.015	0.3

Calibration parameters of the velocity deficit model

A summary of the considered calibration parameters of the Gaussian velocity deficit model in FLORIS is provided in Table 4.6. The parameters k_a and k_b are used to calculate the relationship between the wake-width and the ambient TI (see Section 3.2.1). The downstream location of the regime change from near-wake to far-wake is determined with the use of the parameters α and β .

Calibration parameters and setup of the wake deflection model

The setup of the wake deflection model is modified in order to better match the results from wake deflection calculations by FAST.Farm: The inclusion of secondary wake steering effects and yaw-added wake deficit recovery are both deactivated in FLORIS, because they are not considered in FAST.Farm either. Furthermore, the calculations of the initial wake deflection angle at the rotor $\theta_{w,rotor}$ (Equation 3.12) and the corresponding wake deflection in the near-wake δ_0 (Equation 3.13) are adapted with the following equations:

$$\delta_{w,rotor} = d_m \theta_m c_T^{d_p}, \quad (4.3)$$

$$\delta_0 = x_0 \theta_{w,rotor}, \quad (4.4)$$

where d_m and d_p are calibration parameters. In addition, the parameters k_a and k_b are calibrated separately for the wake deflection computation, thus they are re-labelled to $k_{a,dfl}$ and $k_{b,dfl}$. The limits of all parameters for the optimisation are given in Table 4.7.

Table 4.7: Calibration parameters of the wake deflection model in FLORIS and their boundaries for the optimisation.

Parameter	Lower bound	Upper bound
d_m	0.01	3.0
d_p	0.5	6.0
$k_{a,dfl}$	0.05	6.0
$k_{b,dfl}$	0.0	0.02

4.4.2 Optimisation of FLORIS model parameters

The optimisation of the calibration parameters from FLORIS is performed by using a Sequential Least Squares Programming (SLSQP) algorithm embedded in the Python-scipy library in version 1.7.1 [143]. The cost functions are formulated as minimisation problems and are different for the velocity deficit model and the wake deflection model. They are explained in the following in conjunction with the results of the optimisation.

Velocity deficit calculation

The cost function for the optimisation of the parameters from the velocity deficit model is defined as:

$$\Psi_{opt}^i = \underset{\Psi^i}{\operatorname{argmin}} \sqrt{\frac{1}{n} \sum P_{FLORIS}^i(\Psi) - P_{FFarm}^i}, \quad (4.5)$$

where $\Psi = [k_a \ k_b \ \alpha \ \beta]$ are the parameters to be calibrated, $P^i = [P_1^i \dots P_n^i]$ is the turbine power for n turbines and i corresponds to the combination of all considered lateral offset locations y_{off} of the turbines as defined in Table 4.6.

The calibrated parameters as function of the wind speed and AS are displayed for a turbine spacing of 7 D in Figure 4.25 (results for the other turbine spacings are provided in the Appendix A.3). It can be observed that k_a is close to the lower boundary while k_b is close to the upper boundary at below-rated wind speeds. A change of these trends can be seen at above-rated wind speeds. These results are in agreement with the findings in [142].

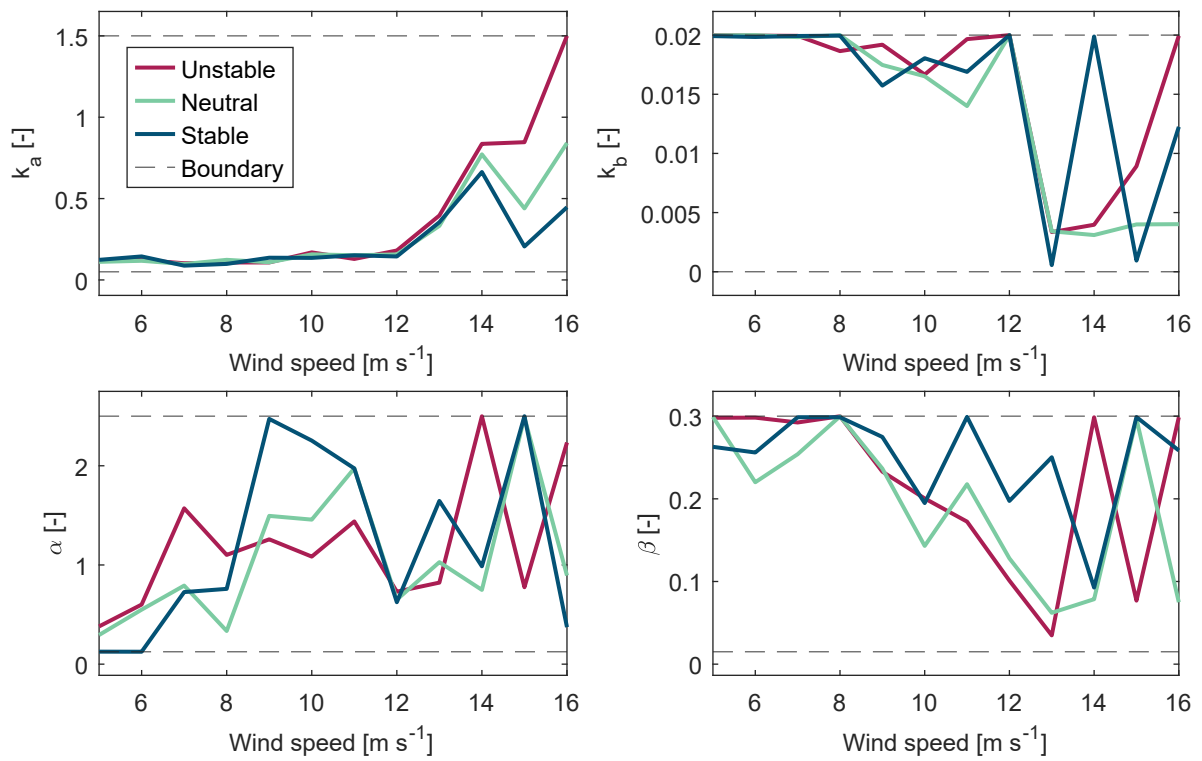


Figure 4.25: Calibrated parameters of the Gaussian velocity deficit model in FLORIS for a longitudinal turbine spacing of 7D.

Table 4.8: Calibrated values of the parameters from the wake deflection model in FLORIS.

Atmospheric stability	d_m	d_p	$k_{a,dfl}$	$k_{b,dfl}$
Unstable	0.40	2.19	1.30	4.25×10^{-3}
Neutral	0.45	2.10	4.90	9.40×10^{-4}
Stable	0.41	1.90	8.71	1.93×10^{-2}

Wake-centre deflection calculation

A different cost function is used for the optimisation of the parameters from the wake-centre deflection model. Here, the wake-centre location at various downstream distances $y_{WkC}^i = [y_{WkC,1}^i \dots y_{WkC,n}^i] = [4D, 7D, 10D]$ is compared between the reference FAST.Farm calculations and FLORIS. The cost function is written as:

$$\Psi_{opt}^i = \underset{\Psi^i}{\operatorname{argmin}} \sqrt{\frac{1}{n} \sum y_{WkC,FLORIS}^i(\Psi) - y_{WkC,FFarm}^i}, \quad (4.6)$$

where $\Psi = [d_m \ d_p \ k_{a,dfl} \ k_{b,dfl}]$ are the parameters to be calibrated, n is the amount of considered downstream distances and i indicates the combination of the wind speeds and yaw misalignment angles given in Table 4.5. With this approach, the same parameter set is derived for all wind speeds and yaw misalignment angles, because it must be applicable to all turbines in a wind farm that operate under varying wind speed and yaw misalignment conditions. There are only different parameter sets for changing AS. The considered wind speeds are limited to below-rated conditions, because the wake-deflection model in FAST.Farm is not calibrated for above-rated wind speeds. The calibrated values are summarised in Table 4.8.

5

Structural loads under consideration of wake redirection control

A systematic investigation of the effects connected with wake redirection control is presented in this chapter. In the first two sections, the turbine model and the environmental conditions are defined. In Section 5.3, the structural loads of a free-stream turbine operating with a yaw-misalignment are analysed and the sensitivities examined. The wake characteristics as function of different environmental conditions are discussed in Section 5.4; this knowledge is useful to assess the efficiency of wake the redirection control in different operating conditions of the wind farm. Finally in Section 5.5, the impact of yawed operation in different wake inflow conditions on the structural loads is investigated.

5.1 Wind turbine model and sensor specification

For all the following investigations, the NREL 5 MW reference wind turbine model [144] is used. The specific version is mounted on a monopile for use in offshore environments; the turbine definition comes from the IEA task 23 OC3 phase I project and can be found in [145]. It is a generic turbine model which has similar properties and characteristics as the turbine models from the alpha ventus wind farm. Its key specifications are summarised in Table 5.1.

The turbine's performance and structural loads are analysed at different locations that are specified in Table 5.2. Only a reduced set of sensors is considered in order to condense the results focusing on the most valuable information and to keep the amount of figures within a reasonable amount. For example, the total bending moment at the blade-root includes the

Table 5.1: Key parameters of the NREL 5 MW turbine model [144] in the version of the IEA task 23 OC3 phase I project [145].

Parameter	Value
Hub height	90 m
Rotor diameter D	126 m
Rated power	5 MW
Rated rotor speed	12.1 rpm
Rated wind speed	11.4 m/s
Water depth	20 m

Table 5.2: Considered sensor locations and their abbreviations.

Sensor abbreviation	Description
P_{Gen}	Generator power output including drivetrain losses
$M_{BR,tot}$	Total bending moment at the blade-root
$M_{LSS,tor}$	Torsional moment at the low-speed shaft
$M_{TT,tot}$	Total bending moment at the tower-top
$M_{TT,yaw}$	Yaw moment at the tower-top
$M_{TB,tot}$	Total bending moment at the tower-base

combined effects from the flapwise and edgewise loading.

5.2 Definition of environmental conditions

For the assessment of wake redirection control and its effects on the power generation and structural loading of wind turbines, short-term and long-term environmental conditions are defined. The short-term statistics are given for a time period of ten minutes, while the long-term statistics provide the distribution for a period of years (e.g. Weibull distribution of the wind speed).

Two sets of short-term environmental conditions are used. One set contains synthetically generated conditions to isolate the effects of certain parameters. The other set is based on measured atmospheric quantities from the FINO1 meteorological mast in the North Sea to represent realistic offshore conditions. The parameters for the short-term conditions include the TI , the power law shear exponent α_{shear} and the atmospheric stability. They serve as inputs for the wind field generation with the Mann model (see Section 3.1.1); additionally, the

Table 5.3: Definition of synthetic short-term atmospheric conditions. The notation $[a : q : b]$ is used, hence a parameter is varied within the bounds a and b with steps of q .

Parameter	Value
Wind speed at hub height [m/s]	[4 : 1 : 20]
TI [%]	[4, 7, 10, 15]
Atmospheric stability (power law shear exponent α_{shear})	[unstable, neutral, stable] (0.03) (0.1) (0.2)

atmospheric stability class is used to determine the parameters L_M and Γ of the Mann model according to Table 3.1.

5.2.1 Synthetic short-term atmospheric conditions

A set of synthetic meteorological conditions is defined and summarised in Table 5.3. The values for the TI range from 4 % corresponding to low turbulence conditions to 15 % which is equivalent to high turbulence conditions that, for instance, can occur in the wake. The three classes of atmospheric stability are directly connected to the values defining the vertical wind shear using the power law shear exponent α_{shear} . A weak vertical wind shear is used for unstable conditions whereas a strong wind shear is used for stable conditions.

5.2.2 Measured short-term atmospheric conditions

Data from the FINO1 meteorological mast [146] are processed to obtain statistics for the TI and vertical wind shear as function of the mean wind speed at 90 m height and the atmospheric stability. Atmospheric stability is computed using the bulk Richardson number (Equation 2.9). Hereby, the sea surface temperature measured with a buoy, the air temperature at 30 m height as well as the mean wind speed at 30 m height serve as inputs. The measurement height at 30 m is chosen to be within the surface layer. The bulk Richardson number is then converted to the dimensionless height ζ with the relationship defined in Equation 2.8. The data are classified in three atmospheric stability classes, i.e. unstable, neutral and stable by using the intervals given in Table 2.2.

The statistics for the TI at 90 m height and the power law shear exponent α_{shear} are shown in Figure 5.1. The data are filtered for the wind direction sector $210 - 280^\circ$ because of the free-stream conditions for the years 2011-2014. The lowest turbulence levels occur in stable conditions, while in unstable conditions the TIs are the highest. Overall, with less than 8 %, the mean TI is low, which is typical for offshore locations. The value of α_{shear} is the highest for stable conditions and the lowest for unstable conditions. The α_{shear} increases with the wind

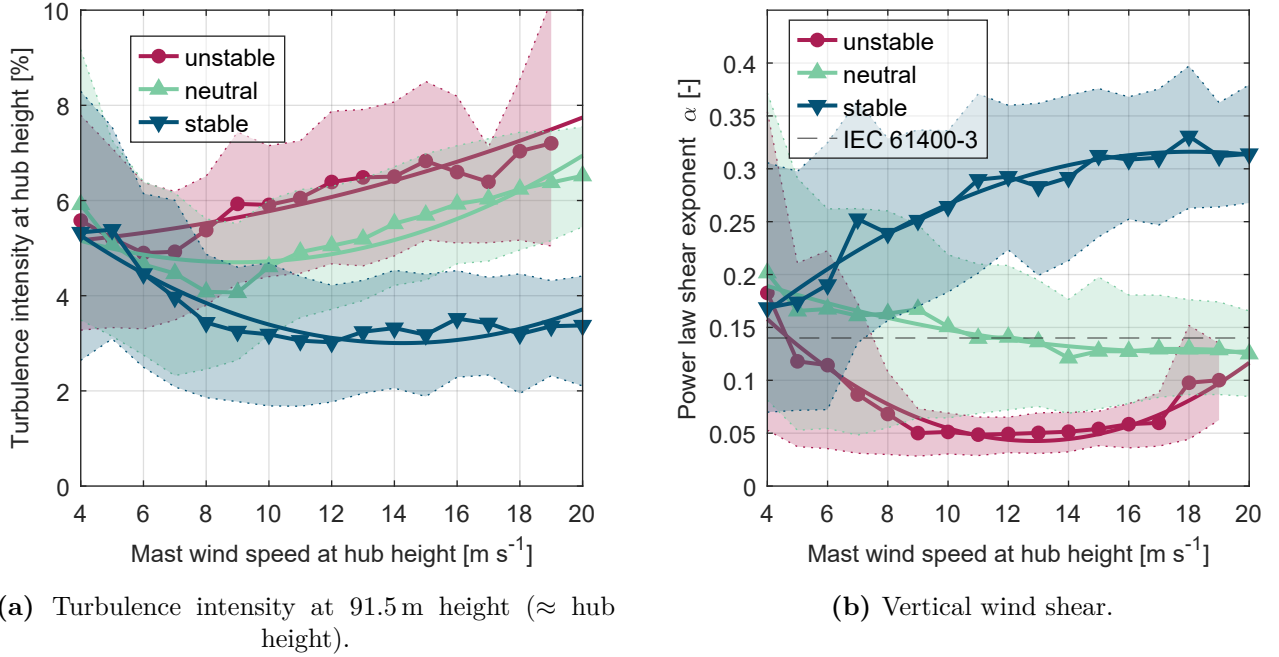


Figure 5.1: Aggregated environmental conditions from the FINO1 meteorological mast for the years 2011-2014. Wind direction sector: 210 – 280°. Shaded area indicates 15th and 85th percentiles.

speed in stable conditions, whereas in unstable conditions it decrease. For neutral conditions, the mean of α_{shear} is nearly constant over all the wind speeds and is close to the value of $\alpha_{\text{shear}} = 0.14$, recommended by the IEC 61400-3 for offshore conditions.

5.2.3 Measured long-term atmospheric conditions

The long-term distribution of the mean wind speed at 90 m height at FINO1 is plotted in Figure 5.2. Only free-stream conditions are considered by using data from the years 2011-2014 and within the wind direction sector 210 – 280°. A Weibull distribution is obtained with the shape parameter $k = 2.52$ and the scale parameter $C = 12.52 \text{ m s}^{-1}$.

5.3 Structural loads of a free-stream turbine during yawed operation

The wake redirection wind farm control strategy requires that the individual turbines within the wind farm operate with large yaw errors ($\theta_m > 10^\circ$) for a longer time period. The resulting asymmetric loading of the rotor has effects on the structural fatigue loads of the wind turbine components. Therefore, it is necessary to investigate the structural loads during yawed operation and to assess the potential negative effects on the fatigue loads and the corresponding implications on the components' lifetime.

The effects of yawed operation on the structural loads was researched in previous studies,

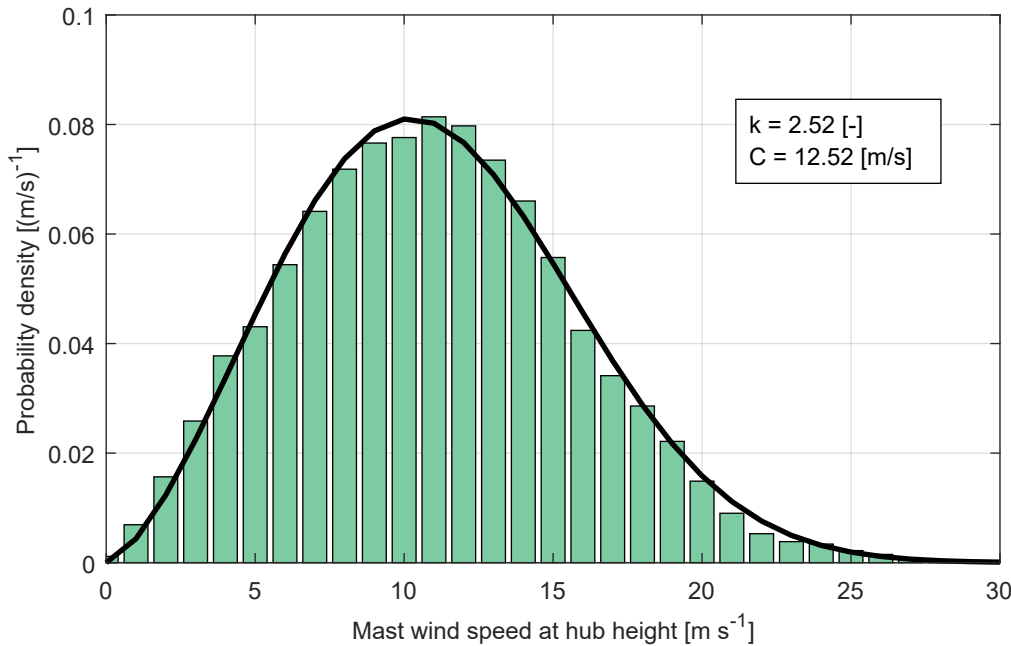


Figure 5.2: Weibull probability density function for the wind speed at 91.5 m height at the FINO1 meteorological mast for the years 2011-2014. Wind direction sector: 210 – 280°. Total number of events: approximately 60 000.

on which the analyses in this chapter are based. In particular, the fatigue and ultimate loads during yawed operation were analysed in [147] by using measurement data and by performing simulations of a 1.5 MW wind turbine. They used version 8 of the FAST tool for the simulations and essentially validated the tool for the calculation of structural loads under yawed operation with the measurements. Potential load alleviation at the blade-root by performing yaw misalignment was studied in [148]. It was shown that the alternating loads resulting from vertical wind shear can effectively be reduced by operating the wind turbine with a yaw misalignment.

In this section, the effects of yawed operation on the fatigue loads are investigated for the NREL 5 MW (for more information on the turbine model, see Section 5.1). The load distributions at different components are presented and their dependency on various environmental conditions is discussed.

5.3.1 Load case definition and simulation setup

The simulations of the NREL 5 MW turbine are set up based on the synthetic short-term atmospheric conditions defined in Section 5.2.1. For long-term evaluations, the Weibull distribution from Figure 5.2 is used for the mean wind speed. The turbine's yaw misalignment angle changes from -30° to 30° in steps of 2.5° . Each operating condition is simulated with six random realisations of the turbulent wind field with a length of ten minutes (the wind fields are

periodic and the transients at the beginning of a simulation are omitted). This leads to 30600 simulations in total. The aeroelastic simulations are performed with the tool OpenFAST (see Section 3.3.2).

The fatigue loads at the wind turbine are examined by evaluating the DELs. Short-term DELs are calculated based on Equation 2.18. Long-term DELs are computed with Equation 2.19 with the use of weighting factors based on the Weibull distribution for the mean wind speed (Figure 5.2).

5.3.2 Structural load distributions at component level

Distributions of the DELs are investigated as a function of the mean wind speed and the yaw misalignment angle. In Figures 5.3-5.6, the load distributions at different locations of the wind turbine are shown as contour plots. In each plot, the results from stable conditions with strong vertical wind shear and low TI are compared against the results from unstable conditions with weak vertical wind shear and high TI . Complementary results from further environmental conditions are provided in the Appendix A.4. All results are normalised with respect to the DELs with zero yaw misalignment for each considered wind speed bin.

In general, the fatigue loads are highly dependent on the wind speed and the yaw misalignment angle. In Figure 5.3, the DELs of the total bending moment at the blade-root are shown. For the stable AS case, at below rated wind speeds, the normalised loads are below 1 for positive yaw misalignment angles whereas they exceed 1 for negative yaw misalignment angles. For above rated conditions, the opposite behaviour can be seen. Similar trends are observed for unstable AS (Figure 5.3 (b)) in below rated conditions. However, at higher wind speeds yawed operation leads to higher loads for yaw misalignment angles less than -10° . The comparison between the stable and unstable case reveals larger gradients for the loads in stable AS. This can be explained by the combined effects of vertical wind shear, TI and yaw misalignment angle as it is discussed in [148]: The load variations on the blades caused by vertical wind shear can be increased or reduced depending on the yaw misalignment angle. With increasing turbulence levels, the influence of vertical wind shear and yaw misalignment on the fatigue loads becomes less pronounced.

The fatigue load distributions for the torsional moment at the LSS are shown in Figure 5.4. The torsional loads tend to decrease under yawed operation. However, at wind speeds above rated and high yaw misalignment angles ($|\Theta_m| > 15^\circ$) the loads are increased compared to zero yaw misalignment. This can be attributed to effects from the control system of the turbine. With increasing yaw misalignment angles, the wind speed at which the turbine reaches rated power is shifted to higher wind speeds compared to normal operation. The opposite behaviour is found for wind speeds below rated power; here, the loads are reduced at higher yaw misalignment angles because the rated power is not yet reached.

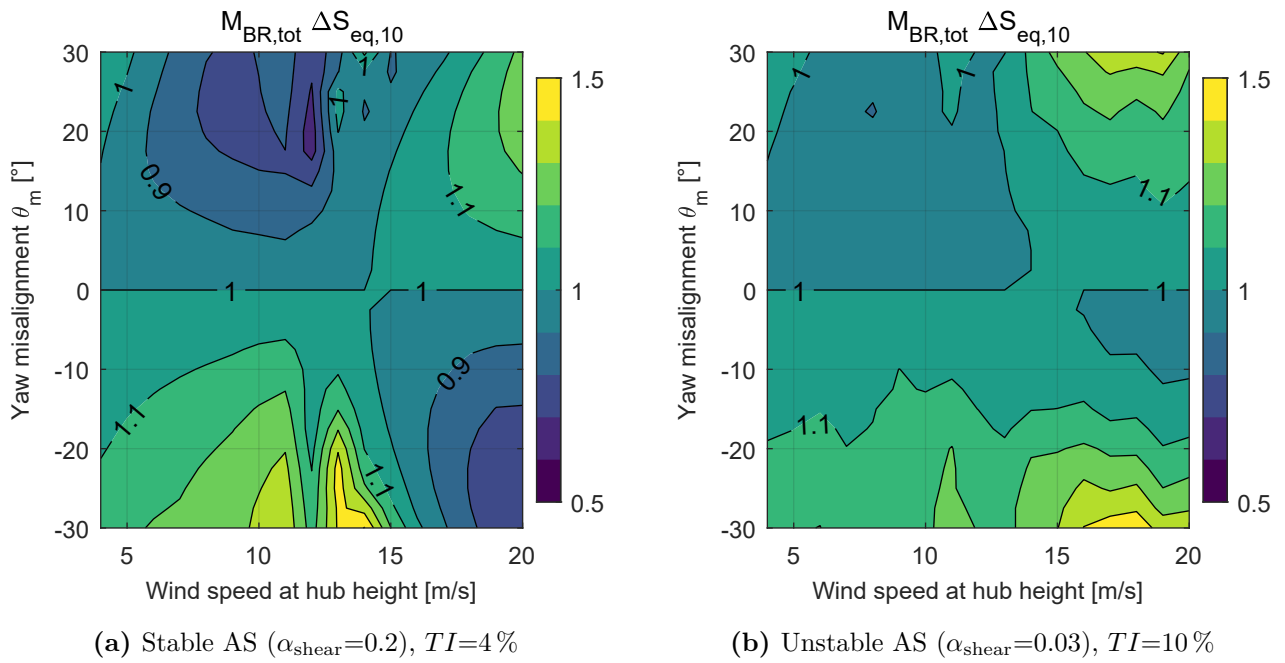


Figure 5.3: Load distributions of the total bending moment at the blade-root. Results are shown by means of the seed average and normalised with the values at $\theta_m = 0^\circ$.

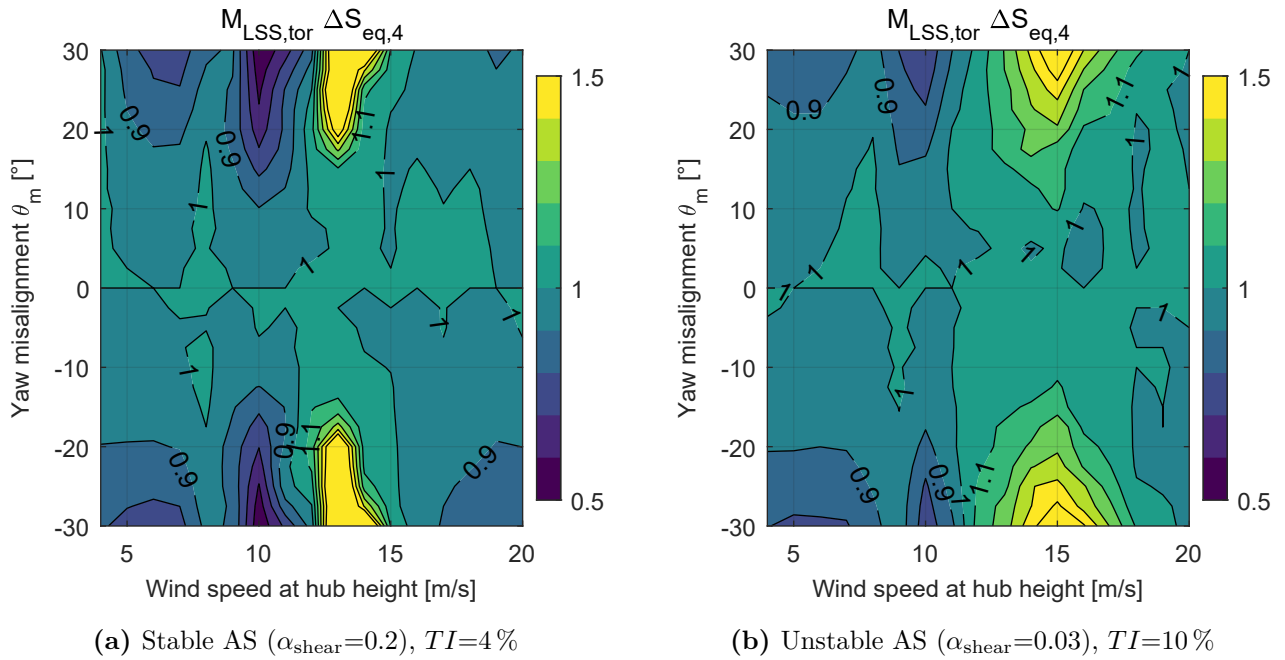


Figure 5.4: Load distributions of the torsional moment at the low-speed shaft. Results are shown by means of the seed average and normalised with the values at $\theta_m = 0^\circ$.

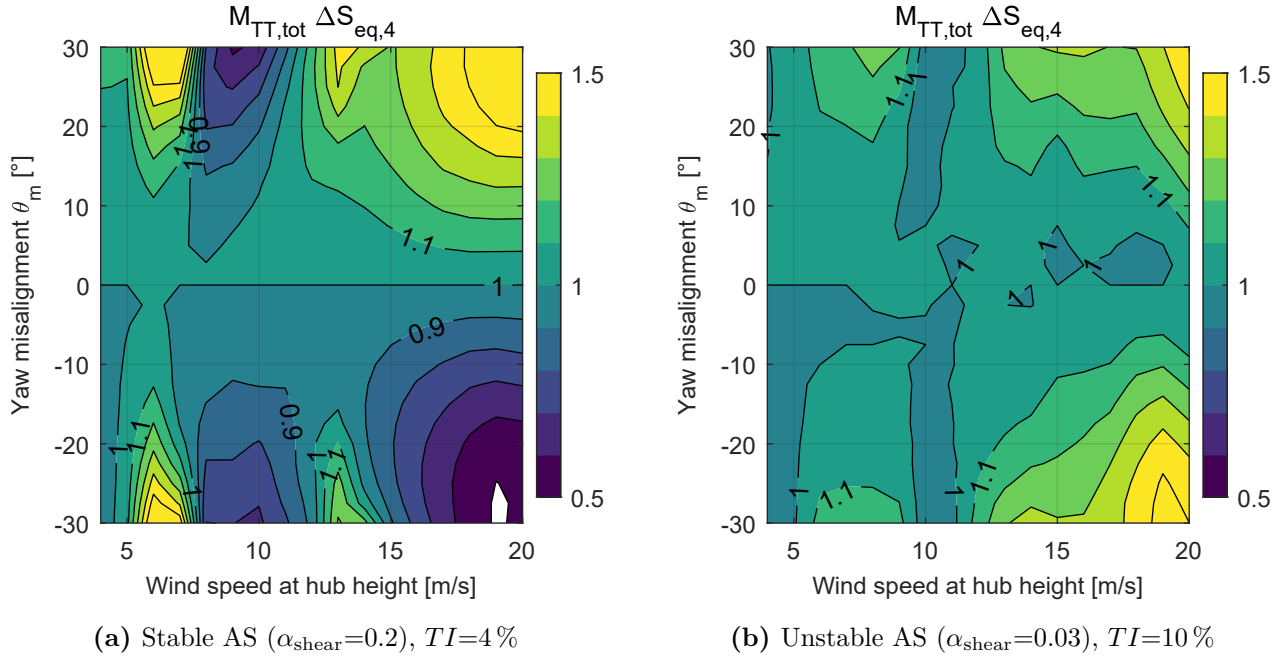


Figure 5.5: Load distributions of the total bending moment at the tower-top. Results are shown by means of the seed average and normalised with the values at $\theta_m = 0^\circ$.

The load distributions of the total bending moment at the tower-top are strongly dependent on the atmospheric conditions (see Figure 5.5). For the stable AS case, areas of load reduction and load amplification can be identified, whereas yawed operation tends to increase the loads at all wind speeds for the unstable AS case. Especially at wind speeds above rated with a negative yaw misalignment angle, opposite behaviour can be observed between the stable (loads are decreased) and unstable case (loads are increased).

The effects of yaw misalignment on the fatigue loads of the total bending moment at the tower-base are most significant around the wind speed of rated power (Figure 5.6). In this region, similar characteristics of the load pattern are found compared to the torsional moment at the LSS. Significant influence on the loads comes from the control system and changing wind speeds of rated power due to yaw misalignment. In below rated wind speeds, fatigue loads for all yaw misalignment angles are close to the loads at zero yaw misalignment.

5.3.3 Long-term evaluation

A long-term evaluation of the fatigue loads is performed to gain an impression on the equivalent loads for a wind speed range and to evaluate different atmospheric conditions (atmospheric stability and TI) together in one plot. Therefore, the long-term DELs are calculated for each yaw misalignment angle based on the Weibull distribution for the wind speed (Figure 5.2); only wind speeds below rated power ($4-11 \text{ m s}^{-1}$) are considered because it is assumed that wake redirection control is mostly relevant in this region.

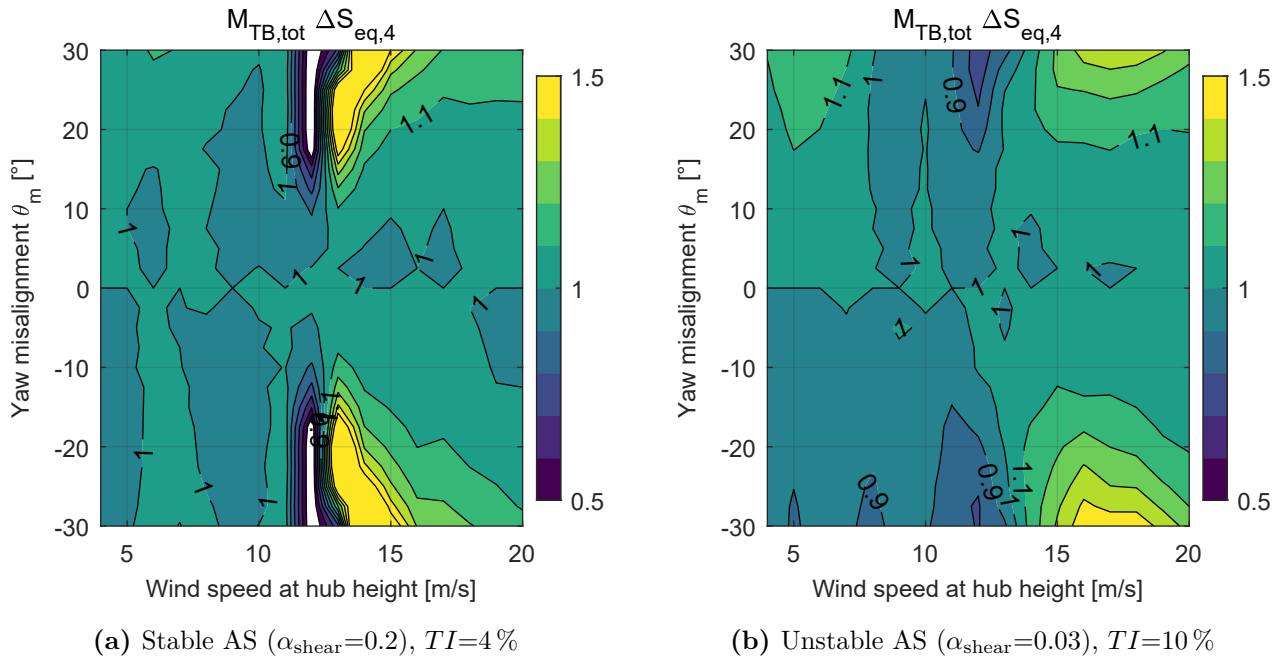
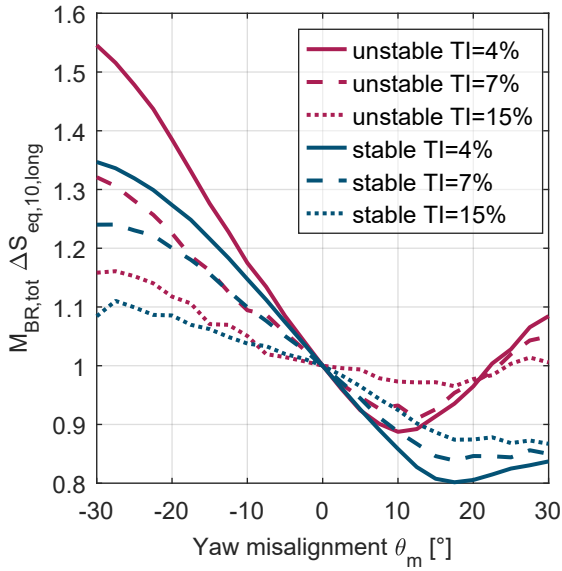


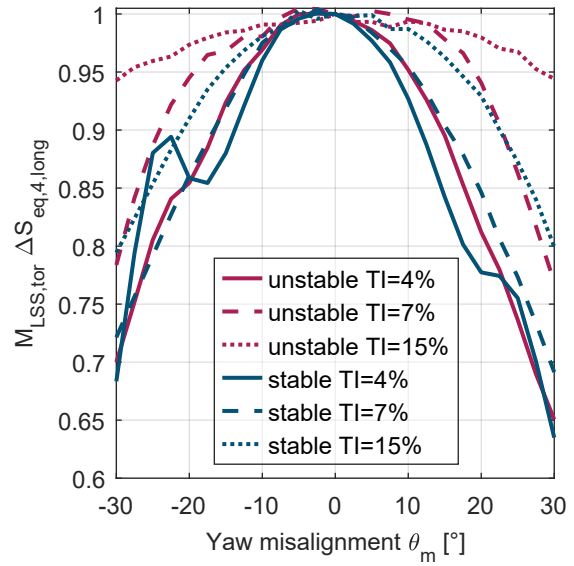
Figure 5.6: Load distributions of the total bending moment at the tower-base. Results are shown by means of the seed average and normalised with the values at $\theta_m = 0^\circ$.

It is observed that the long-term DELs of the total bending moment at the blade-root are significantly increased (up to Factor 1.5) at negative yaw misalignment angles for all atmospheric conditions (see Figure 5.7 (a)). Hereby, the loads are increased more with respect to $\theta_m = 0^\circ$ in unstable conditions than in stable conditions for the same TI . This can be explained with the vertical wind shear which is stronger in stable conditions than in unstable conditions and leads to already increased loads at zero yaw-misalignment. Hence, the relative load increase in unstable conditions is higher. For positive yaw misalignment angles, the loads are alleviated in stable conditions. This is also the case in unstable conditions except for high yaw misalignment angles ($\theta_m > 20^\circ$) at which the loads are slightly higher compared to zero yaw misalignment. The load peaks become lower with increasing turbulence levels because the relative influence of the vertical wind shear is less compared to low turbulence conditions.

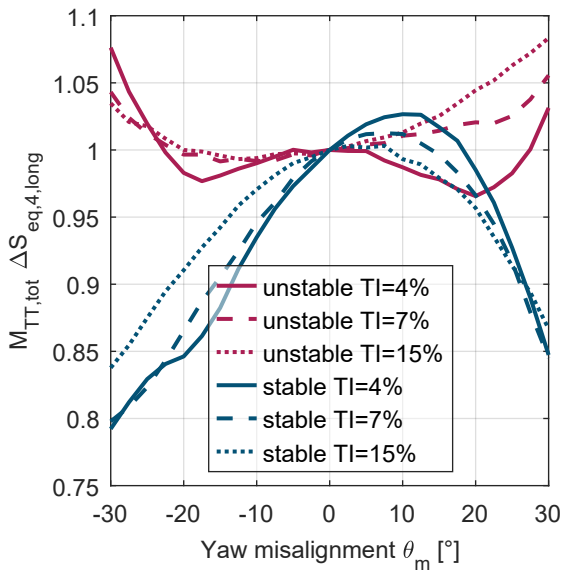
For the other considered locations (Figures 5.7 (b)-(d)), the loads are reduced with respect to increasing/decreasing yaw misalignment angles for most of the atmospheric conditions. Exceptions of this trend are found for the total bending moment at the tower-top (increased DELs by up to 10%) and for the total bending moment at the tower-base where the loads are slightly higher, up to 5% in stable conditions with a low TI .



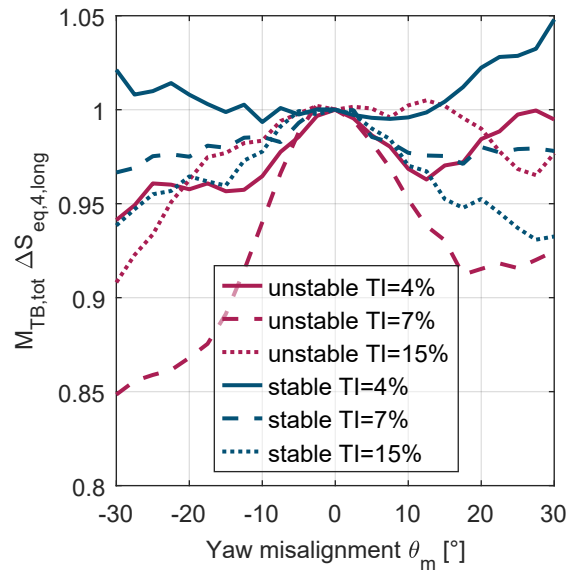
(a) Total bending moment at the blade-root.



(b) Torsional moment at the low-speed shaft.



(c) Total bending moment at the tower-top.



(d) Total bending moment at the tower-base.

Figure 5.7: Long-term DEL distributions at various locations based on the Weibull distribution given in Figure 5.2 for below rated wind speeds ($4 - 11 \text{ m s}^{-1}$). Results are normalised with the values at $\theta_m = 0^\circ$.

5.3.4 Conclusions

Fatigue load distributions at different locations and their dependency on changing atmospheric conditions and yaw misalignment angles are investigated in this chapter. Different trends of the loads with respect to changing yaw misalignment angles are identified at the considered locations. The biggest effects of yaw misalignment on the load variations are found for stable AS with strong vertical wind shear and low TI . In contrast, the influence of yaw misalignment on the fatigue loads becomes less important in unstable AS with low vertical wind shear and high TI . The analysis of the long-term DELs for below rated wind speeds shows decreased loads for the majority of components and atmospheric conditions. However, the long-term fatigue loads of the total bending moment at the blade-root are significantly increased for negative yaw-misalignment angles.

When applying wake redirection control, yawed operation can lead to increased or decreased fatigue loads based on the component, atmospheric conditions and yaw misalignment angle. A reduction in loads at one location is often penalised with an amplification of loads at another location. A parallel reduction of fatigue loads for all components is normally not possible. Nevertheless, strategies or operational points can be found that can minimise the fatigue loads and also allow some yaw misalignment for enabling wake redirection control.

The present results are only valid for the simulated turbine model NREL 5 MW. Other turbine models might show different load characteristics and should be investigated separately.

5.4 Single wake characteristics

The structural loads of waked turbines are significantly affected by the wakes of upstream turbines. Changing atmospheric conditions lead to different wake characteristics and different structural load distributions at the waked turbine. In this chapter, the atmospheric conditions and their effects on the wake characteristics are investigated. In particular, the effects on the wake meandering as well as the effects on the resulting wake profiles (velocity, TI) are analysed. For the study on the induced structural loads at the waked turbines, the reader is referred to Section 5.5.

5.4.1 Load case definition and simulation setup

The synthetic atmospheric conditions given in Table 5.3 are used to set up the simulations. In addition, a variation of these atmospheric conditions is introduced by using different levels of vertical wind shear by varying the exponent of the power law $\alpha_{shear} = 0.0 - 0.3$; the shear exponent is explicitly mentioned when it is varied. Each operating condition is simulated with six turbulent wind field realisations with a length of 30 minutes in order to capture the wake meandering with a low frequency adequately (the wind fields are periodic and transients at the beginning of a simulation are omitted).

The aeroelastic simulations are performed with a single NREL 5 MW turbine model in the tool FAST.Farm to be able to evaluate the wake characteristics. The tilt angle of the turbine's main shaft is set to zero (instead of 5°), thus no vertical wake deflection due to an inclined shaft is expected. The effects of this change on the power performance and loads are not studied because the focus is on the wake characteristics and their dependency on the inflow conditions.

5.4.2 Wake meandering characteristics

The wake meandering is investigated in terms of its magnitude with respect to varying environmental conditions. Therefore, statistics of the time series of the wake centre displacement are computed. The results from the standard deviation of the wake centre displacement in lateral and vertical directions are plotted against downstream distance for different environmental conditions in Figure 5.8. It is observed that both the lateral and vertical wake meandering become stronger with increasing TI . Unstable atmospheric conditions imply greater magnitudes of wake meandering followed by neutral and stable AS for the same turbulence levels. This can be seen in the gradients with regard to increasing downstream distance: with increasing turbulence and decreasing atmospheric stability (from stable to unstable), the slope of the standard deviation of the wake centre displacement becomes higher. By comparing the wake meandering for the two directions, it can be seen that the lateral wake meandering has higher magnitudes than the vertical wake meandering. This is caused by the turbulent length scales that are larger in the horizontal direction compared to the vertical direction.

More details on the wake centre displacement in terms of the PDF are provided for a downstream distance of 7 D in Figure 5.9. Here, the distribution of the wake displacement becomes fully visible. For example, the wake centre is displaced by up to 100 m ($\approx 1.5 R$) in the lateral direction in unstable AS with a $TI = 10\%$. In contrast, the largest displacement in the lateral direction is only ≈ 18 m in stable AS with a $TI = 4\%$. Overall, the trends identified in Figure 5.8 are also seen in the PDFs of the wake centre displacement: With decreasing stability (from stable to unstable) and increasing turbulence levels, the PDF becomes wider with a less distinct peak at zero wake centre displacement. Additionally, lower magnitudes of wake centre

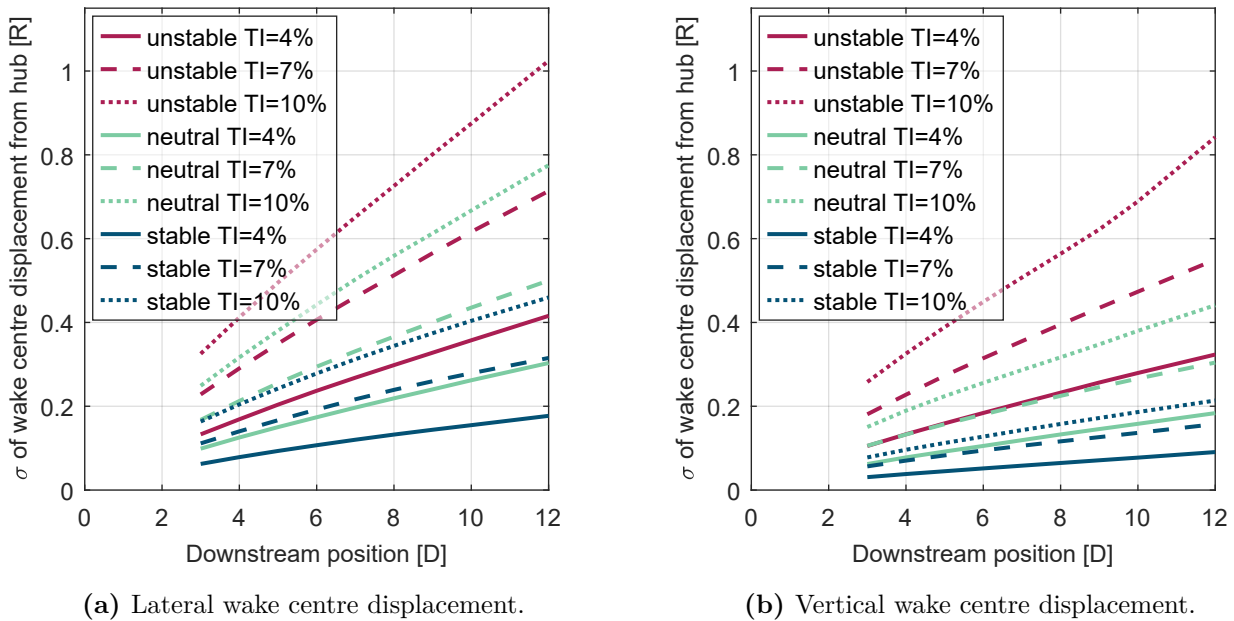


Figure 5.8: Wake centre displacement statistics given as standard deviation σ . Results show the mean value of all wind speeds (see Table 5.3) and corresponding six seeds normalised by the rotor radius R .

displacement leading to narrower PDFs are observed in the vertical direction compared to the lateral direction. However, for instance in unstable AS, wake centre displacements of nearly ± 100 m can still be observed. This translates to wake centre displacements in the negative direction that are below the surface. From a modelling point of view at the current state of FAST.Farm, this is possible because it is a result of the wake meandering modelling (see Section 3.3.3) which does not take the surface explicitly as a lower meandering limit into account.

5.4.3 Wake profiles

The wake characteristics are examined in terms of the aggregated profiles at different downstream distances and varying environmental conditions. The analysis is split into two parts. At first, a uniform wind profile is assumed, thus vertical wind shear is not included. Consequently, only the turbulent structures of the wind field have an effect on the wake. The uniform wind profile enables a consistent study of the radial profiles because an average over the azimuth can be calculated. This is visualised in Figure 5.10 by plotting the contour of the TI for a simulation with and without vertical wind shear. In the second part, vertical wind shear is considered and its effects on the wake calculation are discussed.

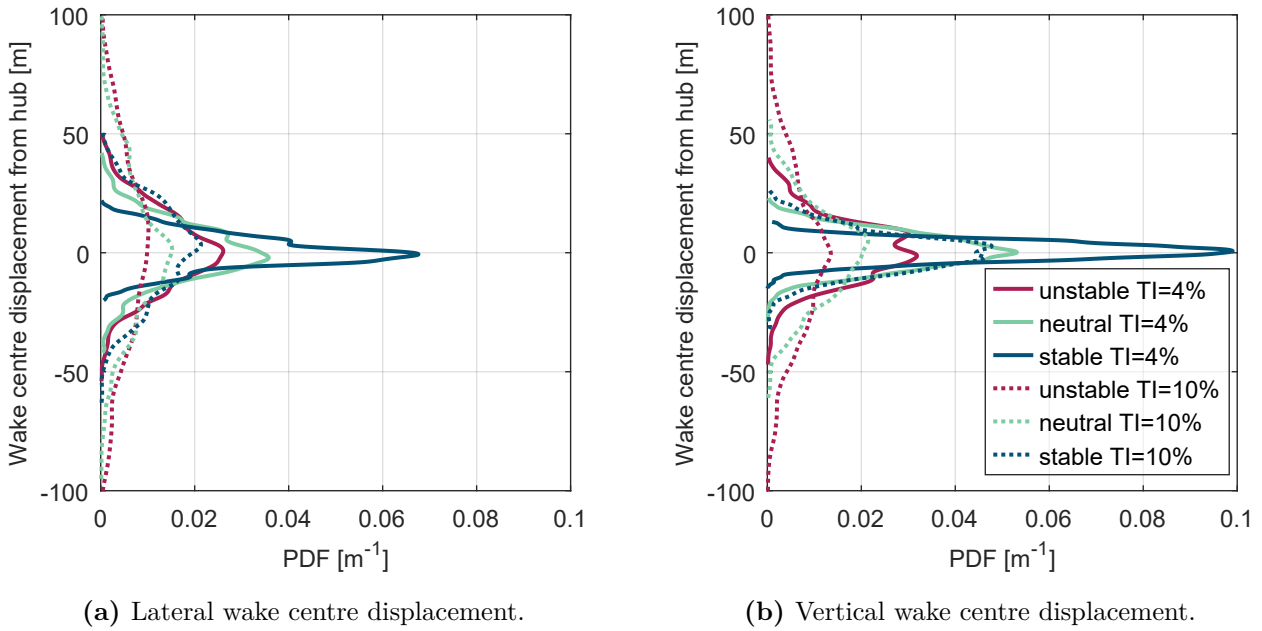


Figure 5.9: Probability density function of the wake centre displacement measured from the hub at a downstream distance of $7D$. Mean wind speed is 8 m s^{-1} and the wind profile includes vertical wind shear. Results show the mean value of six seeds.

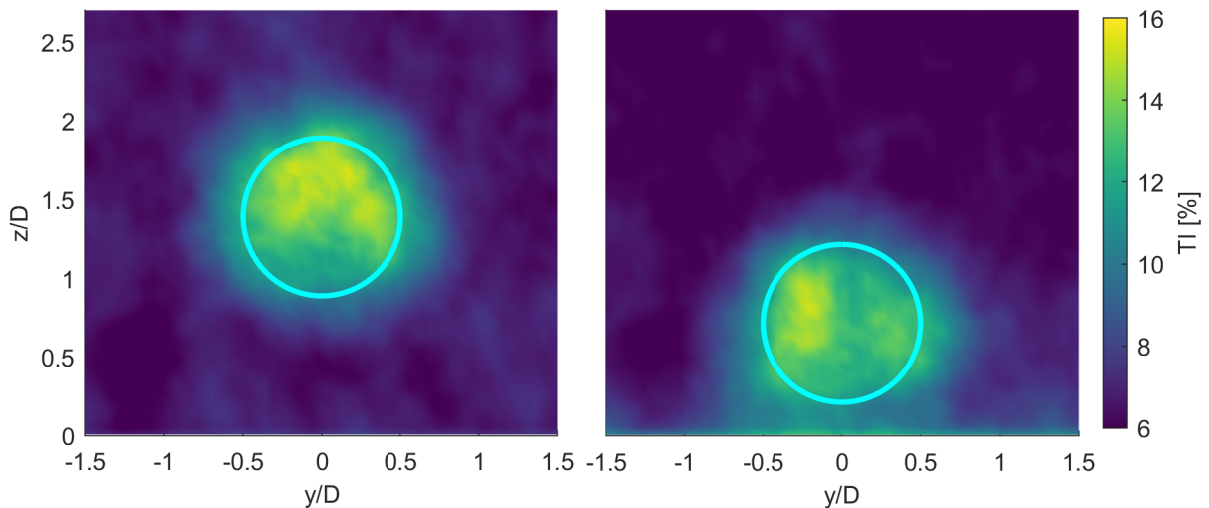


Figure 5.10: Contour plot of the TI at the yz -plane $7D$ downstream from a FAST.Farm simulation. The mean wind speed is 8 m s^{-1} in neutral AS with an ambient TI of 7% . Left: uniform wind profile without vertical wind shear; right: vertical wind shear based on the power law with the exponent $\alpha_{shear} = 0.1$. The location of the turbine's rotor is indicated by the circle. The spatial coordinates are normalised by the rotor diameter D .

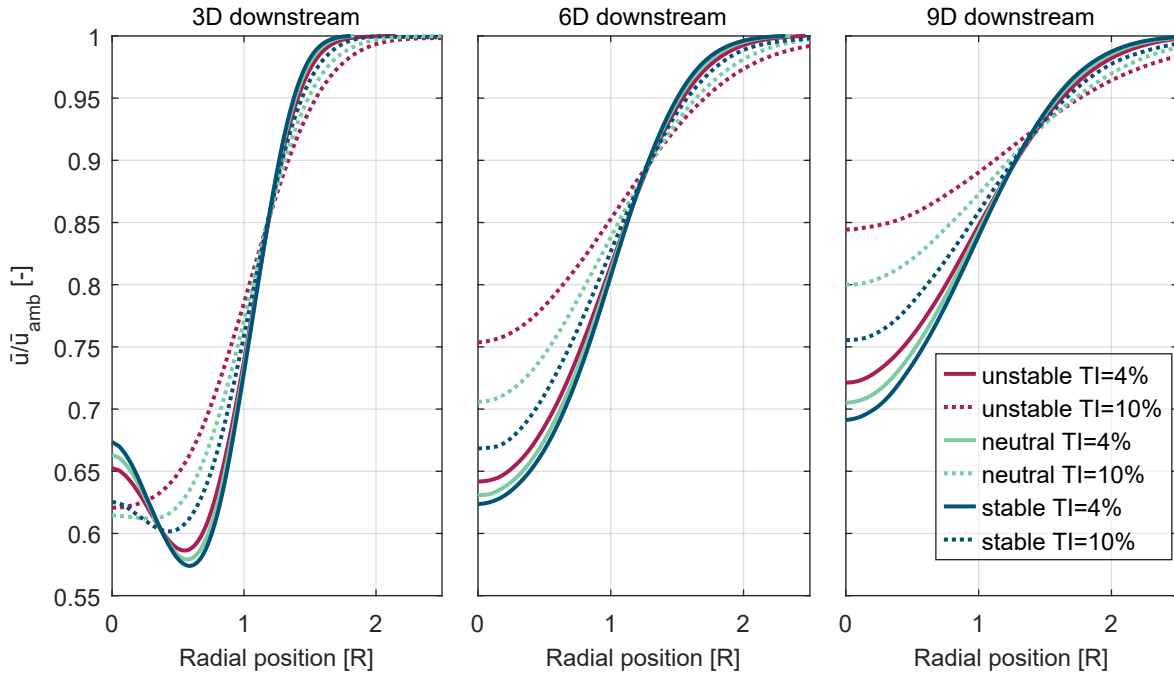


Figure 5.11: Velocity deficit profiles at different downstream distances behind the rotor in the FFoR. Mean wind speed is $\bar{u}_{amb} = 8 \text{ m s}^{-1}$ and the wind profile is uniform (no vertical wind shear). The radial position is normalised by the rotor radius R .

Uniform wind profile: no vertical wind shear

The radial profile of the velocity deficit is shown for different downstream distances and various environmental conditions in Figure 5.11. The profiles are derived by computing the mean value over the azimuth for a fixed radial location; they are normalised by the ambient mean wind speed of $\bar{u}_{amb} = 8 \text{ m s}^{-1}$. It is observed that the recovery of the velocity deficit is faster (at the same downstream distance) with increasing ambient TI and decreasing AS (from stable to unstable). For example, at a downstream distance of 6D, the wind speed is recovered to $\approx 75\%$ of the ambient wind speed in unstable AS ($TI_{amb} = 10\%$), whereas only $\approx 62\%$ are reached in stable atmospheric conditions having an $TI_{amb} = 4\%$.

It is found that the differences of the wake deficit recovery between the atmospheric stability classes are higher for highly turbulent conditions ($TI_{amb} = 10\%$). In contrast, the effects from AS on the wake deficit recovery are negligible for the case of low atmospheric turbulence ($TI_{amb} = 4\%$). An explanation is found by identifying the influence of wake meandering on the wake deficit recovery. This effect can be visualised by looking into the wake deficit calculation in the MFoR (see Figure 5.12), which is an available output channel of FAST.Farm. The wake deficit in the MFoR depends only on the ambient turbulence level; it is not affected by the structure of the turbulence that is different for the considered AS classes. Consequently, wake recovery is influenced by the wake meandering; with decreasing AS (from stable to unstable)

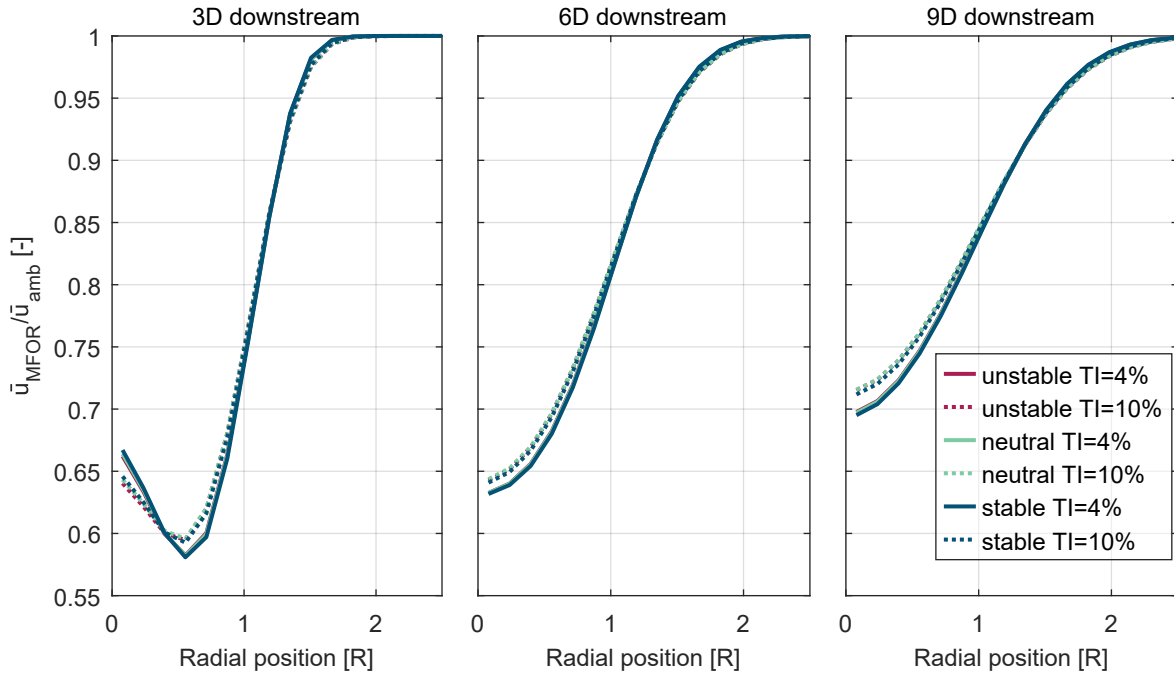


Figure 5.12: Velocity deficit profiles at different downstream distances behind the rotor in the MFoR. Mean wind speed is $\bar{u}_{amb} = 8 \text{ m s}^{-1}$ and the wind profile is uniform (no vertical wind shear). The radial position is normalised by the rotor radius R .

and increasing TI the wake meandering becomes stronger (see Section 5.4.2), thus the recovery of the wake deficit is faster.

The turbulence in the wake is investigated by looking into the radial distribution of the TI in Figure 5.13. In particular, the resulting TI labelled as TI_{total} is considered, which includes the contributions from the ambient turbulence, the wake-added turbulence and the apparent turbulence from the wake meandering. The results show that the turbulence levels in the wake are significantly increased compared to the ambient turbulence. The relative increase in the wake's turbulence is found to be higher for lower ambient turbulence levels. For example, at a downstream distance of $6D$, the turbulence in the wake increases by a factor of ≈ 3 for the low ambient $TI_{amb} = 4\%$, while it increases by a factor of ≈ 1.8 for the high ambient $TI_{amb} = 10\%$.

The turbulence level in the wake is highest for unstable conditions followed by neutral and stable conditions. However, the differences between the different atmospheric conditions are small (up to $\Delta TI_{total} = 3\%$). Nevertheless, it shows that the influence of the wake meandering on the TI in the wake is not negligible. This can also be seen in the radial expansion of the increased turbulence from the wake which is wider for higher ambient turbulence and unstable conditions due to the wake meandering. Overall, lower turbulence levels are found with increasing downstream distances as a result of less wake-added turbulence due to smaller velocity shear in the wake and less apparent turbulence due to smaller velocity deficits.

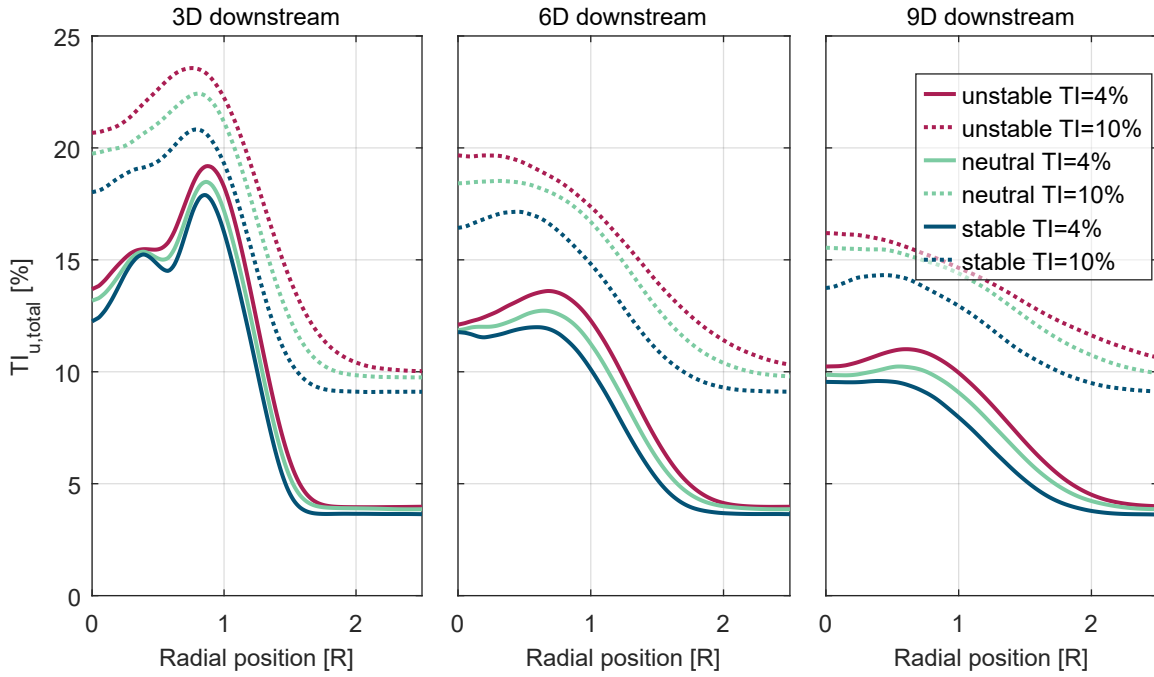


Figure 5.13: TI profiles at different downstream distances behind the rotor. Mean wind speed is $\bar{u}_{amb} = 8 \text{ m s}^{-1}$ and the wind profile is uniform (no vertical wind shear). The radial position is normalised by the rotor radius R .

Effects of vertical wind shear

The effects of vertical wind shear on the velocity profiles in the wake and the implemented modelling approach in FAST.Farm are analysed and discussed. A sensitivity study of the spatial turbulence intensity around the rotor $TI_{amb,Rotor}$ with regard to different environmental conditions and vertical wind shear is presented in Figure 5.14. The $TI_{amb,Rotor}$ is calculated by FAST.Farm in each time step according to Equation 3.18 and is used as an input for the eddy viscosity calculation. Higher values of $TI_{amb,Rotor}$ lead to increased values of the eddy viscosity which eventually leads to a faster wake recovery as consequence. A clear trend of higher $TI_{amb,Rotor}$ with higher shear exponents α_{shear} , i.e. stronger vertical wind shear, can be seen. Differences between the considered ASs are found to be small for the same ambient turbulence level compared to the sensitivity arising from the vertical wind shear and ambient TI .

The consequences of the identified sensitivity of the $TI_{amb,Rotor}$ with respect to the vertical wind shear are investigated specifically for the defined synthetic atmospheric conditions (see Section 5.2.1). In Figure 5.15, the $TI_{amb,Rotor}$ as well as the resulting eddy viscosity ν_T are plotted. The strong influence of the vertical wind shear on the eddy viscosity is confirmed. Hence, in stable atmospheric conditions connected with the strongest wind shear, significantly larger values of ν_T are found compared to the neutral and unstable AS. Conversely, when

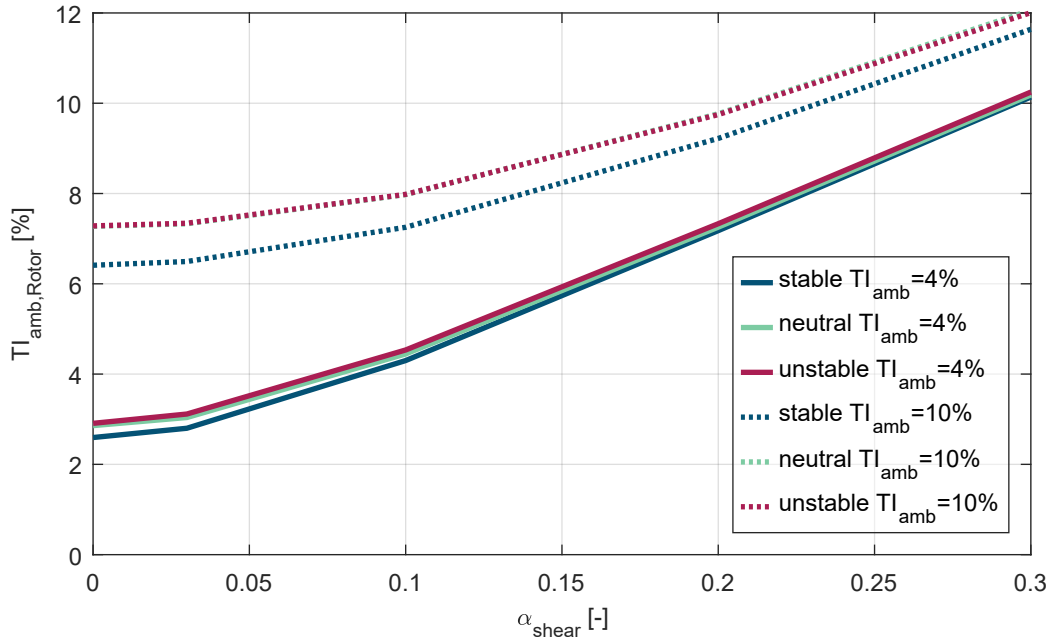


Figure 5.14: Mean value over time of the $TI_{amb,Rotor}$ calculated with Equation 3.18 for different environmental conditions at a wind speed of 8 m s^{-1} .

vertical wind shear is negligible the highest values of ν_T occur in unstable conditions followed by neutral and stable AS; however, the differences between the stability classes are much smaller compared to the case with vertical wind shear.

The velocity deficit at hub height is shown at different downstream distances in Figure 5.16. It is plotted in the FFor, thus the wake recovery includes contributions from the small-scale turbulence as well as from the wake meandering. For low ambient turbulence ($TI = 4\%$), the wake recovery is very similar for the different ASs, showing that less velocity deficit recovery in the MFor is compensated by the stronger wake meandering with decreasing AS (from stable to unstable). The influence of the wake meandering on the wake recovery is higher for highly turbulent conditions ($TI = 10\%$), where the fastest wake recovery is seen for unstable AS followed by neutral and stable AS.

The wake recovery rate is related to the momentum fluxes in the vertical and lateral directions (see Section 2.3.1); higher momentum fluxes amplify the turbulent mixing. Hence, the wake recovery rate is increasing with decreasing AS (from stable to unstable). The vertical wind shear profile is a consequence of the prevailing turbulent conditions in the flow (see Section 2.1.3). In neutral atmospheric conditions, the vertical wind shear is to a large extent dependent on the surface roughness. Higher roughness lengths lead to more friction and higher kinematic shear stresses (expressed as $\overline{u'w'}$), thus a stronger vertical wind shear profile develops. However, in non-neutral atmospheric conditions, the momentum fluxes are impacted by the thermal stratification and a different equilibrium in the vertical wind shear is reached compared to

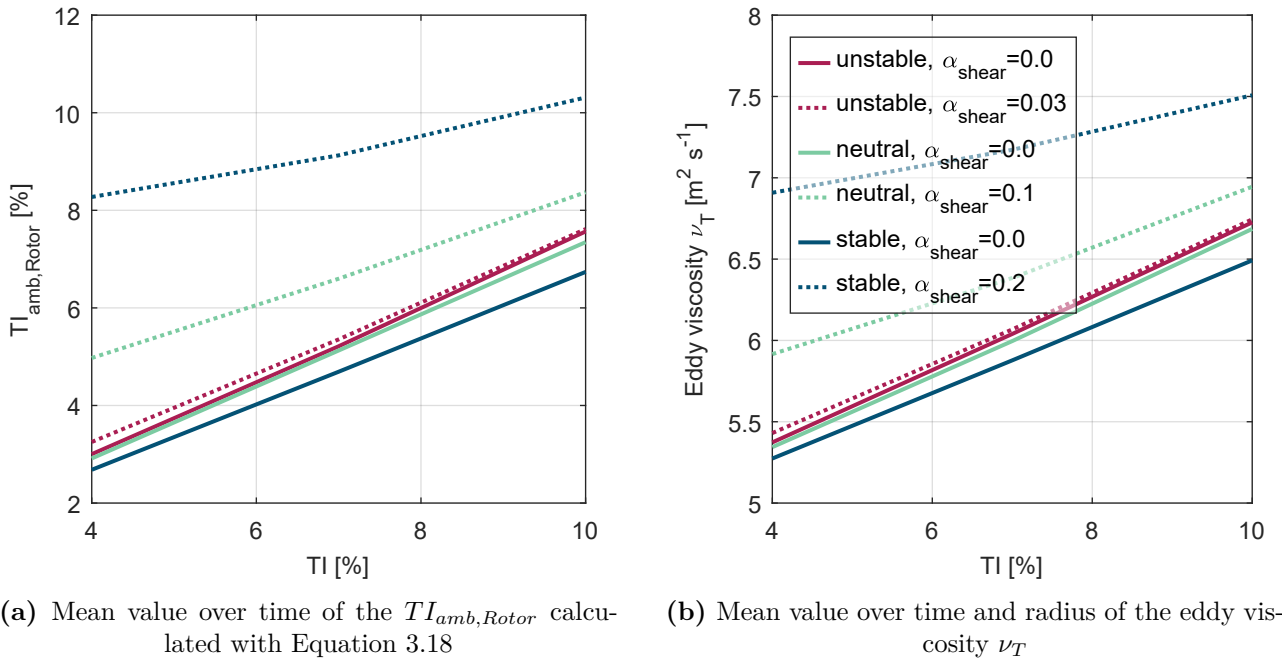


Figure 5.15: Sensitivity of quantities relevant for the wake deficit calculation in FAST.Farm with respect to the ambient TI . Synthetic environmental conditions (see Section 5.2.1) at a wind speed of 8 m s^{-1} .

neutral AS. For example in the case of stable AS, the vertical momentum flux is damped and a stronger vertical wind shear profile evolves. In the current implementation of FAST.Farm, higher vertical wind shear leads to increased eddy viscosity which eventually is followed by better wake recovery rates in the MFoR. This is in contrast to the physical processes in the stable ABL. As a consequence, the wake recovery rates in stable AS are likely to be overestimated by FAST.Farm in the current version. A correction of the eddy viscosity calculation that is dependent on the AS would be needed but is part of future work.

5.4.4 Conclusions

The wake characteristics behind a single wind turbine are studied with respect to varying environmental conditions and their modelling in FAST.Farm are discussed. The magnitude of wake meandering depends on the AS and the ambient turbulence level. The strongest wake meandering in both the lateral and vertical directions occurs in unstable and highly turbulent conditions, whereas significantly less wake meandering is observed in stable AS with low ambient TI . The resulting wake profiles are investigated with respect to the velocity deficit and TI .

The wake recovery rates for the different ASs are similar for the case of low ambient turbulence ($TI = 4\%$). For highly turbulent conditions ($TI = 10\%$), the wake recovers faster in unstable conditions compared to neutral and stable AS. The influence of vertical wind shear

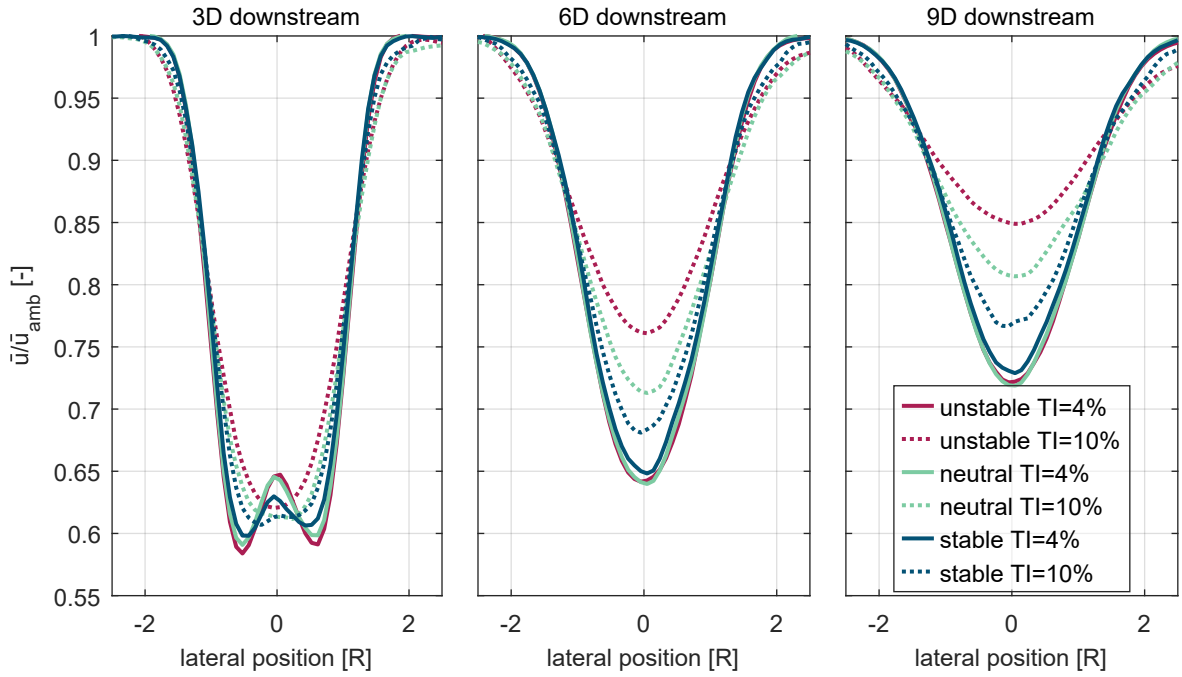


Figure 5.16: Velocity deficit profiles at hub height at different downstream distances behind the rotor in the FFoR. Mean wind speed is $\bar{u}_{amb} = 8 \text{ m s}^{-1}$ and vertical wind shear is included as defined in Table 5.3. The lateral position is normalised by the rotor radius R .

on the wake recovery rate and its treatment in FAST.Farm are examined. Stronger vertical wind shear leads always to faster wake recovery in FAST.Farm. This is for instance contrary to physical considerations in a stable ABL where the momentum exchange in the vertical direction is typically lower compared to neutral and unstable conditions. It is concluded that the wake recovery rate for stable AS is likely overpredicted to be by FAST.Farm in the current implementation. The implications on the results, especially the structural loads of the waked turbine (Section 5.5), are regarded of minor importance because the observed trends in the analysed load distributions will remain the same (although with a slightly different magnitude) if the wake recovery rate is weaker.

With respect to wake redirection control, the results indicate that the potential power maximisation by deflecting the wake is higher in stable AS due to slower wake recovery rates compared to neutral and unstable conditions. Additionally, the turbulence levels in the wake are lower and narrower in the lateral location for stable AS compared to neutral and unstable AS; hence, a deflection of the wake should be more effective to lower the structural loads in stable AS.

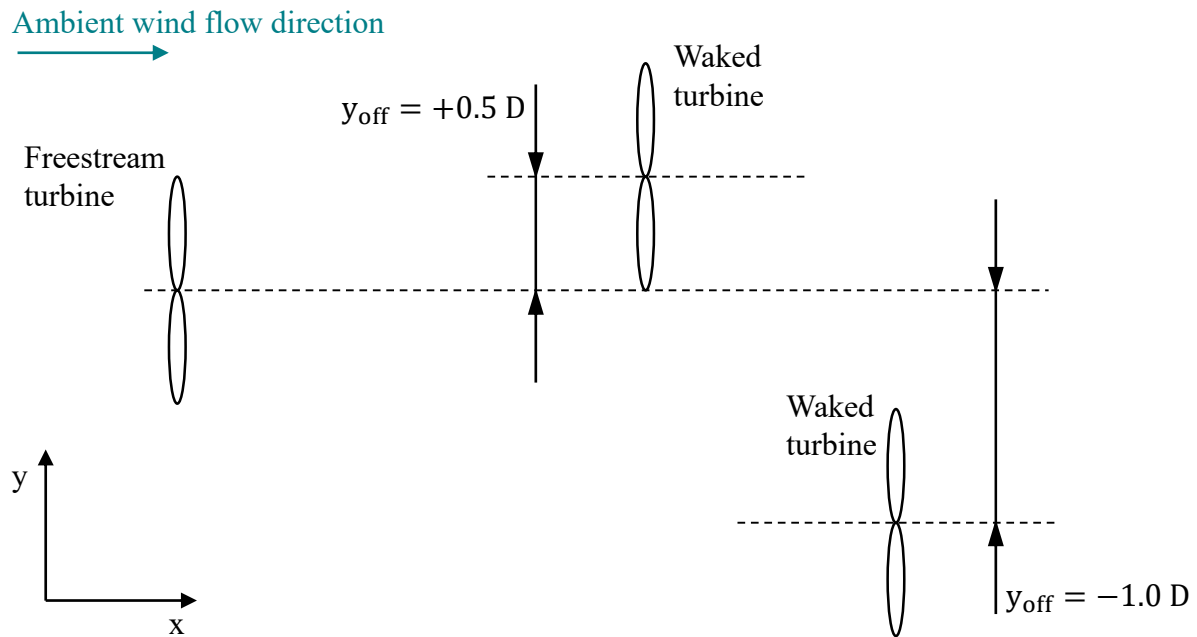


Figure 5.17: Turbine positioning for the investigation of the waked turbine's response with respect to changing wake conditions. The offset in the lateral direction of the waked turbine with respect to the first turbine is set as y_{off} in turbine diameters D .

5.5 Structural loads of a waked turbine during yawed operation

The wake redirection control strategy for wind farms requires usually to not only operate the free-stream turbines with yaw misalignment, but also the turbines that experience wake conditions from upstream located turbines. Therefore, an investigation of the structural loads of a waked turbine is performed, which is operated under yaw misalignment and subjected to different wake scenarios. The aim is to determine if the resulting load distributions are different from the load distributions of a free-stream turbine (analysed in Section 5.3). In addition, the sensitivity of the effects on the structural loads from changing wake locations is examined which could be a result of a redirected wake from an upstream located turbine under yawed operation.

5.5.1 Load case definition and simulation setup

A configuration of two NREL 5 MW turbines is set up in the simulation tool FAST.Farm. Their relative positioning is varied in the longitudinal direction by the offset x_{off} (turbine spacing) and in the lateral direction by the offset y_{off} as shown in Figure 5.17. The simulations are performed based on the measured environmental conditions (described in Section 5.2.2) in order to use realistic combinations of the wind speed, TI as well as vertical wind shear and to limit the amount of simulations instead of permuting all the variables. For each operating condition, two simulations with different wind field realisations and a length of 30 min are

Table 5.4: Definition of operating conditions for the investigation of yawed operation in wake conditions. The notation $[a : q : b]$ is used, hence a parameter is varied within the bounds a and b with steps of q .

Parameter	Value
Wind speed at hub height [m/s]	[5 : 1 : 11]
Longitudinal turbine spacing x_{off} [D]	[5, 7, 9]
Lateral turbine spacing y_{off} [D]	[-1.25 : 0.25 : 1.25]
Yaw misalignment angle of the 2 nd turbine $\theta_{m,T2}$ [$^{\circ}$]	[-30 : 5 : 30]

conducted. The yaw misalignment angle of the second turbine $\theta_{m,T2}$ is varied from -30° to 30° . The upstream turbine operates with zero yaw misalignment and it is assumed that the wake effects from this turbine are similar to the wake effects from a turbine that operates with yaw misalignment. A summary of the operating conditions is provided in Table 5.4 which results in ≈ 18000 simulations.

5.5.2 Structural load distributions at component level

Distributions of the structural loads with respect to changing yaw misalignment angles at different locations of the wind turbine are evaluated. Besides the changing environmental conditions, the inflow conditions are modified by the wake of an upstream turbine. The results are exemplarily displayed for a free-stream wind speed of 7 m s^{-1} and a longitudinal turbine spacing of $x_{off} = 7 D$ in the Figures 5.18-5.22; in each plot, the results from unstable and stable atmospheric conditions are directly compared. Complementary results for additional operating conditions are provided in the Appendix A.5. All results are normalised with respect to the value of the free-stream turbine at zero yaw misalignment, which is plotted to enable a direct comparison.

The mean value of the generator power is plotted for changing yaw misalignment angles and wake centre locations indicated by the lateral offset value y_{off} in Figure 5.18. It is obvious that the power production becomes lower with increasing wake portions overlapping the rotor; it is lowest for a full wake scenario ($y_{off} = 0 D$). In contrast, at lateral wake centre offset positions of $\pm 1.25 D$, the power loss due to the wind speed deficit from the upstream turbine becomes less than 3% compared to free-stream conditions. The relative power loss with regard to yaw misalignment is on a similar level for all wake scenarios (differences of less than 3%). The difference between unstable and stable AS is highest for the full-wake scenario. Here, the power loss is $\approx 51\%$ in unstable AS, while it is $\approx 54\%$ in stable AS due to less wake recovery. With decreasing wake overlapping, the differences between unstable and stable AS become lower.

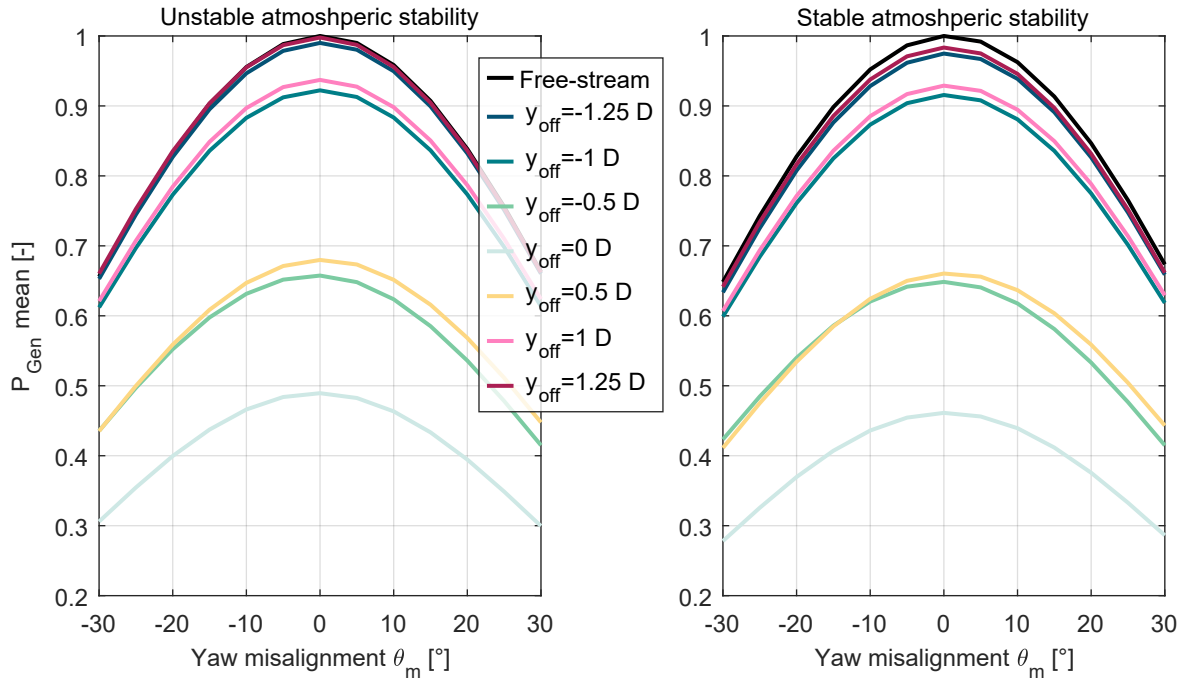


Figure 5.18: Distributions of the generator power from the waked turbine. The free-stream wind speed is 7 m s^{-1} and the turbine spacing distance in the longitudinal direction is $7D$. Results are shown by means of the seed average and normalised with the values at $\theta_m = 0^\circ$ of the upstream located turbine.

The load distributions of the total bending moment at the blade-root are shown in Figure 5.19. The trends seen in the free-stream conditions are also visible for the different wake scenarios: Higher loads are caused by negative yaw misalignment angles, while the loads are reduced with increasing yaw misalignment angles for the majority of lateral wake offset conditions. It is observed that the loads tend to be higher for negative lateral wake offsets compared to free-stream conditions, whereas they become lower for positive lateral wake offset conditions. This can be explained by the interaction of the gravitational force and the aerodynamic tangential force acting on the blades. Their resulting force causes higher load amplitudes in the case of negative lateral wake offset, in which the wake overlaps the region of the rotor where the blades move upward (also discussed in [149]). In stable atmospheric conditions, vertical wind shear plays a significant role and it is observed that the loads are increased to a lower extent due to different wake conditions compared to unstable AS. One could even define a sweet spot at a lateral wake offset $y_{off} = 0.5D$, where the blade loads are considerably reduced compared to the other wake conditions.

In Figure 5.20, results from the fatigue loads of the torsional moment at the LSS are plotted. It is found that the loads tend to be higher in predominantly partial wake situations as it is the case for lateral wake offsets of $y_{off} = \pm 0.5D$. The sensitivity with regard to yaw misalignment depends on the wake situation: For positive lateral wake offsets, the load maximum tends to

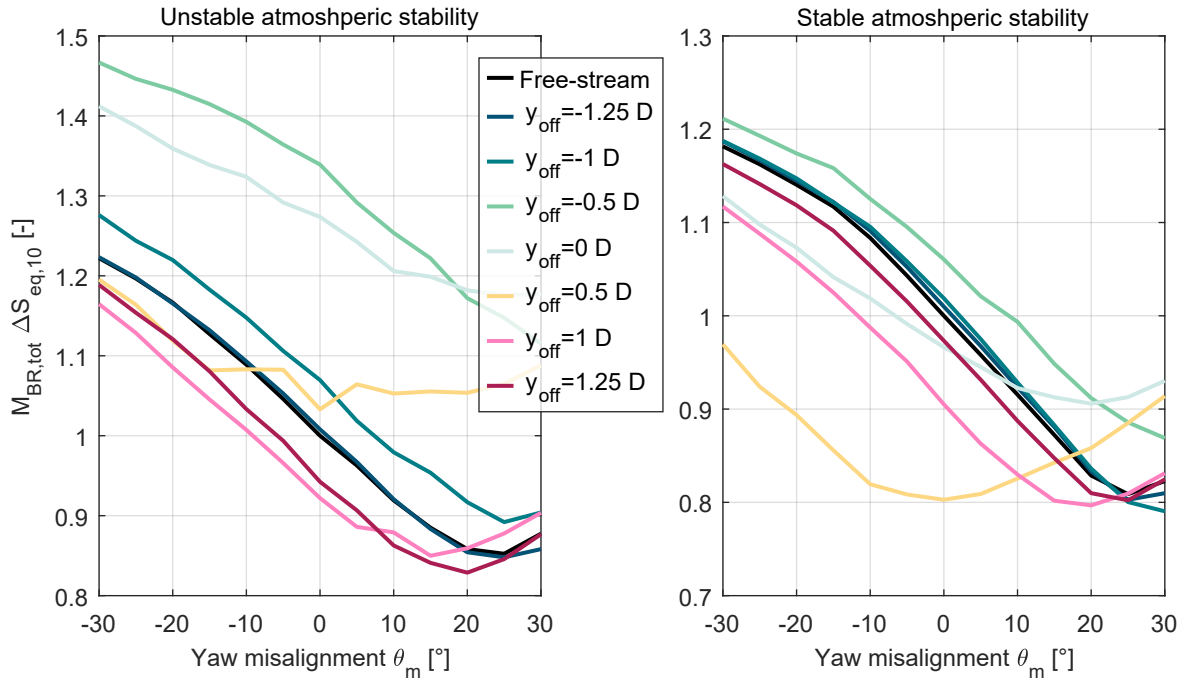


Figure 5.19: Load distributions of the total bending moment at the blade-root from the waked turbine. The free-stream wind speed is 7 m s^{-1} and the turbine spacing distance in the longitudinal direction is $7D$. Results are shown by means of the seed average and normalised with the values at $\theta_m = 0^\circ$ of the upstream located turbine.

occur at negative yaw misalignment angles, while for negative lateral wake offsets, the load maximum is found to be at positive yaw misalignment angles. Hereby, load maxima occur at greater yaw misalignment angles in unstable conditions, whereas they appear close to zero yaw misalignment in stable AS. Note that a considerable scatter range of the results is seen for this sensor especially in unstable conditions, which is dependent on the wind field realisation and turbine location within the wind field.

The loads at the tower top (Figure 5.21) and the tower base (Figure 5.22) in terms of the DEL of the total bending moment are mainly driven by the wake condition; the dependency on the yaw misalignment angle is less pronounced. In addition, significant differences between the considered atmospheric stabilities are found. At the tower top for stable AS, the loads are increased by up to a factor of 5 for zero yaw misalignment compared to free-stream conditions; in unstable AS, the increase in loads for zero yaw misalignment is less (factor 3). At the tower base, the increase in loads is less significant with factor 3 in stable AS and factor 2 in unstable AS. The influence of yaw misalignment on the loads is dependent on the wake condition and the AS. Overall, the wake's effects on the loads become most substantial for lateral wake offsets between $y_{off} = -0.75 D$ and $y_{off} = +0.75 D$.

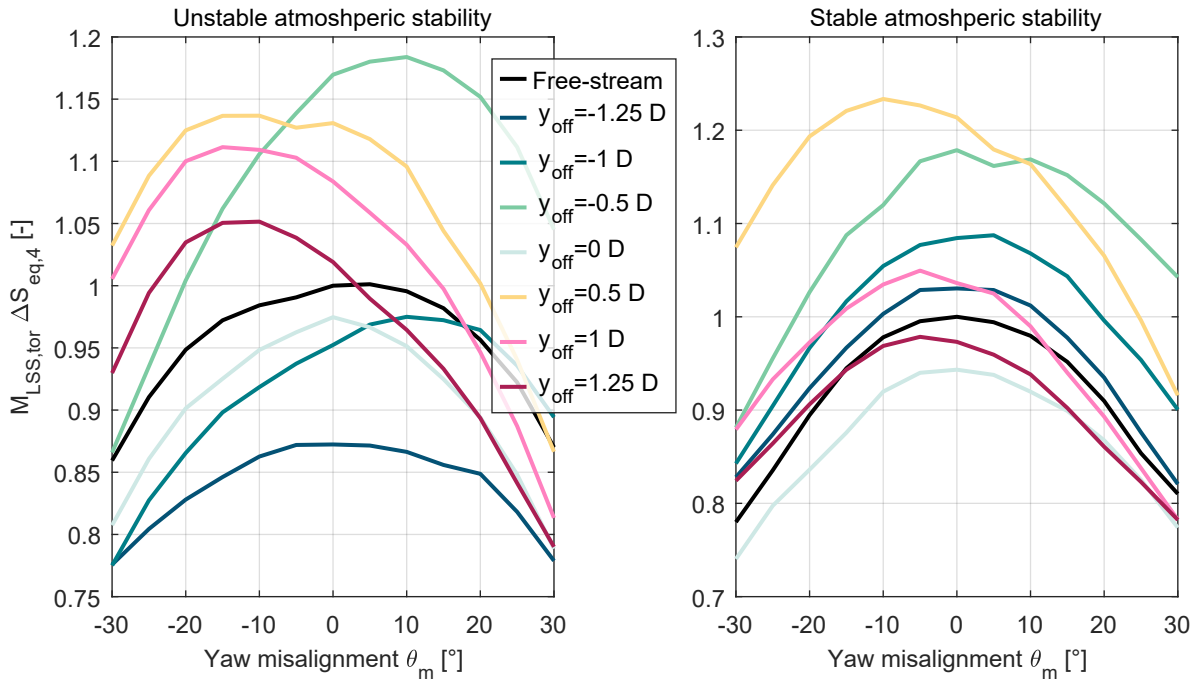


Figure 5.20: Load distributions of the torsional moment at the low-speed shaft from the waked turbine. The free-stream wind speed is 7 m s^{-1} and the turbine spacing distance in the longitudinal direction is $7D$. Results are shown by means of the seed average and normalised with the values at $\theta_m = 0^\circ$ of the upstream located turbine.

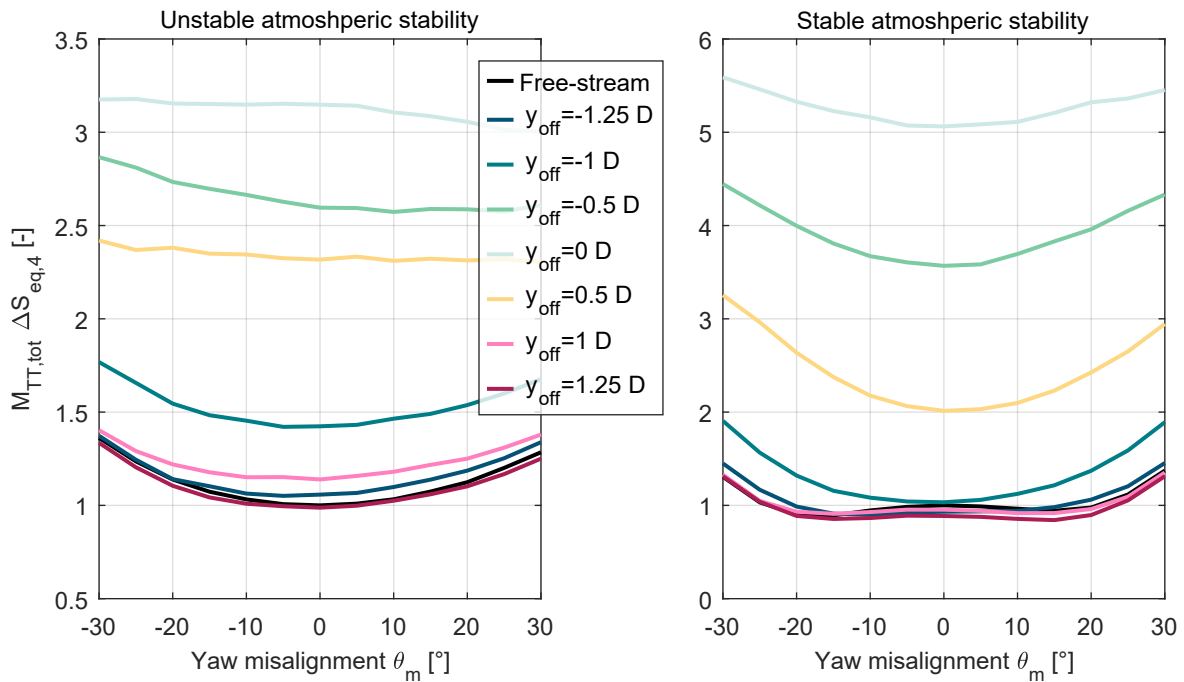


Figure 5.21: Load distributions of the total bending moment at the tower-top from the waked turbine. The free-stream wind speed is 7 m s^{-1} and the turbine spacing distance in the longitudinal direction is $7D$. Results are shown by means of the seed average and normalised with the values at $\theta_m = 0^\circ$ of the upstream located turbine.

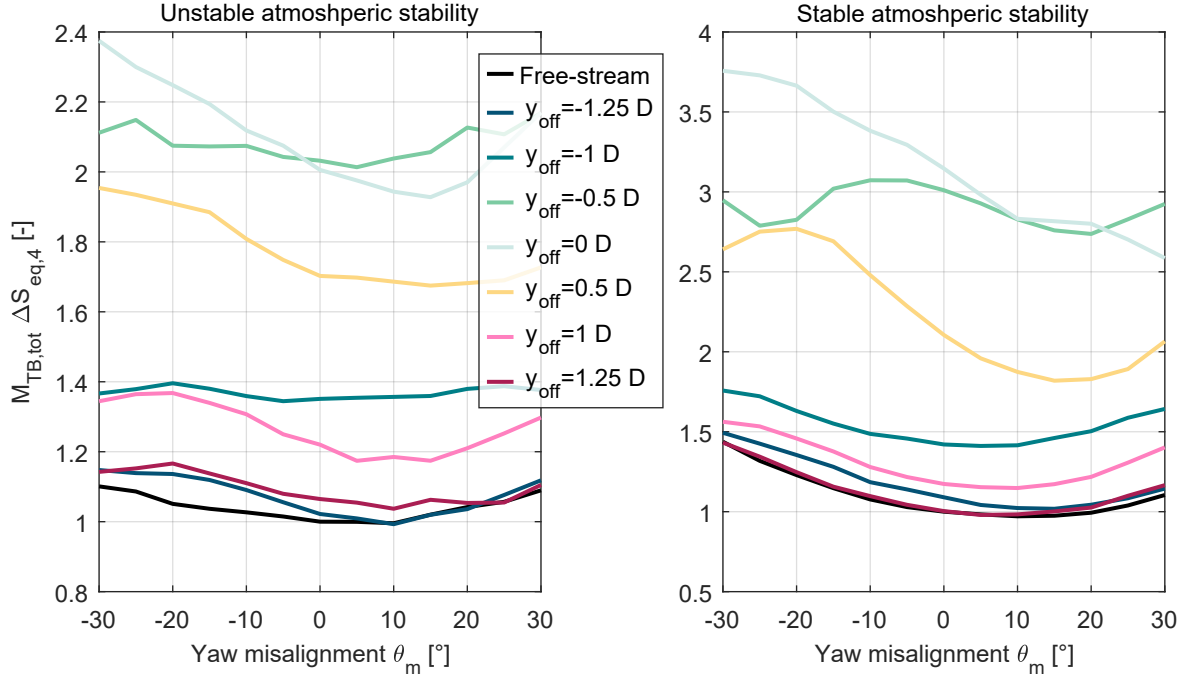


Figure 5.22: Load distributions of the total bending moment at the tower-base from the waked turbine. The free-stream wind speed is 7 m s^{-1} and the turbine spacing distance in the longitudinal direction is $7D$. Results are shown by means of the seed average and normalised with the values at $\theta_m = 0^\circ$ of the upstream located turbine.

5.5.3 Conclusions

The sensitivity of the load distributions at different locations on yaw misalignment is investigated in combination with varying wake scenarios. The results from changing wake conditions are compared with the load distributions in free-stream conditions. The loads are a complex function of the environmental conditions, yaw misalignment angle and wake condition; the main dependencies are summarised in the following:

- For the same environmental conditions, the loads depend on the yaw misalignment angle and wake scenario. Especially for lateral wake offsets between $y_{off} = -0.75D$ and $y_{off} = 0.75D$ (partial wake situations), the load distributions with respect to yaw misalignment differ significantly from free-stream conditions. On the one hand, this is caused by the wake directly, which increases the TI in the wake and leads to alternating loads in the rotating system due to partial overlapping with the rotor. In addition, the operating point of the waked turbine is changed because of the wind speed deficit in the wake, which also results in variations of the load distributions. With increasing lateral wake offsets $y_{off} > |0.75D|$, the load distributions are less influenced by the wake and become more similar to the load distributions in free-stream conditions.
- The gradients of the structural loads with respect to the lateral wake offset are high for

wake offset locations between $y_{off} = -0.75 D$ and $y_{off} = 0.75 D$. In this region, a wake redirection control strategy is likely to be more efficient for load balancing.

- The general characteristics of the load distributions are similar for changing environmental conditions. Different environmental conditions lead normally to varying load magnitudes and shifted load maxima with respect to the yaw misalignment. Vertical wind shear has a significant influence on the load distributions, especially when combined with partial wake scenarios.
- A directional dependency of the loads is found with respect to the lateral wake offset: The loads tend to be higher for negative lateral wake offsets compared to the loads from the same positive lateral wake offsets.

6

Optimisation of wind farm operation

For a concept demonstration, reference wind farm configurations are optimised based on different objectives that include the maximisation of the power output and the management of fatigue loads. The focus is the wake-redirection control concept which is applied to achieve the defined objectives; other control methods (e.g. axial induction control) are not considered. The load cases including the definition of different wind farm configurations are introduced in Section 6.1. The yaw angles of the turbines are then optimised in Section 6.2 by using the low-order flow model FLORIS that is augmented with a surrogate model for the fatigue loads in the optimisation procedure. The optimisation results are reassessed in Section 6.3 by using aeroelastic simulations; the long-term effects on both power and loads are investigated and detailed analyses of specific operating points are performed.

6.1 Load case definition

A three-turbine and a five-turbine configuration are set up with NREL 5 MW turbines. A summary of the operating conditions is provided in Table 6.1. The longitudinal spacing of the turbines is controlled by the parameter x_{off} for the three-turbine case. Changes in the wind direction are covered by the lateral offset parameter y_{off} ; the turbines are placed in line when $y_{off} = 0$ (see also Figure 5.17 for visualisation).

The simulations are performed based on the measured environmental conditions at FINO1 (described in Section 5.2.2) to provide a realistic joint probability of the wind speed, TI as well as vertical wind shear and to limit the number of simulations. For the assessment of the optimisation results with aeroelastic simulations in FAST.Farm (Section 6.3), two simulations

Table 6.1: Definition of operating conditions for assessing the optimised wind farm operation. The notation $[a : q : b]$ is used, hence a parameter is varied within the bounds a and b with steps of q . For a visualisation of the layout-parameters, see Figure 5.17.

Parameter	Value	
Wind farm setup	3 turbines	5 turbines
Wind speed at hub height [m/s]	[5 : 1 : 10]	
Longitudinal turbine spacing x_{off} [D]	[5, 7, 9]	7
Lateral turbine spacing y_{off} [D]	[-1.25 : 0.25 : 1.25]	
Atmospheric stability	[unstable, neutral, stable] (see Section 5.2 for the definition)	

with different wind field realisations with a length of 30 min are conducted for each operating condition. The focus is on the below-rated conditions because the effects from wake-redirecting control are expected to be more significant compared to above-rated conditions. Furthermore, the wake-deflection correction model in FAST.Farm has not been calibrated for above-rated wind speeds.

6.2 Optimisation of yaw angles

The optimisation of yaw angles is performed with the tool FLORIS together with a SLSQP algorithm embedded in the Python-scipy library in version 1.7.1 [143]. The resulting yaw angles from this steady state optimisation are then applied in the aeroelastic simulations in FAST.Farm in Section 6.3. The model parameters of FLORIS are calibrated in Section 4.4 with respect to reference results from FAST.Farm to improve the model fidelity. In addition, FLORIS is paired with a surrogate model representing the structural loading of the turbines. Hence, the optimisation with objectives associated with the structural loading of the turbines can be conducted.

6.2.1 Surrogate model for the structural loads

For the optimisation of the operation strategies that take into account the structural loading, an adequate representation of the structural loads at each turbine is required. Since the structural loads are a complex function of the operating conditions and detailed aeroelastic simulations for each operating condition are computationally expensive, the application of computationally efficient surrogate models offers a solution, e.g. [150, 151]. With this load mapping functions, one can estimate the load variation at a turbine in a wind farm based on the operating conditions in a fast and efficient manner. Different methods can be applied in order to derive the

Table 6.2: Dimensions of the look-up table defining the load surrogate model. The notation $[a : q : b]$ is used, hence a parameter is varied within the bounds a and b with steps of q . For a visualisation of the layout-parameters, see Figure 5.17.

Parameter	Value
Wind speed at hub height [m/s]	[5 : 1 : 11]
Longitudinal turbine spacing x_{off} [D]	[5, 7, 9]
Lateral turbine spacing y_{off} [D]	[-1.25 : 0.25 : 1.25]
Yaw misalignment angle of the waked turbine $\theta_{m,Twake}$ [$^{\circ}$]	[-30 : 5 : 30]
Atmospheric stability	[unstable, neutral, stable] (see Section 5.2 for the definition)

load mapping function, which include for instance nearest-neighbour interpolation, polynomial chaos expansion, universal Kriging or quadratic response surface [150]. The surrogate model is typically conditioned by means of a large database consisting of the results from aeroelastic simulations for various operating conditions.

In the present case, a surrogate model for the turbine loads needs to cover the operating conditions defined in Table 6.1. Consequently, a simplified load mapping function is implemented, which is essentially a look-up table based on the results from the aeroelastic simulations in Section 5.5. In particular, the look-up table has 5 dimensions that are described in Table 6.2. The surrogate model contains the information of the fatigue loads at the sensor locations provided in Table 5.2. The main assumption of this surrogate model is that only single wake effects from one upstream located turbine are considered. Hence, it is assumed that the wake-effects from further upstream located turbines are negligible because of their large longitudinal distance ($\geq 10D$ in this study) to the turbine, for which the loads are calculated. In addition, for the optimisation of operation strategies, only relative values of the loads with respect to a reference value (e.g. in free-stream conditions) are required. The load mapping function interpolates in this multi-dimensional look-up table linearly and maps the DEL of the desired component according to the given inflow conditions as described in Figure 6.1.

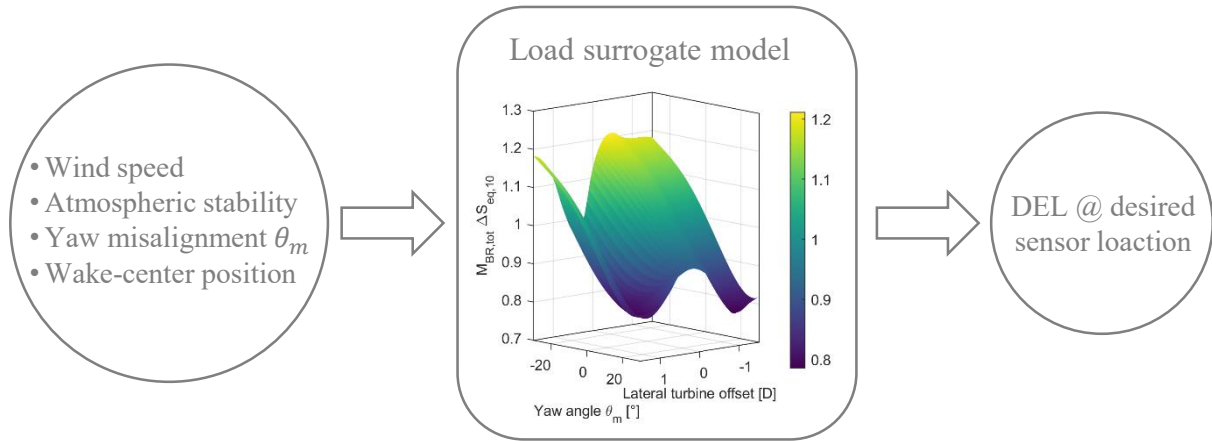


Figure 6.1: Process of calculating the fatigue load at a desired sensor location based on varying operational conditions using the load surrogate model.

6.2.2 Cost functions for different objectives

In total, five different operation strategies are defined which are summarised in Table 6.3. The strategy 0 is the reference scenario that implies no collective control of the wind turbines, thus the yaw misalignment angles of all turbines remain zero. Pure maximisation of the collective wind farm power output through wake-redirection control is achieved with strategy A. For the optimisation, the values of the power output are normalised by the values from strategy 0. Note that all objective functions are formulated as minimisation problems and the limits of the yaw angles within the optimisation are set to $\pm 30^\circ$; the yaw angle of the last turbine in the stream wise direction is limited to $\pm 3^\circ$, because there is no effect on a further downstream located turbine.

In strategy B, the cost function of strategy A is extended by the inclusion of the turbine loads at five different locations that need to be minimised ($M_{BR,tot}$, $M_{LSS,tot}$, $M_{TT,tot}$, $M_{TT,yaw}$, $M_{TB,tot}$). The loads are normalised by the value from strategy 0 at each turbine correspondingly in order to be used in the same cost function as the power. The formulation of the cost function for strategy C is similar to strategy B, but it applies a weighting factor of three to the loads. The weighting factor serves the purpose of assigning a higher priority to the loads but its value is chosen arbitrarily. In Strategy D, the aim is to maximise the collective power output of all turbines, while only the fatigue loads at the blade-root of all turbines are minimised.

Table 6.3: Definition of the optimisation functions for the wind farm operation strategies. P_i is the power of the turbine i . L_i^k refers to the load k ($k = M_{BR,tot}, M_{LSS,tot}, M_{TT,tot}, M_{TT,yaw}, M_{TB,tot}$) of the turbine i . The values of P and L are normalised by the values from the strategy 0 (no wind farm control).

Strategy	Description	Objective function	Constraints
0	No wind farm control	-	$\theta_m^i = 0^\circ$
A	Power maximisation	$\operatorname{argmin}_{\theta_m^i} \sum_i -P_i$	$\theta_m^{1..N_t-1} \in -30^\circ, 30^\circ $ $\theta_m^{N_t} \in -3^\circ, 3^\circ $
B	Power maximisation and fatigue load minimisation	$\operatorname{argmin}_{\theta_m^i} \sum_i \left(-P_i + \sum_k L_i^k \right)$	$\theta_m^{1..N_t-1} \in -30^\circ, 30^\circ $ $\theta_m^{N_t} \in -3^\circ, 3^\circ $
C	Power maximisation and fatigue load minimisation weighted with factor 3	$\operatorname{argmin}_{\theta_m^i} \sum_i \left(-P_i + 3 \sum_k L_i^k \right)$	$\theta_m^{1..N_t-1} \in -30^\circ, 30^\circ $ $\theta_m^{N_t} \in -3^\circ, 3^\circ $
D	Power maximisation and minimisation of the fatigue loads at the blade-root weighted with factor 3	$\operatorname{argmin}_{\theta_m^i} \sum_i \left(-P_i + 3 L_i^{M_{BR,tot}} \right)$	$\theta_m^{1..N_t-1} \in -30^\circ, 30^\circ $ $\theta_m^{N_t} \in -3^\circ, 3^\circ $

6.3 Assessment of wind farm operation strategies

The results from the optimisation of the operation strategies with different objective functions are assessed with aeroelastic simulations in FAST.Farm. Consequently, the yaw angle of the turbines is set based on the optimisation results; it is kept constant for the entire simulation, hence there is no dynamic change of the nacelle orientation. The simulations are performed following the definition of the operating conditions in Table 6.1. A long-term evaluation is conducted in Section 6.3.1 where the results from different operating conditions are condensed into an aggregated quantity such as the long-term DEL or the AEP. For specific cases, a more detailed analysis is provided in Section 6.3.2, which shows the dependencies of the structural loads on the wind direction.

6.3.1 Long-term evaluation

The different operation strategies optimised in Section 6.2 are evaluated by calculating the aggregated results in terms of the AEP and the long-term DELs at different locations of the wind turbines. The AEP is computed in a simplified version following the formula:

$$AEP = \sum_i \sum_j w_{WS,i} w_{WD,j} \bar{P}_{farm}, \quad (6.1)$$

where the index i indicates the simulated wind speeds ($4-10 \text{ m s}^{-1}$) and the weighting factor $w_{WS,i}$ is based on the Weibull distribution given in Figure 5.2. The index j refers to the simulated lateral turbine spacings y_{off} (equivalent to the wind direction) and the corresponding weighting factor $w_{WD,j}$ is set to unity in order to weight the different wind directions equally. The variable \bar{P}_{farm} gives the mean value of the combined power production of all turbines over the simulation length for an operating condition. The calculation of the long-term DEL is based on Equation 2.19 and uses the same weighting factors as introduced for the AEP calculation. Additionally, the mean value of the TI at the rotor centre is calculated in the same way as the AEP, but both weighting factors are set to unity.

The results from the three-turbine scenario with a longitudinal spacing of the turbines of $x_{off} = 7D$ are shown in Figure 6.2. All results are normalised by the results from strategy 0 and for each turbine respectively. The analysis of the power production (Figure 6.2 (a)) shows that the highest AEP is achieved with strategy A ($\approx 2\%$ higher compared to Strategy 0), in which only the power is maximised without considering the structural loads. Slightly less AEP is possible with strategy B, in which the loads are taken into account equally weighted as the turbine's power. The strategies C and D produce significantly less AEP compared to strategy 0. The AEP with strategy C is $\approx 5\%$ less. The AEP results from strategy D are highly sensitive to the atmospheric stability (4% less AEP in unstable AS and 13% less in stable AS compared

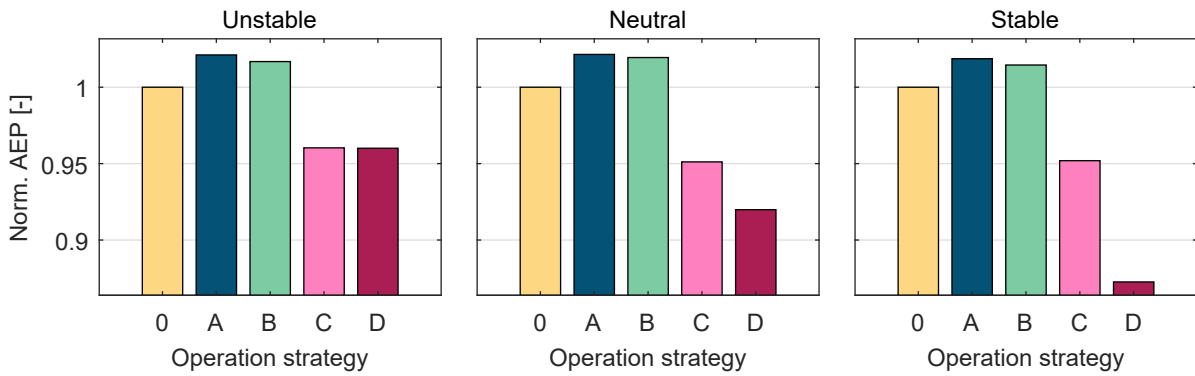
to strategy 0), while the power production with the other strategies is similar among the ASs.

The Figures 6.2 (b)-(f) provide the aggregated results of the fatigue loads from various locations at the turbines. The loads at the blade-root tend to be higher (up to $\approx 8\%$ in unstable AS) when applying the strategies A and B, while they are mostly alleviated compared to strategy 0 when using the strategies C and D. Consequently, the loads at the blade-root can be related to the AEP and a higher AEP coincides with higher fatigue loads at the blade-root. Note that this analysis includes all wind directions equally; a more detailed analysis including the dependency of the results on the wind direction is provided in Section 6.3.2. With strategy D, the loads are significantly reduced by up to 25% at turbine 1 in stable atmospheric conditions, thus the results prove that the yaw angle optimisation works as it is intended by the cost function. The highest load reduction potential for the loads at the blade-root is identified in stable AS and can be related to the higher vertical wind shear compared to neutral and unstable conditions. The effects of the different strategies on the fatigue loads at the blade-root of turbine 3 are not as visible as for the other turbines due to the limitations of the yaw angle to $\pm 3^\circ$ in the optimisation. Hence, they are mainly influenced by the changing inflow conditions resulting from different wake-centre locations.

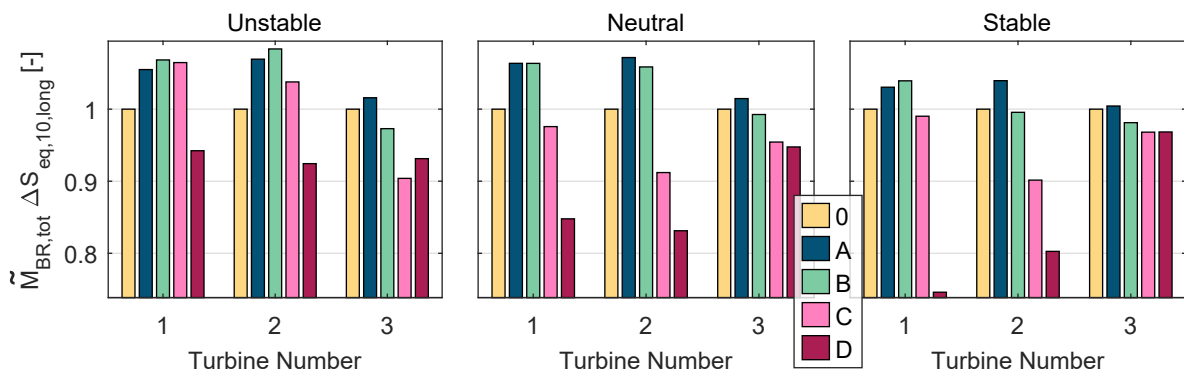
The DELs of the torsional moment at the LSS are mostly reduced when using the optimised strategies compared to the reference strategy 0. Only slight increases of the long-term DEL by up to 2.5% are seen for the strategies A and B. The highest reduction of the fatigue loads is observed by $\approx 34\%$ at turbine 1 in stable AS when using strategy D. The reduction of the fatigue loads at this location is mainly driven by the applied yaw-misalignment at the turbine itself, which is discussed in the Sections 5.3 and 5.5.

The yaw-misalignment of the rotor leads to higher fatigue loads for the yawing moment at the tower-top. This can be seen from the results of the free-stream turbine 1 in Figure 6.2 (d). Most notably in stable conditions implying strong vertical wind shear, the loads are increased by up to 16% when using strategy D compared to strategy 0. An analysis is performed, in which the yawing loads at the tower top are correlated with the loads at the blade-root and in which the results from Section 5.3 are taken into account. It is found that the fatigue loads at the blade-root (total bending moment) are alleviated more with higher yaw-misalignment angles especially in conditions with strong vertical wind shear and low TI . In contrast, in these conditions, the yawing fatigue loads at the tower top are increased with higher yaw-misalignment angles.

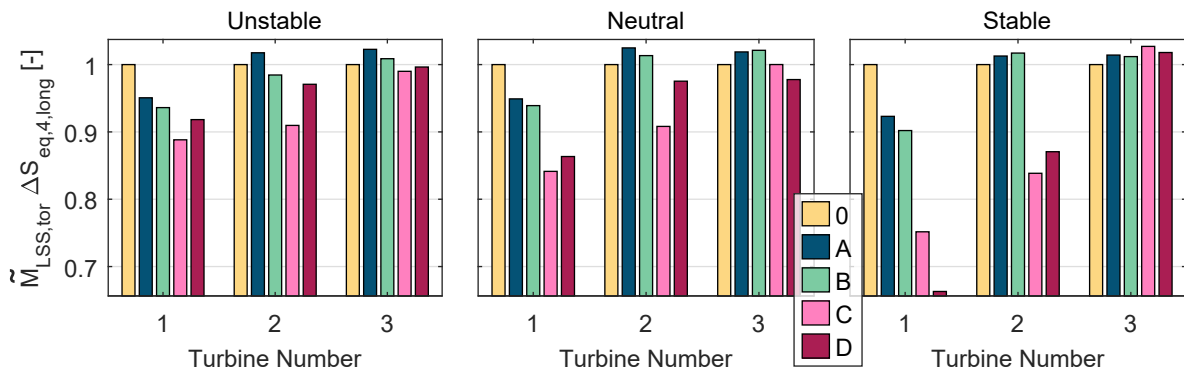
The analysis of the DELs of the total bending moment at the tower-top shows mostly load reductions except at the turbine 1 in unstable conditions, where they are slightly increased by up to 2% (6.2 (e)). The load reduction potential at this location at the free-stream turbine depends on the AS and, especially, the vertical wind shear. In stable conditions, there is high load reduction potential, whereas in unstable conditions the loads are moderately increased. These findings agree with the observations made in the investigation in Section 5.3. For the



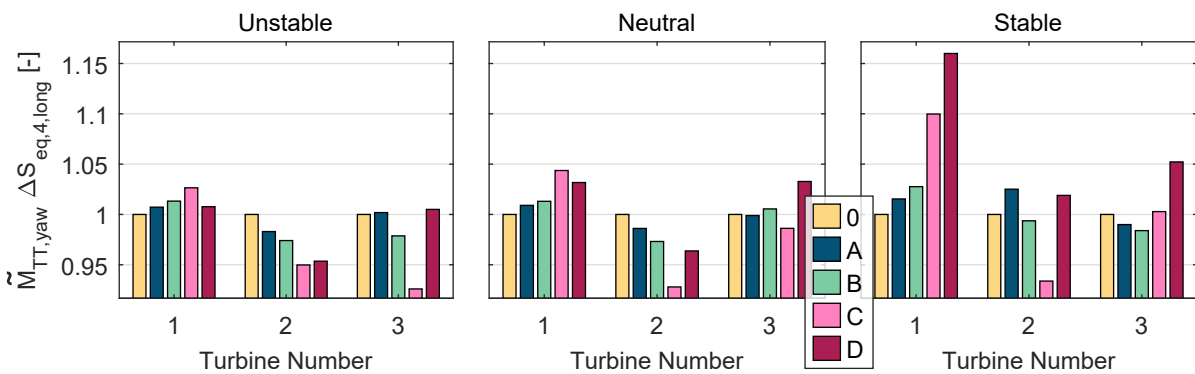
(a) Normalised AEP



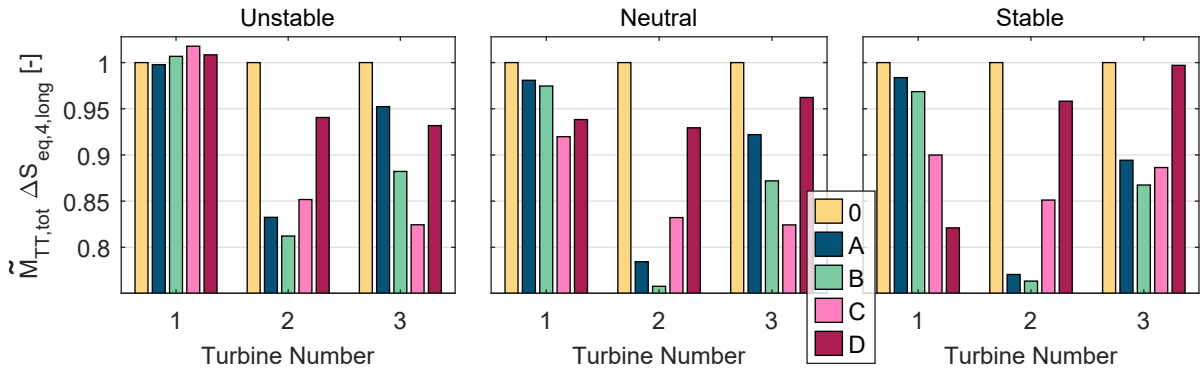
(b) Normalised total bending moment at the blade-root



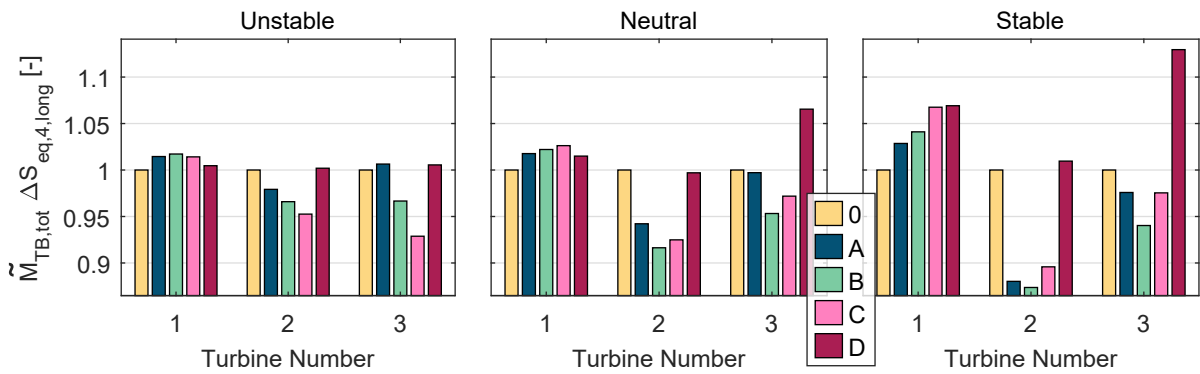
(c) Normalised torsional moment at the low-speed shaft



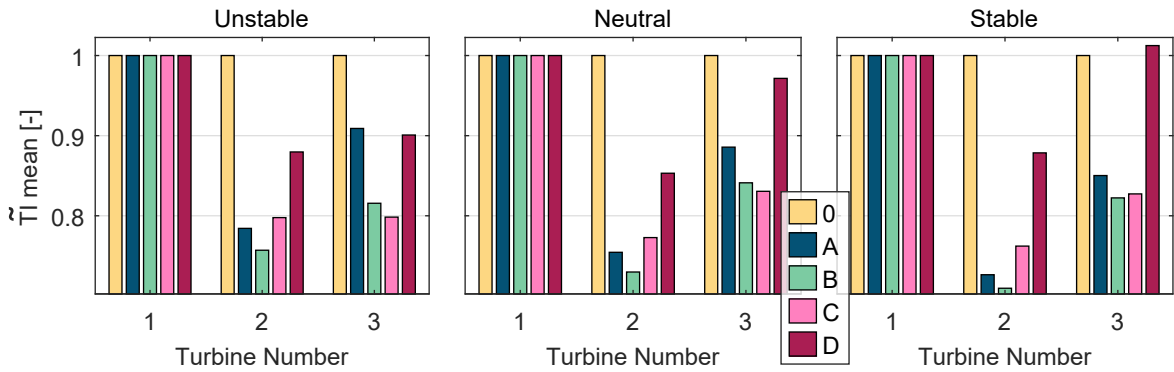
(d) Normalised yawing moment at the tower-top



(e) Normalised total bending moment at the tower-top



(f) Normalised total bending moment at the tower-base



(g) Normalised turbulence intensity (TI) at the rotor centre

Figure 6.2: Long-term evaluation of different operation strategies for the case of three turbines and longitudinal turbine spacing $x_{off} = 7D$. The results are normalised by the results from normal operation (zero yaw-misalignment) and at each turbine separately.

waked turbines, it is found that the fatigue loads at this location are highly correlated with the TI displayed in 6.2 (g). Note that the TI is measured at the rotor centre, hence it can be used as an indicator but it does not provide full details on the inflow conditions including the wake overlap for example.

In Figure 6.2 (f), the DELs of the total moment at the tower-base are plotted. Here, yaw-misalignment results in higher fatigue loads that are up to 2% higher compared to the baseline

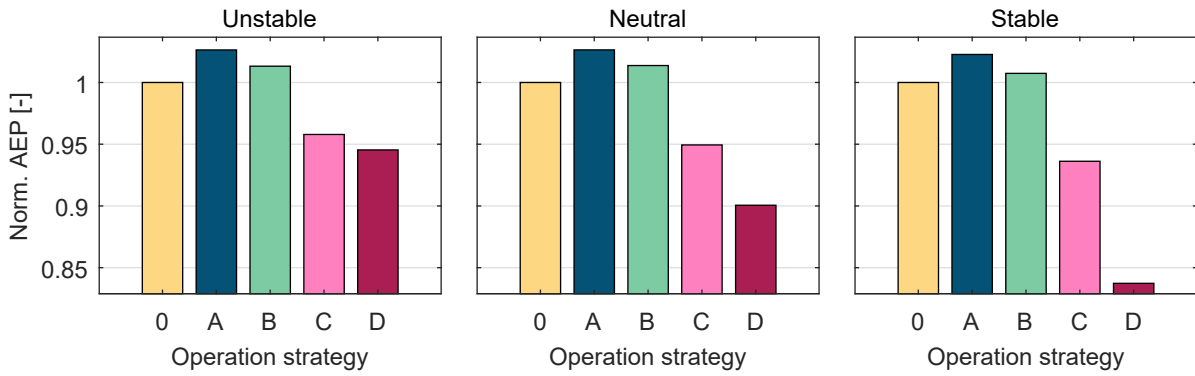
strategy 0 in unstable conditions and up to 7 percent higher in stable AS. These results are consistent with the findings made in Section 5.3; specifically in stable AS and low ambient TI , the fatigue loads are raised with increasing yaw-misalignment angles. As for the total bending moment at the tower-top, a high correlation between the fatigue loads at the tower-base and the TI at the rotor-centre is found. For the strategies A-C, the lower TI is associated with decreased loads compared to strategy 0. However, the loads are increased at the waked turbines when using strategy D (by up to 13% at turbine 3 in stable atmospheric conditions). Consequently, the load reductions at the blade-root are penalised by higher loads at the tower-base.

The results of the long-term analysis for the 5-turbine case are presented in Figure 6.3. Overall, the findings acquired from the 3-turbine case can be transferred to the 5-turbine case; the trends of the performance and load quantities are similar between the two farm configurations. For example, the AEP is higher using the strategies A and B than with the baseline strategy 0, while it is lower when the strategies C and D are used. Similarly to the 3-turbine case, the analysis of the loads can be divided into the free-stream turbine 1, the waked turbines 2-4 and the waked turbine 5, for which the yaw angles are limited to $\pm 3^\circ$. The transferability of the results from the 3-turbine case to the 5-turbine case indicates that the approach of using a surrogate model for the loads generated from single wake situations is applicable to more complex farm configurations with more than 3 turbines.

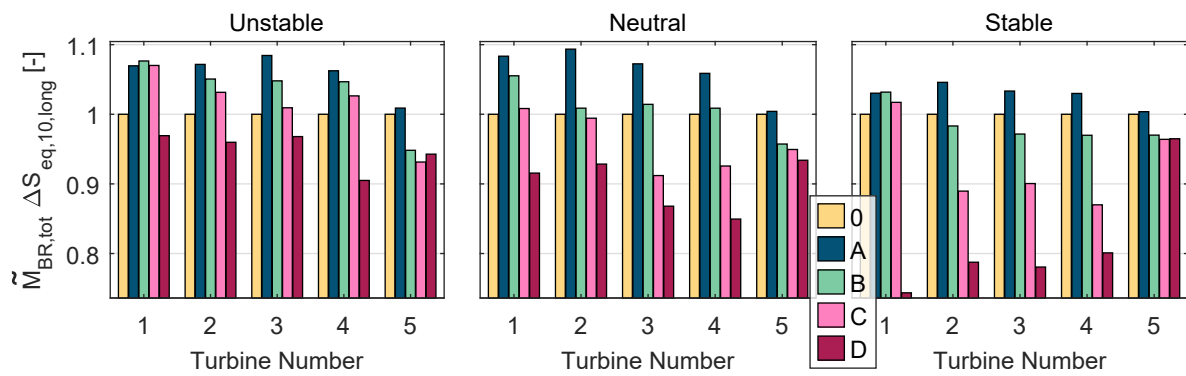
Additional results from other longitudinal turbine spacings are provided in the Appendix A.6. Overall, similar trends are seen for the different considered quantities across the varying turbine spacings. The most obvious discrepancies are found for the AEP: An increase of AEP can be achieved with strategy A by up to 3.5% compared to strategy 0 for a turbine spacing of 5D, while it reduces to 1% for a turbine spacing of 9D.

6.3.2 Detailed evaluation of specific operational points

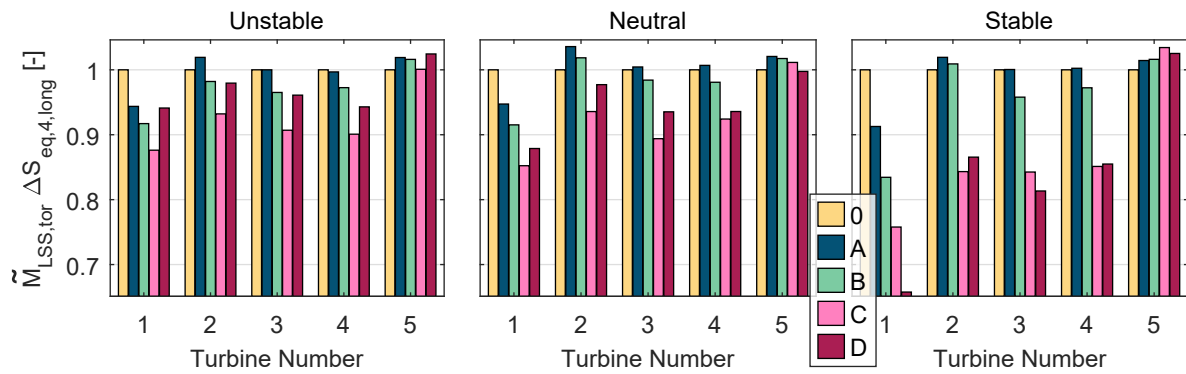
For specific operating conditions from the 3-turbine case, a more detailed analysis is conducted to provide background information for the long-term results in the previous section. In Figure 6.4, the combined power production of all three turbines is plotted against the lateral turbine offset (equivalent to the wind direction) for the different operation strategies. The mean free-stream wind speed is 6 m s^{-1} implying high thrust conditions. It can be observed that a potential increase in power using wake-redirection control is higher in setups where the turbines are closely spaced. In particular, with the strategy A designed for pure power maximisation, the farm power is increased by up to 28.5% compared to strategy 0 for a longitudinal spacing of $x_{off} = 5D$, while it is only increased by up to 13% for $x_{off} = 9D$. This can be explained with the recovery of the velocity deficit. In closely spaced turbine arrays, the velocity deficit is stronger when approaching the downstream turbines compared to widely spaced turbine arrays leading to higher potential power increase when the wakes are redirected.



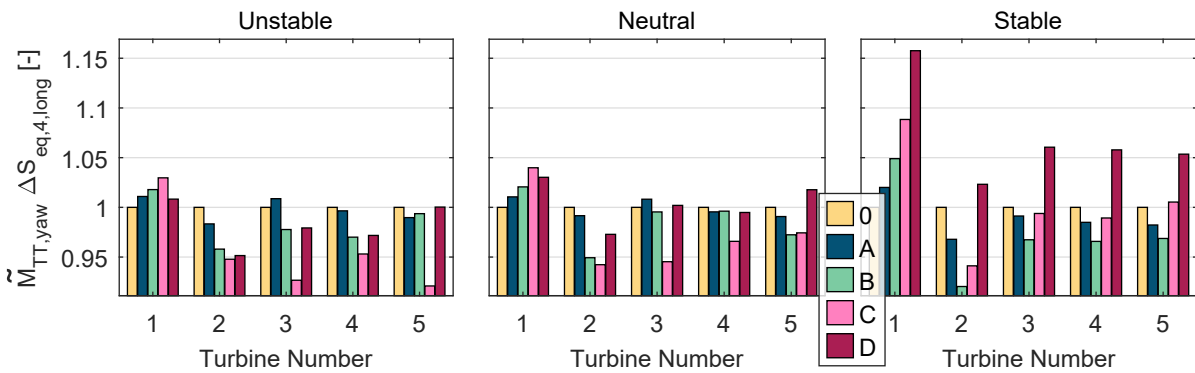
(a) Normalised AEP



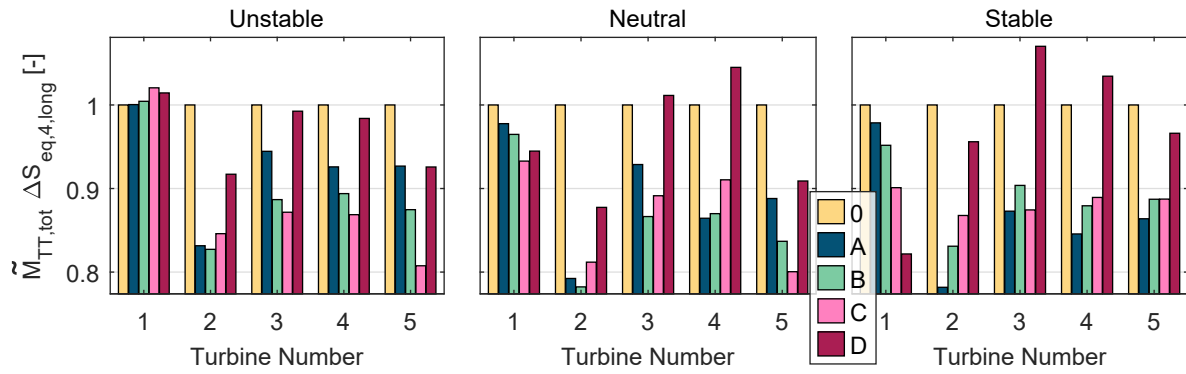
(b) Normalised total bending moment at the blade-root



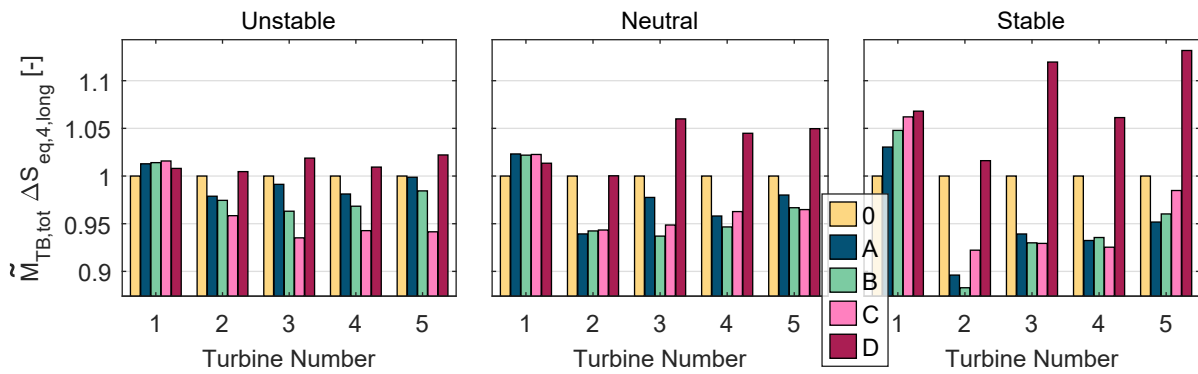
(c) Normalised torsional moment at the low-speed shaft



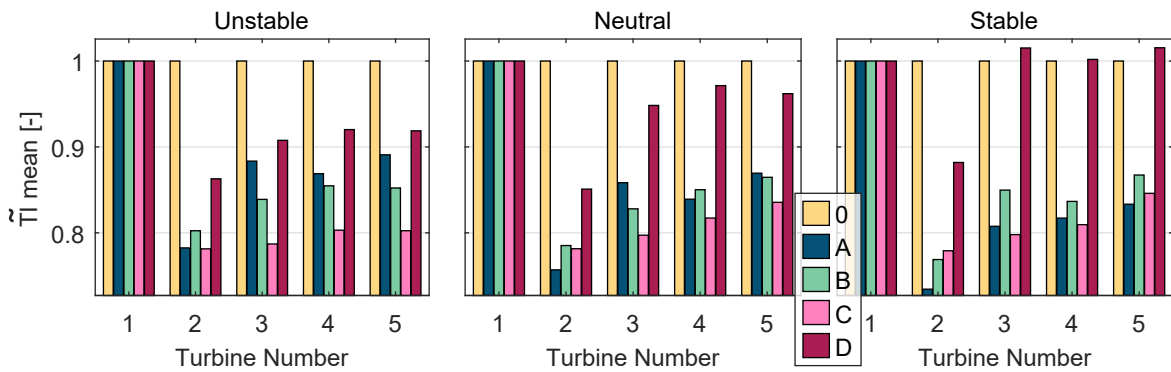
(d) Normalised yawing moment at the tower-top



(e) Normalised total bending moment at the tower-top

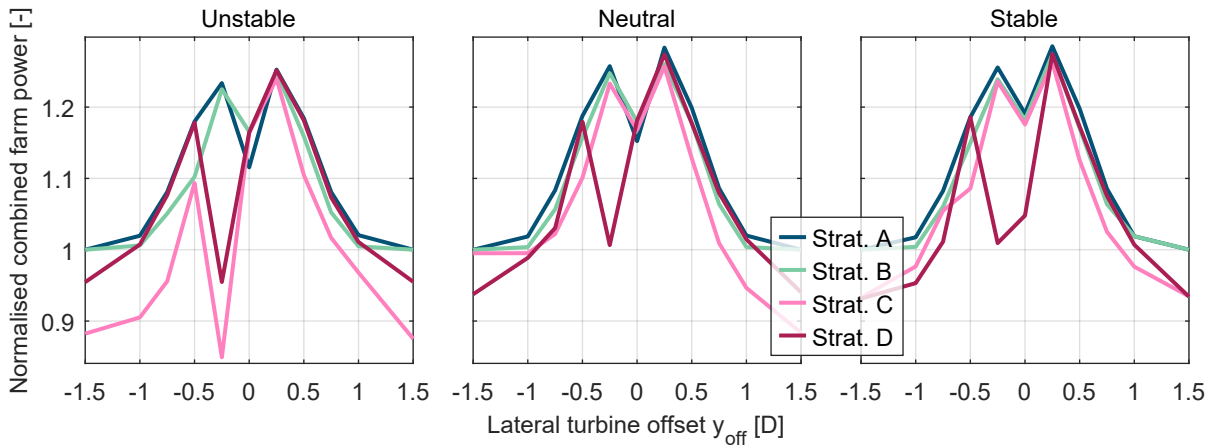


(f) Normalised total bending moment at the tower-base

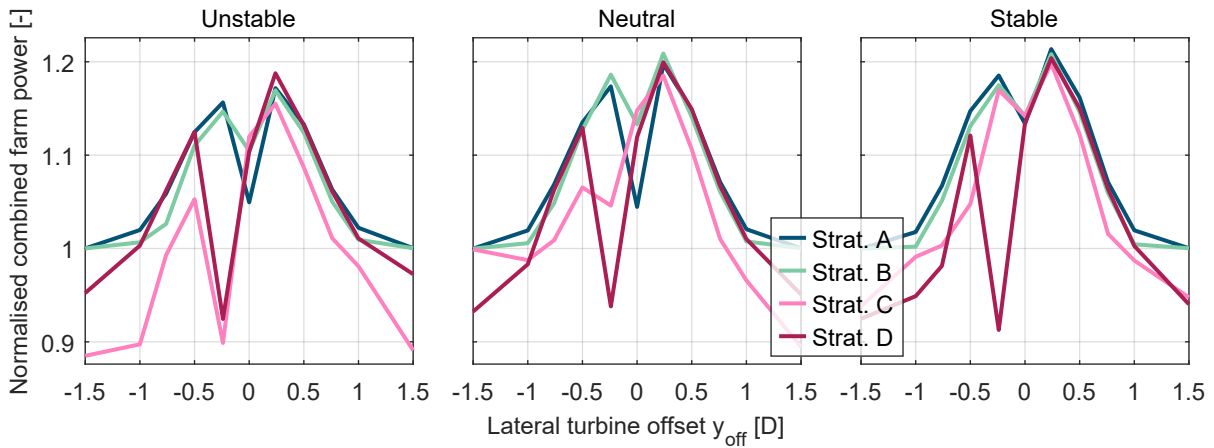


(g) Normalised turbulence intensity (TI) at the rotor centre

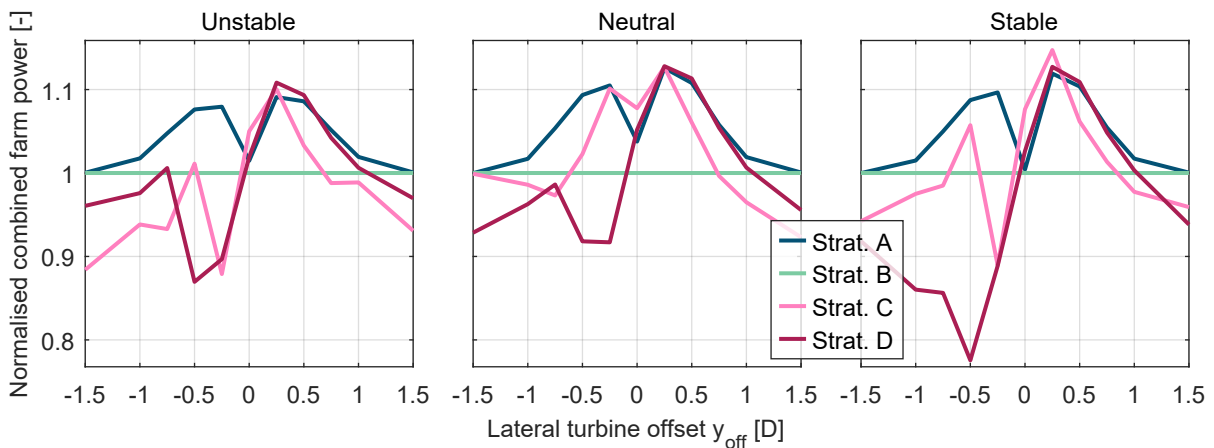
Figure 6.3: Long-term evaluation of different operation strategies for the case of five turbines and longitudinal turbine spacing $x_{off} = 7D$. The results are normalised by the results from normal operation (zero yaw-misalignment) and at each turbine separately.



(a) Longitudinal turbine spacing $x_{off} = 5 D$



(b) Longitudinal turbine spacing $x_{off} = 7 D$



(c) Longitudinal turbine spacing $x_{off} = 9 D$

Figure 6.4: Combined power output of the three turbines normalised by the results from normal operation (zero yaw-misalignment) for different longitudinal turbine spacings. The free-stream wind speed is 6 m s^{-1} .

When comparing the results from the different operation strategies, it is observed that they lead to similar increase in power for positive lateral turbine offsets. For negative lateral turbine offsets, larger discrepancies between the strategies are noticed. The strategies A and B lead to an increase in power. In contrast, a decrease in power can be found for certain lateral turbine offsets using the strategies C and D, because the loads higher have a higher weighting compared to the strategies A and B. At positive lateral turbine offsets, the wakes are redirected avoiding the downstream turbines by applying positive yaw misalignment angles (see Figure 6.7), for which the loads tend to be alleviated more compared to negative yaw misalignment angles (see Section 5.3).

Especially the fatigue loads at the blade-root can be alleviated with positive yaw misalignment of the rotor as can be seen in Figure 6.5. In addition, the fatigue loads of the displayed total bending moment at the blade-root are already reduced at the waked turbines due to the wake conditions at positive lateral turbine offsets as can be seen from the results of the baseline strategy 0 and as it is discussed in Section 5.5. Overall at positive lateral turbine offsets, all strategies lead to load reductions at the blade-root. Here, the load reduction potential is higher in stable atmospheric conditions compared to neutral and unstable AS. At negative lateral turbine offsets, the wakes are redirected past the downstream turbines by using negative yaw misalignment angles which result in increased loads at the blade-root. It is still possible to find yaw misalignment angles that reduce the loads at the blade-root as shown with strategy D, but with lower power production compared to the other strategies.

The consequences from the different operation strategies on the loads at the tower-base are displayed in Figure 6.6. It can be seen that all strategies decrease the fatigue loads at positive lateral turbine offsets in comparison to the baseline strategy 0. With negative lateral turbine offsets, the loads are increased at the free-stream turbine by up to 40% in stable atmospheric conditions due to yaw misalignment. At the waked turbines, effects from yaw misalignment and changing inflow conditions caused by redirected wakes from upstream turbines are added together. However, at turbine 3, the effects from changing wake conditions are dominant due to the limitation of the yaw misalignment angle to $\pm 3^\circ$ in the optimisation (see Figure 6.7). Consequently, an effective redirection of the wake can significantly reduce the loads at the tower-base from a waked turbine. This is more pronounced with the strategies B and C that effectively alleviate the loads at lateral turbine offsets $x_{off} > 0.5 D$.

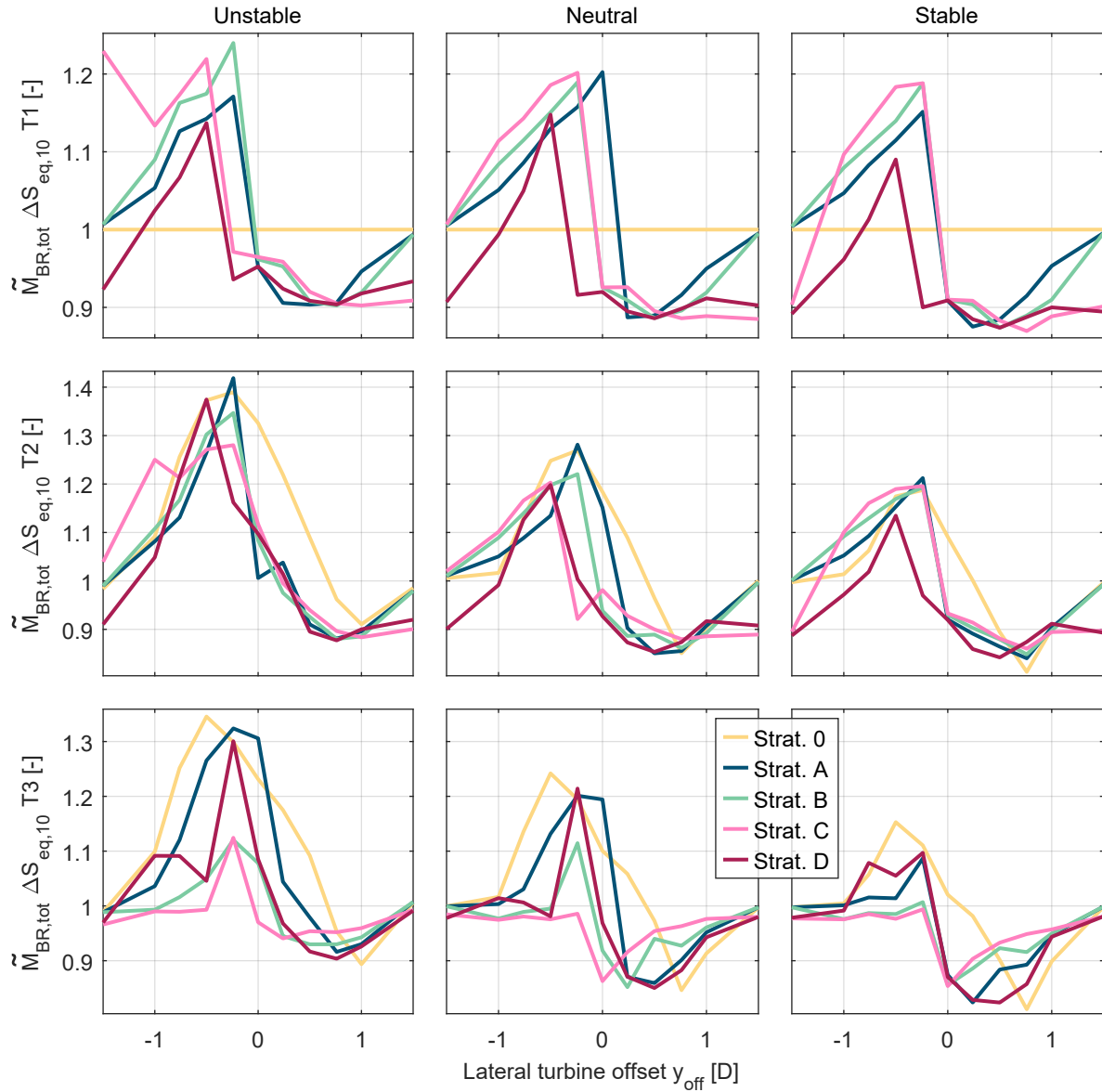


Figure 6.5: Load distributions of the total bending moment at the blade-root for different atmospheric stabilities and the three turbines (T1-T3). The free-stream wind speed is 6 m s^{-1} and the turbine spacing distance in the longitudinal direction is $7D$. Results are shown by means of the seed average and normalised with the values at $\theta_m = 0^\circ$ of the free-stream turbine 1.

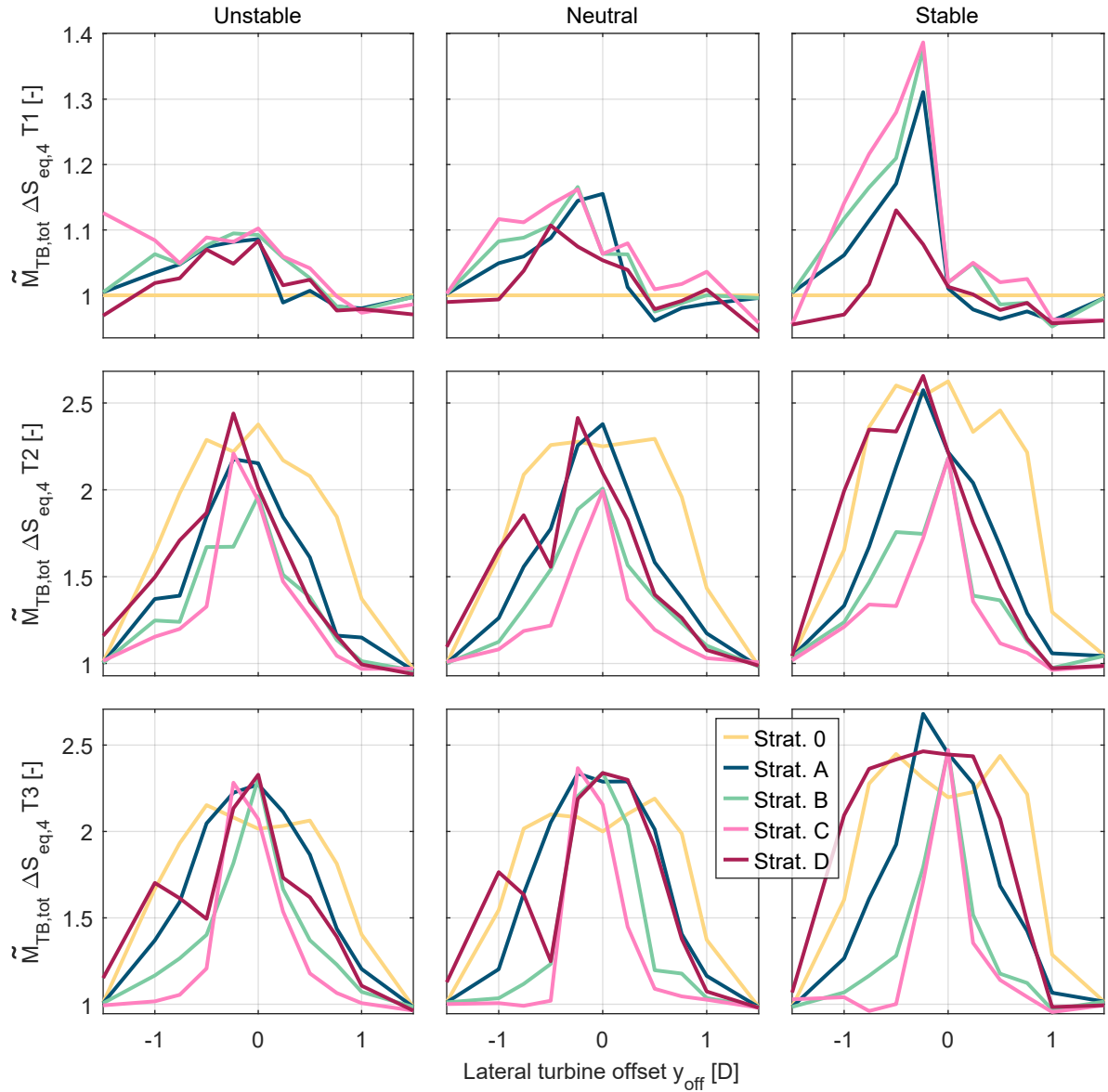


Figure 6.6: Load distributions of the total bending moment at the tower-base for different atmospheric stabilities and the three turbines (T1-T3). The free-stream wind speed is 6 m s^{-1} and the turbine spacing distance in the longitudinal direction is $7D$. Results are shown by means of the seed average and normalised with the values at $\theta_m = 0^\circ$ of the free-stream turbine 1.

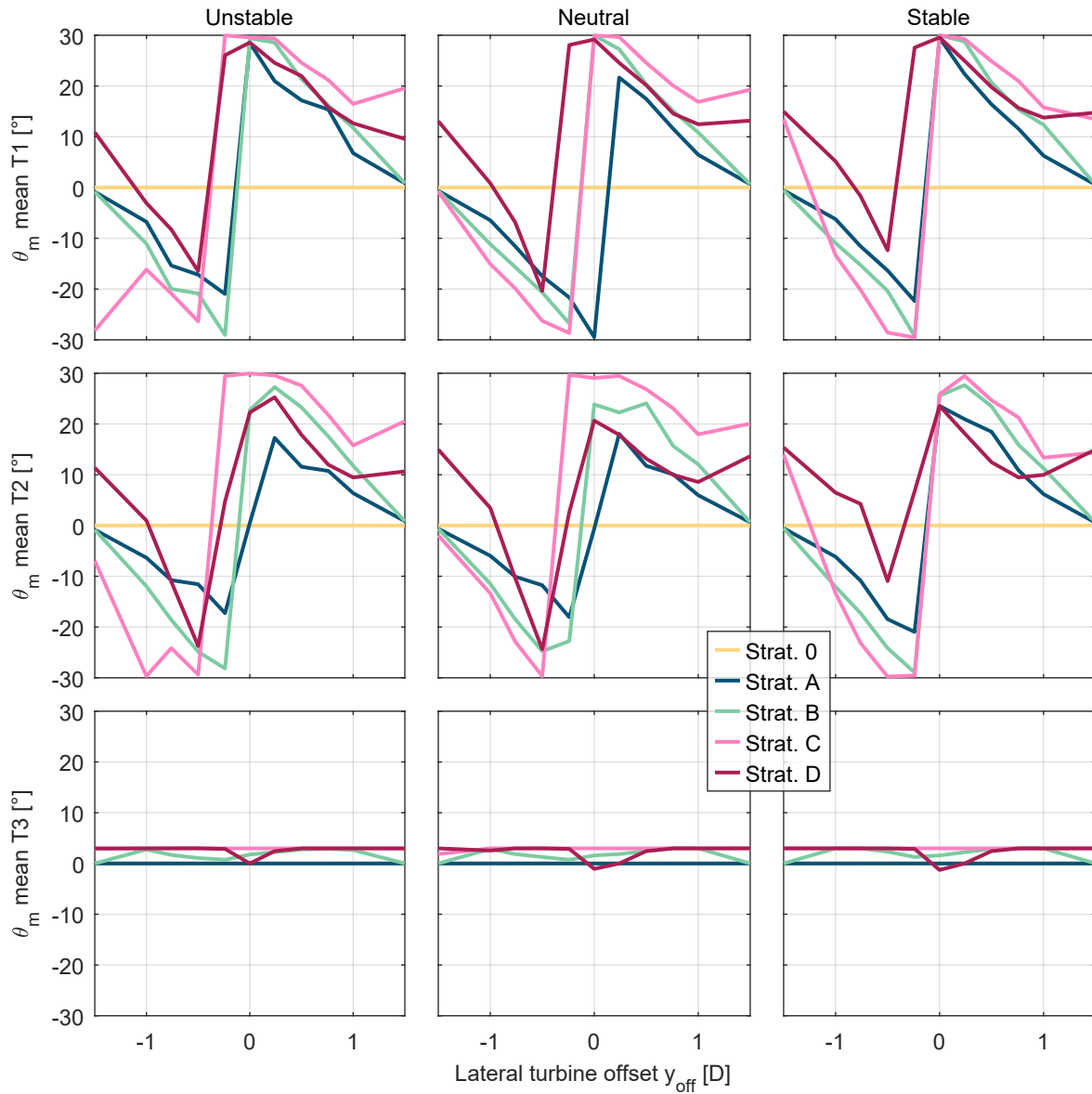


Figure 6.7: Mean nacelle yaw positions for different atmospheric stabilities and the three turbines (T1-T3). The free-stream wind speed is 6 m s^{-1} and the turbine spacing distance in the longitudinal direction is $7D$. Results are shown by means of the seed average.

6.4 Conclusions

The wake-redirection control concept is implemented in various strategies used to operate two wind farm configurations with different objective functions. In a long-term analysis, the performance of the operation strategies is compared. It is found that the AEP of the considered turbine array setups can be increased compared to the baseline scenario, when the main objective is power maximisation while the fatigue loads at the turbines are equally weighted or even not considered. The two main drivers in creating the difference in loads between the baseline and controlled scenarios are the yaw misalignment of the turbines and the changing inflow conditions at waked turbines due to the deflection of the wake from upstream turbines.

A detailed analysis shows that the alleviation of structural loads tends to work better at positive lateral turbine offsets implying positive yaw misalignment angles to redirect the wake. In these configurations, the load reduction at certain components can be combined with an increase in the combined power production. In contrast, at negative lateral turbine offsets, load reductions at specific turbine components typically coincide with losses in the farm power production. Consequently, the strategies that focus on the minimisation of the fatigue loads result in less AEP compared to the baseline strategy.

The consideration of fatigue loads in the optimisation of operation strategies is realised with an efficient surrogate model. With this approach, operating strategies can be derived that can reduce the fatigue loads at specific components significantly. However, significant load reductions, e.g. at the blade-root, are penalised with decreased AEP compared to the baseline case. It is difficult to define a strategy that alleviates the loads for all major wind turbine components. It appears that observed load reductions in the rotating parts are paired with increased load variations in the non-rotating parts of the turbine.

7

Conclusions

7.1 Summary and main conclusions

In this thesis, the wake-redirecting control concept for wind farms was assessed with specific focus on the fatigue loads at the wind turbines. The assessment was structured into three main topics, beginning with an adequate numerical modelling of the aeroelastic interactions between the wind turbines within a wind farm and the Atmospheric Boundary Layer (ABL). In a second step, a detailed investigation of the wake-redirecting control concept was performed and its impact on the fatigue loads were evaluated using realistic offshore environmental conditions. Finally, the gained knowledge was applied to derive strategies that optimise the operation of wind farms for different objectives. With the presented work, a deeper understanding of the structural loads at the wind turbines when applying wind farm control was obtained. Furthermore, an adequate modelling technique that enables a detailed evaluation of the wind farm control concept was demonstrated. This was identified as a major research gap [5] and a key for the bankability of wind farm control described in the introduction section of this thesis. This final chapter provides a summary of the findings and final conclusions.

7.1.1 Calibration and validation of the aeroelastic simulation model

For the aeroelastic simulations, the software FAST.Farm that is based on the Dynamic Wake Meandering (DWM) model was utilised. It was further improved by implementing a model that includes the wake-added small-scale turbulence. The new model was calibrated and validated against high-fidelity Large Eddy Simulations (LES). It was shown that the inclusion of wake-added turbulence is crucial to avoid underestimation of the turbulence in the wake, especially in stable atmospheric conditions, where the ambient turbulence intensity (TI) is low and the meandering of the wake is weak. In these conditions, the wake-added turbulence model reduces significantly the error from the prediction of the turbulence in the wake at a downstream distance of $5D$ from $\approx 75\%$ to $\approx 15\%$ with respect to the LES results for the three velocity components.

FAST.Farm was then validated for the prediction of power output and structural loads in single wake conditions using measurement data from the offshore wind farm alpha ventus. Here, an important prerequisite was the detailed calibration of the aeroelastic model with respect to aerodynamic and mass imbalances as well as a proper representation of the environmental conditions in the simulations. It was shown that FAST.Farm predicts the mean power deficit very accurately compared to the measurements. Fatigue loads were analysed at the blade root and at the tower base of the waked turbine and their dependency on different environmental conditions (wind speed, wind direction) was investigated. Overall, a good agreement between simulations and measurements with deviations of less than 10% was achieved.

A significant influence of the wake-added turbulence on the loads at the tower-base was observed. With the newly implemented wake-added turbulence model, the error in the fatigue loads between simulations and measurements could be significantly reduced from an underestimation of 87% to 2% in full-wake conditions. In analyses of the frequency response, it was shown that an excitation at the tower-base of the waked turbine could be reproduced with FAST.Farm, when the wake-added turbulence model is included. At the same time, the effects of the wake-added turbulence model on the fatigue loads at the blade-root are small; differences between the simulation with and without wake-added turbulence model could be up to 13% . Hence, the increase of the loads at the blade-root for the waked turbine can be mostly attributed to the effects from wake meandering, because the loads amplitude caused by the wake meandering is significantly larger.

7.1.2 Structural loads under consideration of wake redirection control

The effects from wake-redirection control were evaluated in a three steps process. At first, the consequences on the fatigue loads for the different components of a free-stream turbine were analysed, with changing atmospheric conditions and yaw misalignment angles. The biggest effects of yaw misalignment on the load variations were observed for stable Atmospheric Stability (AS) with strong vertical wind shear and low TI . In contrast, the influence of yaw misalignment on the fatigue loads becomes less important in unstable AS with low vertical wind shear and high TI . A long-term analysis for below-rated wind speeds showed that the loads with different yaw misalignment angles are reduced compared to a zero yaw misalignment for the majority of the considered turbine components and atmospheric conditions. However, the long-term fatigue loads of the total bending moment at the blade-root are significantly increased for negative yaw-misalignment angles.

For a potential application of wake redirection control, it is concluded that yawed operation can lead to increased or decreased fatigue loads based on the component, atmospheric conditions and yaw misalignment angle. A reduction in loads at one location is often penalised with an increase of loads at another location. A parallel reduction of fatigue loads for all components is normally not possible. From a long-term perspective, the results indicated that the fatigue loads can be potentially balanced in order to reach the load levels from the operation with zero yaw misalignment.

In a second step, the wake characteristics behind a single wind turbine were studied in order to gain more understanding in which conditions the application of wake redirection control has high potential. The magnitude of wake meandering was found to be dependent on the AS and the ambient turbulence level. The strongest wake meandering in both the lateral and vertical directions was found in unstable and highly turbulent conditions, whereas significantly less wake meandering was observed in stable AS with low ambient TI . In addition, the wake recovery rates were analysed and dependencies on the environmental conditions investigated. Overall, the velocity deficit in the wake recovers faster in unstable conditions with high TI than in neutral and stable AS with lower TI . However, in FAST.Farm, it was found that the treatment of the vertical wind shear in the calculation of the velocity deficit rate leads always to a faster wake recovery with vertical wind gradients increased. This is contrary to the physical understanding in a stable ABL where the momentum exchange in the vertical direction is typically lower compared to neutral and unstable conditions. Consequently, the wake recovery rate for stable AS is likely overpredicted by FAST.Farm in the current implementation. The implications on the results, especially the structural loads of the waked turbine, are regarded of minor importance because the observed trends in the analysed load distributions will remain the same (although with a slightly different magnitude) if the wake recovery rate is weaker.

With respect to wake redirection control, the results indicated that the potential power

maximisation by deflecting the wake is higher in stable AS due to slower wake recovery rates compared to neutral and unstable conditions. Additionally, the turbulence levels in the wake are lower and the wake is narrower in the lateral location for stable AS compared to neutral and unstable AS; hence, a deflection of the wake should be more effective to lower the structural loads from turbulence in stable atmospheric conditions.

In a last step, the effects from yaw-misalignment on the structural loads were examined for a turbine subjected to a wake. For this reason, the results from wake conditions were compared with the load distributions in free-stream conditions. It was concluded that the loads are a complex function of the environmental conditions, yaw misalignment angle and the wake condition. In particular, for the same environmental conditions, the loads are dependent on the yaw misalignment and wake location in the lateral direction. Especially in partial wake situations, where the wake-centre lies between $\pm 0.75 D$ measured from the rotor-centre of the waked turbine (lateral wake-centre offset), the load distributions differ significantly from free-stream conditions. This is primarily caused by the increases of the TI in the wake and alternating loads in the rotating system due to partial wake. In addition, the operational point of the waked turbine is changed because of the wind speed deficit in the wake, which also results in variations of the load distributions. With increasing lateral wake-centre offsets ($> |0.75 D|$), the load distributions are less influenced by the wake and become more similar to the load distributions in free-stream conditions.

The gradients of the structural loads with regard to the lateral wake offset are high for wake-centre offset locations between $\pm 0.75 D$. In this region, a wake redirection control strategy is likely to be more efficient with respect to load balancing, because changes in the lateral wake-centre position lead potentially to higher load reductions. The general characteristics of the load distributions are similar for different environmental conditions. Different environmental conditions lead normally to varying load magnitudes and shifted load maxima with respect to the yaw misalignment angle. Vertical wind shear has a large influence on the load distributions, especially when combined with partial wake scenarios. A directional dependency of the loads is found with respect to the lateral wake offset: The loads tend to be higher for negative lateral wake offsets compared to the loads from the same positive lateral wake offsets, because of higher load amplitudes over one rotor revolution.

Overall, the presented results are valid for the simulated turbine model NREL 5 MW. Other turbine models might show different load characteristics and should be investigated separately.

7.1.3 Optimisation of wind farm operation

The wake-redirectation control concept was employed to optimise the wind farm operation according to different objectives that include the maximisation of the wind farm power output as well as the reduction of fatigue loads. In a long-term analysis, the performance of the operation strategies was evaluated using aeroelastic simulations in FAST.Farm. It was found that the Annual Energy Production (AEP) of the considered turbine array setups can be increased compared to the baseline scenario without wind farm control, when the main objective is set to power maximisation while the fatigue loads at the turbines are not or equally weighted in the cost function for the optimisation. The two main drivers in creating the difference in loads between the baseline and controlled scenario are the yaw misalignment of the turbines and the changing inflow conditions at waked turbines due to the wake deflection from the upstream turbines.

A detailed analysis showed that the alleviation of structural loads tends to work better at positive lateral turbine offsets implying positive yaw misalignment angles to redirect the wake. In these configurations, the load reduction at certain components can be combined with an increase in the power production. In contrast, at negative lateral turbine offsets, load reductions at specific turbine components typically coincide with losses in the wind farm power production. Consequently, the strategies that focus on the minimisation of the fatigue loads result in less AEP compared to the baseline strategy. The consideration of fatigue loads in the optimisation of operation strategies is realised with an efficient surrogate model. With this approach, strategies were derived that are able to reduce the fatigue loads at specific components significantly. However, significant load reductions, for instance at the blade-root, are penalised with decreased AEP compared to the baseline case.

7.2 Outlook

In the future, the increasing penetration of renewable energy resources in the electricity grid will require flexible operation of wind farms. In particular, power generation must be able to follow the actual demand flexibly and to provide ancillary services to support the electricity grid. Therefore, wind farm control will become more important. Besides grid integration, wind farm control aims to optimise the operation of individual turbines with respect to various objectives including power maximisation and balancing of the fatigue loads. For the wake redirection approach as one option for wind farm control, a detailed evaluation was performed in this thesis. However, some simplifications had to be made and some aspects were neglected that should be addressed in future research:

- For the optimisation of operation strategies, more complex wind farm layouts should be investigated compared to the 3 and 5 turbine arrays from this work. In this context,

the generation of the surrogate model including the structural loads for the optimisation should be analysed. In this work, only wake effects from one upstream turbine were considered. It might be necessary to adapt the surrogate model based on the wind farm layout in order to include effects on the loads that are dependent on the farm layout.

- A more sophisticated surrogate model should be used for the optimisation compared to the look-up table approach used in this thesis. This is especially relevant when many operation conditions need to be covered and a full set of simulations for all cases is not feasible. Machine learning based methods in conjunction with the Design of Experiments (DoE) are a promising option as stated in [150].
- For an application of optimised wind farm control strategies in the field, an analysis of the uncertainties should be conducted. It should include uncertainties from wind direction variability, estimation of the environmental conditions, turbine type and turbine specific properties such as imbalances that could change potential benefits on the loads.
- The optimisation of operation strategies should be coupled with information from the electricity market in order to demonstrate their potential value with respect to direct marketing.

From a modelling point of view, the presented approach by using FAST.Farm to perform aeroelastic simulations has proven to give reasonably good results. Nevertheless, some aspects have been identified which should be improved for future studies:

- The comparison of simulation results from FAST.Farm with the measurement data from the alpha ventus wind farm showed good agreement, especially at the tower-base with the newly added wake-added turbulence model. However, analyses of the frequency response at the blade-root revealed that not all phenomena are captured sufficiently by FAST.Farm. Hence, further investigations of the wake and its shape are required (e.g. by using LES) to improve the wake modelling and thus the prediction of structural loads.
- The consideration of vertical wind shear in the calculation of the recovery of the velocity deficit should be investigated in more detail. The current implementation leads to recovery rates that are too high in stable atmospheric conditions compared to unstable and neutral AS. Consequently, the calculation of the velocity deficit recovery should be improved to enable more sophisticated analyses that better differentiate the effects from different ASs
- The current model for the calculation of the wake deflection as using yaw-misaligned operation is heavily dependent on its calibration. The current calibration factors are only applicable in below-rated conditions, in which the rotor thrust is high. Therefore, it is recommended to re-calibrate the model for above-rated conditions or to find a formulation that is more robust with respect to the operating conditions.

A

Appendix

A.1 Additional results from the wake-added turbulence calibration

The Figures A.1-A.11 include additional results from the calibration of the wake-added turbulence model in FAST.Farm that is presented in Section 4.1.

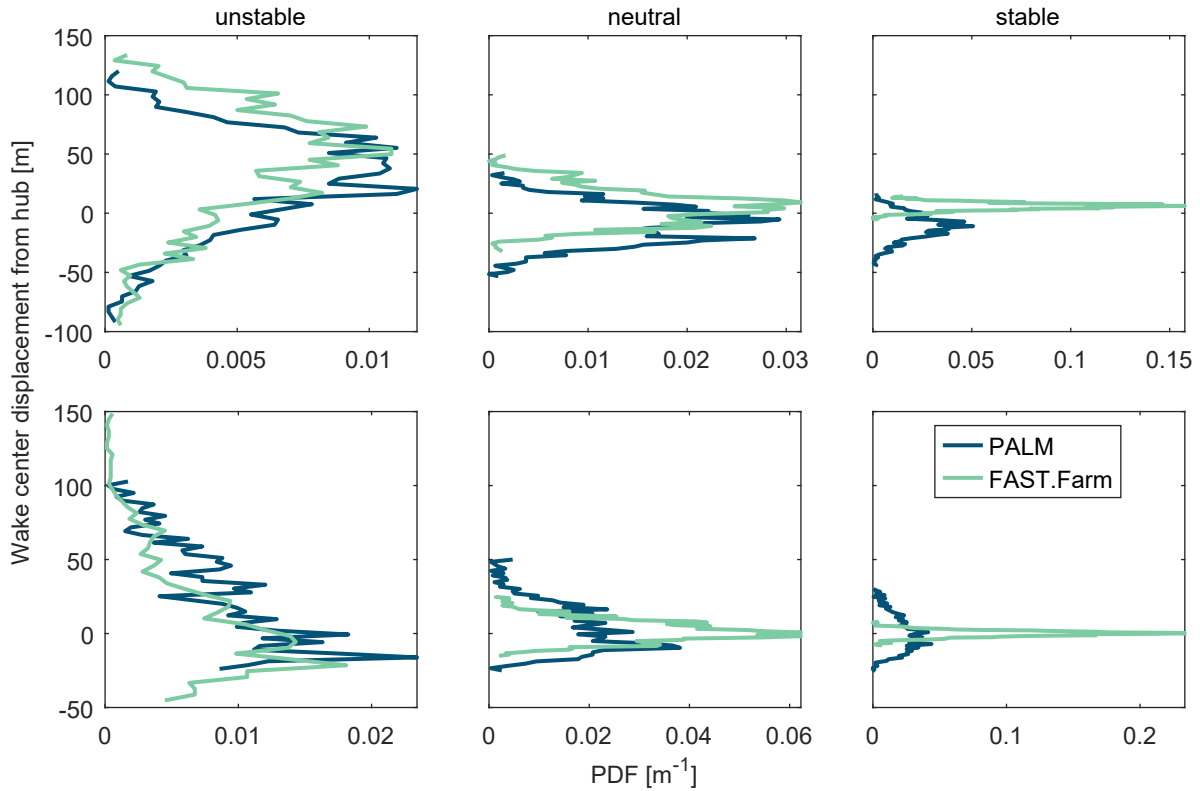


Figure A.1: Histograms of wake centre displacement expressed as probability density function (PDF) relative to the hub of the lower freestream turbine in the lateral (upper row) and vertical (lower row) directions at a downstream distance of $6D$.

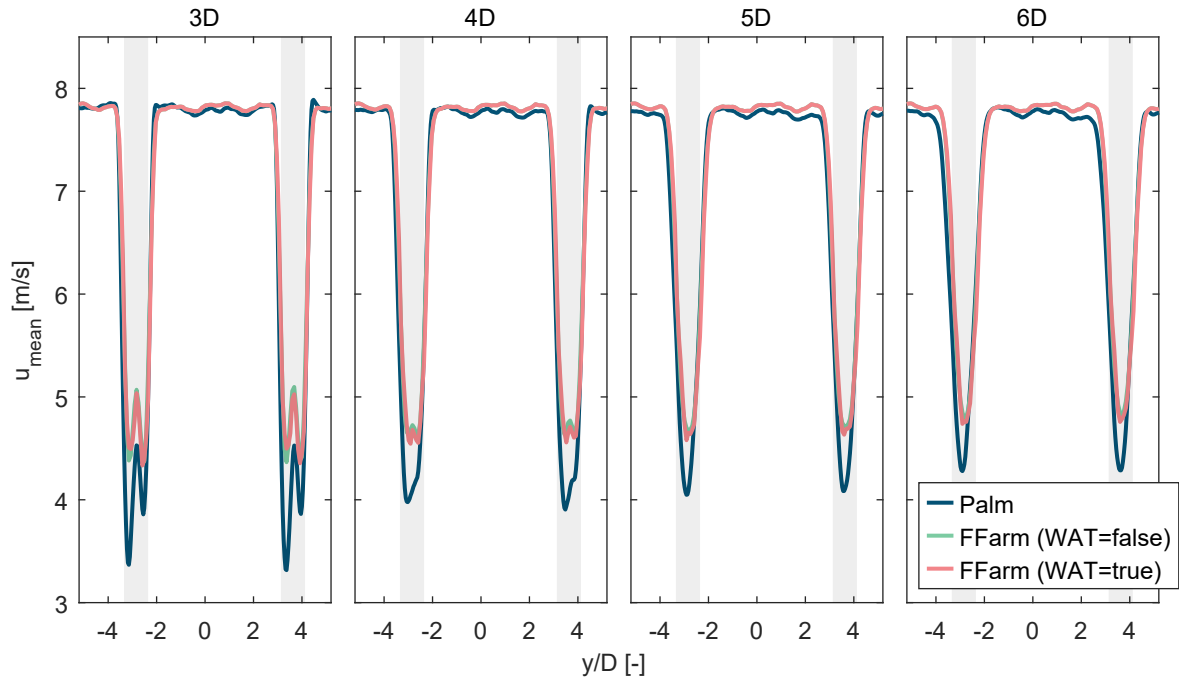


Figure A.2: Mean wind speed of the u-component in the horizontal direction at various downstream distances (3-6 D) at hub height ($z=92$ m) for stable atmospheric conditions. FAST.Farm (FFarm) results are plotted with activated (WAT=true) and deactivated (WAT=false) wake-added turbulence model. The rotor position of the turbines T1 and T4 is indicated by the grey patches.

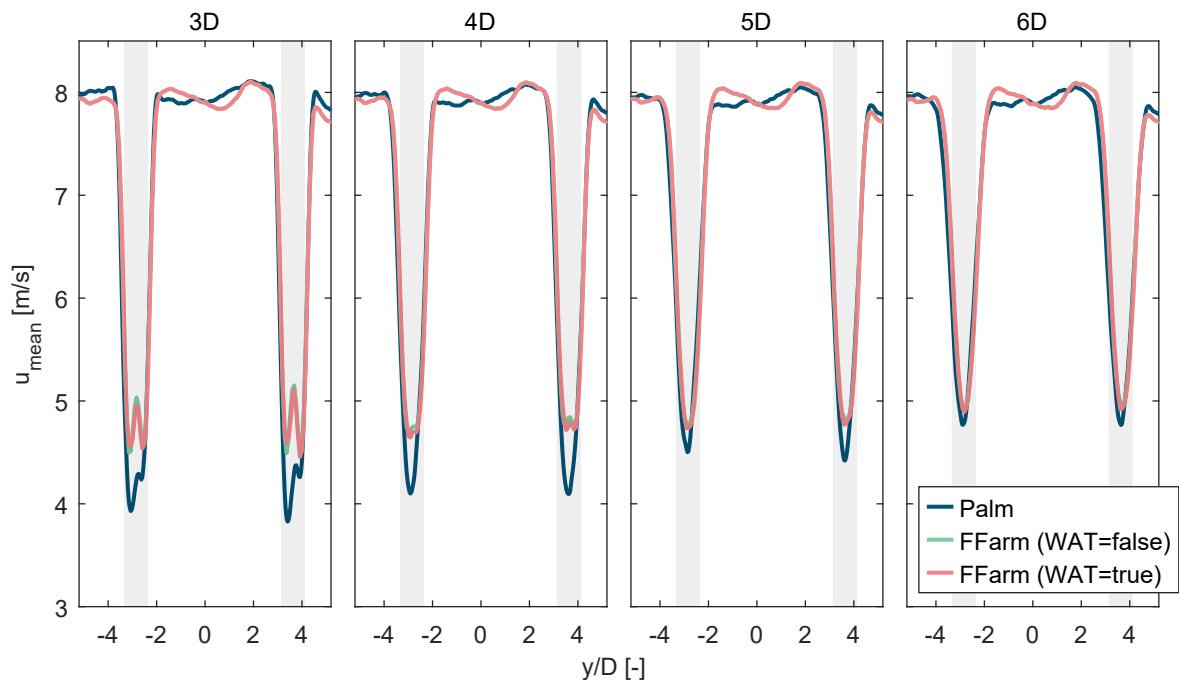


Figure A.3: Mean wind speed of the u-component in the horizontal direction at various downstream distances (3-6 D) at hub height ($z=92$ m) for neutral atmospheric conditions. FAST.Farm (FFarm) results are plotted with activated (WAT=true) and deactivated (WAT=false) wake-added turbulence model. The rotor position of the turbines T1 and T4 is indicated by the grey patches.

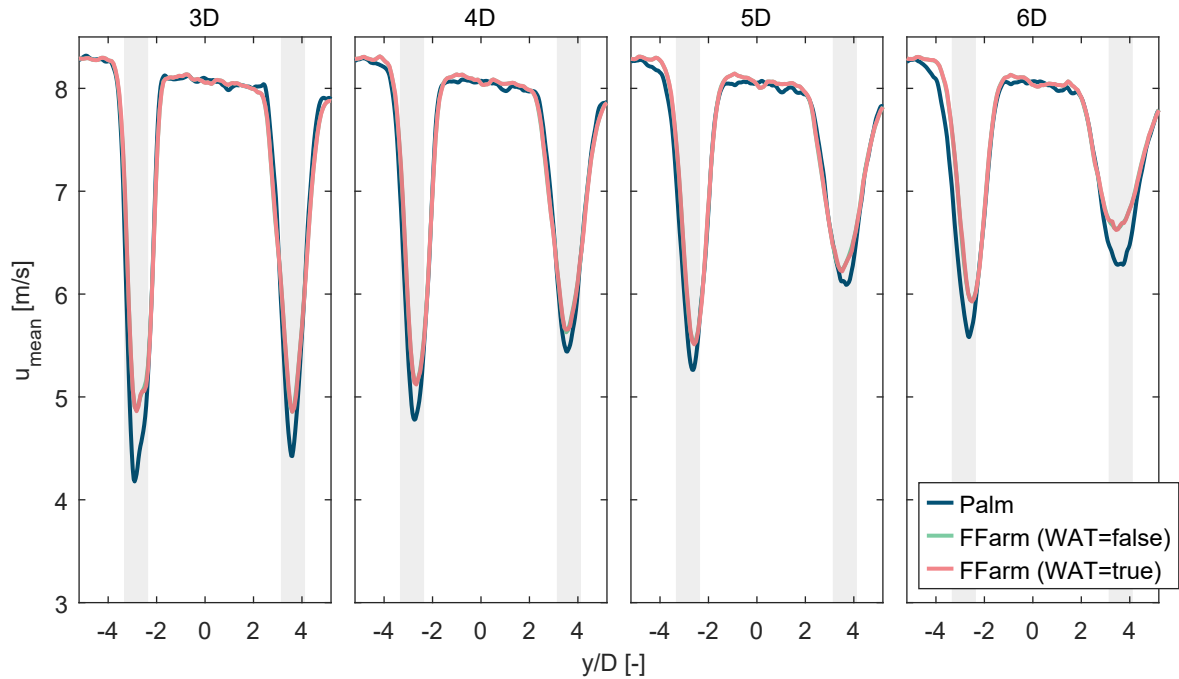


Figure A.4: Mean wind speed of the u-component in the horizontal direction at various downstream distances (3-6 D) at hub height ($z=92$ m) for unstable atmospheric conditions. FAST.Farm (FFarm) results are plotted with activated (WAT=true) and deactivated (WAT=false) wake-added turbulence model. The rotor position of the turbines T1 and T4 is indicated by the grey patches.

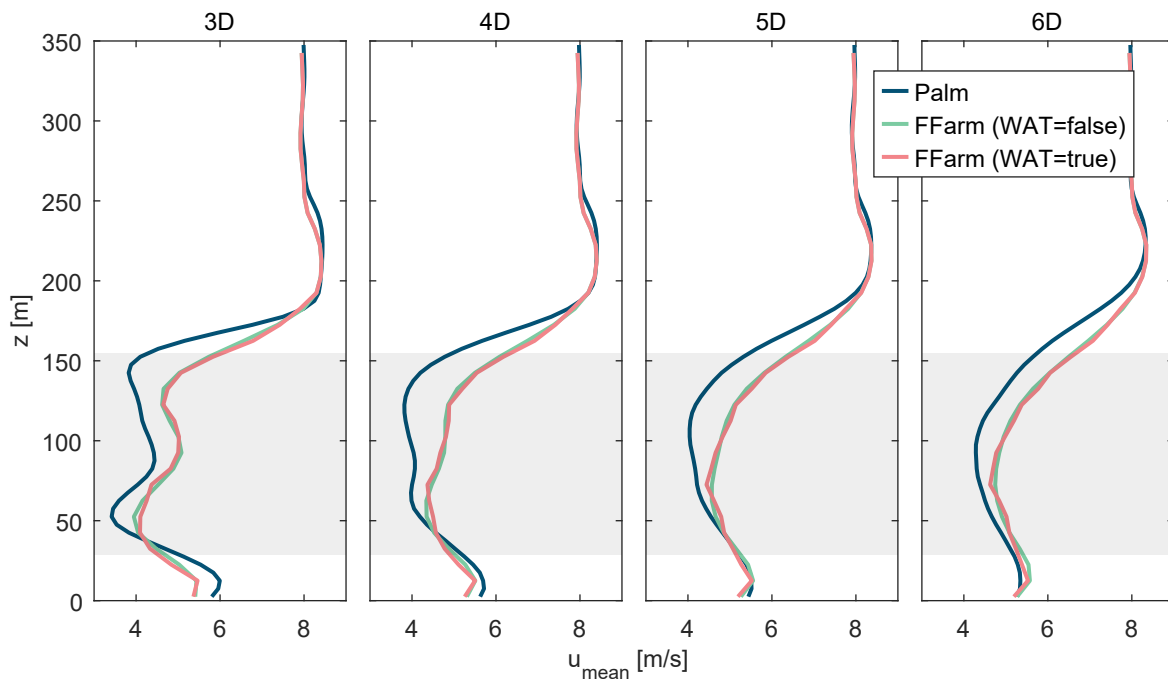


Figure A.5: Mean wind speed of the u-component in the vertical direction at various downstream distances (3-6 D) behind the upper freestream turbine for stable atmospheric conditions. FAST.Farm (FFarm) results are plotted with activated (WAT=true) and deactivated (WAT=false) wake-added turbulence model. The rotor position of the turbines T1 and T4 is indicated by the grey patches.

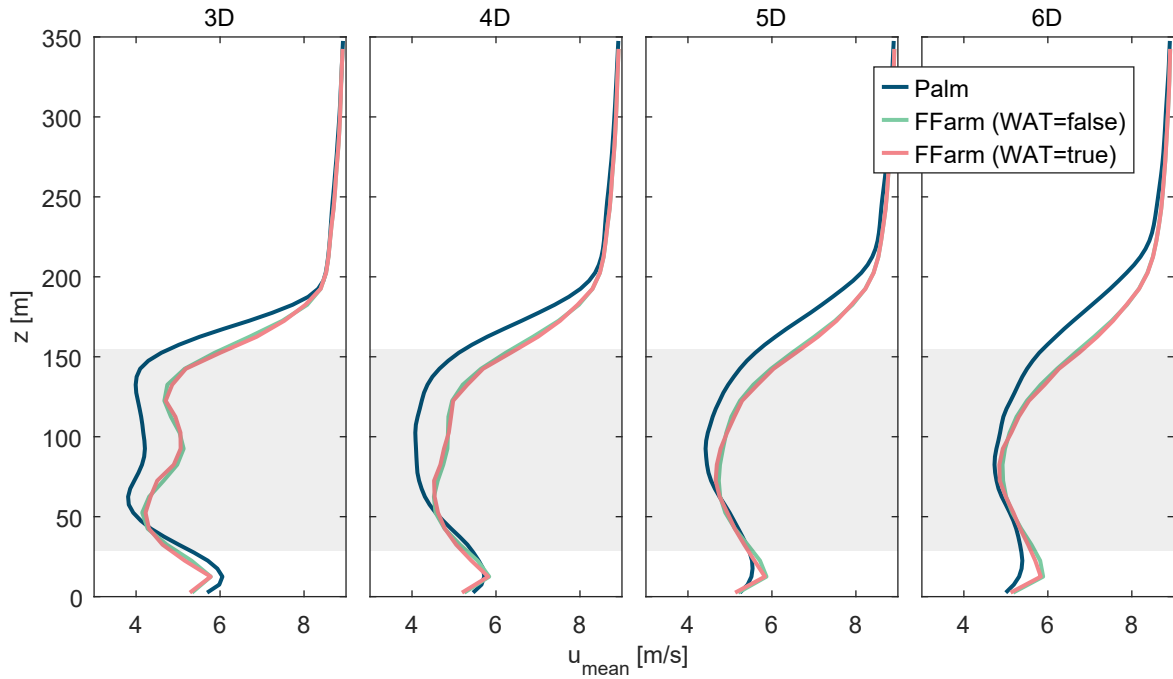


Figure A.6: Mean wind speed of the u-component in the vertical direction at various downstream distances (3-6 D) behind the upper freestream turbine for neutral atmospheric conditions. FAST.Farm (FFarm) results are plotted with activated (WAT=true) and deactivated (WAT=false) wake-added turbulence model. The rotor position of the turbines T1 and T4 is indicated by the grey patches.

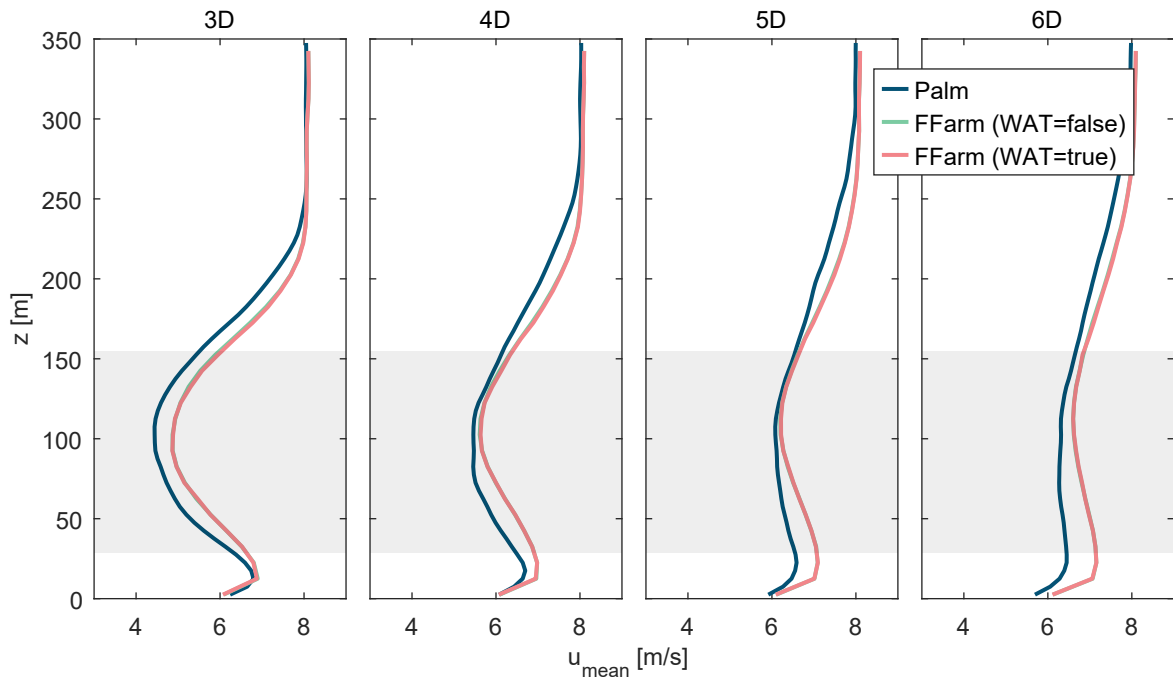


Figure A.7: Mean wind speed of the u-component in the vertical direction at various downstream distances (3-6 D) behind the upper freestream turbine for unstable atmospheric conditions. FAST.Farm (FFarm) results are plotted with activated (WAT=true) and deactivated (WAT=false) wake-added turbulence model. The rotor position of the turbines T1 and T4 is indicated by the grey patches.

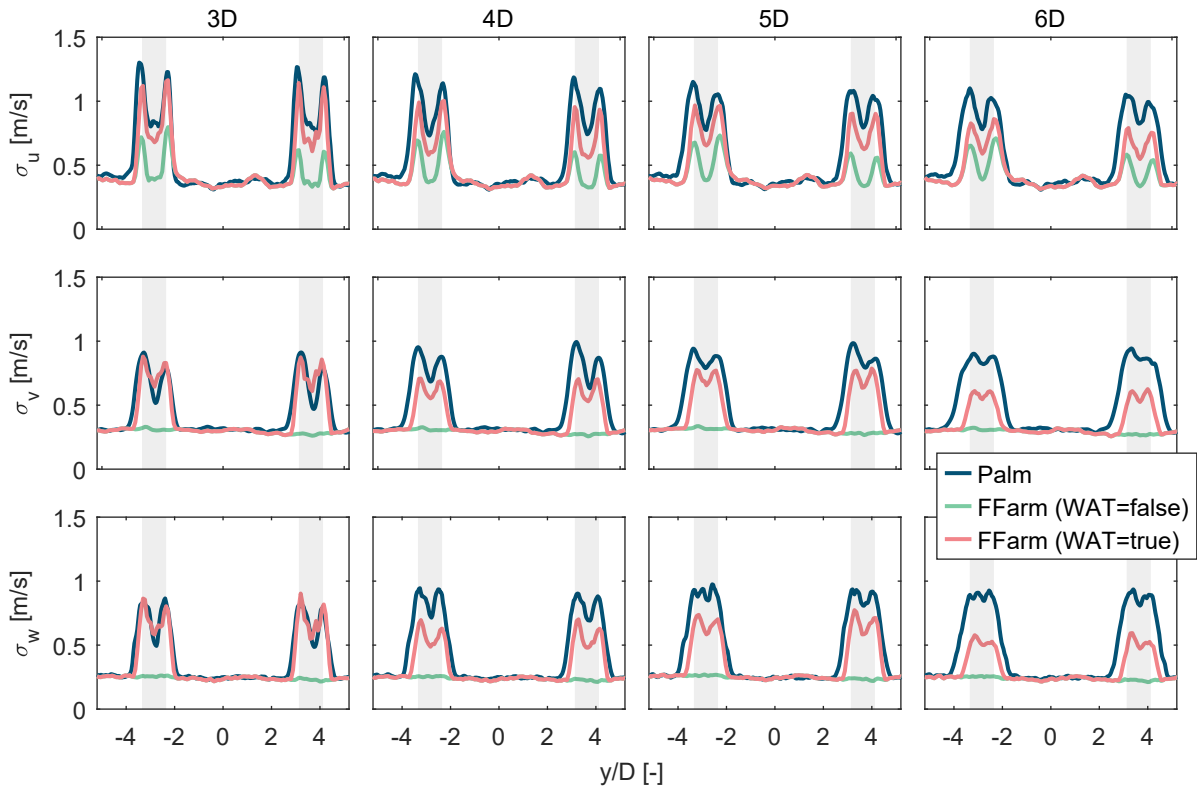


Figure A.8: Turbulence profiles (expressed as standard deviation of the three velocity components $\sigma_{u,v,w}$) in the horizontal direction at various downstream distances (3-6 D) at hub height ($z=92$ m) for neutral atmospheric conditions. FAST.Farm (FFarm) results are plotted with activated (WAT=true) and deactivated (WAT=false) wake-added turbulence model. The rotor position of the turbines T1 and T4 is indicated by the grey patches.

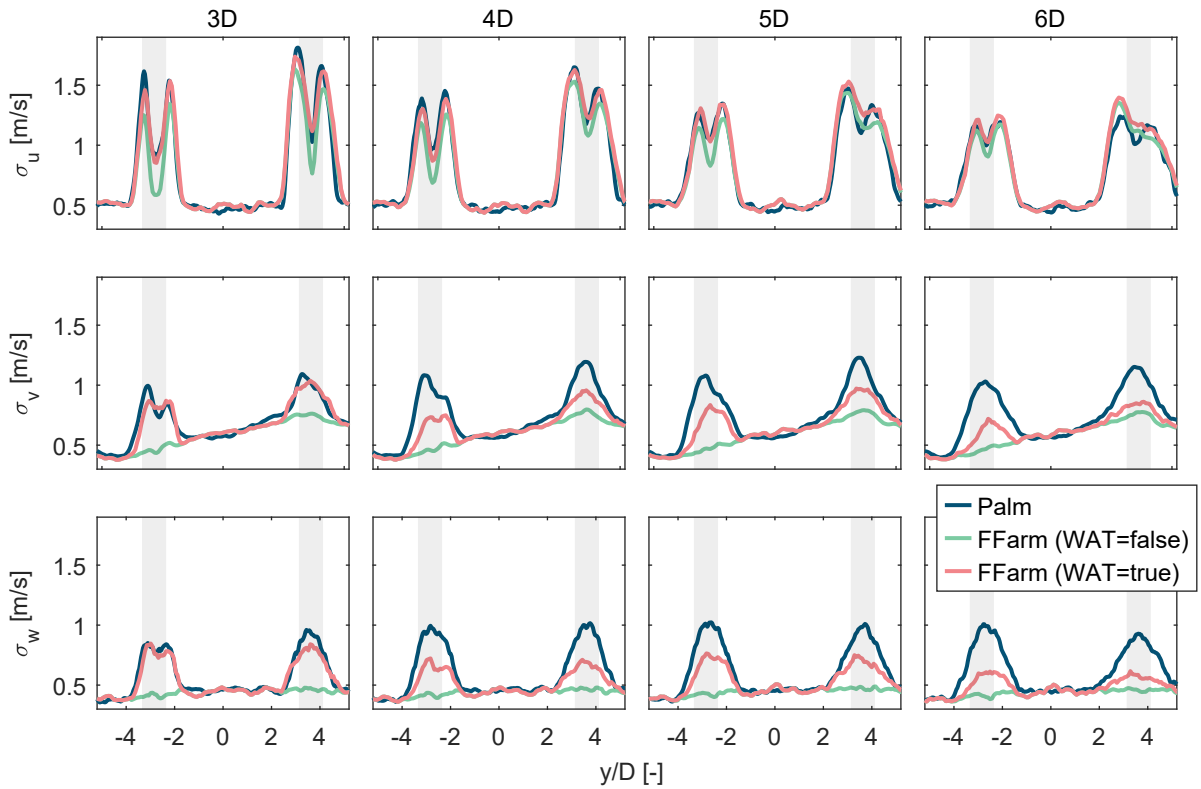


Figure A.9: Turbulence profiles (expressed as standard deviation of the three velocity components $\sigma_{u,v,w}$) in the horizontal direction at various downstream distances (3-6 D) at hub height ($z=92$ m) for unstable atmospheric conditions. FAST.Farm (FFarm) results are plotted with activated (WAT=true) and deactivated (WAT=false) wake-added turbulence model. The rotor position of the turbines T1 and T4 is indicated by the grey patches.

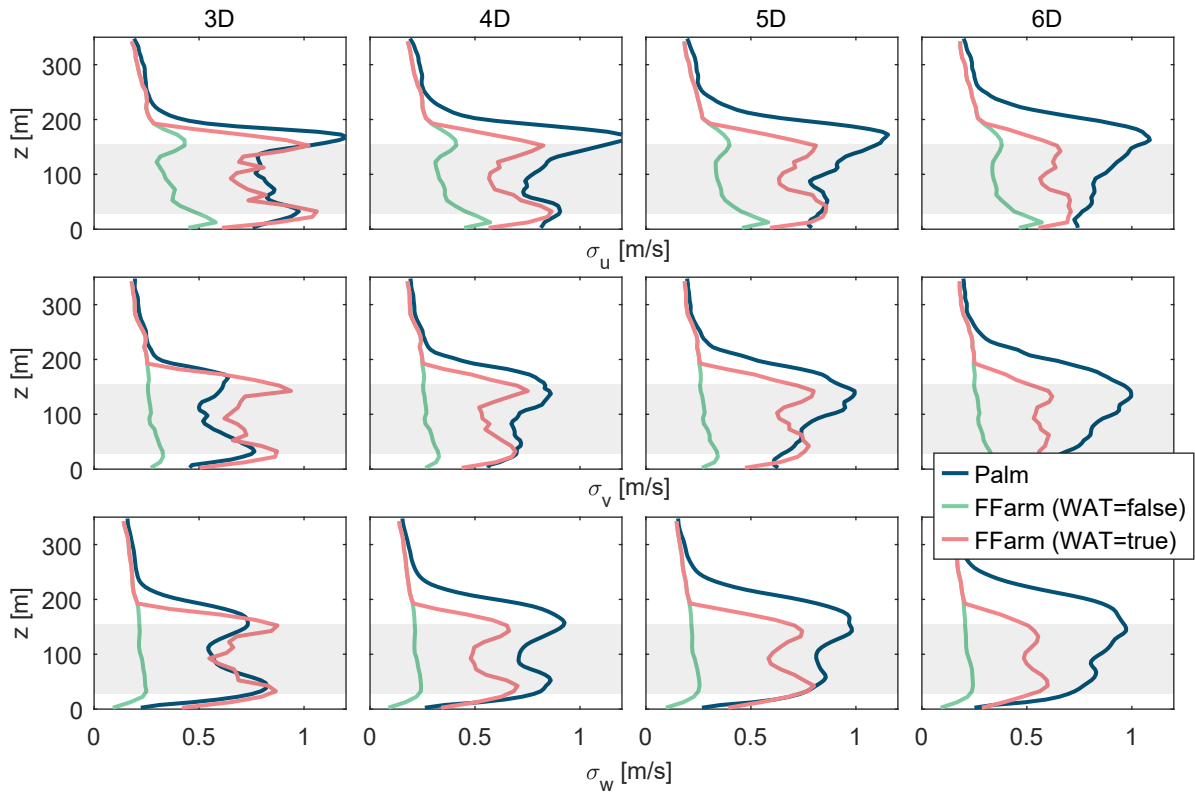


Figure A.10: Turbulence profiles (expressed as standard deviation of the three velocity components $\sigma_{u,v,w}$) in the vertical direction at various downstream distances (3-6 D) behind the upper freestream turbine for neutral atmospheric conditions. FAST.Farm (FFarm) results are plotted with activated (WAT=true) and deactivated (WAT=false) wake-added turbulence model. The rotor position of the turbines T1 and T4 is indicated by the grey patches.

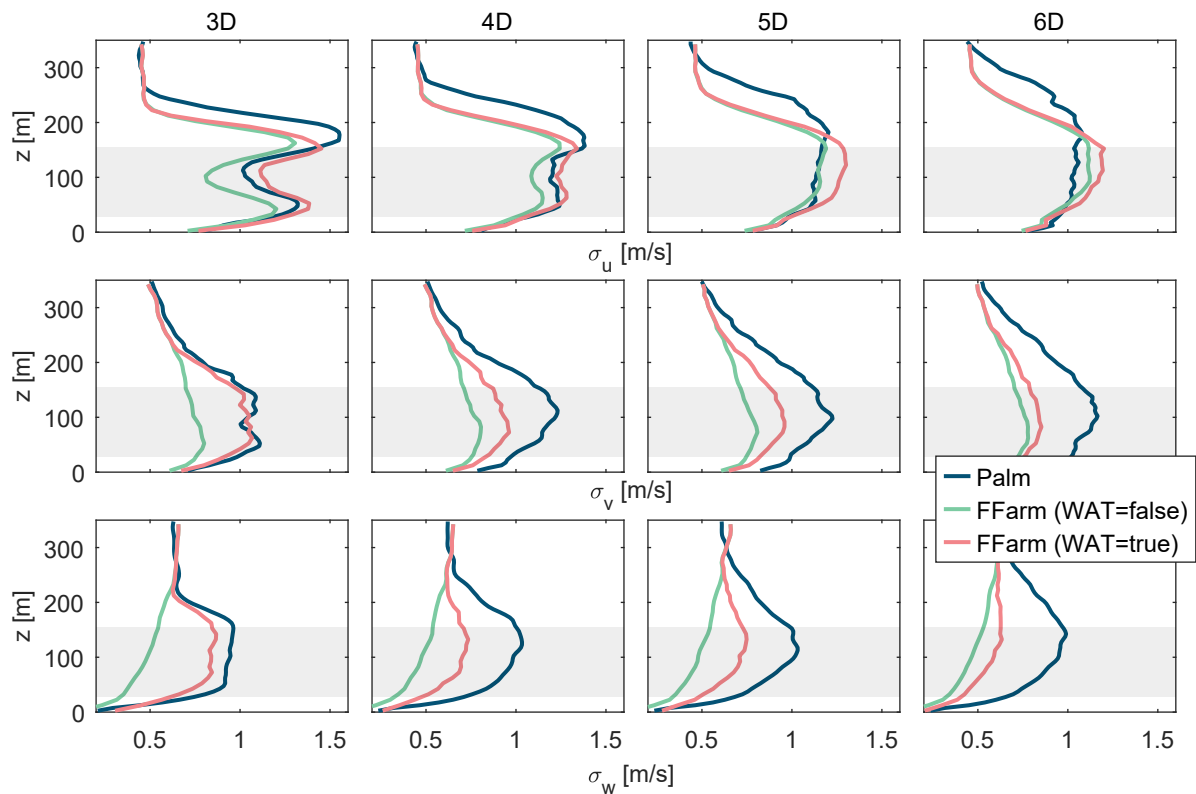


Figure A.11: Turbulence profiles (expressed as standard deviation of the three velocity components $\sigma_{u,v,w}$) in the vertical direction at various downstream distances (3-6 D) behind the upper freestream turbine for unstable atmospheric conditions. FAST.Farm (FFarm) results are plotted with activated (WAT=true) and deactivated (WAT=false) wake-added turbulence model. The rotor position of the turbines T1 and T4 is indicated by the grey patches.

A.2 Additional results from the OpenFAST validation

The Figure A.12 includes additional results from the validation of the simulation tool OpenFAST that is presented in Section 4.2.

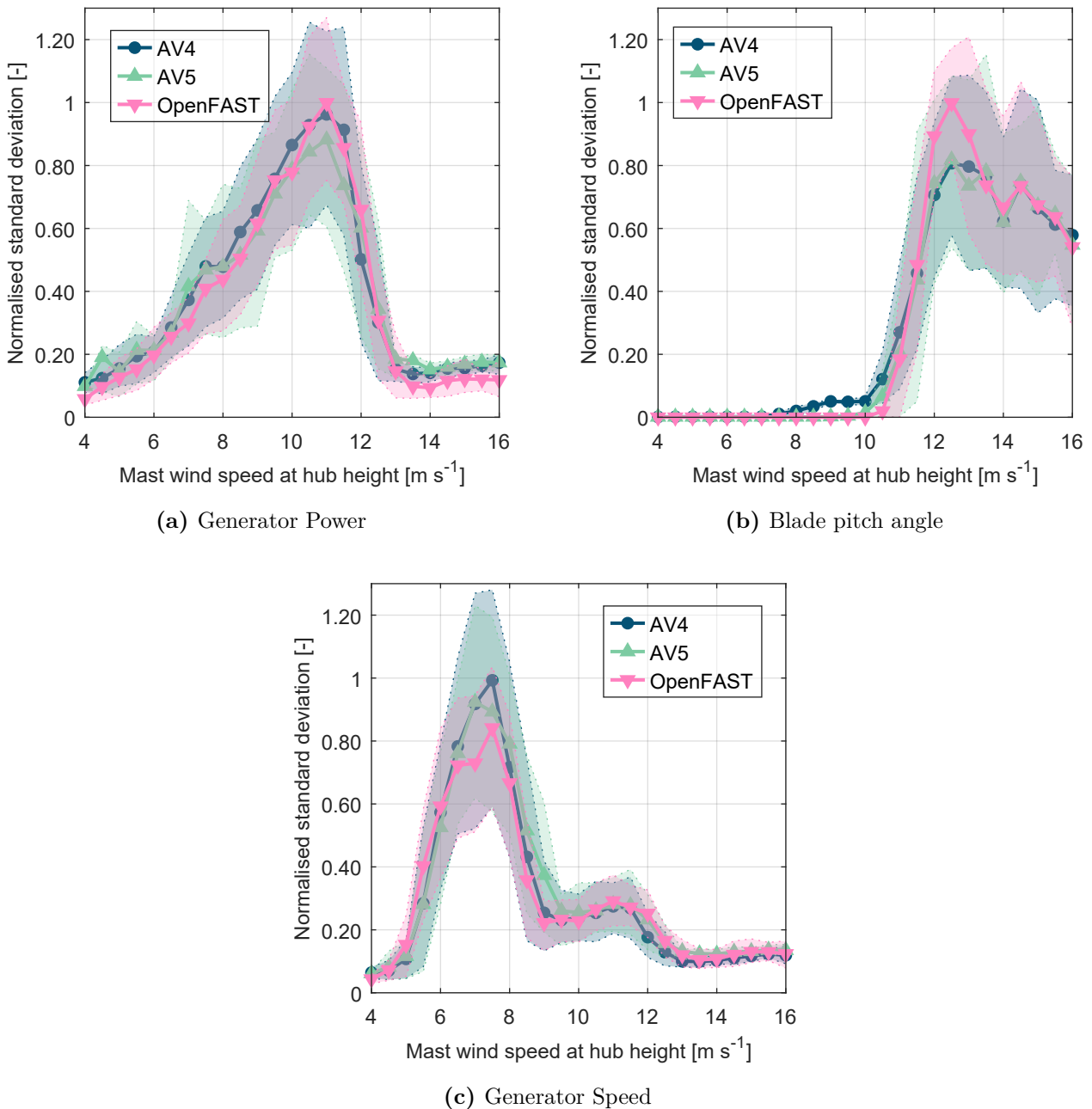


Figure A.12: Comparison of freestream (wind direction 240°-252°) turbine performance characteristics between measurements (AV4, AV5) and simulations (OpenFAST: results are shown with calibration based on AV4). Statistics are shown as mean values per wind bin. Shaded area indicates 15th and 85th percentiles.

A.3 Additional results from the FLORIS calibration

The Figures A.13 and A.14 include additional results from the calibration of FLORIS that is presented in Section 4.4.

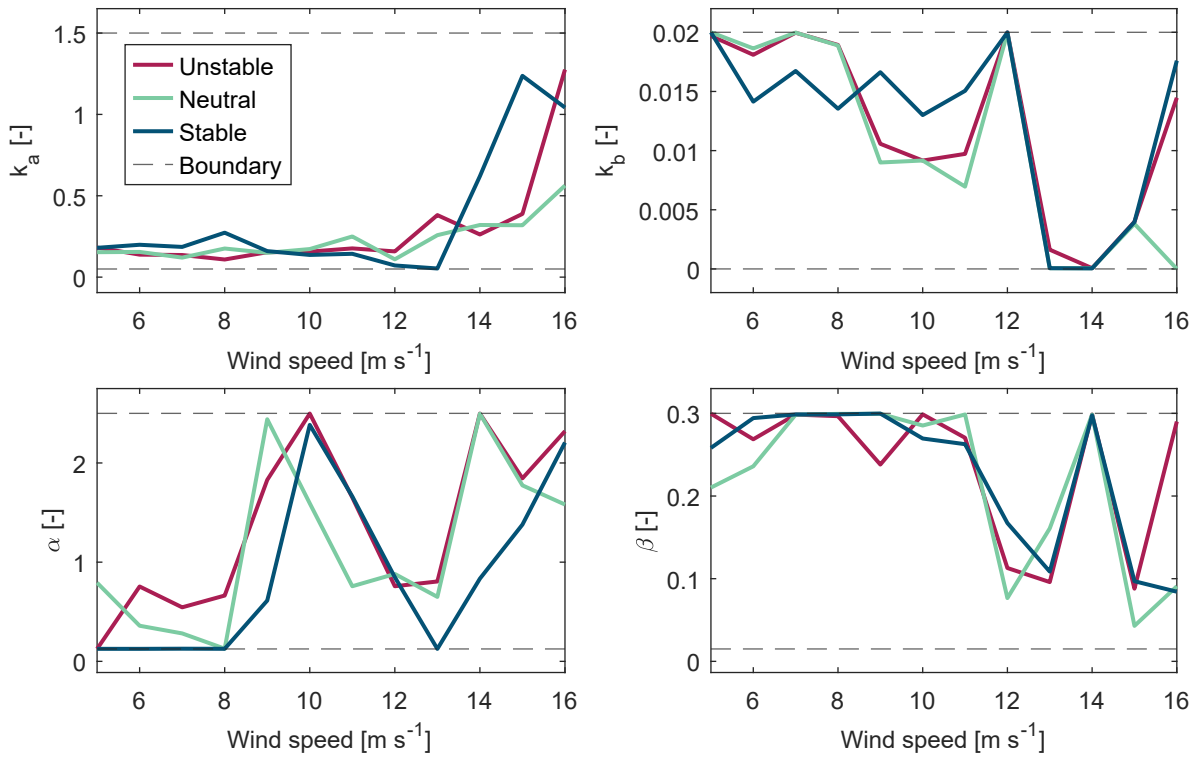


Figure A.13: Calibrated parameters of the Gaussian velocity deficit model in FLORIS for a longitudinal turbine spacing of 5 D.

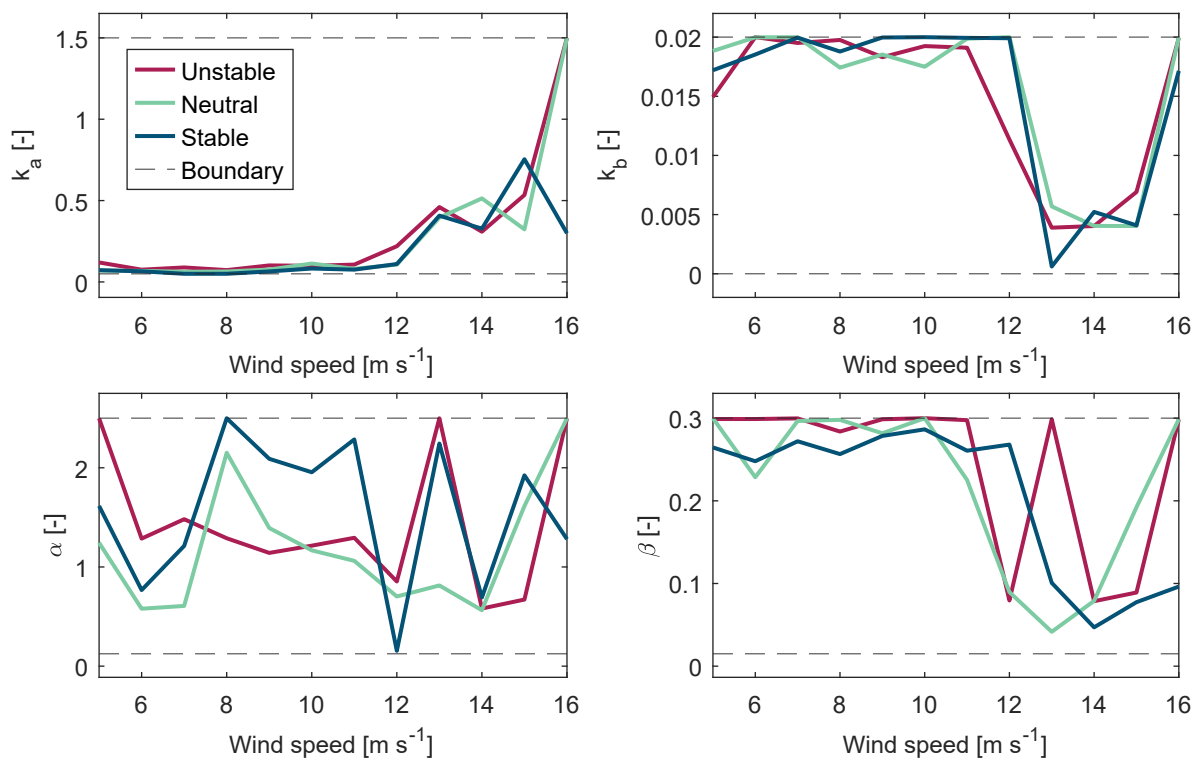


Figure A.14: Calibrated parameters of the Gaussian velocity deficit model in FLORIS for a longitudinal turbine spacing of 9D.

A.4 Additional load distributions of a free stream turbine in yawed operation

A.4.1 Short-term evaluation

The Figures A.15-A.29 contain additional results from the short-term investigation of the load distributions of a free stream turbine in yawed operation that is presented in Section 5.3.

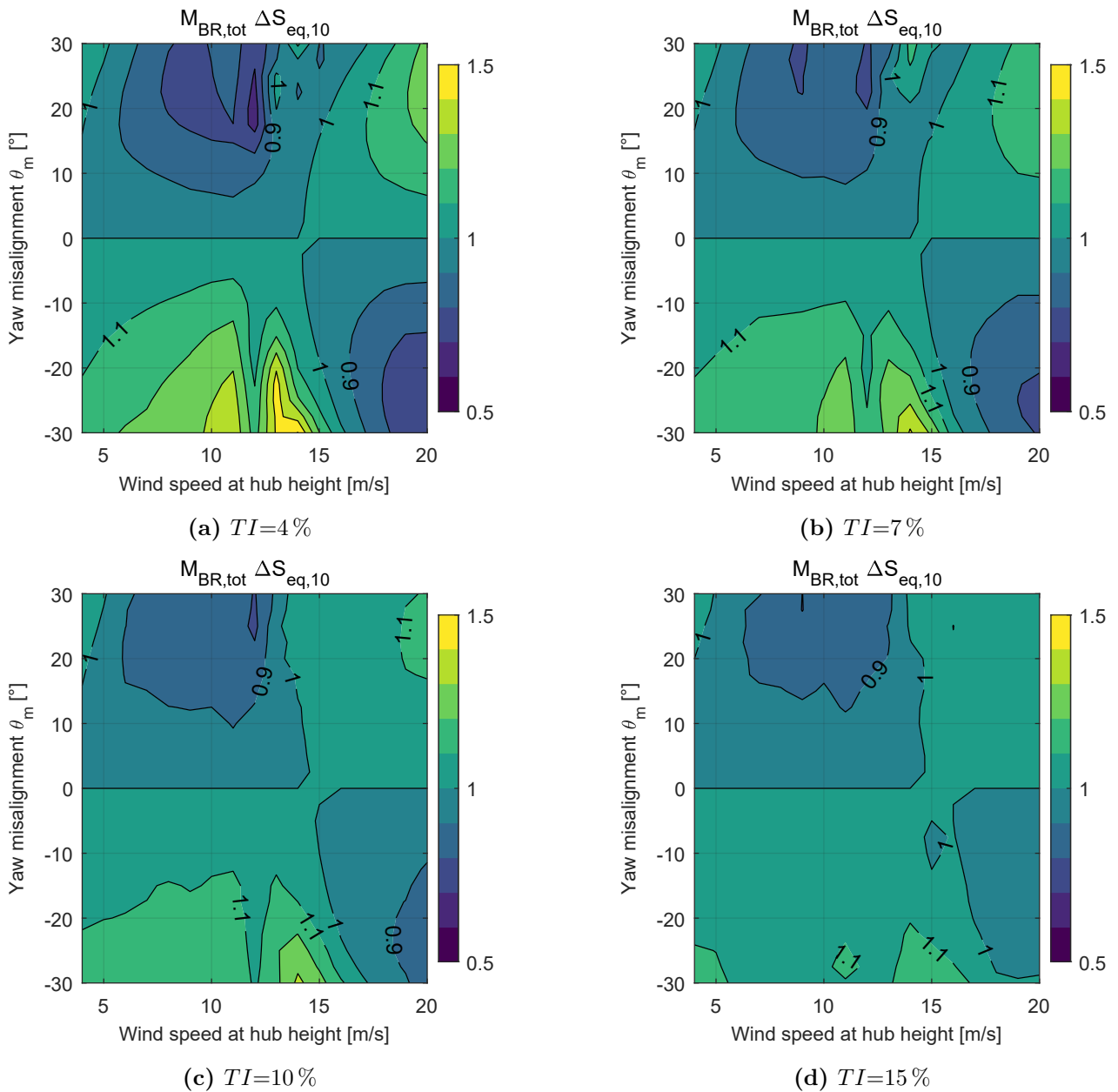


Figure A.15: Load distributions of the total bending moment at the blade-root for stable atmospheric conditions ($\alpha_{shear}=0.2$) and different TIs . Results are shown by means of the seed average and normalised with the values at $\theta_m = 0^\circ$.

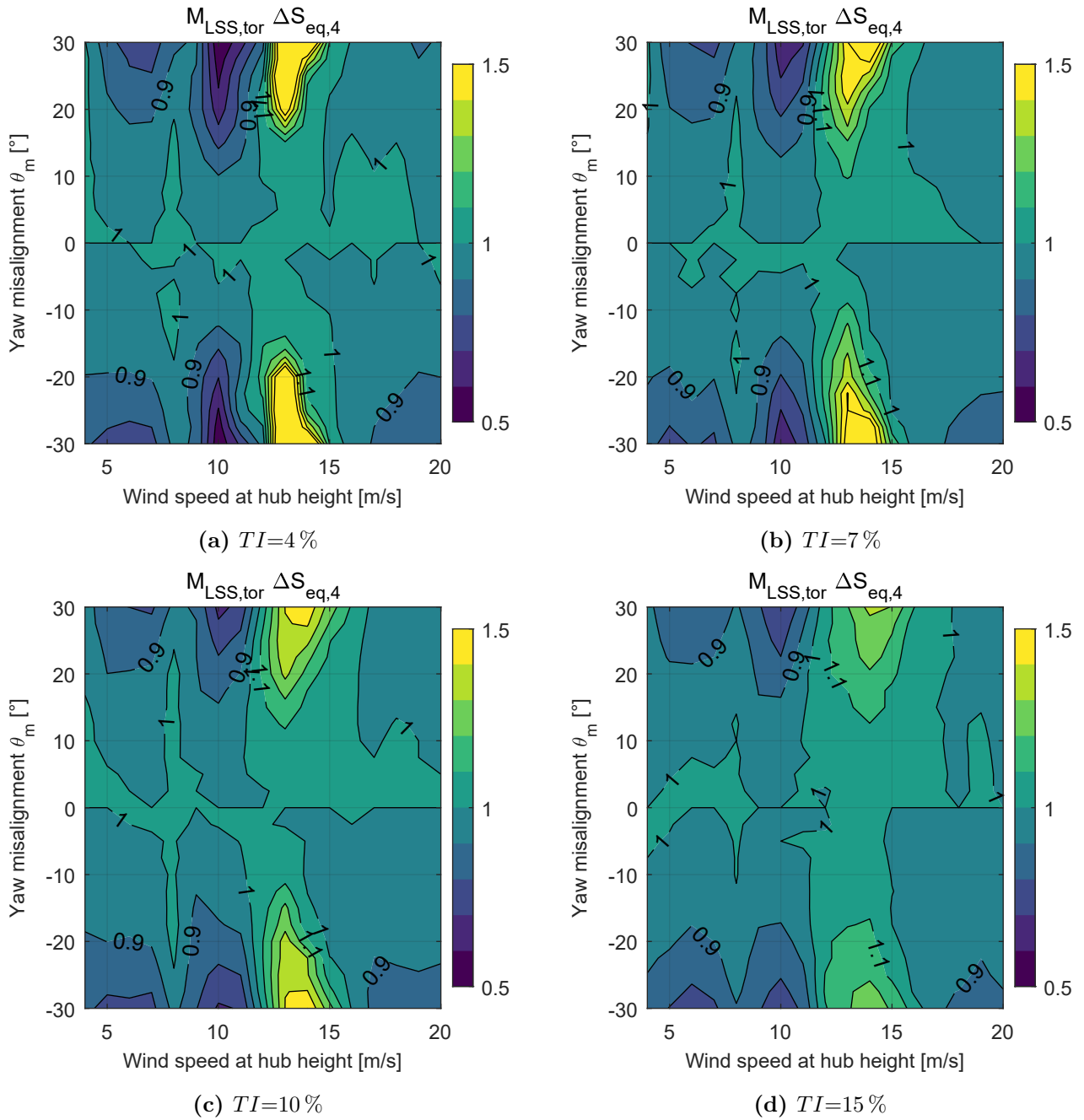


Figure A.16: Load distributions of the torsional moment at the low-speed shaft for stable atmospheric conditions ($\alpha_{\text{shear}}=0.2$) and different TIs . Results are shown by means of the seed average and normalised with the values at $\theta_m = 0^\circ$.

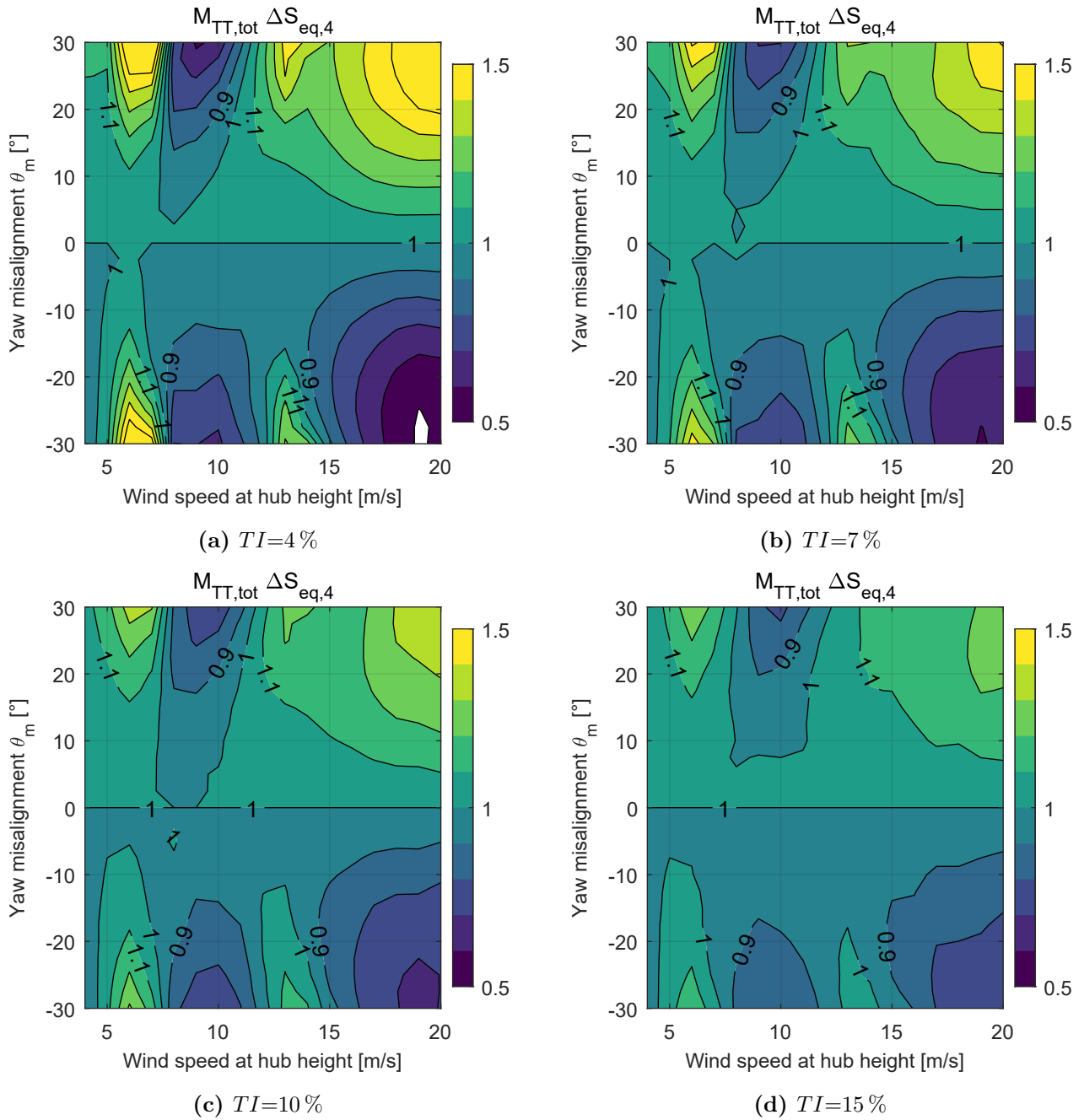


Figure A.17: Load distributions of the total bending moment at the tower-top for stable atmospheric conditions ($\alpha_{\text{shear}}=0.2$) and different TIs . Results are shown by means of the seed average and normalised with the values at $\theta_m = 0^\circ$.

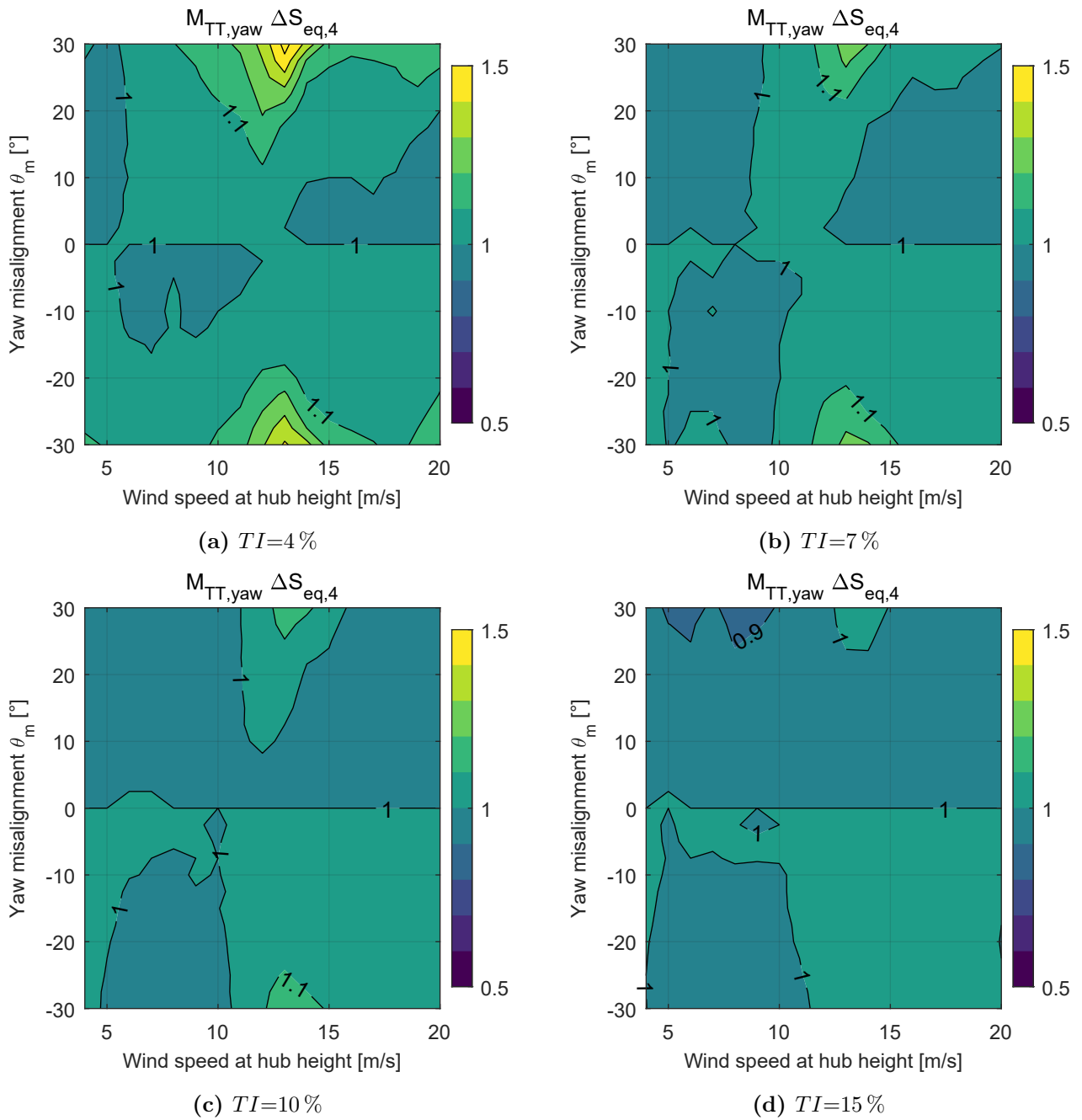


Figure A.18: Load distributions of the yawing moment at the tower-top for stable atmospheric conditions ($\alpha_{shear}=0.2$) and different TIs . Results are shown by means of the seed average and normalised with the values at $\theta_m = 0^\circ$.

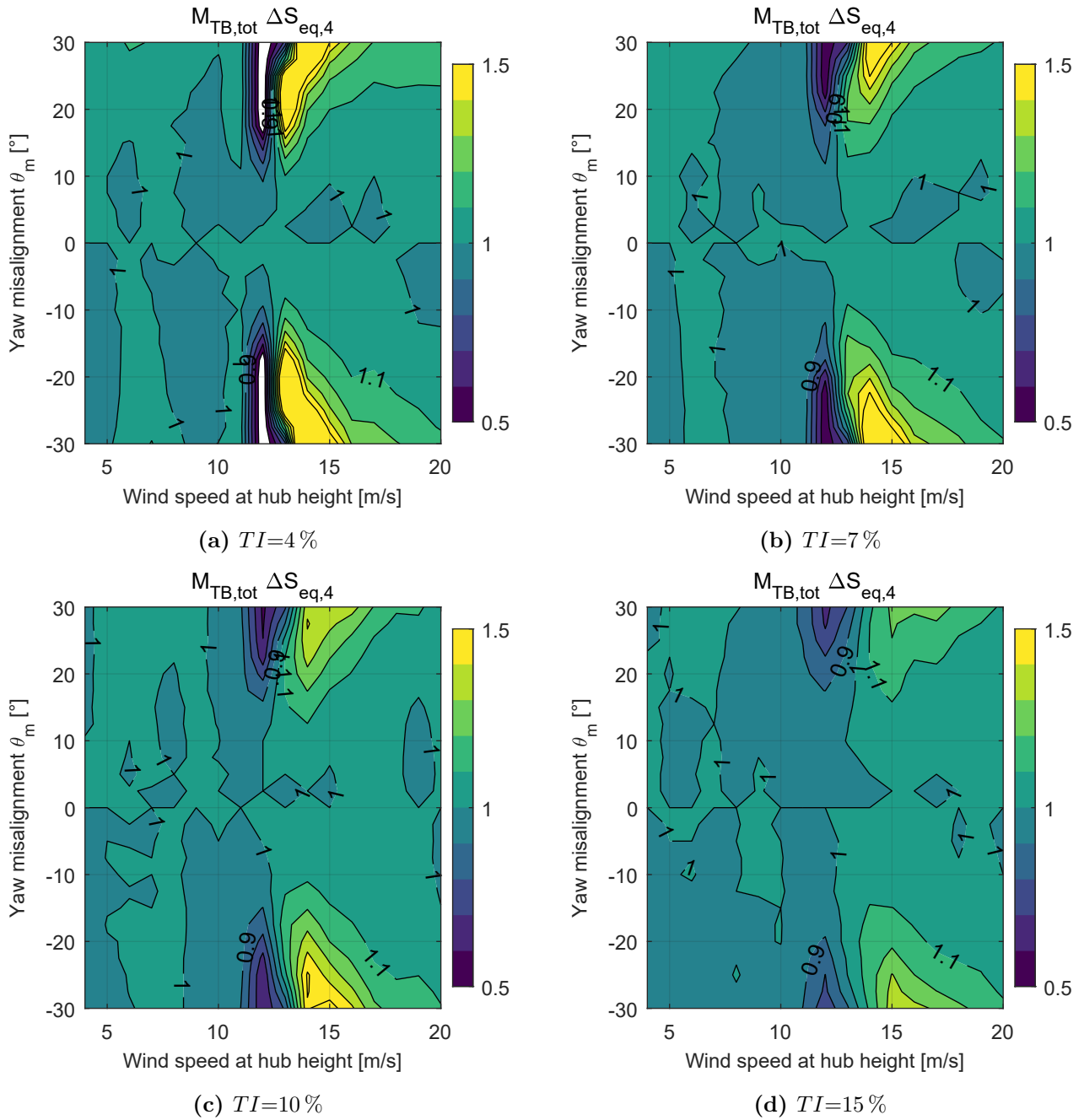


Figure A.19: Load distributions of the total bending moment at the tower-base for stable atmospheric conditions ($\alpha_{\text{shear}}=0.2$) and different TIs . Results are shown by means of the seed average and normalised with the values at $\theta_m = 0^\circ$.

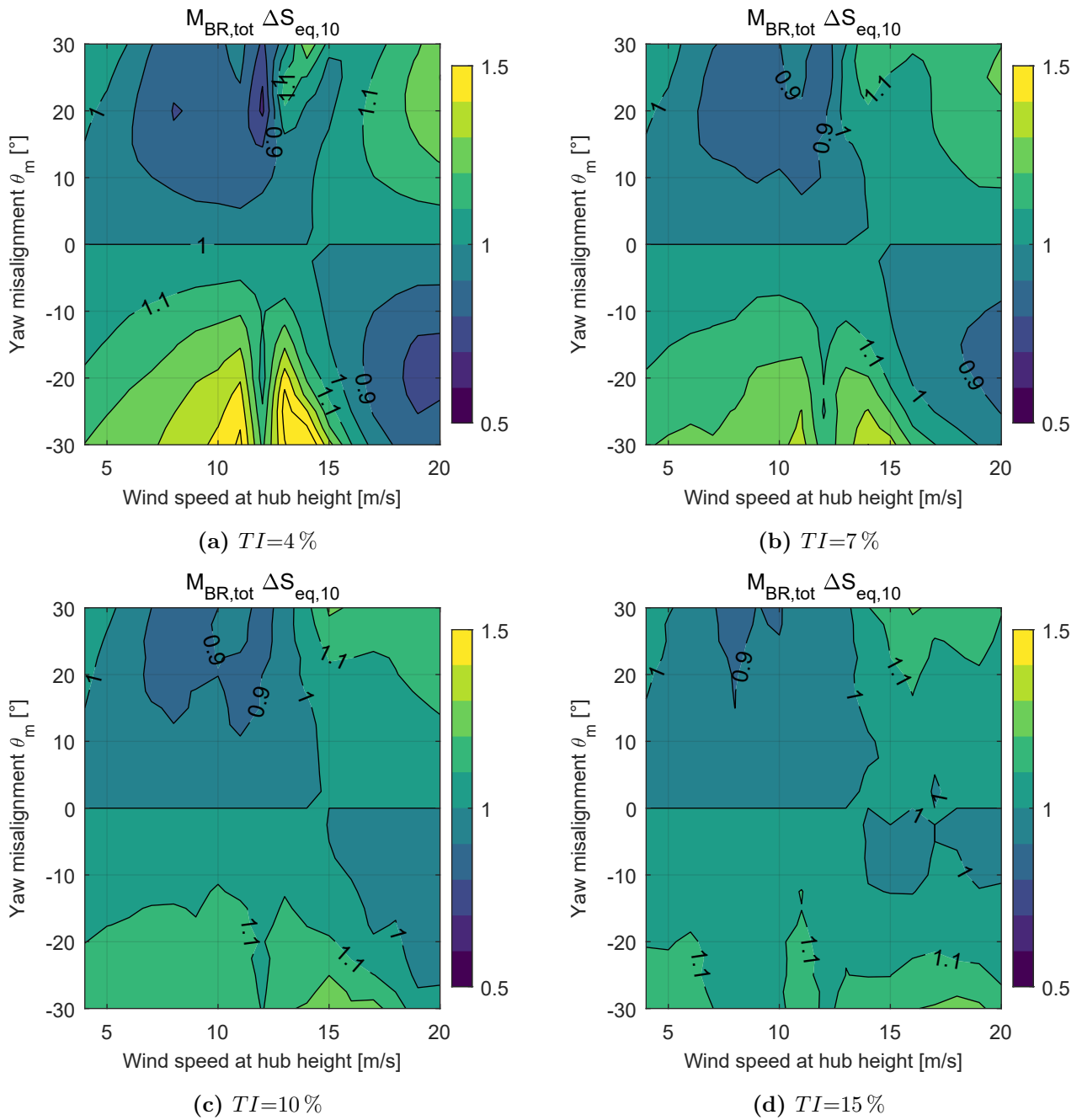


Figure A.20: Load distributions of the total bending moment at the blade-root for neutral atmospheric conditions ($\alpha_{shear}=0.1$) and different TIs . Results are shown by means of the seed average and normalised with the values at $\theta_m = 0^\circ$.

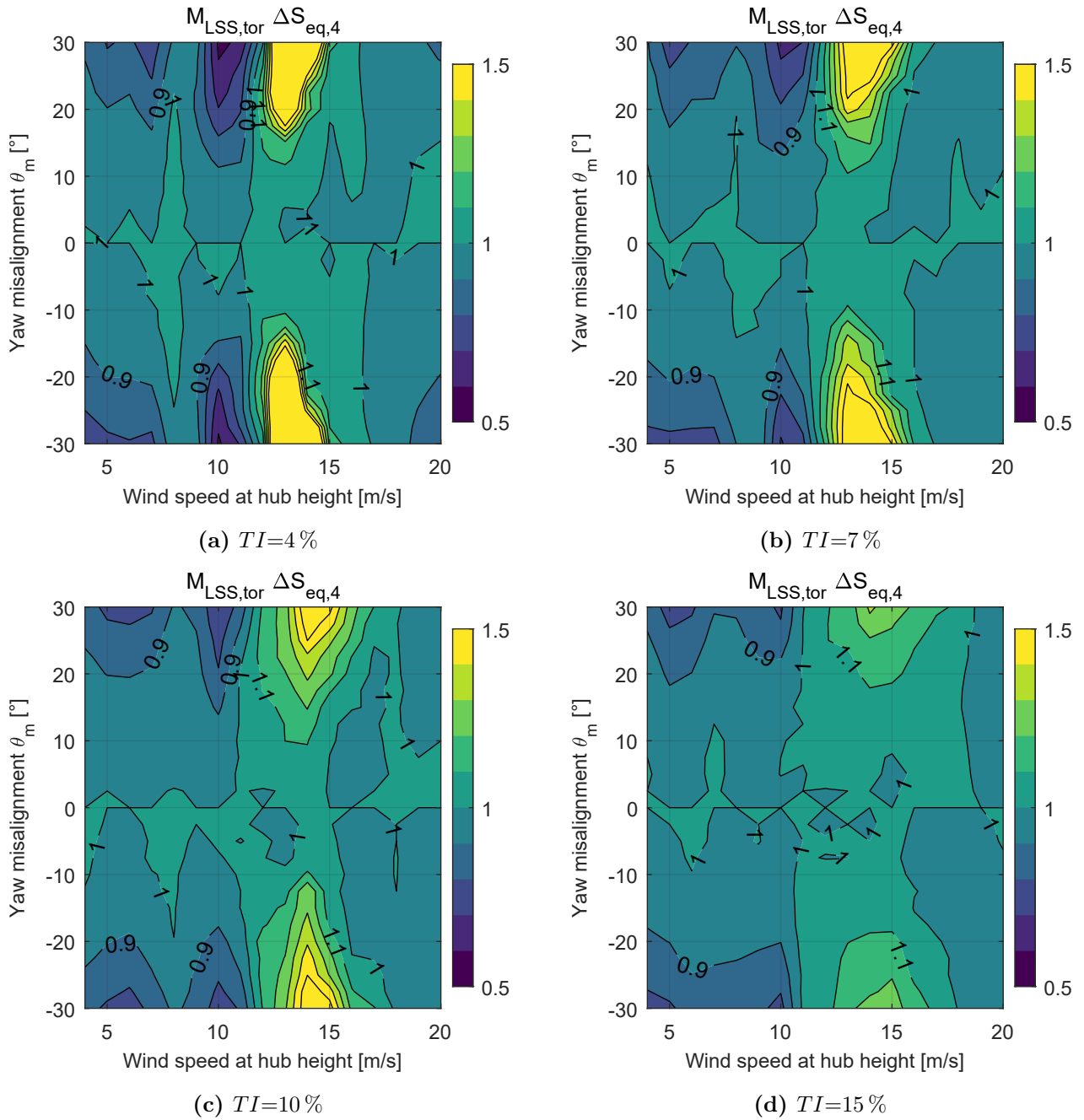


Figure A.21: Load distributions of the torsional moment at the low-speed shaft for neutral atmospheric conditions ($\alpha_{\text{shear}}=0.1$) and different TIs . Results are shown by means of the seed average and normalised with the values at $\theta_m = 0^\circ$.

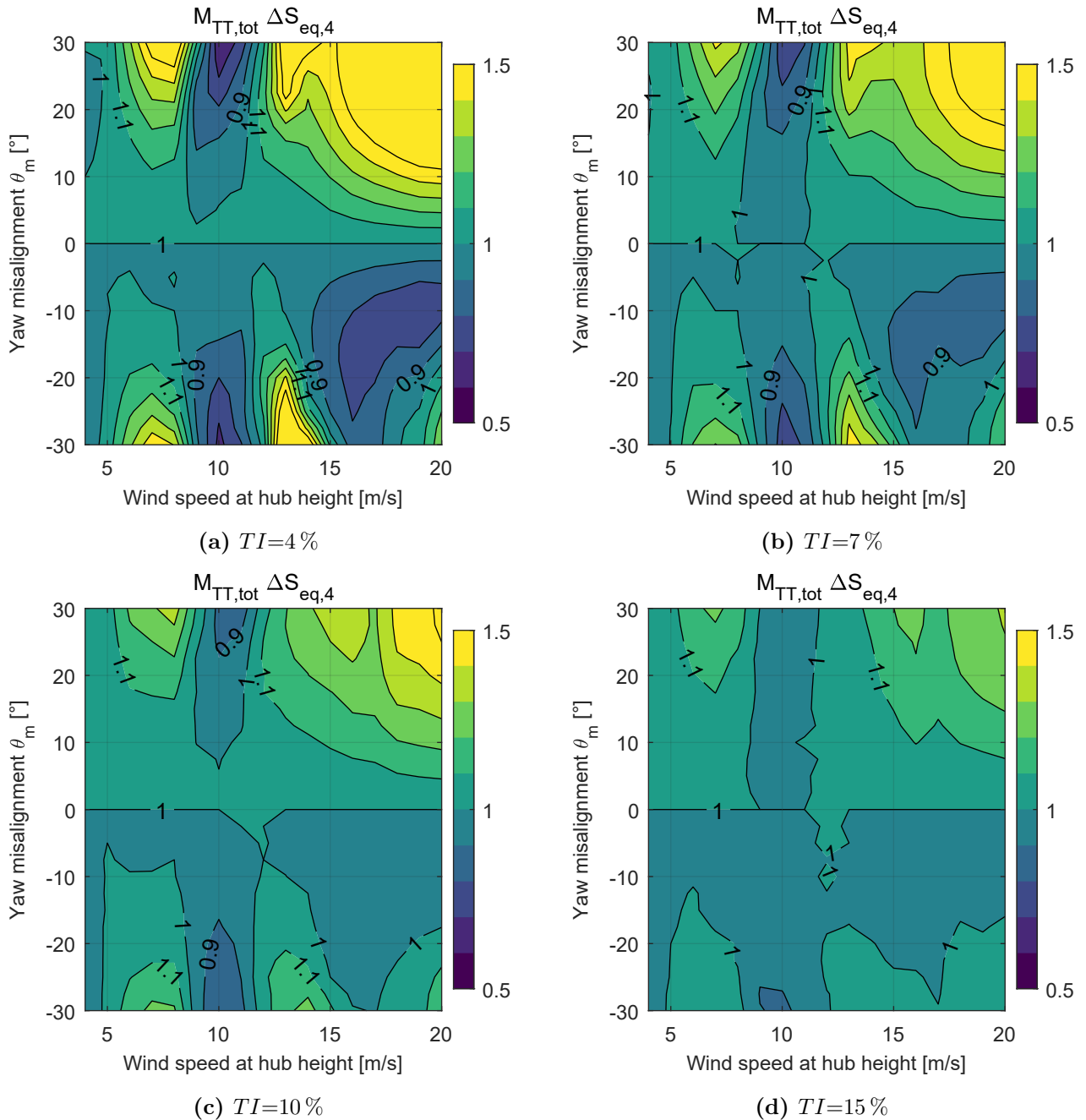


Figure A.22: Load distributions of the total bending moment at the tower-top for neutral atmospheric conditions ($\alpha_{\text{shear}}=0.1$) and different TIs . Results are shown by means of the seed average and normalised with the values at $\theta_m = 0^\circ$.

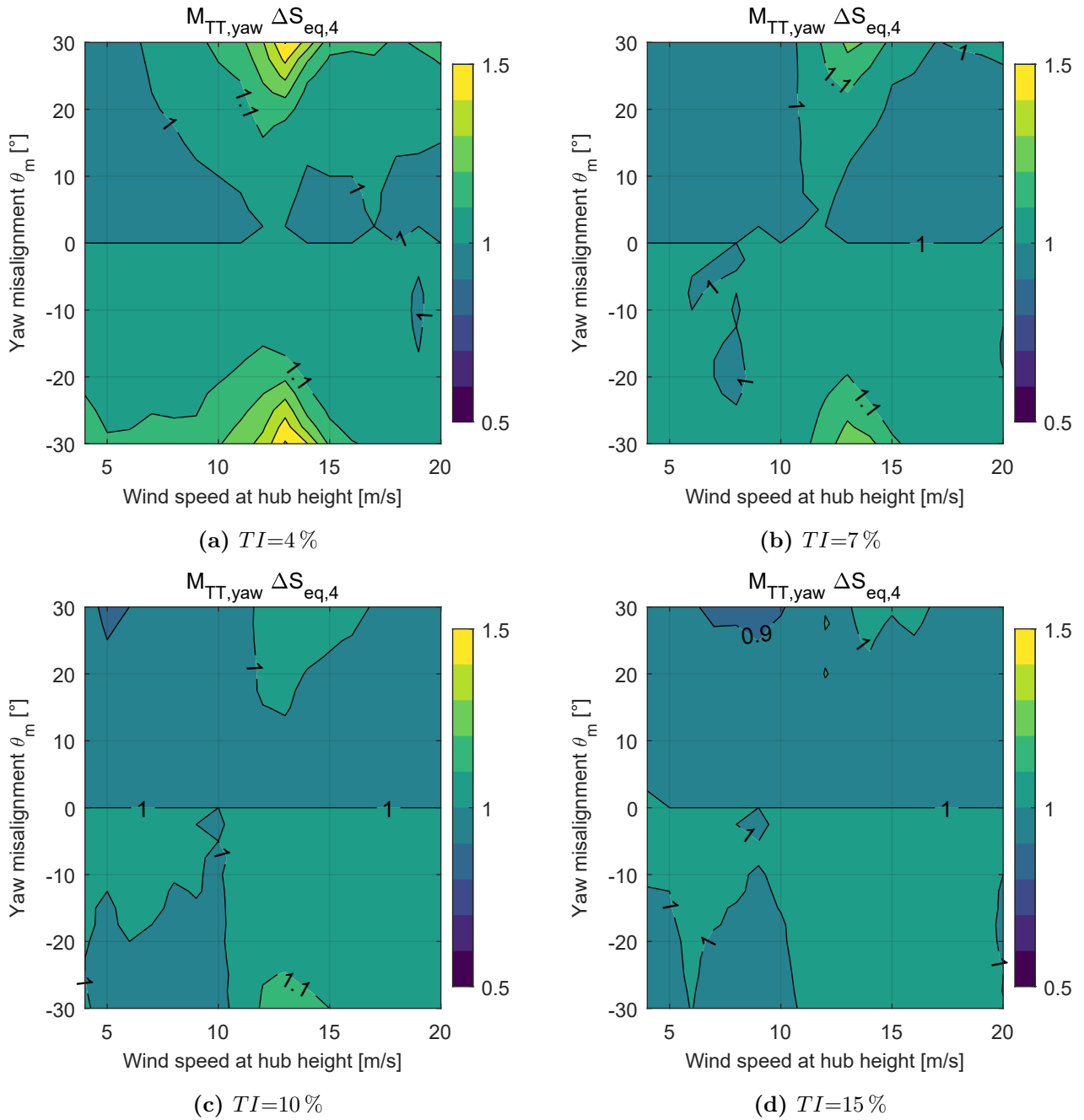


Figure A.23: Load distributions of the yawing moment at the tower-top for neutral atmospheric conditions ($\alpha_{\text{shear}}=0.1$) and different TIs . Results are shown by means of the seed average and normalised with the values at $\theta_m = 0^\circ$.

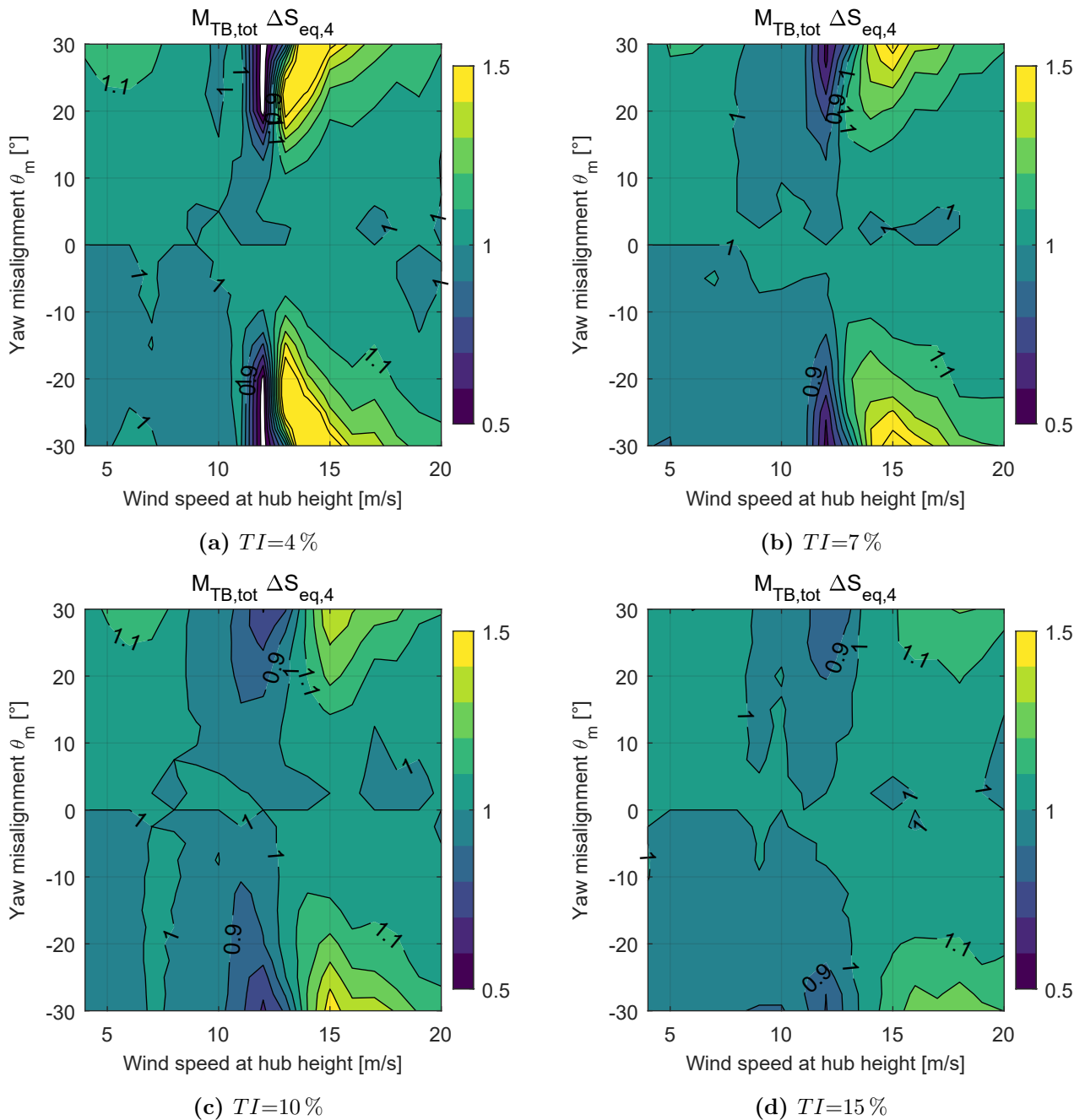


Figure A.24: Load distributions of the total bending moment at the tower-base for neutral atmospheric conditions ($\alpha_{\text{shear}}=0.1$) and different TIs . Results are shown by means of the seed average and normalised with the values at $\theta_m = 0^\circ$.

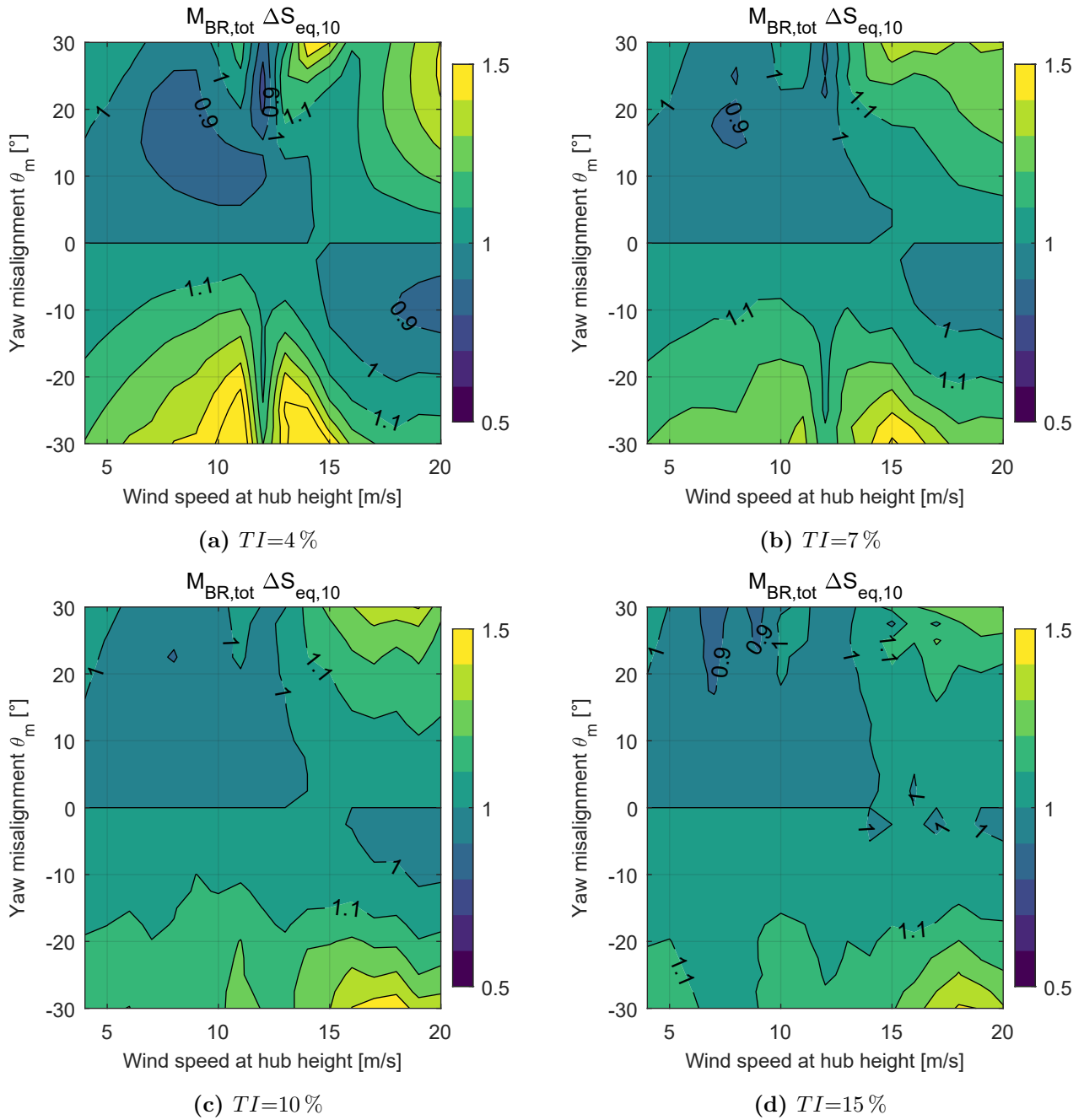


Figure A.25: Load distributions of the total bending moment at the blade-root for unstable atmospheric conditions ($\alpha_{shear}=0.03$) and different TIs . Results are shown by means of the seed average and normalised with the values at $\theta_m = 0^\circ$.

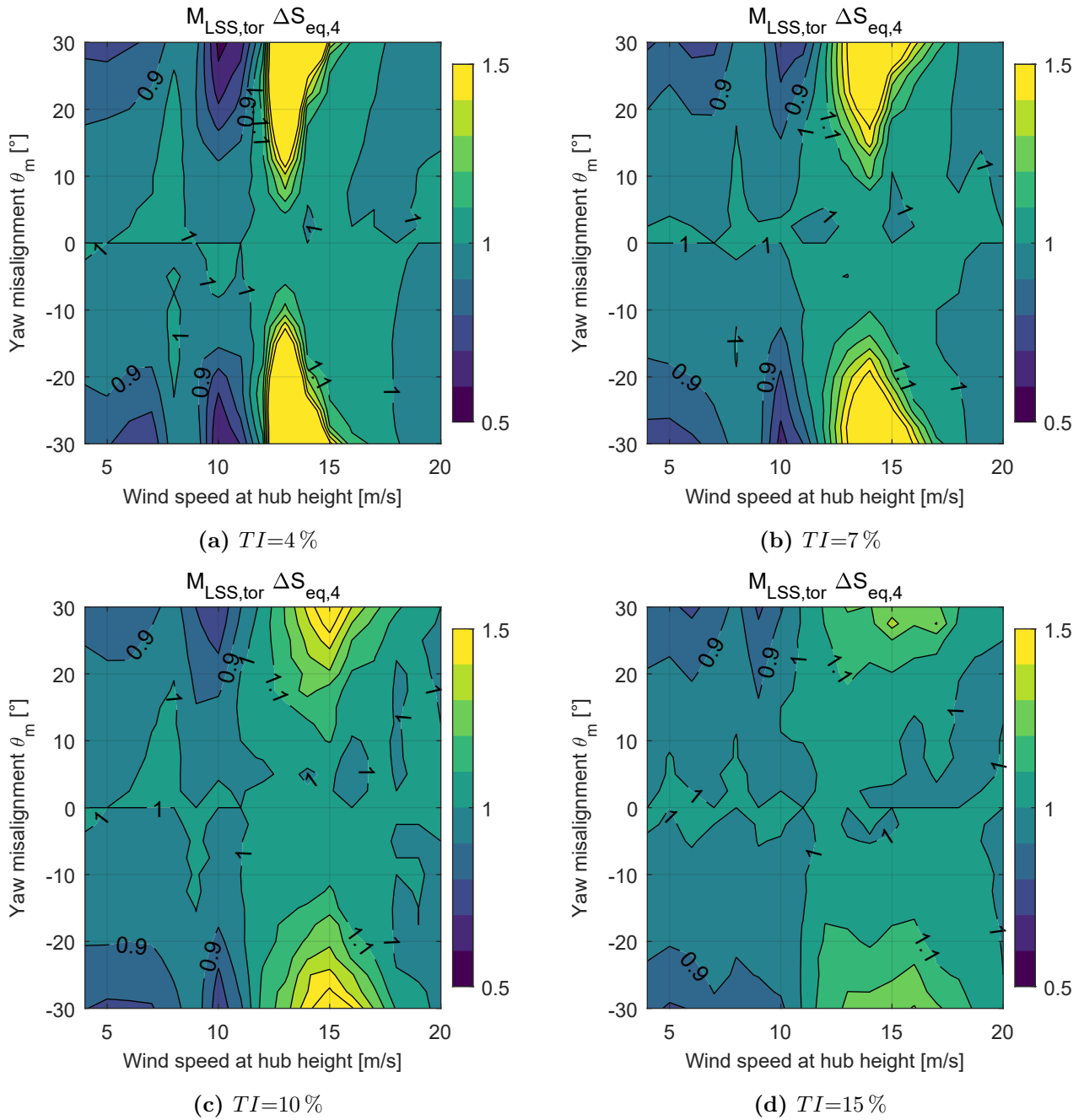


Figure A.26: Load distributions of the torsional moment at the low-speed shaft for unstable atmospheric conditions ($\alpha_{\text{shear}}=0.03$) and different TIs . Results are shown by means of the seed average and normalised with the values at $\theta_m = 0^\circ$.

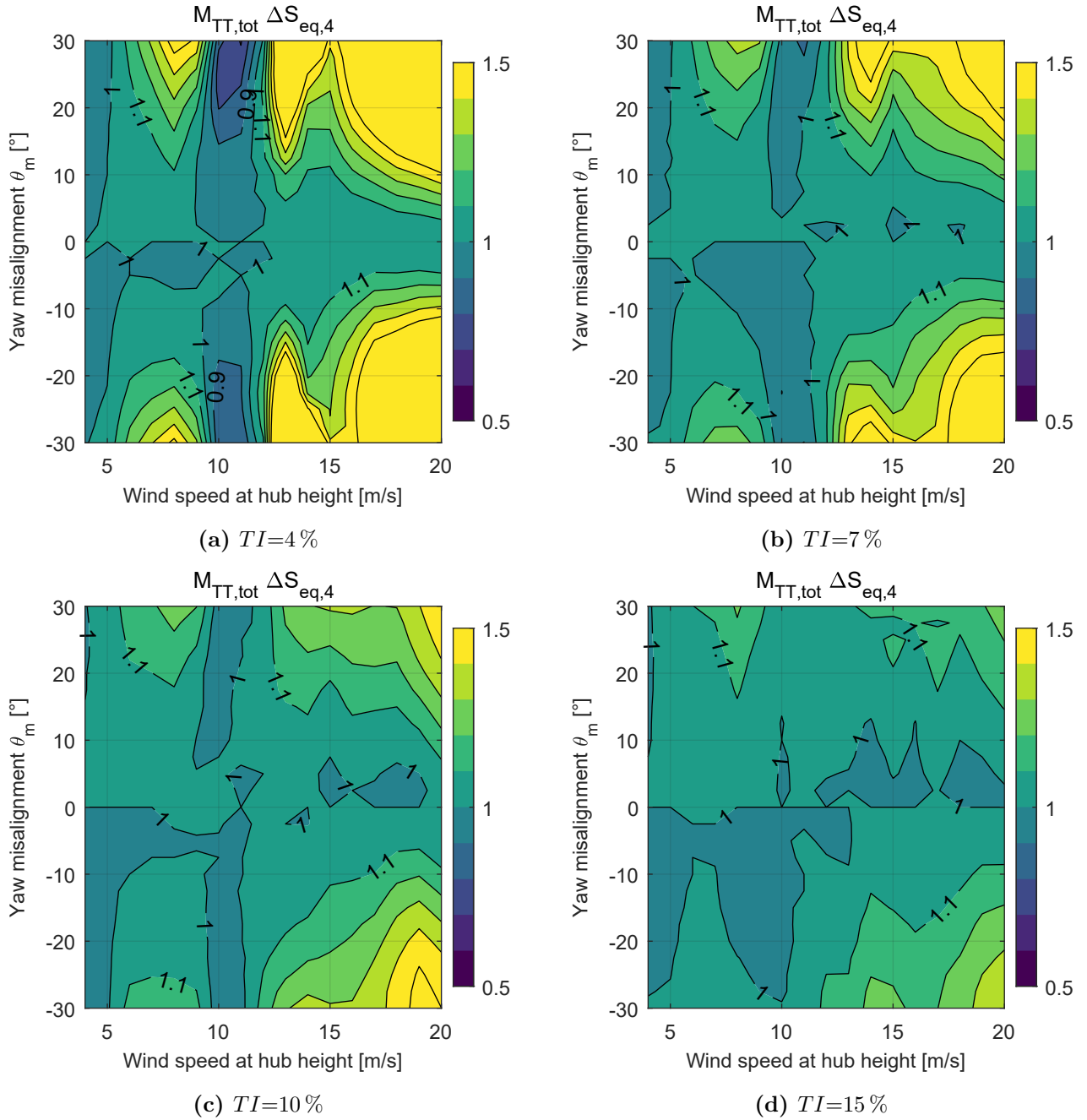


Figure A.27: Load distributions of the total bending moment at the tower-top for unstable atmospheric conditions ($\alpha_{shear}=0.03$) and different TIs . Results are shown by means of the seed average and normalised with the values at $\theta_m = 0^\circ$.

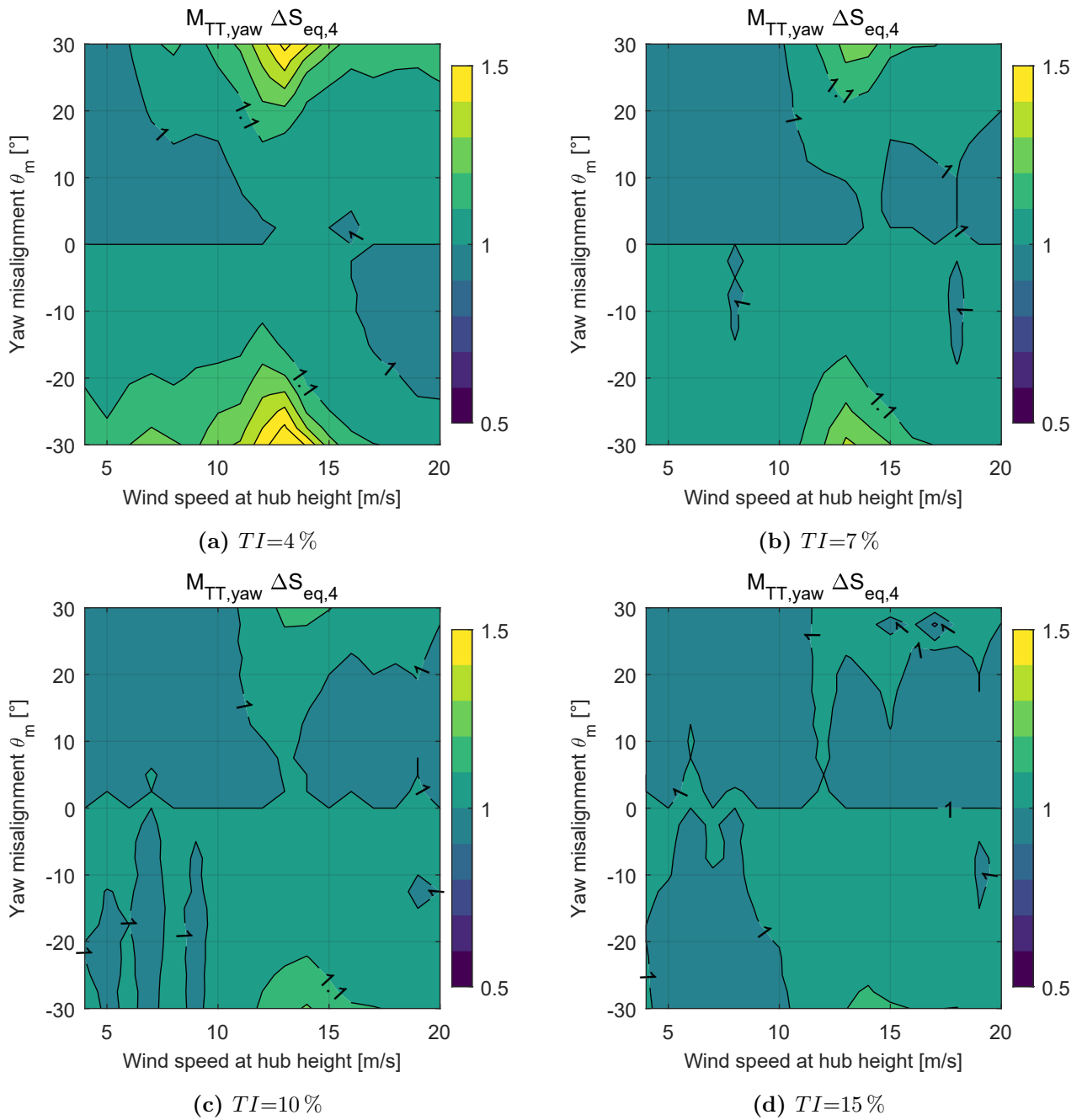


Figure A.28: Load distributions of the yawing moment at the tower-top for unstable atmospheric conditions ($\alpha_{shear}=0.03$) and different TIs . Results are shown by means of the seed average and normalised with the values at $\theta_m = 0^\circ$.

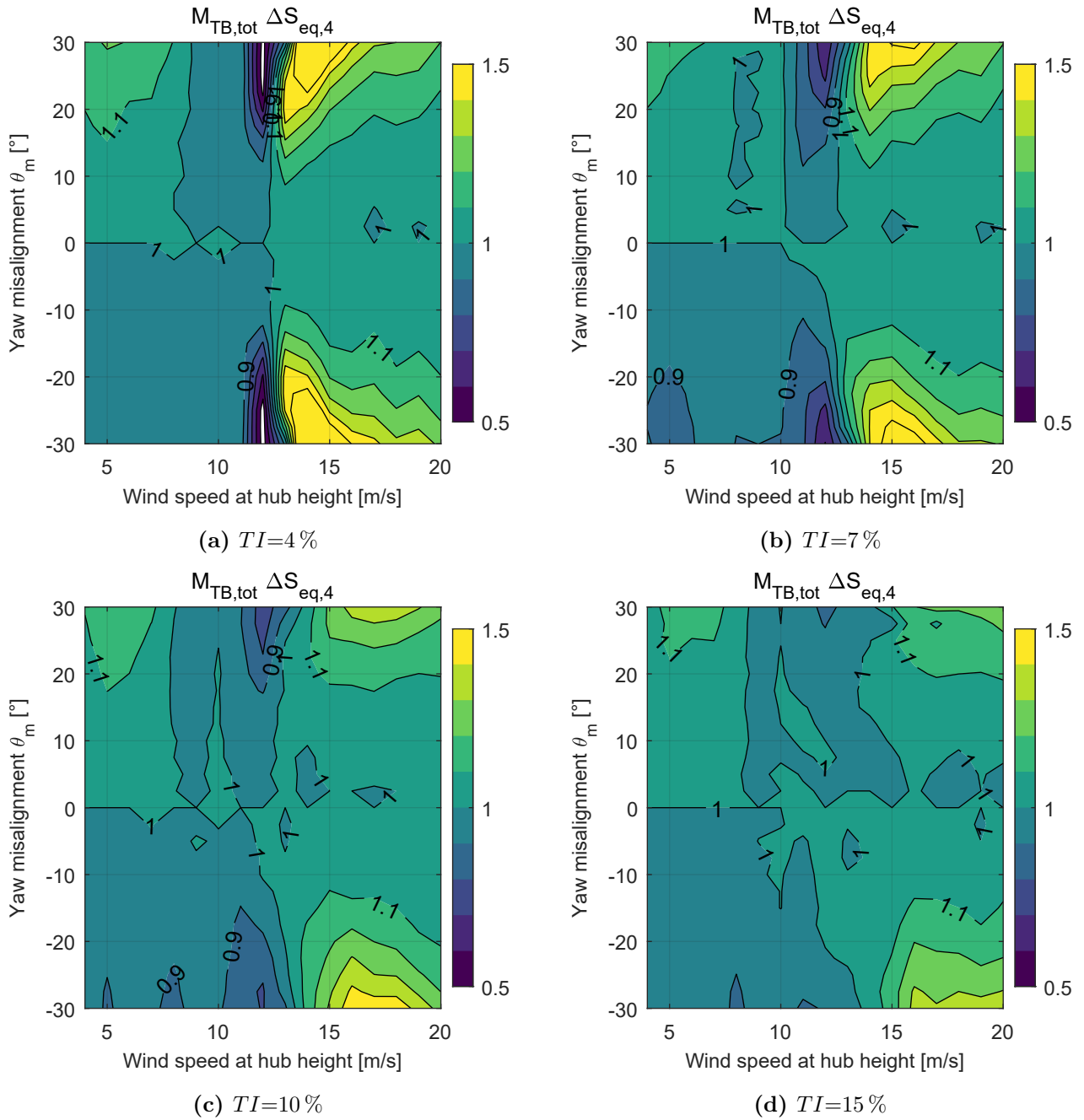
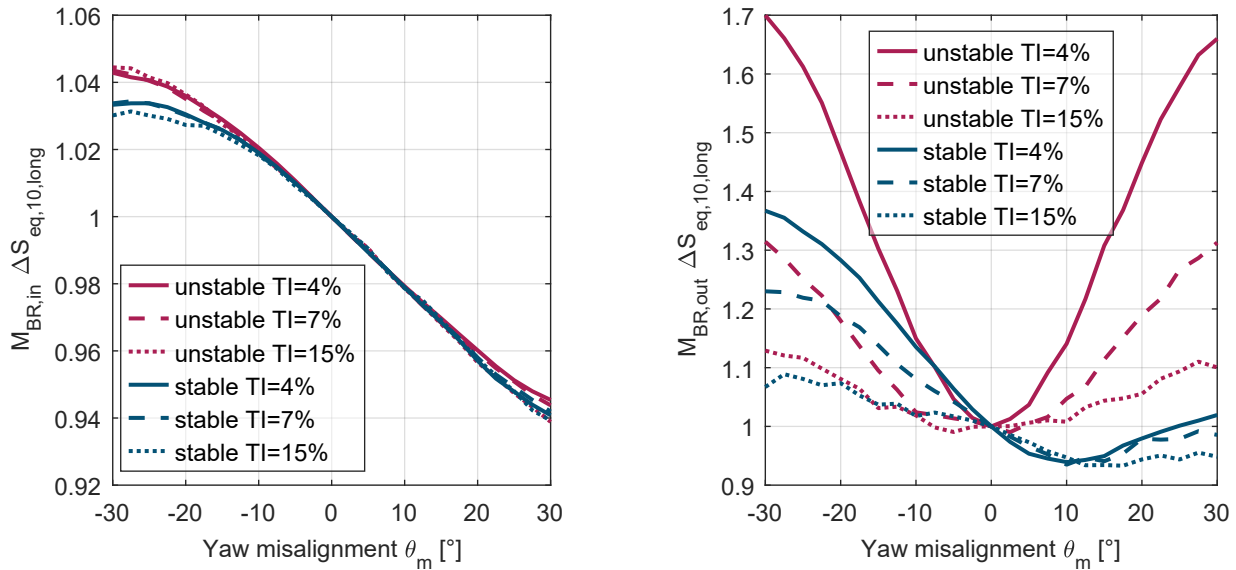


Figure A.29: Load distributions of the total bending moment at the tower-base for unstable atmospheric conditions ($\alpha_{\text{shear}}=0.03$) and different TIs . Results are shown by means of the seed average and normalised with the values at $\theta_m = 0^\circ$.

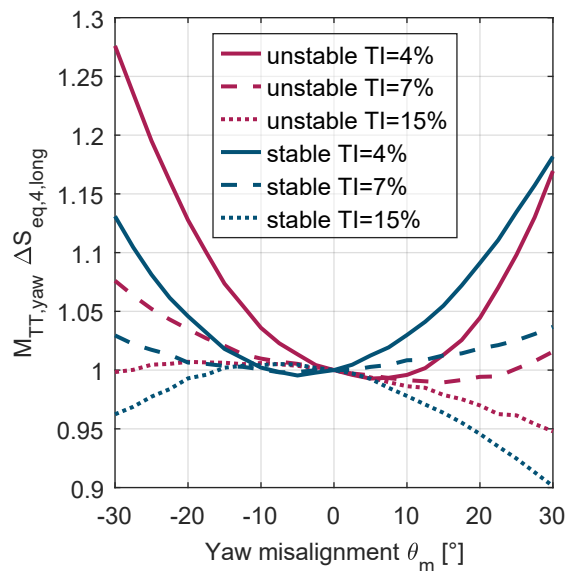
A.4.2 Long-term evaluation

The Figures A.30-A.32 contain additional results from the long-term investigation of the load distributions of a free stream turbine in yawed operation that is presented in Section 5.3.



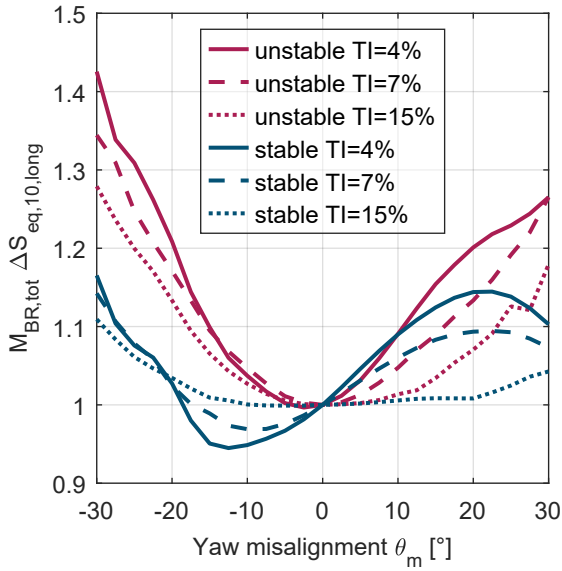
(a) In-plane bending moment at the blade-root.

(b) Out-of-plane bending moment at the blade-root.

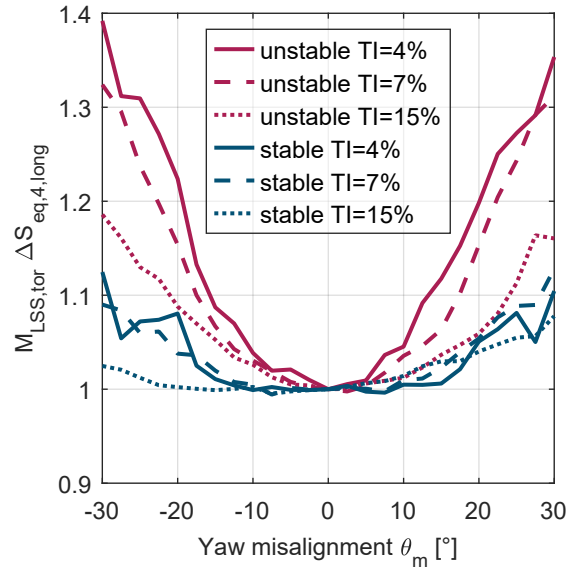


(c) Yawing moment at the tower-top

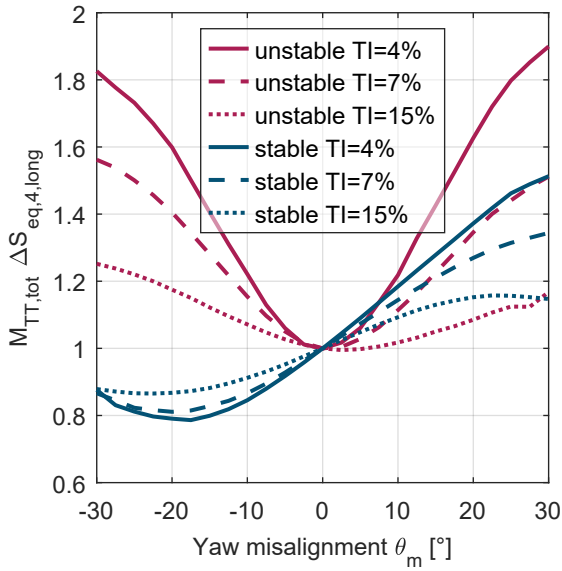
Figure A.30: Long-term DEL distributions at various locations based on the Weibull distribution given in Figure 5.2 for below rated wind speeds ($4 - 11 \text{ m s}^{-1}$). Results are normalised with the values at $\theta_m = 0^\circ$.



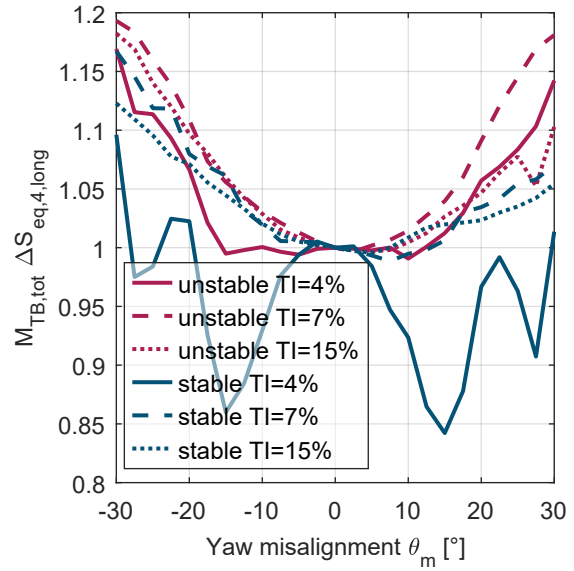
(a) Total bending moment at the blade-root.



(b) Torsional moment at the low-speed shaft.

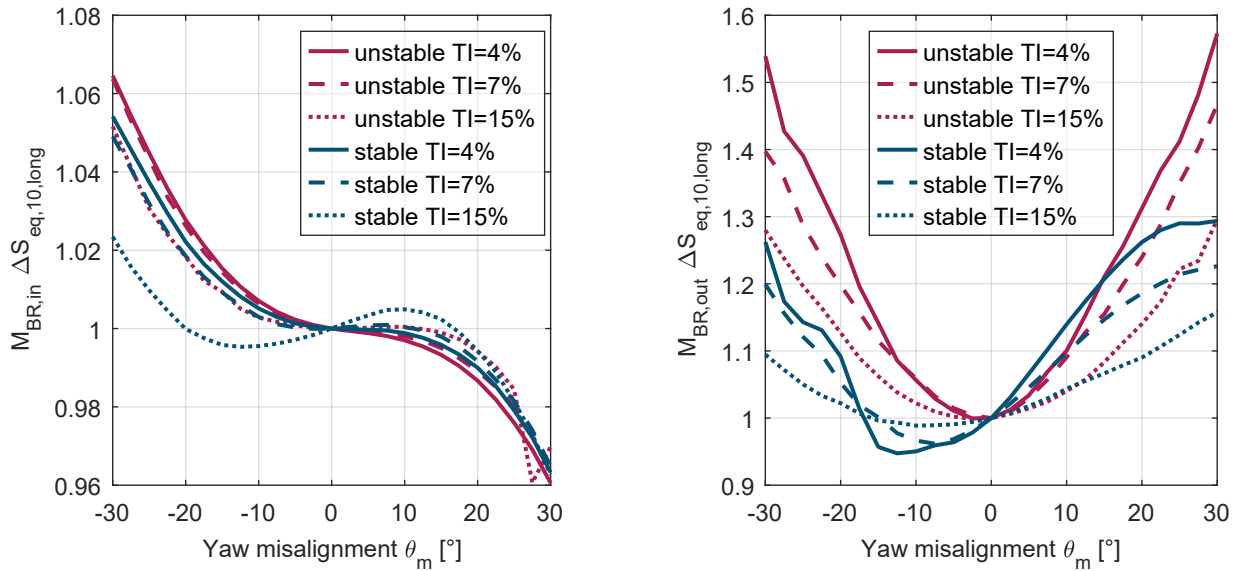


(c) Total bending moment at the tower-top.



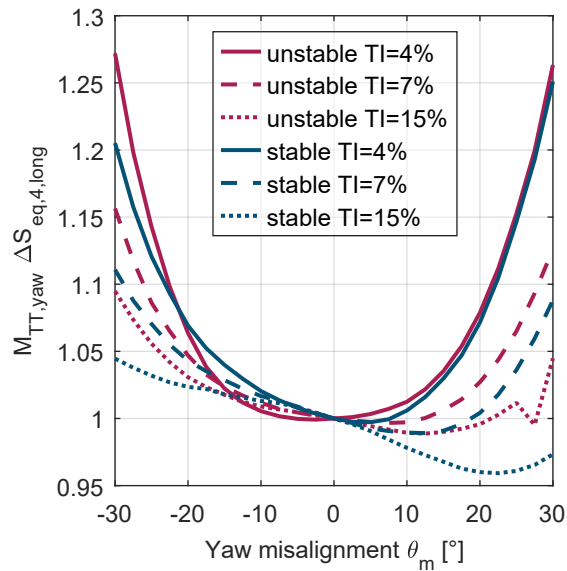
(d) Total bending moment at the tower-base.

Figure A.31: Long-term DEL distributions at various locations based on the Weibull distribution given in Figure 5.2 for above rated wind speeds ($12 - 20 \text{ ms}^{-1}$). Results are normalised with the values at $\theta_m = 0^\circ$.



(a) In-plane bending moment at the blade-root.

(b) Out-of-plane bending moment at the blade-root.



(c) Yawing moment at the tower-top

Figure A.32: Long-term DEL distributions at various locations based on the Weibull distribution given in Figure 5.2 for above rated wind speeds ($12 - 20 \text{ m s}^{-1}$). Results are normalised with the values at $\theta_m = 0^\circ$.

A.5 Additional load distributions of a waked turbine in yawed operation

The Figures A.33-A.47 contain additional results from the investigation of the load distributions of a waked turbine in yawed operation that is presented in Section 5.5.

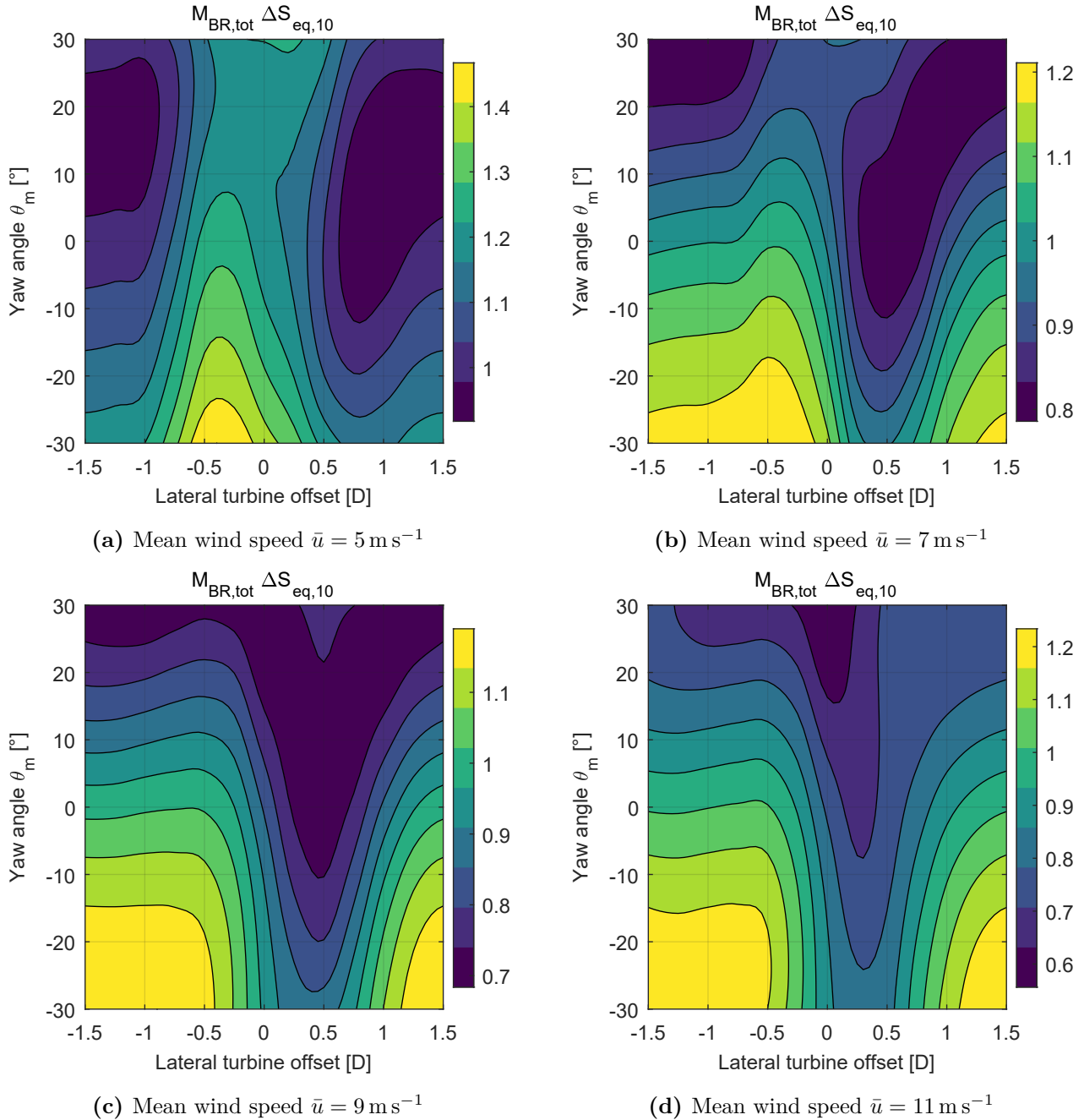


Figure A.33: Load distributions of the total bending moment at the blade-root for stable atmospheric conditions ($\alpha_{shear}=0.2$) and different wind speeds. Results are shown by means of the seed average and normalised with the values at $\theta_m = 0^\circ$ of the free stream turbine.

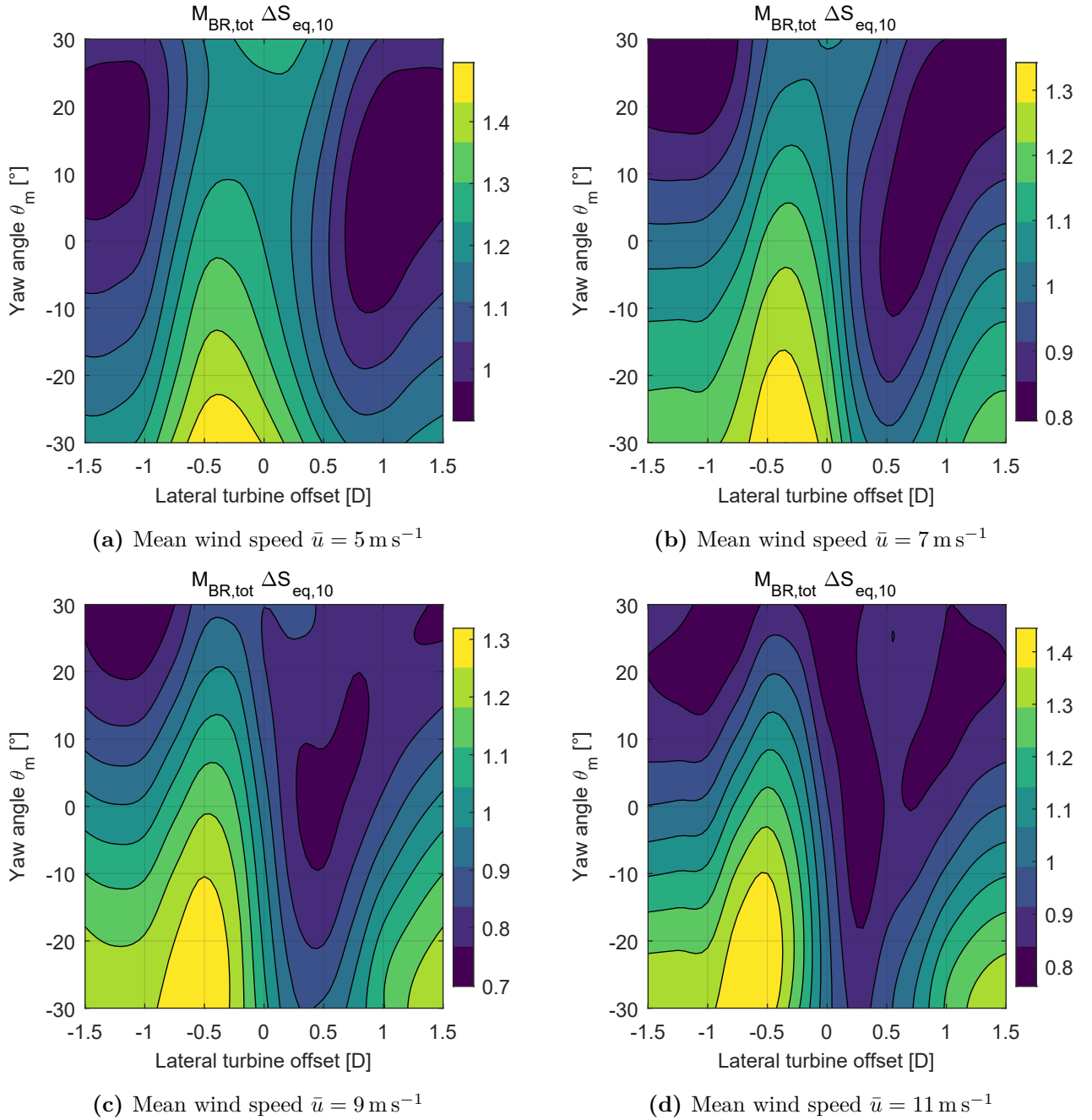


Figure A.34: Load distributions of the total bending moment at the blade-root for neutral atmospheric conditions ($\alpha_{\text{shear}}=0.1$) and different wind speeds. Results are shown by means of the seed average and normalised with the values at $\theta_m = 0^\circ$ of the free stream turbine.

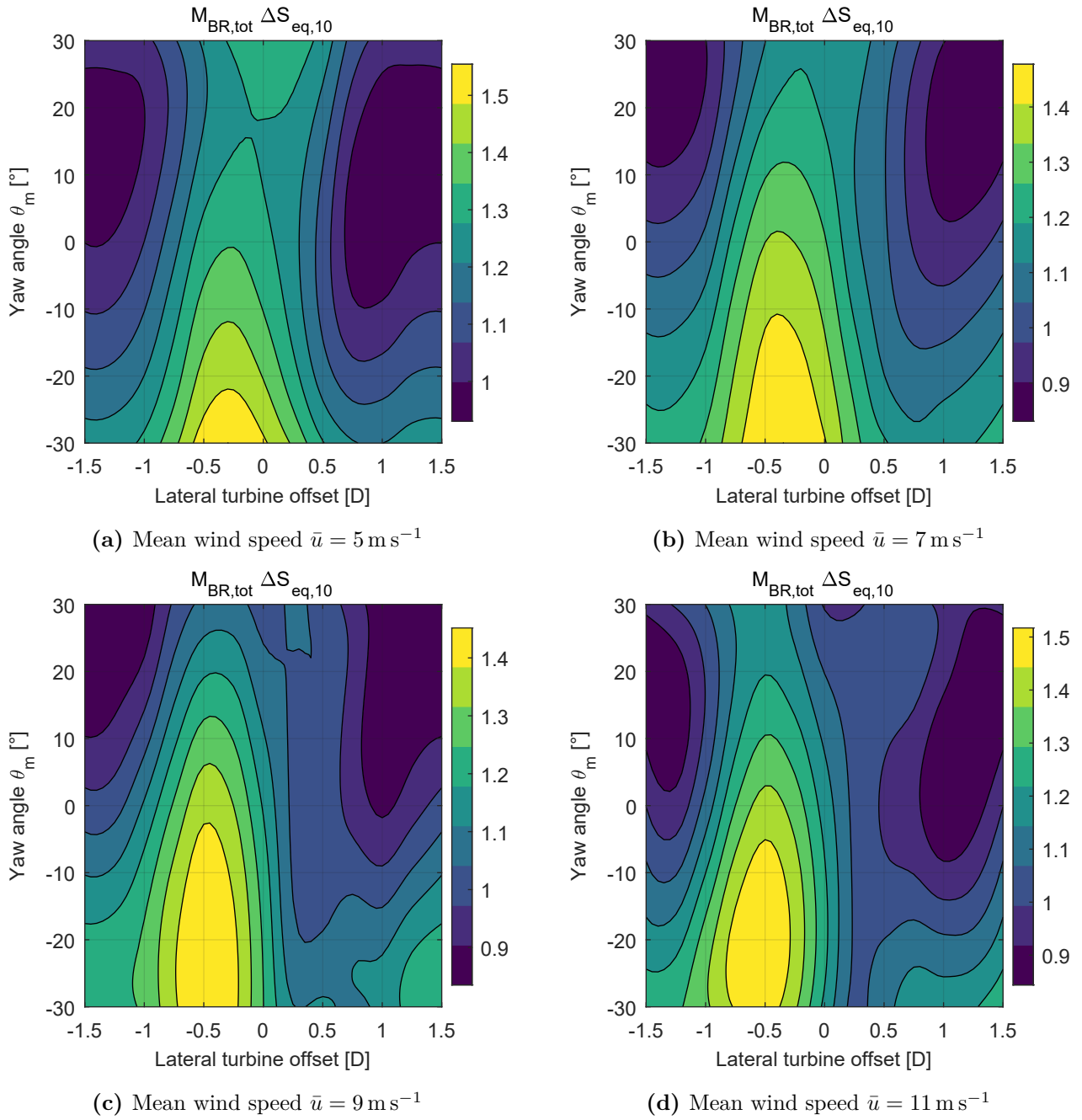


Figure A.35: Load distributions of the total bending moment at the blade-root for unstable atmospheric conditions ($\alpha_{shear}=0.03$) and different wind speeds. Results are shown by means of the seed average and normalised with the values at $\theta_m = 0^\circ$ of the free stream turbine.

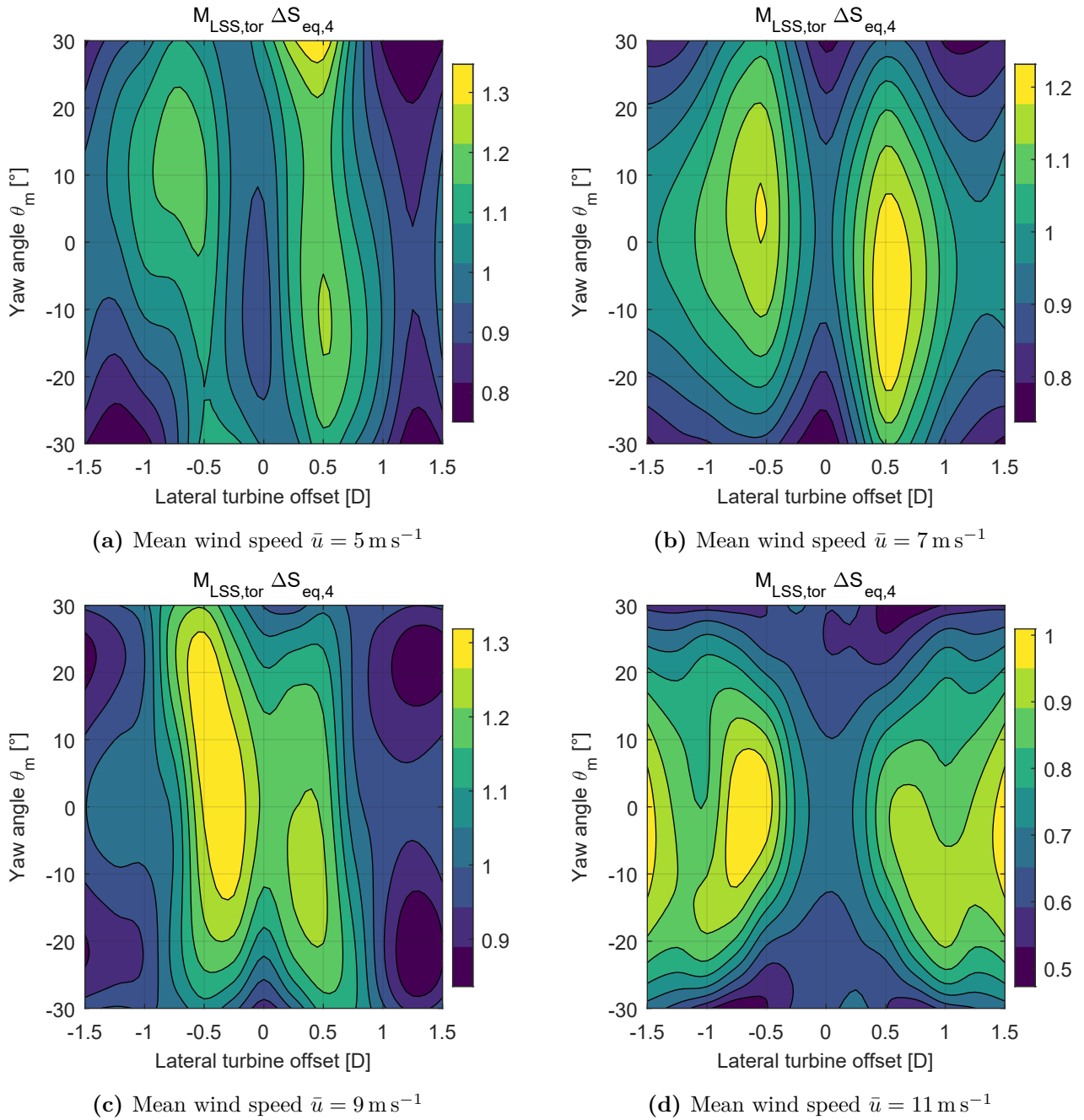


Figure A.36: Load distributions of the torsional moment at the low-speed shaft for stable atmospheric conditions ($\alpha_{\text{shear}}=0.2$) and different wind speeds. Results are shown by means of the seed average and normalised with the values at $\theta_m = 0^\circ$ of the free stream turbine.

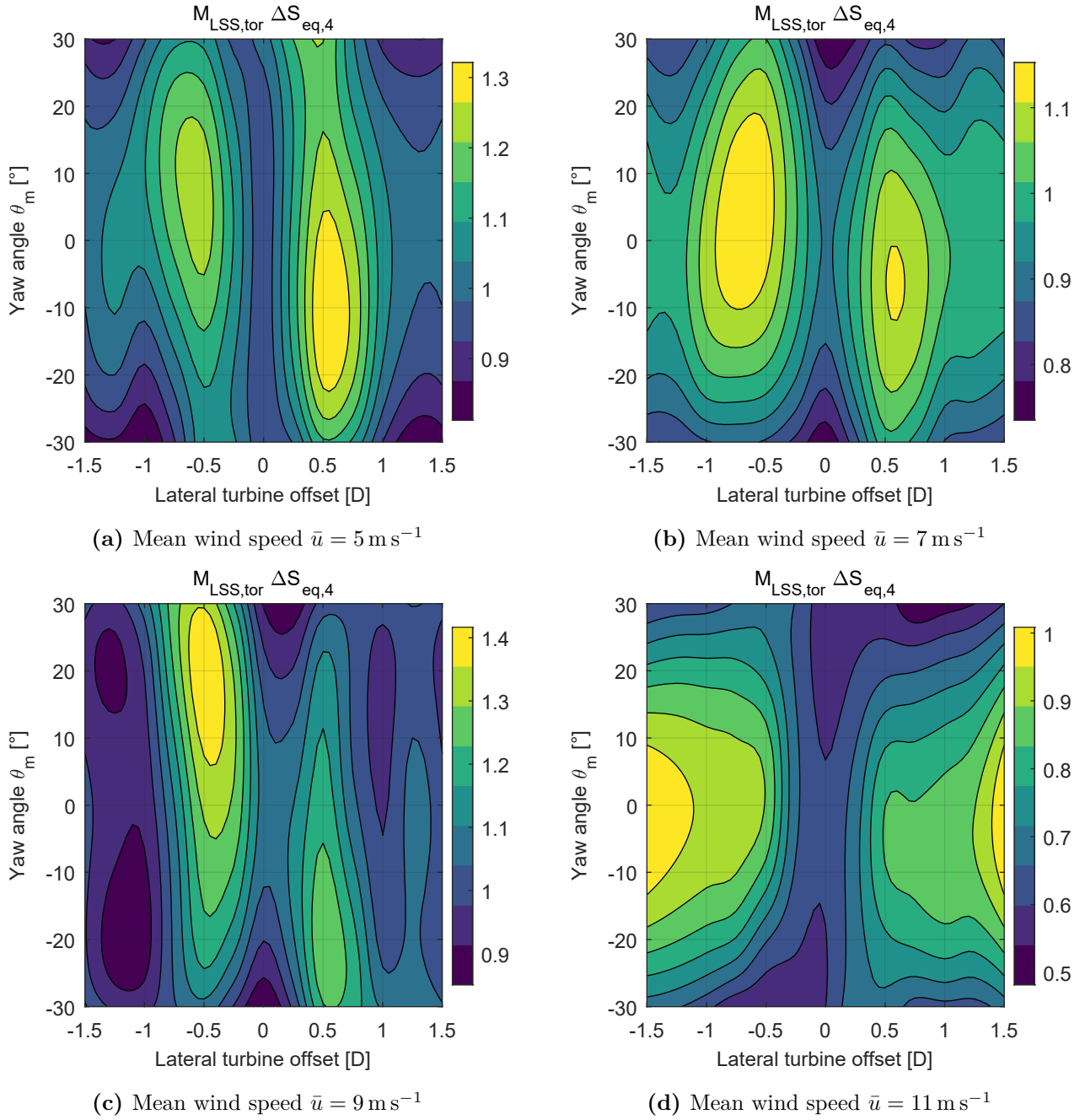


Figure A.37: Load distributions of the torsional moment at the low-speed shaft for neutral atmospheric conditions ($\alpha_{\text{shear}}=0.1$) and different wind speeds. Results are shown by means of the seed average and normalised with the values at $\theta_m = 0^\circ$ of the free stream turbine.

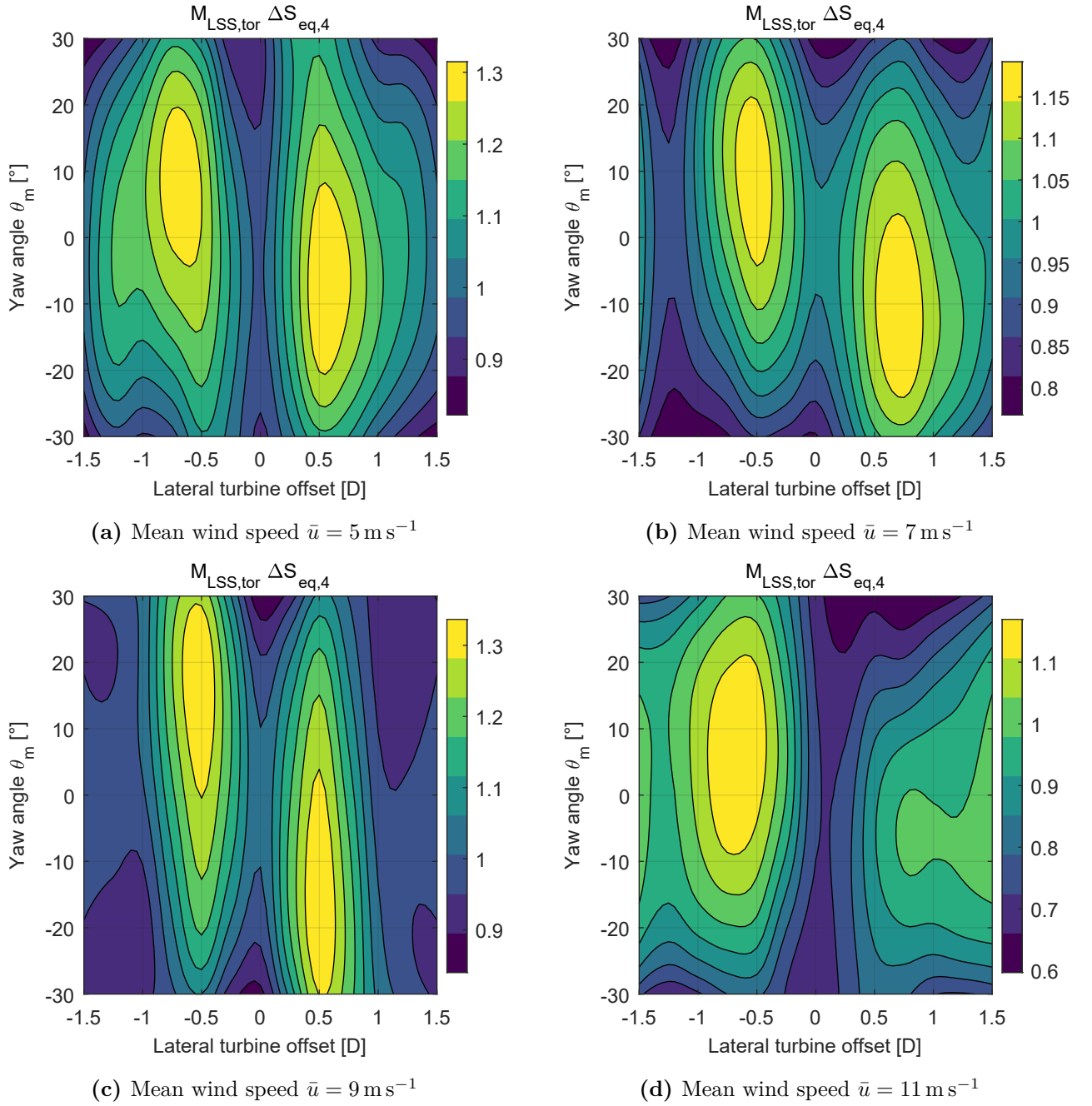


Figure A.38: Load distributions of the torsional moment at the low-speed shaft for unstable atmospheric conditions ($\alpha_{\text{shear}}=0.03$) and different wind speeds. Results are shown by means of the seed average and normalised with the values at $\theta_m = 0^\circ$ of the free stream turbine.

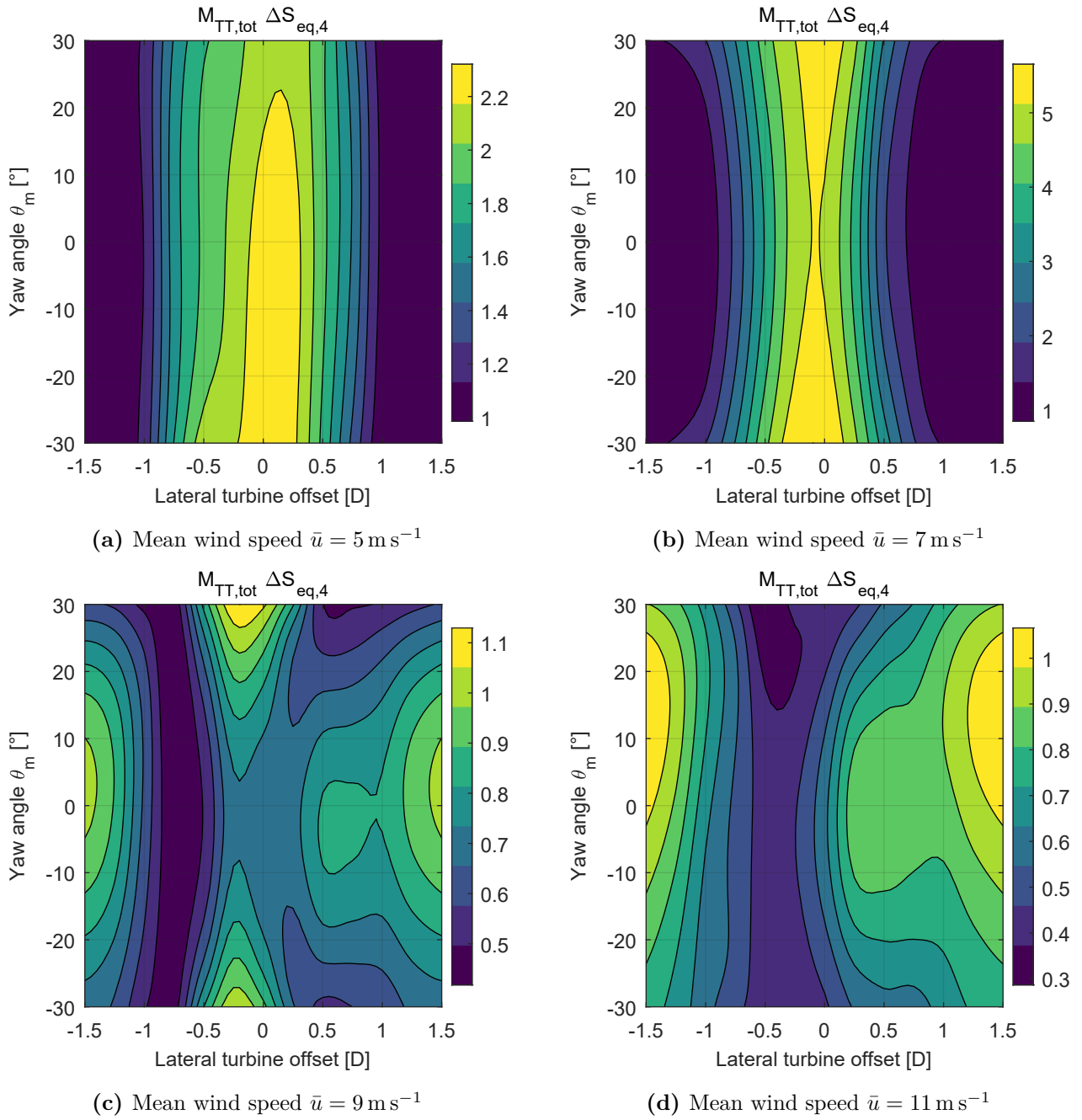


Figure A.39: Load distributions of the total bending moment at the tower-top for stable atmospheric conditions ($\alpha_{\text{shear}}=0.2$) and different wind speeds. Results are shown by means of the seed average and normalised with the values at $\theta_m = 0^\circ$ of the free stream turbine.

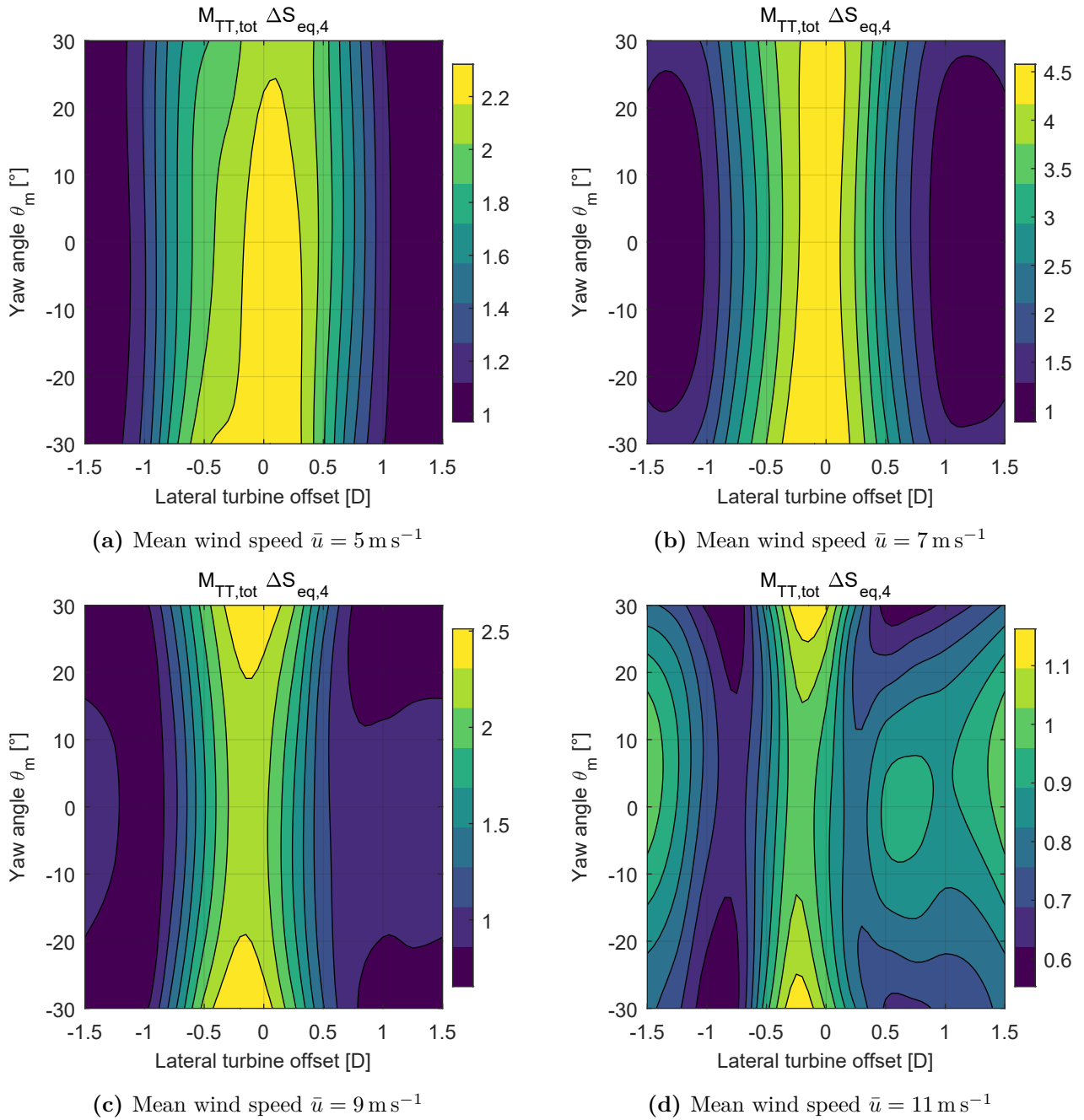


Figure A.40: Load distributions of the total bending moment at the tower-top for neutral atmospheric conditions ($\alpha_{\text{shear}}=0.1$) and different wind speeds. Results are shown by means of the seed average and normalised with the values at $\theta_m = 0^\circ$ of the free stream turbine.

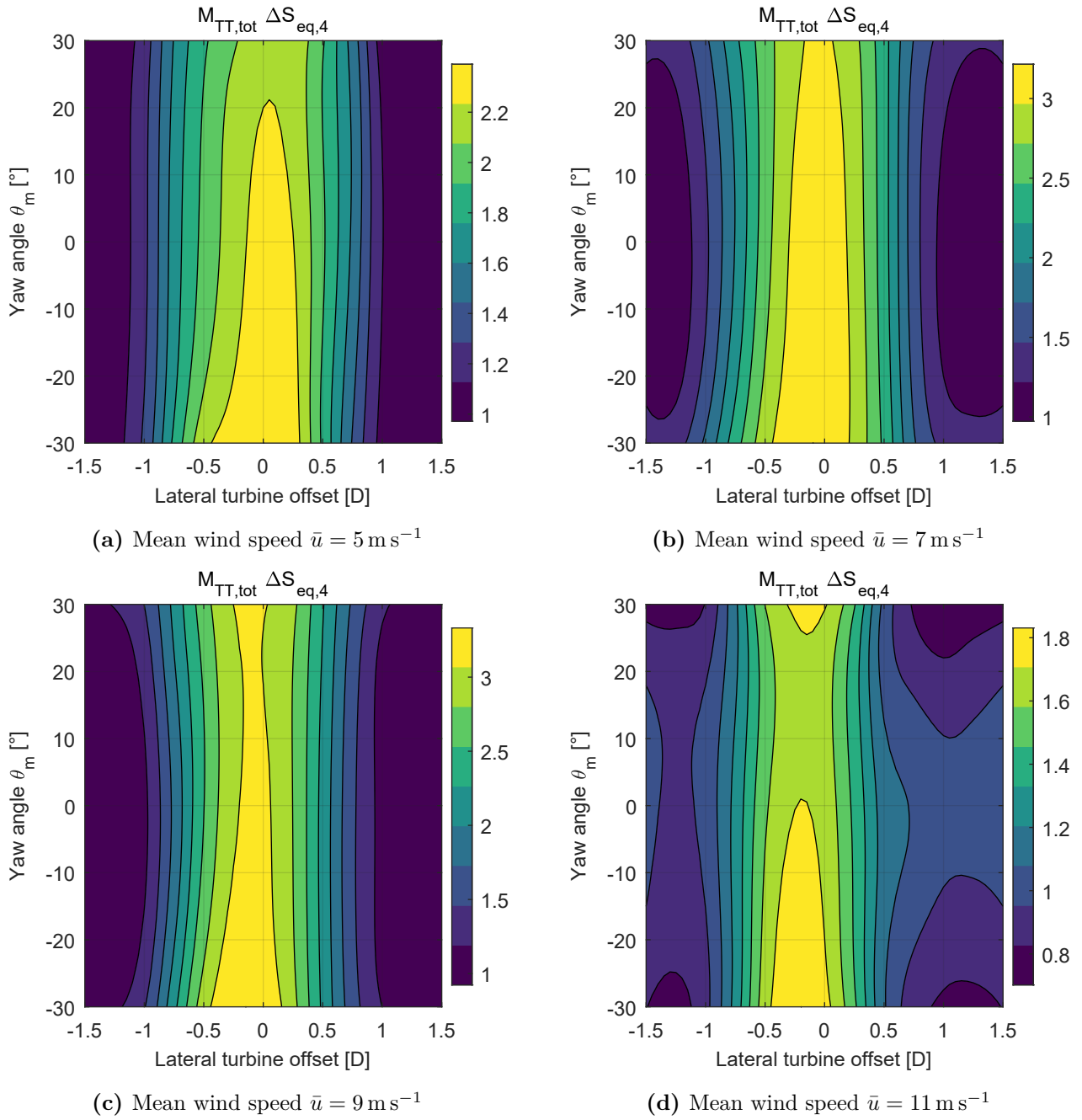


Figure A.41: Load distributions of the total bending moment at the tower-top for unstable atmospheric conditions ($\alpha_{\text{shear}}=0.03$) and different wind speeds. Results are shown by means of the seed average and normalised with the values at $\theta_m = 0^\circ$ of the free stream turbine.

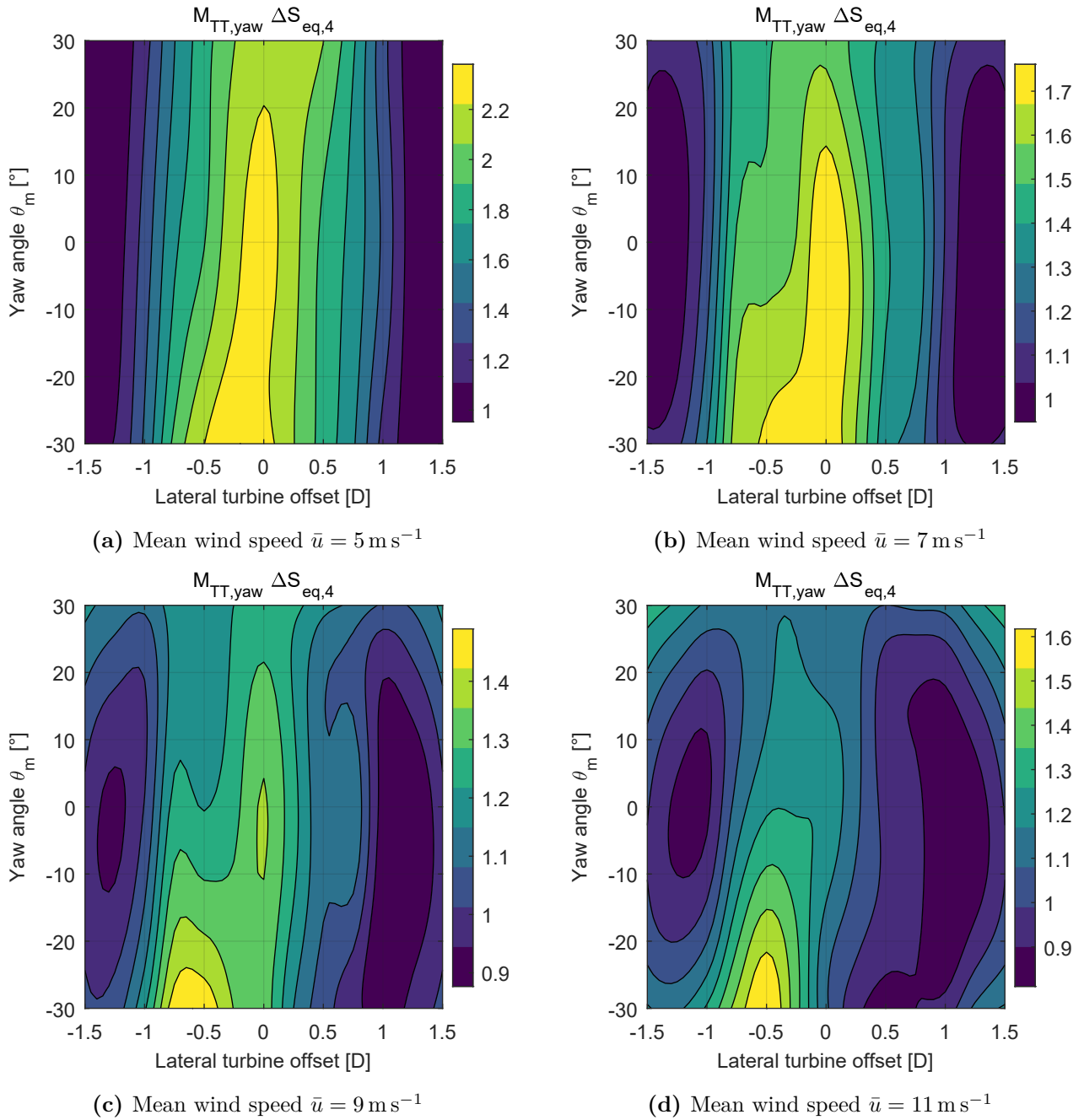


Figure A.42: Load distributions of the yawing moment at the tower-top for stable atmospheric conditions ($\alpha_{\text{shear}}=0.2$) and different wind speeds. Results are shown by means of the seed average and normalised with the values at $\theta_m = 0^\circ$ of the free stream turbine.

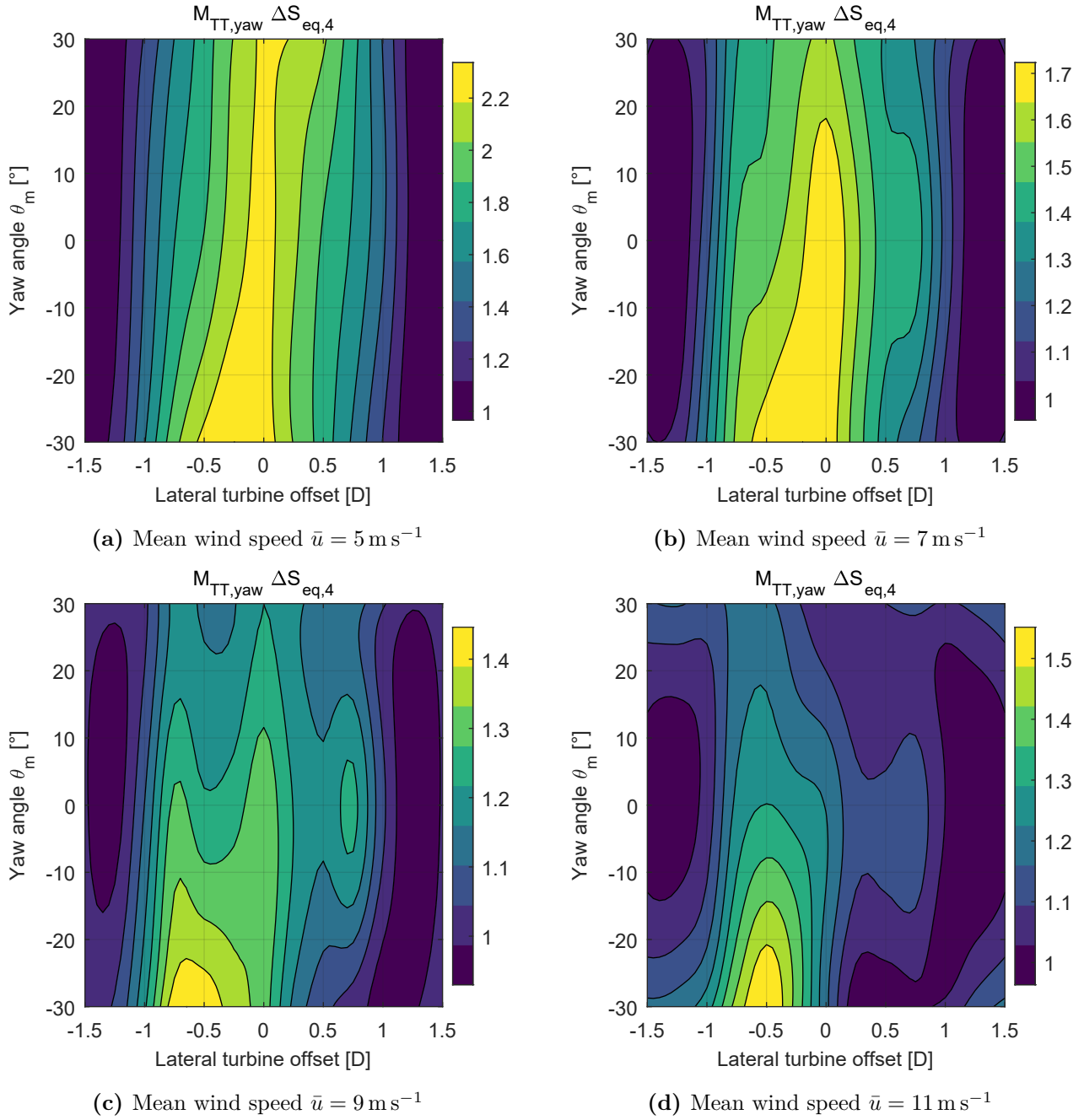


Figure A.43: Load distributions of the yawing moment at the tower-top for neutral atmospheric conditions ($\alpha_{\text{shear}}=0.1$) and different wind speeds. Results are shown by means of the seed average and normalised with the values at $\theta_m = 0^\circ$ of the free stream turbine.

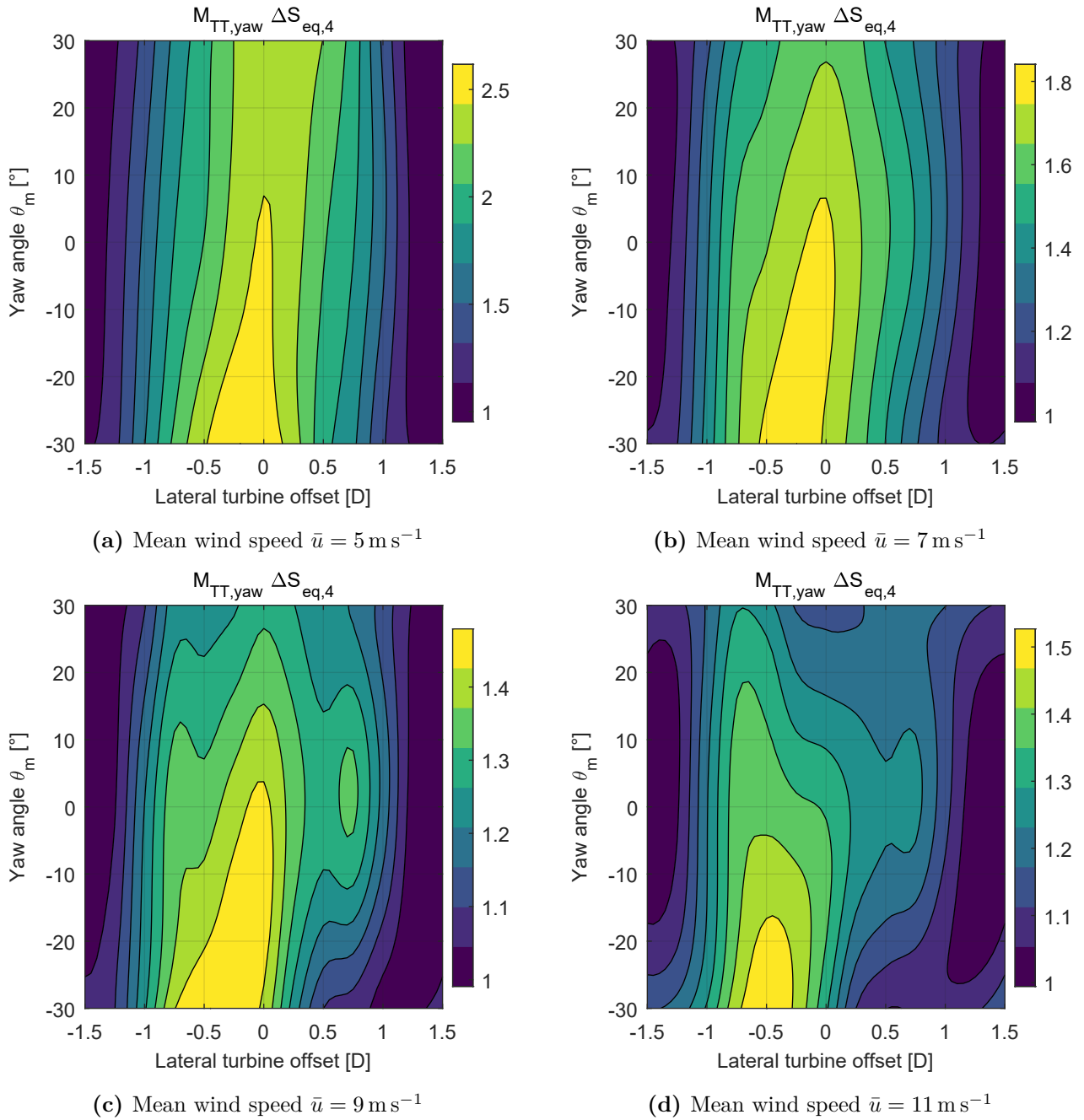


Figure A.44: Load distributions of the yawing moment at the tower-top for unstable atmospheric conditions ($\alpha_{shear}=0.03$) and different wind speeds. Results are shown by means of the seed average and normalised with the values at $\theta_m = 0^\circ$ of the free stream turbine.

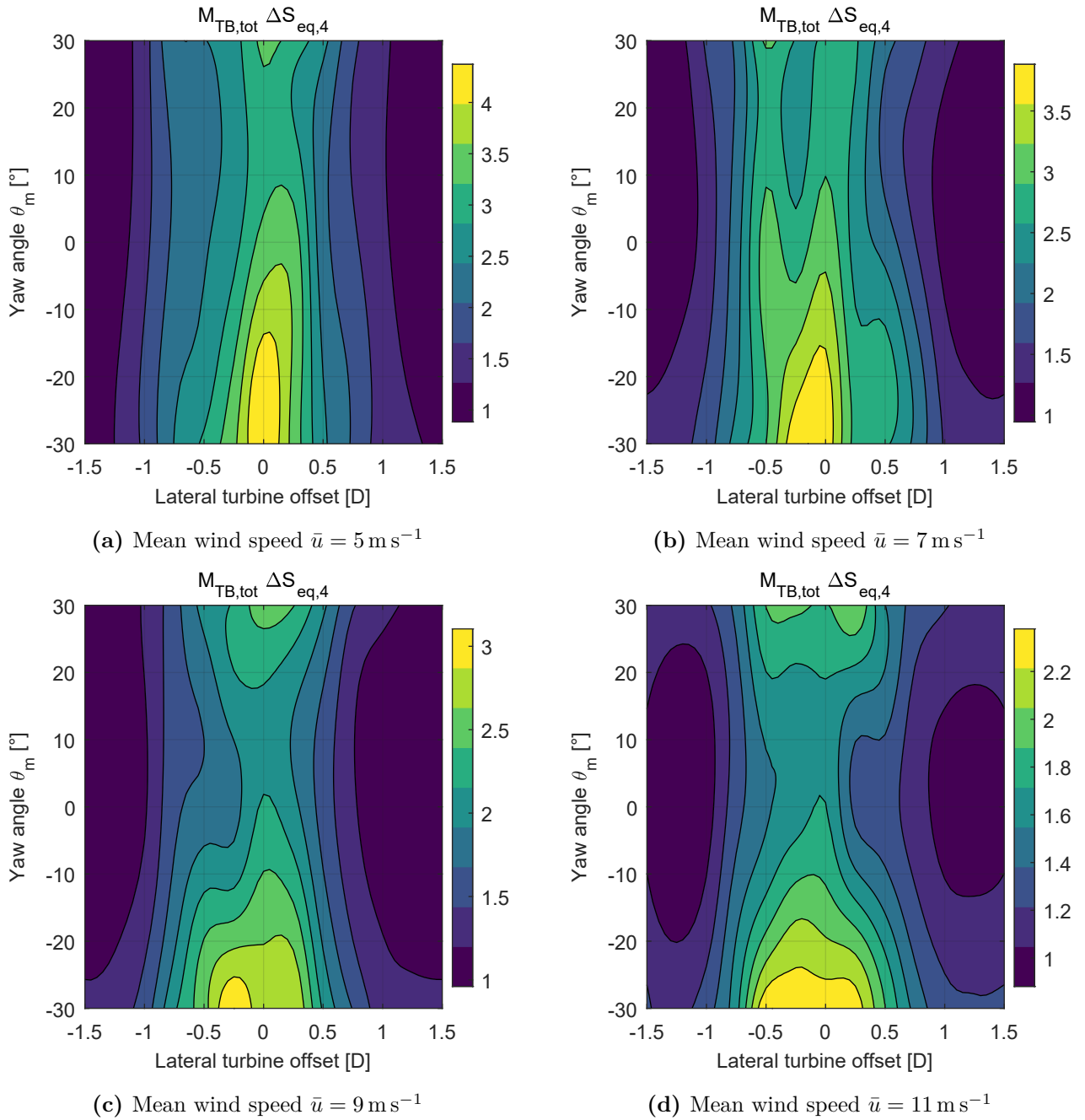


Figure A.45: Load distributions of the total bending moment at the tower-base for stable atmospheric conditions ($\alpha_{\text{shear}}=0.2$) and different wind speeds. Results are shown by means of the seed average and normalised with the values at $\theta_m = 0^\circ$ of the free stream turbine.

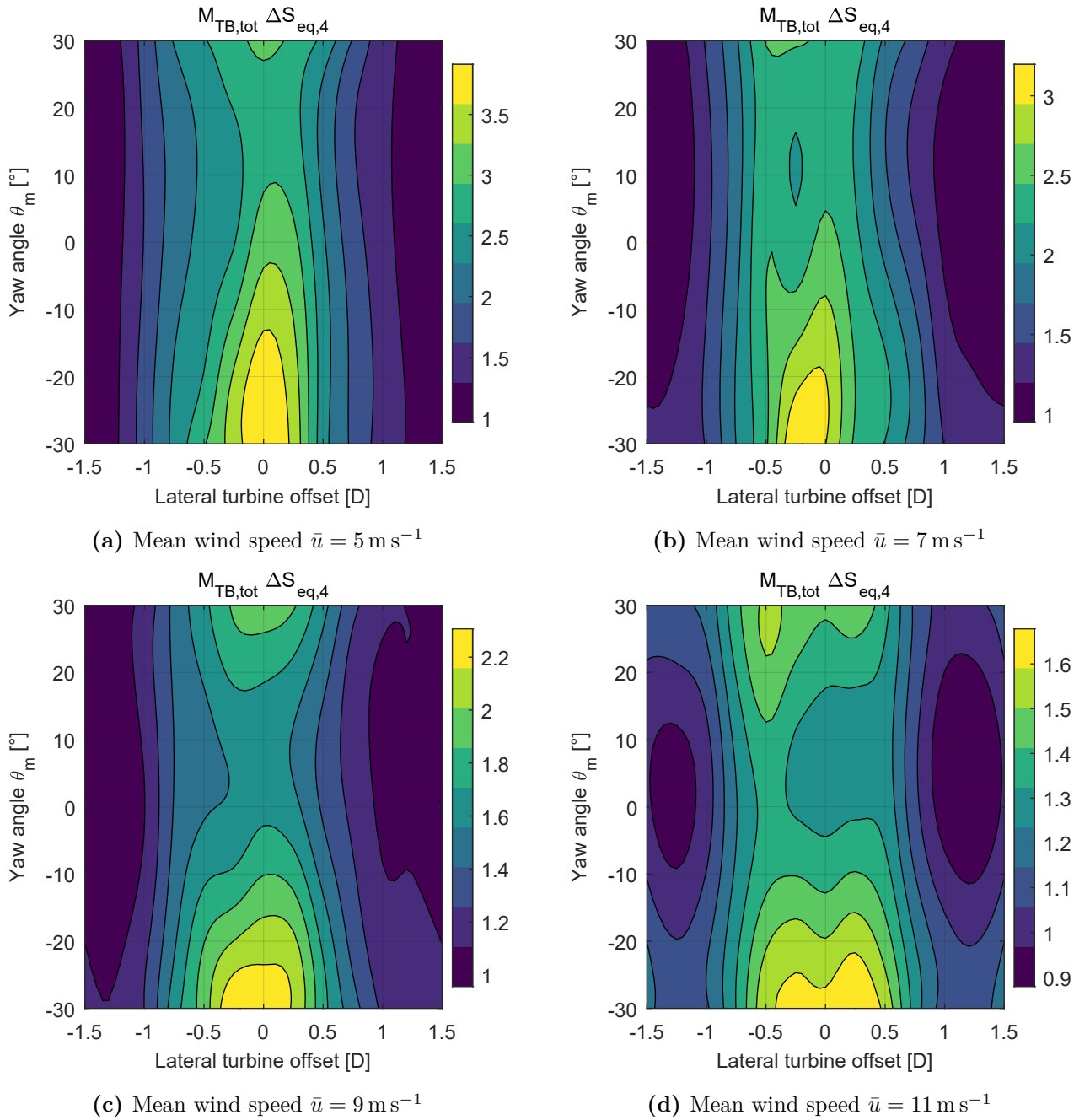


Figure A.46: Load distributions of the total bending moment at the tower-base for neutral atmospheric conditions ($\alpha_{\text{shear}}=0.1$) and different wind speeds. Results are shown by means of the seed average and normalised with the values at $\theta_m = 0^\circ$ of the free stream turbine.

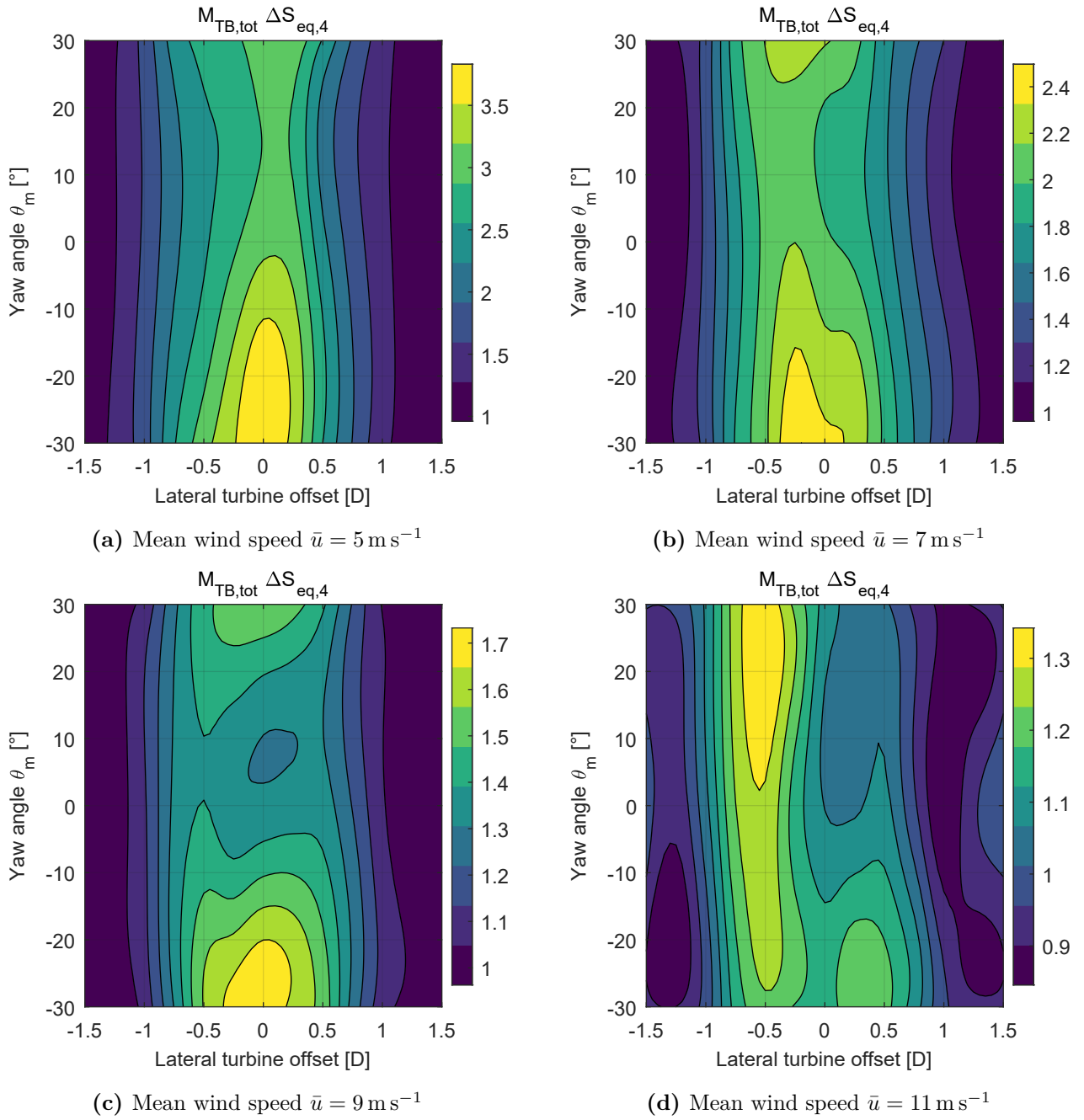
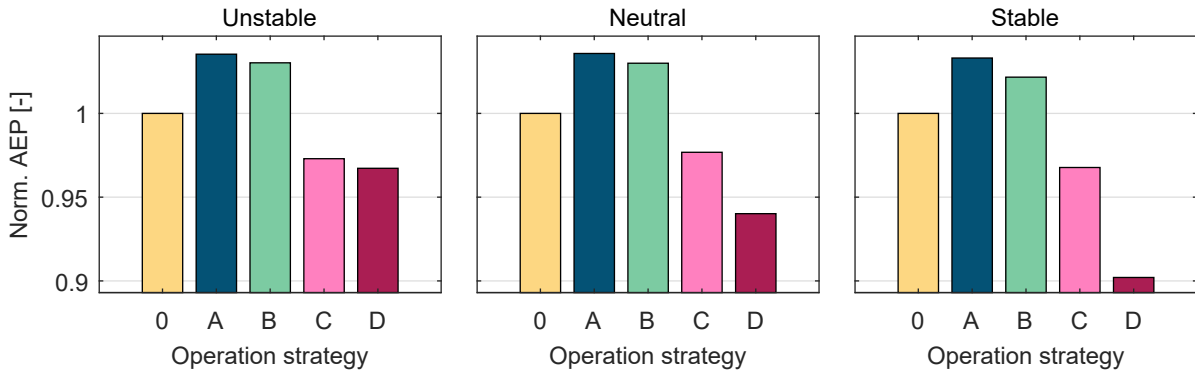


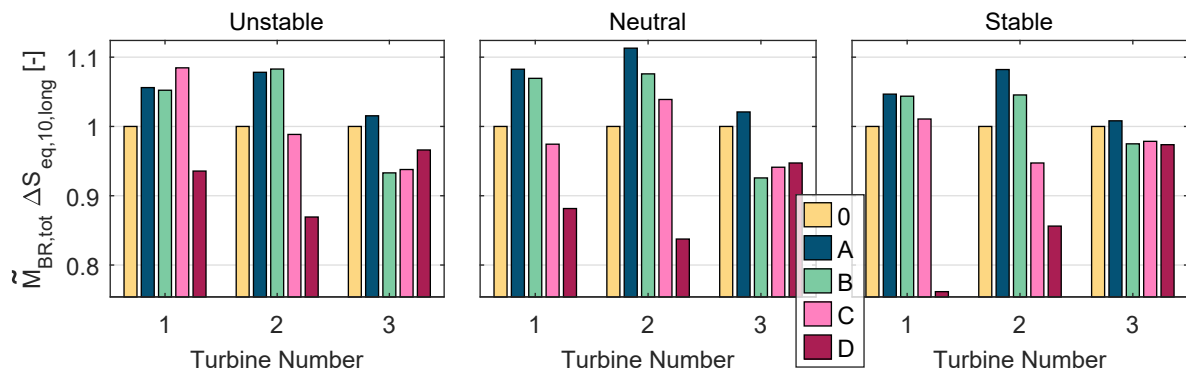
Figure A.47: Load distributions of the total bending moment at the tower-base for unstable atmospheric conditions ($\alpha_{\text{shear}}=0.03$) and different wind speeds. Results are shown by means of the seed average and normalised with the values at $\theta_m = 0^\circ$ of the free stream turbine.

A.6 Additional results from the optimisation of operation strategies

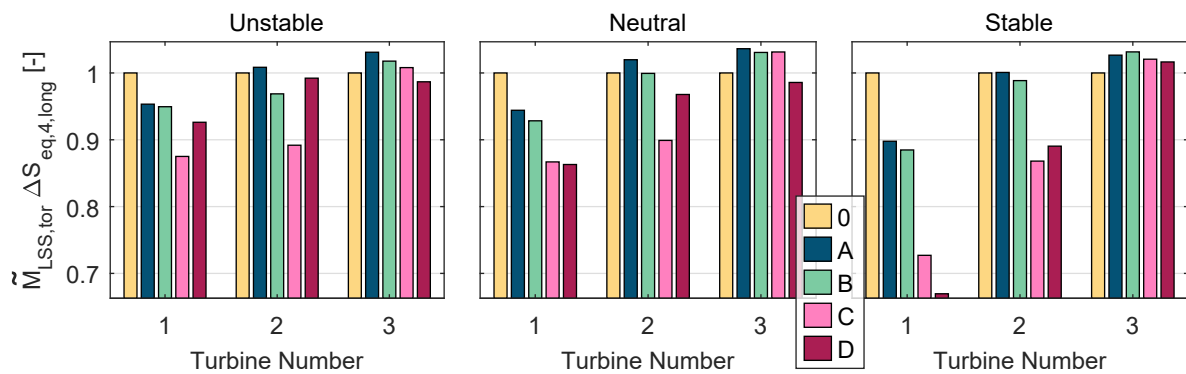
The Figures A.48 and A.49 contain additional results from the investigation of optimised wind farm operation strategies that is presented in Section 6.3.



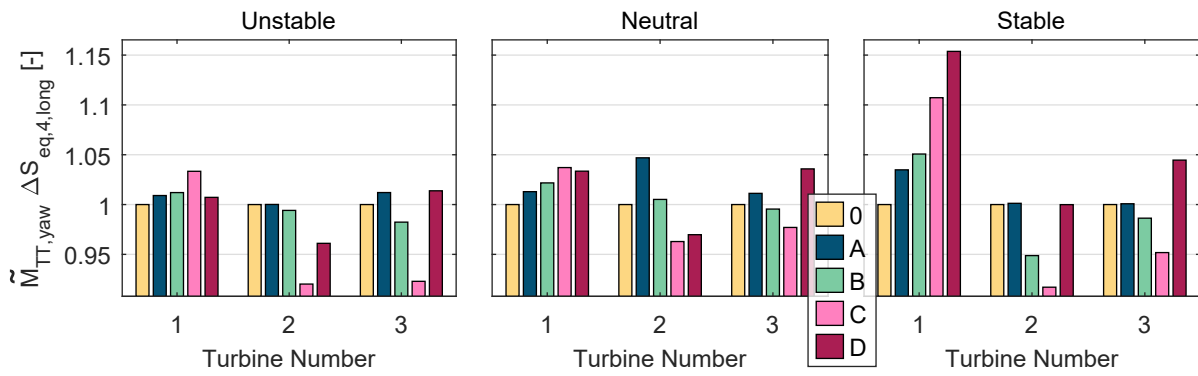
(a) Normalised AEP



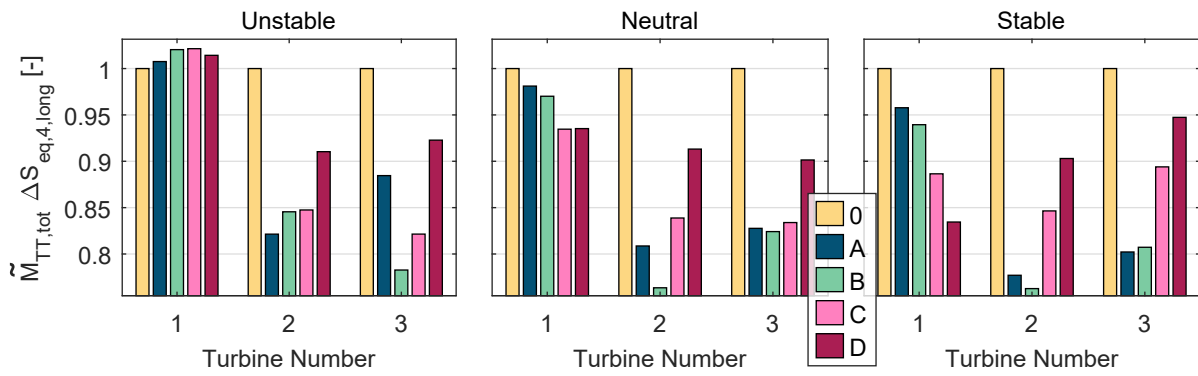
(b) Normalised total bending moment at the blade-root



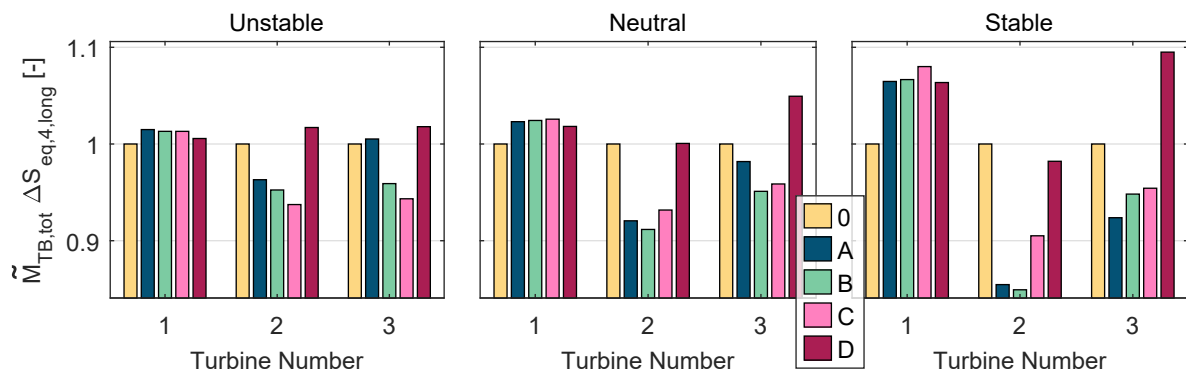
(c) Normalised torsional moment at the low-speed shaft



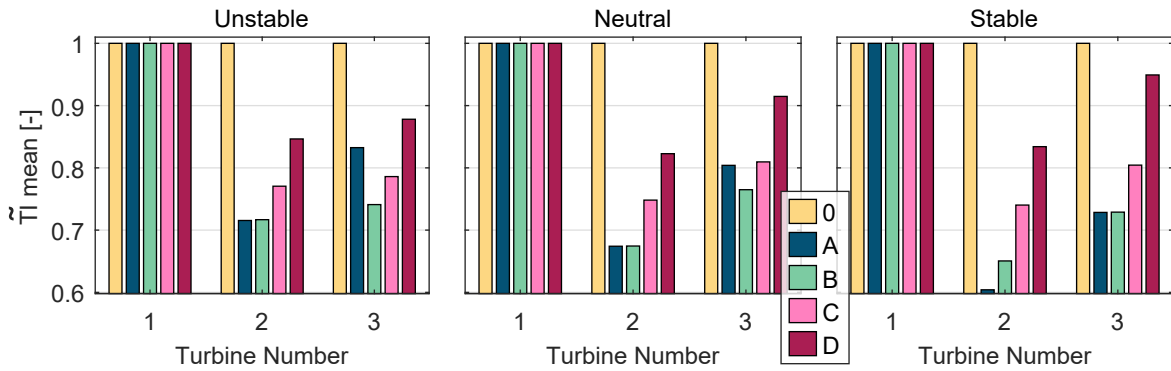
(d) Normalised yawing moment at the tower-top



(e) Normalised total bending moment at the tower-top

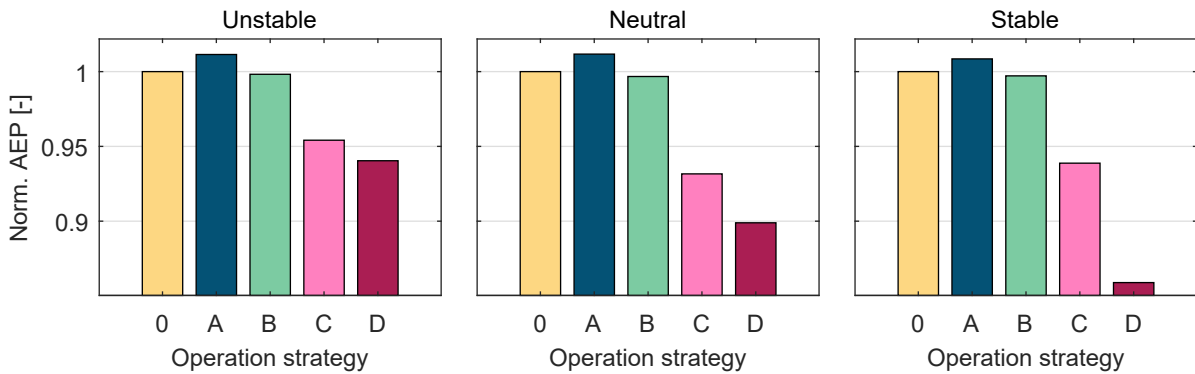


(f) Normalised total bending moment at the tower-base

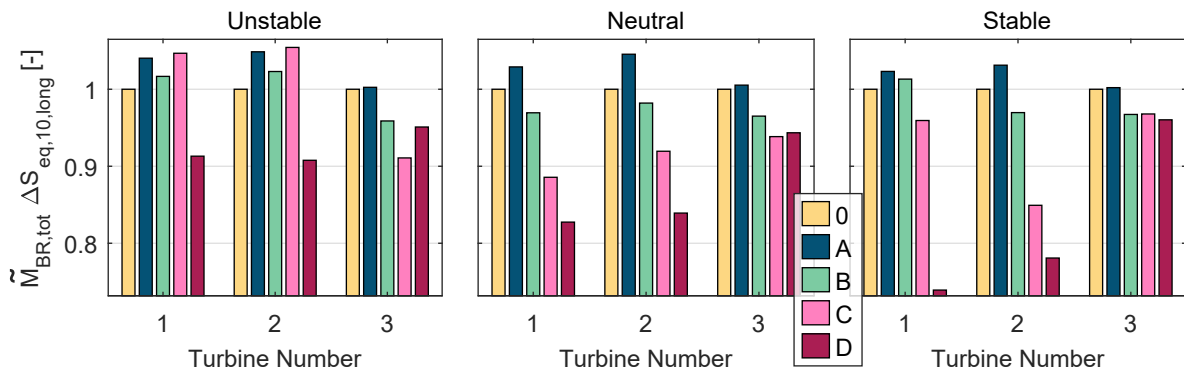


(g) Normalised turbulence intensity (TI) at the rotor centre

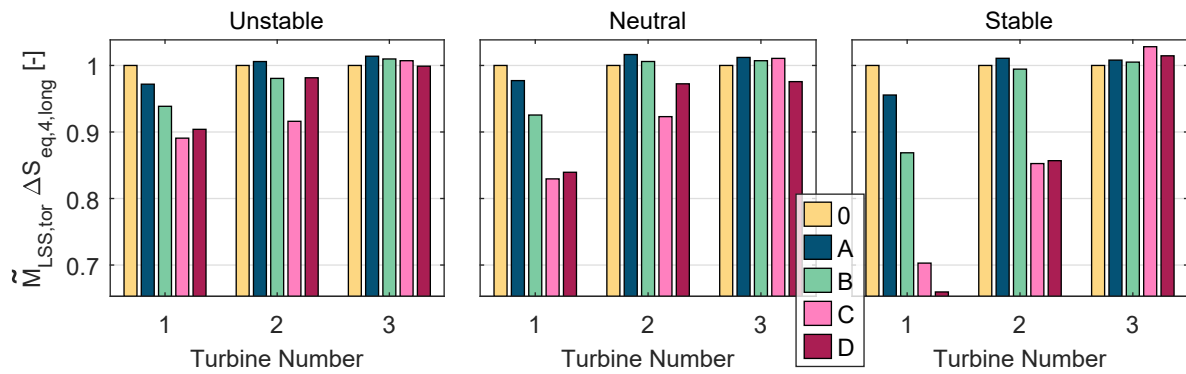
Figure A.48: Long-term evaluation of different operation strategies for the case of three turbines and longitudinal turbine spacing $x_{off} = 5D$. The results are normalised by the results from normal operation (zero yaw-misalignment) and at each turbine separately.



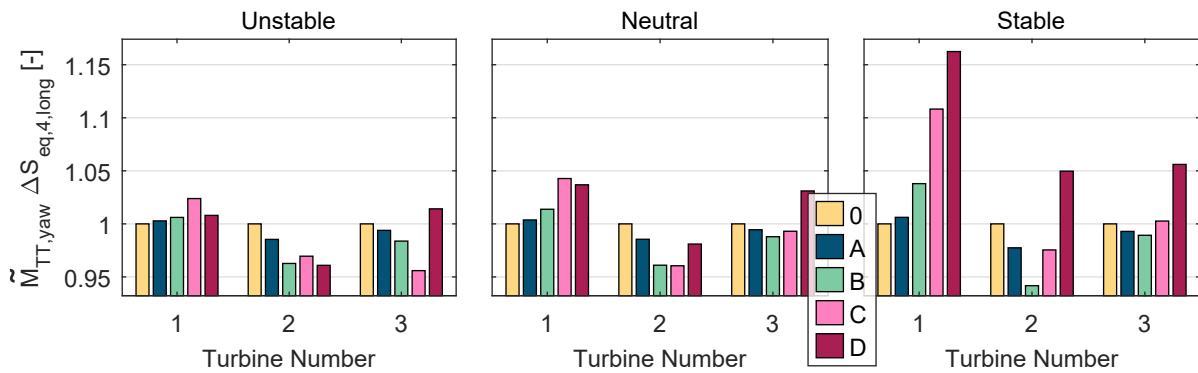
(a) Normalised AEP



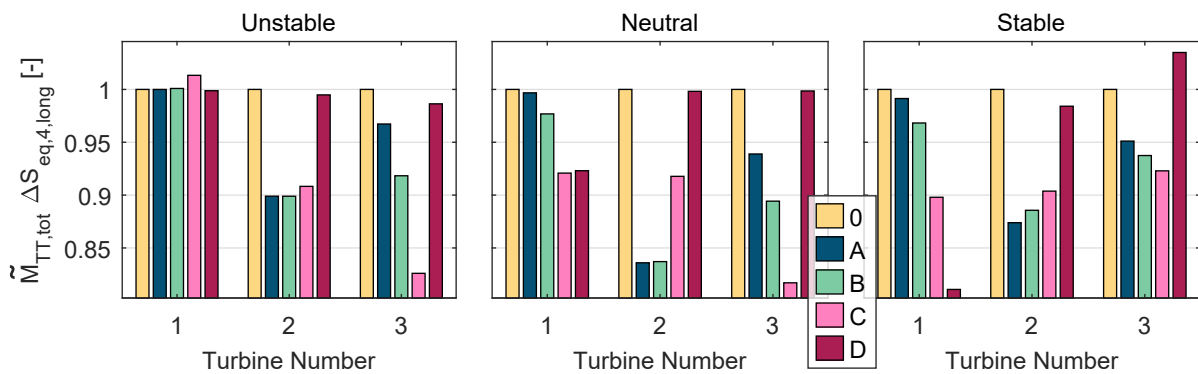
(b) Normalised total bending moment at the blade-root



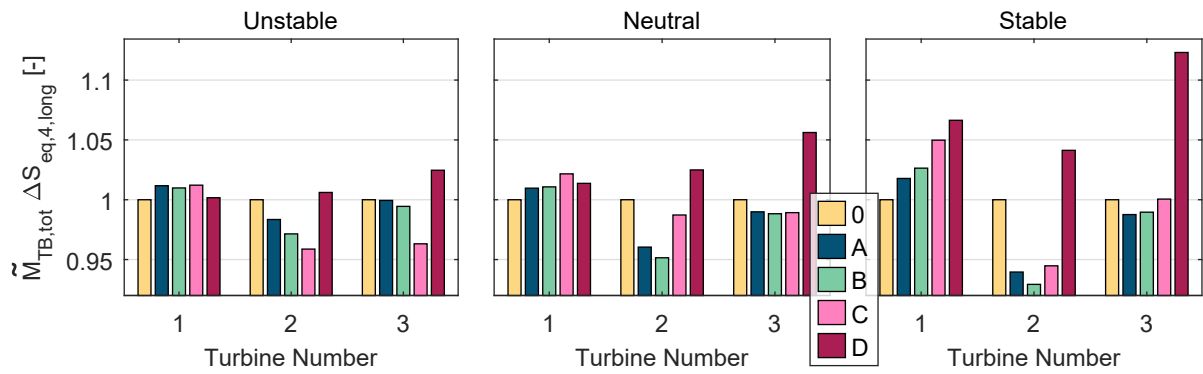
(c) Normalised torsional moment at the low-speed shaft



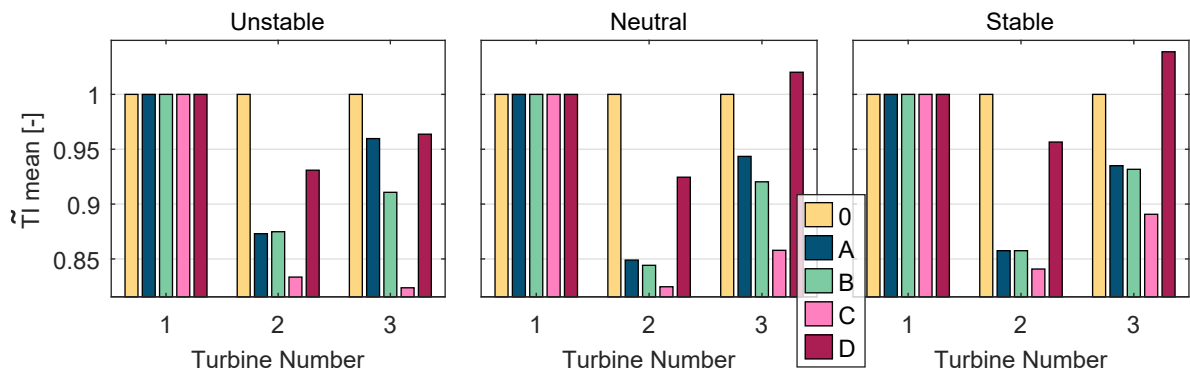
(d) Normalised yawing moment at the tower-top



(e) Normalised total bending moment at the tower-top



(f) Normalised total bending moment at the tower-base



(g) Normalised turbulence intensity (TI) at the rotor centre

Figure A.49: Long-term evaluation of different operation strategies for the case of three turbines and longitudinal turbine spacing $x_{off} = 9D$. The results are normalised by the results from normal operation (zero yaw-misalignment) and at each turbine separately.

A.7 Manual of the wake-added turbulence feature in FAST.Farm

A.7.1 Background

The wake modeling in FAST.Farm is based on the DWM model. This model was introduced by [11] and includes three core parts which are the calculation of the wake deficit, the wake meandering and the wake-added turbulence. In the current version 3.0.0 of FAST.Farm as part of the OpenFAST framework that is officially released by NREL, the calculation of the wake-added turbulence is not included. Therefore, it was implemented in the course of the work leading to this thesis and the publication [124].

A.7.2 Implementation

The implementation of wake-added turbulence includes three major additions to the FAST.Farm code:

1. A new instance of the OpenFAST module InflowWind is initialized for the wake-added turbulence domain; it is reused for each turbine in the simulation domain to ensure computational efficiency (see Figure A.50). The turbulent wind box that is created beforehand with the DTU Mann turbulence generator ([89]) is loaded into this instance of InflowWind. In the course of a FAST.Farm simulation, the wake-added turbulence wind field is propagated with the ambient wind speed at hub height.
2. The scaling factor k_{mt} is calculated in the meandering frame of reference on an axisymmetric grid inside FAST.Farm's WD module. The calculation is based on the quasi-steady velocity deficit and its radial gradient, which are already available inside the WD module.
3. In the module AWAE of FAST.Farm, the velocities of the wake-added turbulence field are interpolated based on their spatial location and scaled with the spatially interpolated value of the factor k_{mt} . The resulting velocities are added to the ambient wind vector via vector addition in the low- and high-resolution domains of FAST.Farm and transformed from the meandering frame of reference to the fixed frame of reference.

The usage of the InflowWind module from OpenFAST for the wake-added turbulence domain is motivated by the usage of code that is already existent. However, this approach has some implications explained in the following:

- The scaling factor k_{mt} is computed on an axisymmetric grid around the wake center (similar to the calculation of the velocity deficit). Given the dimensions of this grid (typically in the order of 1-2D for the radius) and the turbine's hub height, parts of

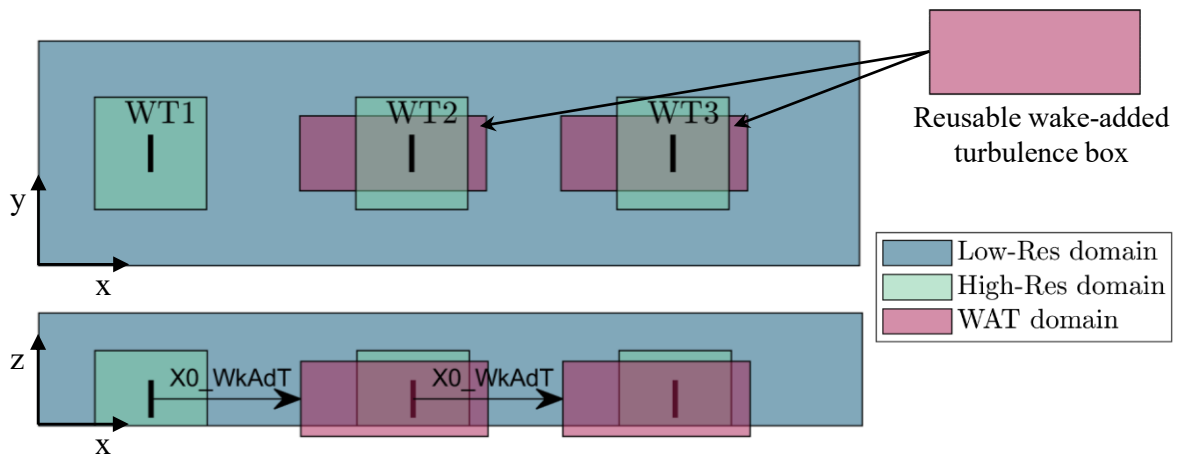


Figure A.50: Illustration of the different domains in a FAST.Farm simulation for a three turbine case. The box containing the turbulence information for the wake-added turbulence is reused for the wake of each individual turbine.

the grid are below the ground as it is displayed in Figure A.50. When interpolating the velocities of the wake-added turbulence box, negative locations in the wake-added turbulence box would be requested. This is not allowed in the InflowWind module because it is originally coded for the representation of turbulent wind flows above the ground. Therefore, the reference height in InflowWind is shifted upwards in order to avoid this issue (see Section A.7.3). The interpolation of the velocities of the wake-added turbulence domain is then also shifted by the same value as the reference height.

- The wake-added turbulence box provides turbulent fluctuations around zero mean velocity. However, for the propagation of the wake-added turbulence, a velocity is needed which is typically the mean wind speed at hub height. The implementation of the HAWC format in the InflowWind module allows to specify a reference velocity that is not necessarily added as the mean velocity to the turbulent fluctuations. Therefore, the usage of the HAWC format for the wake-added turbulence domain is currently mandatory.

The definition of the wake-added turbulence domain is similar to the definition of the low-resolution and high-resolution domains of FAST.Farm. It uses a Cartesian grid and the nomenclature for its definition is adapted from the low/high-resolution domains of FAST.Farm

A.7.3 Setup

The setup of the wake-added turbulence feature includes two steps. First, dedicated parameters for the wake-added turbulence domain must be set in the main input file of FAST.Farm. Second, an additional input file of the InflowWind module must be set up for the wake-added turbulence box.

Parameters in the main input file of FAST.Farm

The parameters for setting up the wake-added turbulence module are summarized in Table A.1; they are added to the main input file of FAST.Farm.

Setup of the InflowWind input file for the wake-added turbulence

The wake-added turbulence module of FAST.Farm requires the setup of an additional input file of the InflowWind module. The relevant parameters are explained in the following:

- **WindType:** In the current state, only `WindType=5` can be used which corresponds to the HAWC format and essentially turbulence fields from the Mann turbulence generator [89].
- **RefHt_Hawc:** The reference height is the vertical center of the grid. It should be chosen with a large shift upwards in order to avoid that points with negative z -coordinates are requested (see Section A.7.2).
- **ScaleMethod:** It is important that the turbulence used for the wake-added turbulence has a standard deviation of 1 m/s. Consequently, the method for scaling the turbulence should be chosen accordingly if the generated turbulence does not meet this criterion itself.
- **URef:** This parameter defines the speed at which the wake-added turbulence field is propagated downstream. It is recommended to use the mean wind speed at hub height.
- **WindProfile:** This parameter should be set to -1 in order to not add any mean flow velocity to the turbulent fluctuations.

Table A.1: Additional parameters in the main input file of FAST.Farm for the setup of the wake-added turbulence module

Parameter	Value [Unit]	Description
WkAdT	<true/false>	Switch for turning on and off wake-added turbulence
WkAdTinflowFile	<Path to InflowWind input file>	Name of file containing InflowWind module input parameters for wake added turbulence
nX_WkAdT	<Integer Number> [-]	Number of spatial nodes in X direction for wake-added turbulence grid
nY_WkAdT	<Integer Number> [-]	Number of spatial nodes in Y direction for wake-added turbulence grid
nZ_WkAdT	<Integer Number> [-]	Number of spatial nodes in Z direction for wake-added turbulence grid
X0_WkAdT	<Real Number> [m]	Origin of spatial nodes in X direction for wake-added turbulence grid measured from the turbine's location (see Figure A.50)
Y0_WkAdT	<Real Number> [m]	Origin of spatial nodes in Y direction for wake-added turbulence grid
Z0_WkAdT	<Real Number> [m]	Origin of spatial nodes in Z direction for wake-added turbulence grid. Should be set in accordance with the reference height of the turbulence box in the InflowWind module
dX_WkAdT	<Real Number> [m]	Spacing of spatial nodes in X direction for wake-added turbulence grid
dY_WkAdT	<Real Number> [m]	Spacing of spatial nodes in Y direction for wake-added turbulence grid
dZ_WkAdT	<Real Number> [m]	Spacing of spatial nodes in Z direction for wake-added turbulence grid
k_m1_WkAdT	<Real Number> (Default=1.48)	Calibrated parameter for the influence of the wake deficit in the wake-added turbulence
k_m2_WkAdT	<Real Number> (Default=1.01)	Calibrated parameter for the influence of the radial velocity gradient of the wake deficit in the wake-added turbulence

Bibliography

- [1] European Commission, “Communication from the Commission to the European Parliament, the Council, the European Economic and Social Committee and the Committee of the Regions: An EU Strategy to harness the potential of offshore renewable energy for a climate neutral future,” 2020. [Online]. Available: <https://eur-lex.europa.eu/legal-content/EN/TXT/?uri=COM:2020:741:FIN>
- [2] S. Lüers, “Status des Offshore-Windenergieausbaus in Deutschland,” Deutsche WindGuard GmbH, Tech. Rep., 2020. [Online]. Available: https://www.wind-energie.de/fileadmin/redaktion/dokumente/publikationen-oeffentlich/themen/06-zahlen-und-fakten/Status_des_Offshore-Windenergieausbaus_-_Jahr_2020.pdf
- [3] P. Veers, K. Dykes, E. Lantz, S. Barth, C. L. Bottasso, O. Carlson, A. Clifton, J. Green, P. Green, H. Holttinen, D. Laird, V. Lehtomäki, J. K. Lundquist, J. Manwell, M. Marquis, C. Meneveau, P. Moriarty, X. Munduate, M. Muskulus, J. Naughton, L. Pao, J. Paquette, J. Peinke, A. Robertson, J. Sanz Rodrigo, A. M. Sempreviva, J. C. Smith, A. Tuohy, and R. Wisser, “Grand challenges in the science of wind energy,” *Science*, vol. 366, no. 6464, p. eaau2027, 2019, doi: 10.1126/science.aau2027.
- [4] M. Boccolini, E. Bossanyi, S. Bourne, A. Dombrowski, G. Ferraro, K. Harman, N. Hille, L. Landberg, T. Levick, A. Manjock, T. Mercer, A. Neubert, R. Ruisi, and N. Skeen, “Wind Farm Control: The Route to Bankability,” 2021. [Online]. Available: <https://www.dnv.com/Publications/wind-farm-control-198162>
- [5] J. W. van Wingerden, P. A. Fleming, T. Göçmen, I. Eguinoa, B. M. Doekemeijer, K. Dykes, M. Lawson, E. Simley, J. King, D. Astrain, M. Iribas, C. L. Bottasso, J. Meyers, S. Raach, K. Kölle, and G. Giebel, “Expert Elicitation on Wind Farm Control,” *Journal of Physics: Conference Series*, vol. 1618, p. 022025, 2020, doi: 10.1088/1742-6596/1618/2/022025.
- [6] P. Doubrawa, E. W. Quon, L. A. Martínez-Tossas, K. Shaler, M. Debnath, N. Hamilton, T. G. Herges, D. Maniaci, C. L. Kelley, A. S. Hsieh, M. L. Blaylock, P. Laan, S. J. Andersen, S. Krüger, M. Cathelain, W. Schlez, J. Jonkman, E. Branlard, G. Steinfeld, S. Schmidt, F. Blondel, L. J. Lukassen, and P. Moriarty, “Multimodel validation of single

- wakes in neutral and stratified atmospheric conditions,” *Wind Energy*, vol. 23, no. 11, pp. 2027–2055, 2020, doi: 10.1002/we.2543.
- [7] P. Weihing, “Numerical Study of Transition, Flow Separation and Wake Phenomena of Wind Turbines with Enhanced Hybrid RANS/LES Methods,” Ph.D. dissertation, University of Stuttgart, 2021.
- [8] J. Wang, C. Wang, F. Campagnolo, and C. L. Bottasso, “Wake behavior and control: comparison of LES simulations and wind tunnel measurements,” *Wind Energy Science*, vol. 4, no. 1, pp. 71–88, 2019, doi: 10.5194/wes-4-71-2019.
- [9] E. Schwarz, “CFD-based studies of active wind turbine load control by means of trailing edge flaps,” Ph.D. dissertation, University of Stuttgart, 2020.
- [10] D. Bensason, E. Simley, O. Roberts, P. Fleming, M. Debnath, J. King, C. Bay, and R. Mudafort, “Evaluation of the potential for wake steering for U.S. land-based wind power plants,” *Journal of Renewable and Sustainable Energy*, vol. 13, no. 3, p. 033303, 2021, doi: 10.1063/5.0039325.
- [11] G. C. Larsen, H. A. Madsen, K. Thomsen, and T. J. Larsen, “Wake meandering: a pragmatic approach,” *Wind Energy*, vol. 11, no. 4, pp. 377–395, 2008, doi: 10.1002/we.267.
- [12] J. M. Jonkman, J. Annoni, G. Hayman, B. Jonkman, and A. Purkayastha, “Development of FAST.Farm: A New Multi-Physics Engineering Tool for Wind-Farm Design and Analysis,” in *35th Wind Energy Symposium*. Grapevine, Texas: American Institute of Aeronautics and Astronautics, 2017. doi: 10.2514/6.2017-0454.
- [13] Ø. W. Hanssen-Bauer, J. B. de Vaal, M. Tutkun, H. Asmuth, S. Ivanell, and R. Stenbro, “Dependence of wind turbine loads on inlet flow field,” *Journal of Physics: Conference Series*, vol. 1618, no. 6, p. 062065, 2020, doi: 10.1088/1742-6596/1618/6/062065.
- [14] I. Reinwardt, L. Schilling, P. Dalhoff, D. Steudel, and M. Breuer, “Dynamic wake meandering model calibration using nacelle-mounted lidar systems,” *Wind Energy Science*, vol. 5, no. 2, pp. 775–792, 2020, doi: 10.5194/wes-5-775-2020.
- [15] IEC, “61400-1 ed. 4: Wind energy generation systems - part 1: Design requirements,” International Electrotechnical Commission, Geneva, Switzerland, 2019.
- [16] A. C. Kheirabadi and R. Nagamune, “A quantitative review of wind farm control with the objective of wind farm power maximization,” *Journal of Wind Engineering and Industrial Aerodynamics*, vol. 192, pp. 45–73, 2019, doi: 10.1016/j.jweia.2019.06.015.
- [17] P. M. O. Gebraad, “Data-Driven Wind Plant Control,” Ph.D. dissertation, TU Delft, 2014.
- [18] P. M. O. Gebraad, F. W. Teeuwisse, J. W. van Wingerden, P. A. Fleming, S. D. Ruben, J. R. Marden, and L. Y. Pao, “Wind plant power optimization through yaw control using a parametric model for wake effects - a CFD simulation study,” *Wind Energy*, vol. 19, no. 1, pp. 95–114, 2016, doi: 10.1002/we.1822.
- [19] F. Campagnolo, R. Weber, J. Schreiber, and C. L. Bottasso, “Wind tunnel testing of

- wake steering with dynamic wind direction changes,” *Wind Energy Science*, vol. 5, no. 4, pp. 1273–1295, 2020, doi: 10.5194/wes-5-1273-2020.
- [20] P. Fleming, M. Sinner, T. Young, M. Lannic, J. King, E. Simley, and B. Doekemeijer, “Experimental results of wake steering using fixed angles,” *Wind Energy Science*, vol. 6, no. 6, pp. 1521–1531, 2021, doi: 10.5194/wes-6-1521-2021.
- [21] S. Raach, “Lidar-assisted wake redirection control,” Ph.D. dissertation, University of Stuttgart, 2019.
- [22] I. Eguinoa, T. Göçmen, P. B. Garcia-Rosa, K. Das, V. Petrović, K. Kölle, A. Manjock, M. J. Koivisto, and M. Smailes, “Wind farm flow control oriented to electricity markets and grid integration: Initial perspective analysis,” *Advanced Control for Applications*, 2021, doi: 10.1002/adc2.80.
- [23] M. Vali, V. Petrović, G. Steinfeld, L. Y. Pao, and M. Kühn, “An active power control approach for wake-induced load alleviation in a fully developed wind farm boundary layer,” *Wind Energy Science*, vol. 4, no. 1, pp. 139–161, 2019, doi: 10.5194/wes-4-139-2019.
- [24] B. M. Doekemeijer, J.-W. Van Wingerden, and P. A. Fleming, “A tutorial on the synthesis and validation of a closed-loop wind farm controller using a steady-state surrogate model,” in *2019 American Control Conference (ACC)*. Philadelphia, PA, USA: IEEE, 2019, pp. 2825–2836, doi: 10.23919/ACC.2019.8815126.
- [25] E. Bossanyi, “Combining induction control and wake steering for wind farm energy and fatigue loads optimisation,” *Journal of Physics: Conference Series*, vol. 1037, p. 032011, 2018, doi: 10.1088/1742-6596/1037/3/032011.
- [26] S. K. Kanev, F. J. Savenije, and W. P. Engels, “Active wake control: An approach to optimize the lifetime operation of wind farms,” *Wind Energy*, vol. 21, p. 14, 2018, doi: 10.1002/we.2173.
- [27] M. Kretschmer, S. Raach, J. Taubmann, N. Ruck, and P. W. Cheng, “Wake redirection for active power control: a realistic case study,” *Journal of Physics: Conference Series*, vol. 1618, p. 022059, 2020, doi: 10.1088/1742-6596/1618/2/022059.
- [28] F. Meng, A. W. Hou Lio, and J. Liew, “The effect of minimum thrust coefficient control strategy on power output and loads of a wind farm,” *Journal of Physics: Conference Series*, vol. 1452, no. 1, p. 012009, 2020, doi: 10.1088/1742-6596/1452/1/012009.
- [29] R. B. Stull, Ed., *An Introduction to Boundary Layer Meteorology*. Dordrecht: Springer Netherlands, 1988. doi: 10.1007/978-94-009-3027-8.
- [30] J. C. Kaimal and J. J. Finnigan, *Atmospheric boundary layer flows: their structure and measurement*. New York: Oxford University Press, 1994.
- [31] T. Foken, *Angewandte Meteorologie*. Berlin, Heidelberg: Springer Berlin Heidelberg, 2016. doi: 10.1007/978-3-642-25525-0.

- [32] S. Emeis, *Wind Energy Meteorology*, ser. Green Energy and Technology. Cham: Springer International Publishing, 2018. doi: 10.1007/978-3-319-72859-9.
- [33] D. Etling, *Theoretische Meteorologie: eine Einführung*, 3rd ed. Berlin: Springer, 2008.
- [34] J. Fröhlich, *Large Eddy Simulation turbulenter Strömungen*. Wiesbaden: Teubner, 2006. doi: 10.1007/978-3-8351-9051-1.
- [35] A. Peña, S.-E. Gryning, and J. Mann, “On the Length-Scale of the Wind Profile,” *Quarterly Journal of the Royal Meteorological Society*, vol. 136, no. 653, pp. 2119–2131, 2010, doi: 10.1002/qj.714.
- [36] A. A. Grachev and C. W. Fairall, “Dependence of the Monin-Obukhov Stability Parameter on the Bulk Richardson Number over the Ocean,” *Journal of Applied Meteorology and Climatology*, vol. 36, p. 9, 1997.
- [37] J. A. Businger, J. C. Wyngaard, Y. Izumi, and E. F. Bradley, “Flux-Profile Relationships in the Atmospheric Surface Layer,” *Journal of the Atmospheric Sciences*, vol. 28, no. 2, pp. 181–189, 1971, doi: 10.1175/1520-0469(1971)028<0181:FPRITA>2.0.CO;2.
- [38] A. J. Dyer, “A review of flux-profile relationships,” *Boundary-Layer Meteorology*, vol. 7, no. 3, pp. 363–372, 1974, doi: 10.1007/BF00240838.
- [39] P. Veers, “Fatigue loading of wind turbines,” in *Wind Energy Systems*. Elsevier, 2011, pp. 130–158, doi: 10.1533/9780857090638.1.130.
- [40] R. Gasch, J. Twele, P. Bade, W. Conrad, C. Heilmann, K. Kaiser, R. Kortenkamp, M. Kühn, W. Langreder, J. Liersch, J. Maurer, A. Reuter, M. Schubert, B. Sundermann, and A. Stoffel, *Windkraftanlagen*, R. Gasch and J. Twele, Eds. Wiesbaden: Vieweg+Teubner Verlag, 2005. doi: 10.1007/978-3-322-99446-2.
- [41] A. Nieslony, “Rainflow counting algorithm,” 2021. [Online]. Available: <https://www.mathworks.com/matlabcentral/fileexchange/3026-rainflow-counting-algorithm>
- [42] DNV, “DNV-RP-C203: Fatigue Design of Offshore Steel Structures,” 2011.
- [43] G. C. Larsen, H. A. Madsen, T. J. Larsen, and N. Troldborg, “Wake modeling and simulation,” Danmarks Tekniske Universitet, Risø Nationallaboratoriet for Bæredygtig Energi, Tech. Rep. Risø-R-1653, 2008.
- [44] T. Uchida, T. Yoshida, M. Inui, and Y. Taniyama, “Doppler Lidar Investigations of Wind Turbine Near-Wakes and LES Modeling with New Porous Disc Approach,” *Energies*, vol. 14, no. 8, p. 2101, 2021, doi: 10.3390/en14082101.
- [45] P. J. Ecen, J. W. Wagenaar, and T. G. Bot, “Offshore wind farms: losses and turbulence in wakes,” in *Proceedings of Gotland wake conference*, 2011.
- [46] T. Burton, N. Jenkins, D. Sharpe, and E. Bossanyi, *Wind Energy Handbook: Burton/Wind Energy Handbook*. Chichester, UK: John Wiley & Sons, Ltd, 2011. doi: 10.1002/9781119992714.
- [47] N. Troldborg, “Actuator Line Modeling of Wind Turbine Wakes,” Ph.D. dissertation, Technical University of Denmark, 2008.

- [48] S. Ivanell, “Numerical Computations of Wind Turbine Wakes,” Ph.D. dissertation, Royal institute of technology, Stockholm, 2009.
- [49] R.-E. Keck, R. Mikkelsen, N. Troldborg, M. de Maré, and K. S. Hansen, “Synthetic atmospheric turbulence and wind shear in large eddy simulations of wind turbine wakes,” *Wind Energy*, vol. 17, no. 8, pp. 1247–1267, 2014, doi: 10.1002/we.1631.
- [50] R.-E. Keck, “A consistent turbulence formulation for the dynamic wake meandering model in the atmospheric boundary layer,” Ph.D. dissertation, DTU Wind Energy, Denmark, 2013.
- [51] M. Abkar and F. Porté-Agel, “Influence of atmospheric stability on wind-turbine wakes: A large-eddy simulation study,” *Physics of Fluids*, vol. 27, no. 3, p. 035104, 2015, doi: 10.1063/1.4913695.
- [52] F. Bingöl, J. Mann, and G. C. Larsen, “Light detection and ranging measurements of wake dynamics part I: one-dimensional scanning,” *Wind Energy*, vol. 13, no. 1, pp. 51–61, 2010, doi: 10.1002/we.352.
- [53] J.-J. Trujillo, F. Bingöl, G. C. Larsen, J. Mann, and M. Kühn, “Light detection and ranging measurements of wake dynamics. Part II: two-dimensional scanning,” *Wind Energy*, vol. 14, no. 1, pp. 61–75, 2011, doi: 10.1002/we.402.
- [54] G. España, S. Aubrun, S. Loyer, and P. Devinant, “Spatial study of the wake meandering using modelled wind turbines in a wind tunnel: Spatial study of the wake meandering,” *Wind Energy*, vol. 14, no. 7, pp. 923–937, 2011, doi: 10.1002/we.515.
- [55] M. Bastankhah and F. Porté-Agel, “Wind tunnel study of the wind turbine interaction with a boundary-layer flow: Upwind region, turbine performance, and wake region,” *Physics of Fluids*, vol. 29, no. 6, p. 065105, 2017, doi: 10.1063/1.4984078.
- [56] R.-E. Keck, M. de Maré, M. J. Churchfield, S. Lee, G. Larsen, and H. Aagaard Madsen, “On atmospheric stability in the dynamic wake meandering model,” *Wind Energy*, vol. 17, no. 11, pp. 1689–1710, 2014, doi: 10.1002/we.1662.
- [57] P. A. Fleming, P. M. Gjebraad, S. Lee, J.-W. van Wingerden, K. Johnson, M. Churchfield, J. Michalakes, P. Spalart, and P. Moriarty, “Evaluating techniques for redirecting turbine wakes using SOWFA,” *Renewable Energy*, vol. 70, pp. 211–218, 2014, doi: 10.1016/j.renene.2014.02.015.
- [58] M. Bromm, A. Rott, H. Beck, L. Vollmer, G. Steinfeld, and M. Kühn, “Field investigation on the influence of yaw misalignment on the propagation of wind turbine wakes,” *Wind Energy*, vol. 21, no. 11, pp. 1011–1028, 2018, doi: 10.1002/we.2210.
- [59] M. Bastankhah and F. Porté-Agel, “Experimental and theoretical study of wind turbine wakes in yawed conditions,” *Journal of Fluid Mechanics*, vol. 806, pp. 506–541, 2016, doi: 10.1017/jfm.2016.595.
- [60] Á. Jiménez, A. Crespo, and E. Migoya, “Application of a LES technique to characterize

- the wake deflection of a wind turbine in yaw,” *Wind Energy*, vol. 13, no. 6, pp. 559–572, 2009, doi: 10.1002/we.380.
- [61] N. Marathe, A. Swift, B. Hirth, R. Walker, and J. Schroeder, “Characterizing power performance and wake of a wind turbine under yaw and blade pitch: Power performance and wake of a wind turbine under yaw and blade pitch,” *Wind Energy*, vol. 19, no. 5, pp. 963–978, 2016, doi: 10.1002/we.1875.
- [62] M. Churchfield, Q. Wang, A. Scholbrock, T. Herges, T. Mikkelsen, and M. Sjöholm, “Using High-Fidelity Computational Fluid Dynamics to Help Design a Wind Turbine Wake Measurement Experiment,” *Journal of Physics: Conference Series*, vol. 753, p. 032009, 2016, doi: 10.1088/1742-6596/753/3/032009.
- [63] L. Vollmer, G. Steinfeld, D. Heinemann, and M. Kühn, “Estimating the wake deflection downstream of a wind turbine in different atmospheric stabilities: an LES study,” *Wind Energy Science*, vol. 1, no. 2, pp. 129–141, 2016, doi: 10.5194/wes-1-129-2016.
- [64] F. Porté-Agel, M. Bastankhah, and S. Shamsoddin, “Wind-Turbine and Wind-Farm Flows: A Review,” *Boundary-Layer Meteorology*, vol. 174, no. 1, pp. 1–59, 2020, doi: 10.1007/s10546-019-00473-0.
- [65] M. F. Howland, J. Bossuyt, L. A. Martínez-Tossas, J. Meyers, and C. Meneveau, “Wake structure in actuator disk models of wind turbines in yaw under uniform inflow conditions,” *Journal of Renewable and Sustainable Energy*, vol. 8, no. 4, p. 043301, 2016, doi: 10.1063/1.4955091.
- [66] J. Wang, S. Foley, E. M. Nanos, T. Yu, F. Campagnolo, C. L. Bottasso, A. Zanotti, and A. Croce, “Numerical and Experimental Study of Wake Redirection Techniques in a Boundary Layer Wind Tunnel,” *Journal of Physics: Conference Series*, vol. 854, p. 012048, 2017, doi: 10.1088/1742-6596/854/1/012048.
- [67] W. P. Engels, A. Marina, S. Kanev, and D. van der Hoek, “Condition based control,” ECN, Tech. Rep. ECN-E-017-047, 2017.
- [68] J. Annoni, P. M. O. Gebraad, A. K. Scholbrock, P. A. Fleming, and J.-W. van Wingerden, “Analysis of axial-induction-based wind plant control using an engineering and a high-order wind plant model,” *Wind Energy*, vol. 19, no. 6, pp. 1135–1150, 2016, doi: 10.1002/we.1891.
- [69] F. Campagnolo, V. Petrović, C. L. Bottasso, and A. Croce, “Wind tunnel testing of wake control strategies,” in *2016 American Control Conference (ACC)*. Boston, MA, USA: IEEE, 2016, pp. 513–518, doi: 10.1109/ACC.2016.7524965.
- [70] D. van der Hoek, S. Kanev, J. Allin, D. Bieniek, and N. Mittelmeier, “Effects of axial induction control on wind farm energy production - A field test,” *Renewable Energy*, vol. 140, pp. 994–1003, 2019, doi: 10.1016/j.renene.2019.03.117.
- [71] W. Munters and J. Meyers, “Towards practical dynamic induction control of wind farms: analysis of optimally controlled wind-farm boundary layers and sinusoidal induction con-

- trol of first-row turbines,” *Wind Energy Science*, vol. 3, no. 1, pp. 409–425, 2018, doi: 10.5194/wes-3-409-2018.
- [72] J. A. Frederik, B. M. Doekemeijer, S. P. Mulders, and J. Wingerden, “The helix approach: Using dynamic individual pitch control to enhance wake mixing in wind farms,” *Wind Energy*, vol. 23, no. 8, pp. 1739–1751, 2020, doi: 10.1002/we.2513.
- [73] M. Kretschmer, V. Pettas, and P. W. Cheng, “Effects of wind farm down-regulation in the offshore wind farm alpha ventus,” *Proceedings of the ASME 2019 2nd International Offshore Wind Technical Conference*, p. 10, 2019, doi: 10.1115/IOWTTC2019-7554.
- [74] J. Annoni, A. Scholbrock, M. Churchfield, and P. Fleming, “Evaluating tilt for wind plants,” in *2017 American Control Conference (ACC)*. Seattle, WA, USA: IEEE, 2017, pp. 717–722, doi: 10.23919/ACC.2017.7963037.
- [75] S. Boersma, B. Doekemeijer, P. Gebraad, P. Fleming, J. Annoni, A. Scholbrock, J. Frederik, and J.-W. van Wingerden, “A tutorial on control-oriented modeling and control of wind farms,” in *2017 American Control Conference (ACC)*. Seattle, WA, USA: IEEE, 2017, pp. 1–18, doi: 10.23919/ACC.2017.7962923.
- [76] F. Campagnolo, V. Petrović, J. Schreiber, E. M. Nanos, A. Croce, and C. L. Bottasso, “Wind tunnel testing of a closed-loop wake deflection controller for wind farm power maximization,” *Journal of Physics: Conference Series*, vol. 753, p. 032006, 2016, doi: 10.1088/1742-6596/753/3/032006.
- [77] B. M. Doekemeijer, S. Kern, S. Maturu, S. Kanev, B. Salbert, J. Schreiber, F. Campagnolo, C. L. Bottasso, S. Schuler, F. Wilts, T. Neumann, G. Potenza, F. Calabretta, F. Fioretti, and J.-W. van Wingerden, “Field experiment for open-loop yaw-based wake steering at a commercial onshore wind farm in Italy,” *Wind Energy Science*, vol. 6, no. 1, pp. 159–176, 2021, doi: 10.5194/wes-6-159-2021.
- [78] P. Fleming, J. Annoni, J. J. Shah, L. Wang, S. Ananthan, Z. Zhang, K. Hutchings, P. Wang, W. Chen, and L. Chen, “Field test of wake steering at an offshore wind farm,” *Wind Energy Science*, vol. 2, no. 1, pp. 229–239, 2017, doi: 10.5194/wes-2-229-2017.
- [79] P. Fleming, J. King, K. Dykes, E. Simley, J. Roadman, A. Scholbrock, P. Murphy, J. K. Lundquist, P. Moriarty, K. Fleming, J. van Dam, C. Bay, R. Mudafort, H. Lopez, J. Skopek, M. Scott, B. Ryan, C. Guernsey, and D. Brake, “Initial results from a field campaign of wake steering applied at a commercial wind farm - Part 1,” *Wind Energy Science*, vol. 4, no. 2, pp. 273–285, 2019, doi: 10.5194/wes-4-273-2019.
- [80] M. F. Howland, S. K. Lele, and J. O. Dabiri, “Wind farm power optimization through wake steering,” *Proceedings of the National Academy of Sciences*, vol. 116, no. 29, pp. 14 495–14 500, 2019, doi: 10.1073/pnas.1903680116.
- [81] M. Harrison, E. Bossanyi, R. Ruisi, and N. Skeen, “An initial study into the potential of wind farm control to reduce fatigue loads and extend asset life,” *Journal of Physics: Conference Series*, vol. 1618, p. 022007, 2020, doi: 10.1088/1742-6596/1618/2/022007.

- [82] A. M. Urbán, T. J. Larsen, G. C. Larsen, D. P. Held, E. Dellwik, and D. Verelst, “Optimal yaw strategy for optimized power and load in various wake situations,” *Journal of Physics: Conference Series*, vol. 1102, p. 012019, 2018, doi: 10.1088/1742-6596/1102/1/012019.
- [83] M. Lin and F. Porté-Agel, “Power Maximization and Fatigue-Load Mitigation in a Wind-turbine Array by Active Yaw Control: an LES Study,” *Journal of Physics: Conference Series*, vol. 1618, p. 042036, 2020, doi: 10.1088/1742-6596/1618/4/042036.
- [84] M. T. van Dijk, J.-W. van Wingerden, T. Ashuri, and Y. Li, “Wind farm multi-objective wake redirection for optimizing power production and loads,” *Energy*, vol. 121, pp. 561–569, 2017, doi: 10.1016/j.energy.2017.01.051.
- [85] B. López, A. Guggeri, M. Draper, and F. Campagnolo, “Wake steering strategies for combined power increase and fatigue damage mitigation: an LES study,” *Journal of Physics: Conference Series*, vol. 1618, p. 022067, 2020, doi: 10.1088/1742-6596/1618/2/022067.
- [86] J. Mann, “The spatial structure of neutral atmospheric surface-layer turbulence,” *Journal of Fluid Mechanics*, vol. 273, pp. 141–168, 1994, doi: 10.1017/S0022112094001886.
- [87] S. B. Pope, *Turbulent Flows*, 1st ed. Cambridge University Press, 2000. doi: 10.1017/CBO9780511840531.
- [88] J. Mann, “Wind field simulation,” *Probabilistic Engineering Mechanics*, vol. 13, no. 4, pp. 269–282, 1998, doi: 10.1016/S0266-8920(97)00036-2.
- [89] DTU Wind Energy, “Mann 64bit turbulence generator,” 2021, last access: 2021-04-13. [Online]. Available: <https://www.hawc2.dk/Download/Pre-processing-tools/Mann-64bit-turbulence-generator>
- [90] B. Maronga, M. Gryscha, R. Heinze, F. Hoffmann, F. Kanani-Sühring, M. Keck, K. Ketelsen, M. O. Letzel, M. Sühring, and S. Raasch, “The Parallelized Large-Eddy Simulation Model (PALM) version 4.0 for atmospheric and oceanic flows: model formulation, recent developments, and future perspectives,” *Geoscientific Model Development*, vol. 8, no. 8, pp. 2515–2551, 2015, doi: 10.5194/gmd-8-2515-2015.
- [91] P. Weihing, K. Meister, C. Schulz, T. Lutz, and E. Krämer, “CFD Simulations on Interference Effects between Offshore Wind Turbines,” *Journal of Physics: Conference Series*, vol. 524, p. 012143, 2014, doi: 10.1088/1742-6596/524/1/012143.
- [92] F. Zahle and N. N. Sørensen, “On the Influence of Far-Wake Resolution on Wind Turbine Flow Simulations,” *Journal of Physics: Conference Series*, vol. 75, p. 012042, 2007, doi: 10.1088/1742-6596/75/1/012042.
- [93] L. Klein, J. Gude, F. Wenz, T. Lutz, and E. Krämer, “Advanced computational fluid dynamics (CFD)-multi-body simulation (MBS) coupling to assess low-frequency emissions from wind turbines,” *Wind Energy Science*, vol. 3, no. 2, pp. 713–728, 2018, doi: 10.5194/wes-3-713-2018.
- [94] P. Weihing, C. Schulz, T. Lutz, and E. Krämer, “Comparison of the Actuator Line Model with Fully Resolved Simulations in Complex Environmental Conditions,” *Jour-*

- nal of Physics: Conference Series*, vol. 854, p. 012049, 2017, doi: 10.1088/1742-6596/854/1/012049.
- [95] S. Ivanell, J. N. Sørensen, R. Mikkelsen, and D. Henningson, “Analysis of numerically generated wake structures,” *Wind Energy*, vol. 12, no. 1, pp. 63–80, 2009, doi: 10.1002/we.285. [Online]. Available: <https://onlinelibrary.wiley.com/doi/10.1002/we.285>
- [96] M. J. Churchfield, S. Lee, J. Michalakes, and P. J. Moriarty, “A numerical study of the effects of atmospheric and wake turbulence on wind turbine dynamics,” *Journal of Turbulence*, vol. 13, p. N14, 2012, doi: 10.1080/14685248.2012.668191.
- [97] N. Troldborg, G. C. Larsen, H. A. Madsen, K. S. Hansen, J. N. Sørensen, and R. Mikkelsen, “Numerical simulations of wake interaction between two wind turbines at various inflow conditions,” *Wind Energy*, vol. 14, no. 7, pp. 859–876, 2011, doi: 10.1002/we.433.
- [98] D. Allaerts and J. Meyers, “Gravity Waves and Wind-Farm Efficiency in Neutral and Stable Conditions,” *Boundary-Layer Meteorology*, vol. 166, no. 2, pp. 269–299, 2018, doi: 10.1007/s10546-017-0307-5.
- [99] M. Churchfield, S. Lee, P. Moriarty, L. Martinez, S. Leonardi, G. Vijayakumar, and J. Bresseur, “A Large-Eddy Simulation of Wind-Plant Aerodynamics,” in *50th AIAA Aerospace Sciences Meeting including the New Horizons Forum and Aerospace Exposition*. Nashville, Tennessee: American Institute of Aeronautics and Astronautics, 2012. doi: 10.2514/6.2012-537.
- [100] K. Nilsson, S. Ivanell, K. S. Hansen, R. Mikkelsen, J. N. Sørensen, S.-P. Breton, and D. Henningson, “Large-eddy simulations of the Lillgrund wind farm: LES of the Lillgrund wind farm,” *Wind Energy*, vol. 18, no. 3, pp. 449–467, 2015, doi: 10.1002/we.1707.
- [101] M. Calaf, C. Meneveau, and J. Meyers, “Large eddy simulation study of fully developed wind-turbine array boundary layers,” *Physics of Fluids*, vol. 22, no. 1, p. 015110, 2010, doi: 10.1063/1.3291077.
- [102] A. Stieren and R. J. A. M. Stevens, “Evaluating wind farm wakes in large eddy simulations and engineering models,” *Journal of Physics: Conference Series*, vol. 1934, no. 1, p. 012018, 2021, doi: 10.1088/1742-6596/1934/1/012018.
- [103] M. P. van der Laan, M. C. Kelly, and N. N. Sørensen, “A new k-epsilon model consistent with Monin-Obukhov similarity theory,” *Wind Energy*, vol. 20, no. 3, pp. 479–489, 2017, doi: 10.1002/we.2017.
- [104] T. Koblitz, A. Bechmann, A. Sogachev, N. Sørensen, and P. E. Réthoré, “Computational Fluid Dynamics model of stratified atmospheric boundary-layer flow: CFD model of stratified atmospheric boundary-layer flow,” *Wind Energy*, 2013, doi: 10.1002/we.1684.
- [105] E. Branlard, “Analysis of wind turbine aerodynamics and aeroelasticity using vortex-based methods,” Ph.D. dissertation, DTU Wind Energy, Denmark, 2015.

- [106] N. O. Jensen, “A note on wind generator interaction,” DK-4000 Roskilde, Denmark, Tech. Rep. Risø-M-2411, 1983.
- [107] M. Bastankhah and F. Porté-Agel, “A new analytical model for wind-turbine wakes,” *Renewable Energy*, vol. 70, pp. 116–123, 2014, doi: 10.1016/j.renene.2014.01.002.
- [108] S. Boersma, B. Doekemeijer, M. Vali, J. Meyers, and J.-W. van Wingerden, “A control-oriented dynamic wind farm model: WFSim,” *Wind Energy Science*, vol. 3, no. 1, pp. 75–95, 2018, doi: 10.5194/wes-3-75-2018.
- [109] NREL, “Floris. version 2.4,” 2021. [Online]. Available: <https://github.com/NREL/floris>
- [110] J. King, P. Fleming, R. King, L. A. Martínez-Tossas, C. J. Bay, R. Mudafort, and E. Simley, “Control-oriented model for secondary effects of wake steering,” *Wind Energy Science*, vol. 6, no. 3, pp. 701–714, 2021, doi: 10.5194/wes-6-701-2021.
- [111] A. Niayifar and F. Porté-Agel, “Analytical Modeling of Wind Farms: A New Approach for Power Prediction,” *Energies*, vol. 9, no. 9, p. 741, 2016, doi: 10.3390/en9090741.
- [112] I. Katic, J. Højstrup, and N. O. Jensen, “A simple model for cluster efficiency,” in *European wind energy association conference and exhibition*, vol. 1, Rome, Italy, 1986, pp. 407–410.
- [113] S. Krüger, G. Steinfeld, M. Kraft, and L. J. Lukassen, “Validation of a coupled atmospheric-aeroelastic model system for wind turbine power and load calculations,” 2020,” doi: 10.5194/wes-2020-114.
- [114] J. Jonkman and K. Shaler, “Fast.farm user’s guide and theory manual,” National Renewable Energy Laboratory, Tech. Rep. NREL/TP-5000-78485, 2021.
- [115] B. Jonkman, R. M. Mudafort, A. Platt, M. Sprague, G. Vijayakumar, M. Buhl, S. Ananthan, M. Masciola, M. J. Schmidt, E. Branlard, jjonkman, J. Rood, rdamiani, ashesh2512, K. Bendl, pschuenemann, psakievich, N. KUSUNO, T. Martinez, robynnemurrayNREL, B. Mertz, C. Mylonas, IAbda, J. Rinker, M. Friedrich, P. Bachant, R. Hammond, lapadron, lssraman, mattEhall, and M. Kretschmer, “MatthiasCK/OpenFAST: FAST.Farm with wake-added turbulence,” 2021,” doi: 10.5281/zenodo.4733599.
- [116] J. Jonkman and M. Buhl, “Fast user’s guide,” National Renewable Energy Laboratory, Tech. Rep. NREL/TP-500-38230, 2005.
- [117] A. Ning, G. Hayman, R. Damiani, and J. M. Jonkman, “Development and Validation of a New Blade Element Momentum Skewed-Wake Model within AeroDyn,” in *33rd Wind Energy Symposium*. Kissimmee, Florida: American Institute of Aeronautics and Astronautics, 2015. doi: 10.2514/6.2015-0215.
- [118] J. E. Minnema, “Pitching moment predictions on wind turbine blades using the Beddoes-Leishman model for unsteady aerodynamics and dynamic stall,” Master’s thesis, University of Utah, 1998.
- [119] K. G. Pierce, “Wind Turbine Load Prediction Using the Beddoes-Leishman Model for Unsteady Aerodynamics and Dynamic Stall,” Master’s thesis, University of Utah, 1996.

- [120] R. Damiani, G. Hayman, Q. Wang, and J. M. Jonkman, “Development and Validation of a New Unsteady Airfoil Aerodynamics Model Within AeroDyn,” in *34th Wind Energy Symposium*. San Diego, California, USA: American Institute of Aeronautics and Astronautics, 2016. doi: 10.2514/6.2016-1007.
- [121] P. Doubrawa, J. R. Annoni, and J. M. Jonkman, “Optimization-Based Calibration of FAST.Farm Parameters against Large-Eddy Simulations,” in *2018 Wind Energy Symposium*. Kissimmee, Florida: American Institute of Aeronautics and Astronautics, 2018. doi: 10.2514/6.2018-0512.
- [122] J. Ainslie, “Calculating the flowfield in the wake of wind turbines,” *Journal of Wind Engineering and Industrial Aerodynamics*, vol. 27, no. 1-3, pp. 213–224, 1988, doi: 10.1016/0167-6105(88)90037-2.
- [123] L. A. Martínez-Tossas, E. Branlard, K. Shaler, G. Vijayakumar, S. Ananthan, P. Sakievich, and J. Jonkman, “Numerical investigation of wind turbine wakes under high thrust coefficient,” *Wind Energy*, 2021, doi: 10.1002/we.2688.
- [124] M. Kretschmer, J. Jonkman, V. Pettas, and P. W. Cheng, “FAST.Farm load validation for single wake situations at alpha ventus,” *Wind Energy Science*, vol. 6, no. 5, pp. 1247–1262, 2021, doi: 10.5194/wes-6-1247-2021.
- [125] H. A. Madsen, G. C. Larsen, T. J. Larsen, N. Troldborg, and R. Mikkelsen, “Calibration and Validation of the Dynamic Wake Meandering Model for Implementation in an Aeroelastic Code,” *Journal of Solar Energy Engineering*, vol. 132, no. 4, p. 041014, 2010, doi: 10.1115/1.4002555.
- [126] K. Shaler, J. Jonkman, and N. Hamilton, “Effects of Inflow Spatiotemporal Discretization on Wake Meandering and Turbine Structural Response using FAST.Farm,” *Journal of Physics: Conference Series*, vol. 1256, p. 012023, 2019, doi: 10.1088/1742-6596/1256/1/012023.
- [127] M. Kühn, A. Rott, P. W. Cheng, S. Duty, and K. Argyriadis, “Schlussbericht des RAVE-forschungsprojektes: Adaptive betriebsführung und Regelung von Offshore-Windparks auf Basis spezifischer Betriebsstrategien zur Ertrags-, Lasten- und Netzoptimierung (RAVE-OWP Control); Laufzeit: 01.03.2017-31.10.2020,” Oldenburg, Tech. Rep., 2021. [Online]. Available: <https://www.tib.eu/de/suchen/id/TIBKAT:1800795351/Adaptive-Betriebsf%C3%BChrung-und-Regelung-von-Offshore?cHash=d8ffc465bc4e84162d52d963073e5112>
- [128] W. Popko, M. L. Huhn, A. Robertson, J. Jonkman, F. Wendt, K. Müller, M. Kretschmer, F. Vorpahl, T. R. Hagen, C. Galinos, J.-B. Le Dreff, P. Gilbert, B. Auriac, F. N. Villora, P. Schünemann, I. Bayati, M. Belloli, S. Oh, Y. Totsuka, J. Qvist, E. Bachynski, S. H. Sørum, P. E. Thomassen, H. Shin, F. Vittori, J. Galván, C. Molins, P. Bonnet, T. van der Zee, R. Bergua, K. Wang, P. Fu, and J. Cai, “Verification of a Numerical Model of the Offshore Wind Turbine From the Alpha Ventus Wind Farm Within OC5 Phase III,” in

- Volume 10: Ocean Renewable Energy.* Madrid, Spain: American Society of Mechanical Engineers, 2018. doi: 10.1115/OMAE2018-77589.
- [129] D. Conti, N. Dimitrov, A. Peña, and T. Herges, “Calibration and validation of the dynamic wake meandering model part i: Bayesian estimation of model parameters using spinnerlidar-derived wake characteristics,” *Wind Energy Science Discussions*, vol. 2021, pp. 1–39, 2021, doi: 10.5194/wes-2020-135.
- [130] “German research initiative research at alpha ventus (RAVE),” 2021, last access: 13 January 2021. [Online]. Available: <https://www.rave-offshore.de/en/>
- [131] D. Kaufer and P. W. Cheng, “Validation of an Integrated Simulation Method with High-Resolution Load Measurements of the Offshore Wind Turbine REpower 5M at Alpha Ventus,” *Journal of Ocean and Wind Energy*, vol. 1, no. 1, pp. 30–40, 2014.
- [132] W. Popko, A. Robertson, J. Jonkman, F. Wendt, P. Thomas, K. Müller, M. Kretschmer, T. R. Hagen, C. Galinos, J.-B. Le Dreff, P. Gilbert, B. Auriac, S. Oh, J. Qvist, S. H. Sørum, L. Suja-Thauvin, H. Shin, C. Molins, P. Trubat, P. Bonnet, R. Bergua, K. Wang, P. Fu, J. Cai, Z. Cai, A. Alexandre, and R. Harries, “Validation of Numerical Models of the Offshore Wind Turbine From the Alpha Ventus Wind Farm Against Full-Scale Measurements Within OC5 Phase III,” *Journal of Offshore Mechanics and Arctic Engineering*, vol. 143, no. 1, pp. 012002–(1–18), 2021, doi: 10.1115/1.4047378.
- [133] “alpha ventus,” 2021, last access: 17 November 2021. [Online]. Available: <https://www.alpha-ventus.de/technik>
- [134] A. Westerhellweg, V. Riedel, and T. Neumann, “Comparison of lidar-and uam-based offshore mast effect corrections,” in *Proceedings of EWEA*. Brussels, 2011.
- [135] A. Westerhellweg, B. Cañadillas, A. Beeken, and T. Neumann, “One year of lidar measurements at fino1-platform: Comparison and verification to met-mast data,” in *Proceedings of 10th German wind energy conference DEWEK*. Bremen, 2010.
- [136] V. Pettas, M. Kretschmer, A. Clifton, and P. W. Cheng, “On the effects of inter-farm interactions at the offshore wind farm Alpha Ventus,” *Wind Energy Science*, vol. 6, no. 6, pp. 1455–1472, 2021, doi: 10.5194/wes-6-1455-2021.
- [137] M. Kelly, “From standard wind measurements to spectral characterization: turbulence length scale and distribution,” *Wind Energy Science*, vol. 3, no. 2, pp. 533–543, 2018, doi: 10.5194/wes-3-533-2018.
- [138] A. Westerhellweg, B. Cañadillas, F. Kinder, and T. Neumann, “Wake Measurements at alpha ventus - Dependency on Stability and Turbulence Intensity,” *J. Phys.: Conf. Ser.*, vol. 555, p. 012106, 2014, doi: 10.1088/1742-6596/555/1/012106.
- [139] K. Shaler and J. Jonkman, “FAST.Farm development and validation of structural load prediction against large eddy simulations,” *Wind Energy*, p. we.2581, 2020, doi: 10.1002/we.2581.
- [140] K. Shaler, M. Debnath, and J. Jonkman, “Validation of FAST.Farm Against Full-Scale

- Turbine SCADA Data for a Small Wind Farm,” *Journal of Physics: Conference Series*, vol. 1618, p. 062061, 2020, doi: 10.1088/1742-6596/1618/6/062061.
- [141] A. S. Wise and E. E. Bachynski, “Wake meandering effects on floating wind turbines,” *Wind Energy*, vol. 23, no. 5, pp. 1266–1285, 2020, doi: 10.1002/we.2485.
- [142] M. T. van Beek, A. Viré, and S. J. Andersen, “Sensitivity and Uncertainty of the FLORIS Model Applied on the Lillgrund Wind Farm,” *Energies*, vol. 14, no. 5, p. 1293, 2021, doi: 10.3390/en14051293.
- [143] P. Virtanen, R. Gommers, T. E. Oliphant, M. Haberland, T. Reddy, D. Cournapeau, E. Burovski, P. Peterson, W. Weckesser, J. Bright, S. J. van der Walt, M. Brett, J. Wilson, K. J. Millman, N. Mayorov, A. R. J. Nelson, E. Jones, R. Kern, E. Larson, C. J. Carey, Í. Polat, Y. Feng, E. W. Moore, J. VanderPlas, D. Laxalde, J. Perktold, R. Cimrman, I. Henriksen, E. A. Quintero, C. R. Harris, A. M. Archibald, A. H. Ribeiro, F. Pedregosa, P. van Mulbregt, and SciPy 1.0 Contributors, “SciPy 1.0: Fundamental Algorithms for Scientific Computing in Python,” *Nature Methods*, vol. 17, pp. 261–272, 2020, doi: 10.1038/s41592-019-0686-2.
- [144] J. Jonkman, S. Butterfield, W. Musial, and G. Scott, “Definition of a 5-MW Reference Wind Turbine for Offshore System Development,” Tech. Rep. NREL/TP-500-38060, 2009, doi: 10.2172/947422.
- [145] J. Jonkman and W. Musial, “Offshore Code Comparison Collaboration (OC3) for IEA Task 23 Offshore Wind Technology and Deployment,” Tech. Rep. NREL/TP-5000-48191, 2010, doi: 10.2172/1004009.
- [146] “Bundesamt für Seeschifffahrt und Hydrographie (BSH): Rave measurement database,” 2021, last access: 07 May 2021. [Online]. Available: https://www.bsh.de/EN/TOPICS/Monitoring_systems/MARNET_monitoring_network/RAVE/rave_node.html
- [147] R. Damiani, S. Dana, J. Annoni, P. Fleming, J. Roadman, J. van Dam, and K. Dykes, “Assessment of wind turbine component loads under yaw-offset conditions,” *Wind Energy Science*, vol. 3, no. 1, pp. 173–189, 2018, doi: 10.5194/wes-3-173-2018.
- [148] K. A. Kragh and M. H. Hansen, “Load alleviation of wind turbines by yaw misalignment,” *Wind Energy*, vol. 17, no. 7, pp. 971–982, 2014, doi: 10.1002/we.1612.
- [149] I. Reinwardt, L. Schilling, D. Steudel, N. Dimitrov, P. Dalhoff, and M. Breuer, “Validation of the dynamic wake meandering model with respect to loads and power production,” *Wind Energy Science*, vol. 6, no. 2, pp. 441–460, 2021, doi: 10.5194/wes-6-441-2021.
- [150] N. Dimitrov, M. C. Kelly, A. Vignaroli, and J. Berg, “From wind to loads: wind turbine site-specific load estimation with surrogate models trained on high-fidelity load databases,” *Wind Energy Science*, vol. 3, no. 2, pp. 767–790, 2018, doi: 10.5194/wes-3-767-2018.
- [151] K. Müller, M. Dazer, and P. W. Cheng, “Damage Assessment of Floating Offshore Wind

Turbines Using Response Surface Modeling,” *Energy Procedia*, vol. 137, pp. 119–133, 2017, doi: 10.1016/j.egypro.2017.10.339.

Curriculum Vitae

Matthias Kretschmer was born on September 21st, 1988 in Esslingen am Neckar, Germany and grew up in Emmendingen, Germany, where he obtained his Abitur in 2008. From 2008-2014 he studied aerospace engineering at the University of Stuttgart with specialisations taken in wind energy and fluid mechanics. Besides his studies, he worked as a tutor for the subjects thermodynamics I and II and as a tram driver in Freiburg im Breisgau, Germany. He finalised his studies with the diploma thesis on “Validation of a numerical coupling for the simulation of fluid-structure-interactions” at Stuttgart Wind Energy (SWE).



After his studies he continued at University of Stuttgart as researcher at SWE and PhD candidate. During his time at SWE, he worked on various national and international projects, including LIFES50+ and Floatgen dedicated to floating offshore wind turbines as well as CL-Windcon and OWP Control with respect to wind farm modelling and controls. He performed scientific work within the IEA Task 30 OC5 on full-scale model validation and IEA Task 37 on systems engineering. In addition, he lead projects directly funded by a global turbine manufacturer that dealt with the topics model validation and aeroelastic simulation of wind farms. Overall, his research resulted in more than 10 co-/authored publications in international conferences and journals around the topics of aeroelastic simulation of wind farms, offshore wind, floating offshore wind and wind farm controls. He supervised 20 Bachelor and Master theses and was responsible for teaching activities within the wind energy program of SWE. From October 2018 to January 2019, he performed a research stay at the National Renewable Energy Laboratory (NREL) in Boulder, USA, where he collaborated on the aeroelastic modelling of wind farms.